

CONTINUUM AND ATOMIC
HYDROGEN LINE EMISSION FROM
THE IC5146 GALACTIC COMPLEX

by

JUDITH ANN IRWIN

B.Sc., University of Winnipeg, 1975

A THESIS SUBMITTED IN PARTIAL FULFILLMENT
OF THE REQUIREMENTS FOR THE DEGREE OF
MASTER OF SCIENCE

in the Department

of

Physics

ACCEPTED
FACULTY OF GRADUATE STUDIES

DATE

18 Dec 78

DEAN

© JUDITH ANN IRWIN, 1978
UNIVERSITY OF VICTORIA
July 1978

*All rights reserved. This thesis may not be reproduced
in whole or in part, by mimeograph or other means,
without the permission of the author.*

ABSTRACT

The synthesis interferometer at the Dominion Radio Astrophysical Observatory has been used to map a 2° field around the HII region, IC5146, in the continuum and atomic hydrogen line. Resolutions of $2'.0$ in right ascension and $2'.7$ in declination were obtained as well as $0.66 \text{ km}\cdot\text{s}^{-1}$ in velocity for the HI line.

The flux density of IC5146 is $1.95 \pm 0.05 \text{ Jy}$. The excitation parameter and Lyman continuum luminosity indicate a spectral type of B0V for the exciting star. The continuum brightness distribution is consistent with an electron density distribution which falls off from the centre of the HII region in a Gaussian fashion. The average electron density and total HII mass are 26 cm^{-3} and $12.2 M_\odot$ respectively, for an electron temperature of $7000 \text{ }^\circ\text{K}$.

HI line emission extends over a range of $12 \text{ km}\cdot\text{s}^{-1}$ in radial velocity. Two spin temperatures are inferred from the data. The mass of fine structure HI ($\leq 28'$ in extent) is $230 \pm 50 M_\odot$ for a spin temperature of $120 \text{ }^\circ\text{K}$, and the mass of broad structure HI ($>28'$ in extent) is $2410 \pm 480 M_\odot$ for a spin temperature of $100 \text{ }^\circ\text{K}$.

IC5146 is on the near side of the neutral cloud and there is a deficit of HI at its position and velocity. Gas

from the HII region is expanding on the near side at about $5 \text{ km}\cdot\text{s}^{-1}$ with respect to the HI cloud. The ionization front on the far side is also still expanding into the neutral cloud at about $2 \text{ km}\cdot\text{s}^{-1}$ and there is evidence for the existence of an expanding half-shell of HI on the far side. Hill and Hollenbach's (1978) model for the dissociation of H_2 with a total particle density of 350 cm^{-3} , can account for the observed HI emission. The model implies that IC5146 is 2×10^5 years old, much younger than the associated stellar cluster age of 3×10^6 years.

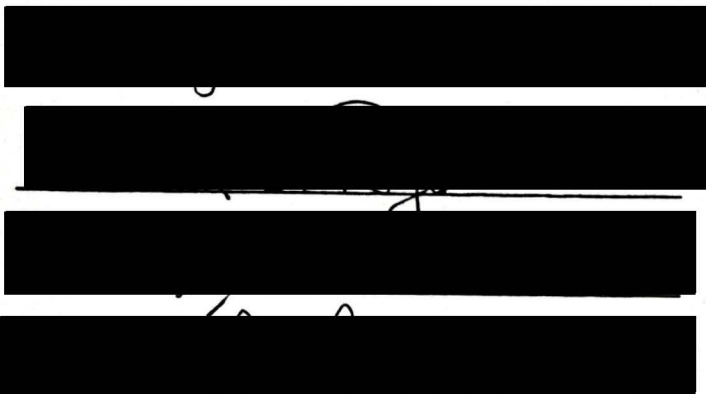


TABLE OF CONTENTS

	<u>Page</u>
ABSTRACT	ii
TABLE OF CONTENTS.....	iv-vi
LIST OF TABLES	vii
LIST OF FIGURES	viii
LIST OF SYMBOLS	xi
ACKNOWLEDGEMENTS	xv
DEDICATION	xvi
CHAPTER 1 INTRODUCTION	1
CHAPTER 2 GENERAL THEORY	9
2.1 Emission and Detection of Radiation in the Radio Region of the Spectrum	9
2.2 Astrophysics and Evolution of a Galactic Cloud Complex and HII Region	12
CHAPTER 3 OBSERVATIONS AND REDUCTIONS	19
3.1 Earth-Rotation Aperture Synthesis	19
3.2 Interferometer Observations and Reductions	23
3.3 26 m Paraboloid Observations and Reductions	31
3.4 Map Manipulations	35
CHAPTER 4 CONTINUUM EMISSION	39
4.1 Extent of the Continuum Emission	39

	<u>Page</u>
4.2 Flux Density	42
4.3 Emission Measures	43
4.4 Relation of Continuum Emission to Stellar Characteristics	48
4.5 Electron Densities and HII Masses	52
CHAPTER 5 ATOMIC HYDROGEN LINE EMISSION	60
5.1 Fine Structure and Broad Structure	60
5.2 Background Brightness Temperature Correction	61
5.3 Spin Temperatures	63
5.3.1 Calculation of T_{s_2} ...	63
5.3.2 The Two-Component Model	64
5.4 Column Densities	66
5.5 Mass of Atomic Hydrogen	71
CHAPTER 6 INTERPRETATION OF THE IC5146 COMPLEX	74
6.1 Dynamics	74
6.2 The Dissociation Model	81
6.3 Evolution	88
CHAPTER 7 SUMMARY	94
7.1 Comparison of the IC5146 Complex to a Theoretical Complex	94
7.2 Main Results from Each Chapter	96

	<u>Page</u>
7.3 Suggestions for Future	
Research	98
REFERENCES	101
APPENDIX A $1^\circ \alpha - \delta$ MAPS	107
APPENDIX B $\alpha - V$ MAPS	123
APPENDIX C $\delta - V$ MAPS	137
APPENDIX D $2^\circ \alpha - \delta$ MAPS	151

LIST OF TABLES

		<u>Page</u>
TABLE I	Coordinates and Optical Size of IC5146	5
TABLE II	Projected Radii of IC5146 Measured in Various Directions	41
TABLE III	Flux Density Measurements of IC5146	44
TABLE IV	Maximum Emission Measures for Various Electron Temperatures	47
TABLE V	Lyman Continuum Luminosities and Excitation Parameters Calculated for IC5146	50
TABLE VI	Predicted Relationships Between \mathcal{L} , U and Spectral Type	51
TABLE VII	Electron Densities and HII Masses Calculated for IC5146	55
TABLE VIII	Velocities and Velocity Ranges of IC5146	76
TABLE IX	Parameters for the Dissociation Model	86

LIST OF FIGURES

	<u>Page</u>
Figure 1.1	Reproductions of the Palomar Observatory Sky Survey prints of IC5146:
	a) O-plate (Blue) 3
	b) E-plate (Red) 4
Figure 3.1	Normalized power output of a multiplying interferometer for a point source passing through the centre of the primary beam 21
Figure 3.2	The supersynthesis interferometer at the Dominion Radio Astrophysical Observatory 25
Figure 3.3	Polar diagram weighting of the 8.6 m paraboloid primary beam as a function of the angular distance from the field centre 26
Figure 3.4	Block diagram of the interferometer receiving system 28
Figure 3.5	The 25.6 m paraboloid at the Dominion Radio Astrophysical Observatory 34

	<u>Page</u>	
Figure 3.6	Sample HI spectrum as observed by the 25.6 m paraboloid	36
Figure 4.1	Continuum map of IC5146	40
Figure 4.2	Observed and predicted brightness distributions of the continuum emission	53
Figure 4.3	Dependence of HII mass on the assumed electron temperature	58
Figure 5.1	Background brightness temperature spectrum	62
Figure 5.2	Integrated hydrogen map	65
Figure 5.3	Declination scans of the integrated hydrogen map	67
Figure 5.4	Fine structure HI column density map	69
Figure 5.5	Broad structure HI column density map	70
Figure 6.1	Fine structure HI integrated over the velocities at which the hole is seen, with the continuum emission outline superimposed	77

	<u>Page</u>
Figure 6.2 Atomic hydrogen density distribution as predicted by the dissociation model	87
Figure 6.3 Dependence of: a) the expansion velocity of IC5146 into the neutral cloud b) the radius of the initial Strömgren sphere c) the age of IC5146 on the maximum density of atomic hydrogen	93
Figure 7.1 Outlines of major features associated with IC5146	95
APPENDIX A 1° α - δ HI maps (interferometer data only) weighted by the 8.6 m polar diagram	107
APPENDIX B α - V HI maps (interferometer data only)	123
APPENDIX C δ - V HI maps (interferometer data only)	137
APPENDIX D 2° α - δ HI maps	151

LIST OF SYMBOLS

$a(\nu, T_e)$	ratio of $\tau(\nu)$ given by Oster (1961) to that given by Altenhoff et al. (1960)
b^{II}	galactic latitude
ba	beam area
B_p	number of beam areas occupied by one map point
$B(\nu)$	monochromatic brightness of a source (watts·m ⁻² ·Hz ⁻¹ ·sr ⁻¹ or mJy·ba ⁻¹) B_{ij} - at map point, ij
c	speed of light (cm·s ⁻¹)
cI	speed of sound in the neutral gas (km·s ⁻¹)
cII	speed of sound in the ionized gas (km·s ⁻¹)
C_p	the area of the sky occupied by one map point (cm ² or pc ²)
$C(\nu, T_e)$	a constant used for calculating emission measures (pc·cm ⁻⁶ ·ba·mJy ⁻¹)
d	distance through the gas along the line of sight d_{ij} - at a map point, ij
D	distance to the exciting star (pc)
D_G	distance from the galactic centre (kpc)
EM	emission measure (pc·cm ⁻⁶ or cm ⁻⁵) EM_{ij} - at a map point, ij EM(max) - maximum
G_{ij}	square of the electron density distribution integrated along the line of sight at a map point, ij
i	east-west map coordinate measured from the map centre
i	subscript indicating which side of the I-front is being referred to
I_o	initial unshielded dissociation rate at the I-front (s ⁻¹)

j	north-south map coordinate measured from map centre
Jy	Jansky (10^{-26} watts \cdot m $^{-2}$ \cdot Hz $^{-1}$)
k	Boltzmann's constant (erg \cdot °K $^{-1}$)
K	dust coefficient (cm 2)
l	diameter of an antenna
l^{II}	galactic longitude
$l.m$	number of points on a map included in a sum
L	separation between antennas
\mathcal{L}	Lyman continuum luminosity of the exciting star (photons \cdot s $^{-1}$)
m_{HI}	mass of the hydrogen atom (g)
M_{\odot}	mass of the sun (g)
M	observed mass (M_{\odot}) M_{HI} - of HI M_{HII} - of HII
n	Volume density (cm $^{-3}$) n_e - of electrons n_{HI} - of HI n_{H_2} - of H $_2$ n_t - of HI and H $_2$ n_o - initial n_{ij} - at a map point, ij n_z - one particular side of the I-front $n(s)$ - at s $n(\rho)$ - at ρ $n(max)$ - maximum $n(min)$ - minimum $n(avg)$ - average
N	column density (cm $^{-2}$) N_{CO} - of CO N_{HI} - of HI N_{H_2} - of H $_2$ N_t - of HI and H $_2$ $N(\rho)$ - at ρ N_{ij} - at a map point, ij $N(max)$ - maximum

N_{ij}	total number of electrons along a line of sight at a map point, ij
P	power
P_r	pressure P_{r_i} - on one particular side of the I-front
r	projected distance from the centre of the HII region r_{ij} - to a map point, ij
R	projected radius of the HII region R_ϕ - measured in a direction, ϕ R_{avg} - average
\mathcal{R}	molecular reformation rate ($\text{cm}^3 \cdot \text{s}^{-1}$)
s	line of sight coordinate through the gas
S_ν	flux density of the source at ν (Jy)
t	age of the HII region
T	temperature ($^\circ\text{K}$) T - electron T_e - spin T^s - cloud T^c - of the background T_1 - of the gas T_2 - of the background and the gas T_{12} - at a map point, ij T_{ij} $T(\nu)$ - at ν $T(V)$ - at V
U	excitation parameter ($\text{pc} \cdot \text{cm}^{-2}$ or cm^{-1})
v_s	shock velocity
V	radial velocity V_1, V_2 - limits of HI detection V^s - systemic V^s - expansion V^{exp} - average expansion V_{avg}
ΔV	velocity separation between maps ($\text{km} \cdot \text{s}^{-1}$)
ΔV_D	width of a purely Doppler broadened line
ΔV_m	measured line width
\mathcal{V}	volume (cm^3)

α	right ascension
α_1	recombination probability to the ground level of the hydrogen atom ($\text{cm}^3 \cdot \text{s}^{-1}$)
α_t	recombination probability to all levels of the hydrogen atom ($\text{cm}^3 \cdot \text{s}^{-1}$)
β	a constant used in the dissociation model equation and introduced from consideration of the curve of growth (cm^{-1})
δ	declination
θ	angular displacement from the centre of the beam
$\kappa_\nu(s)$	absorption coefficient at ν and a distance, s , along the line of sight (cm^{-1})
λ	wavelength
μ_i	mean molecular weight of hydrogen on one particular side of the I-front
ν	frequency
ρ	radial coordinate measured outward from the exciting star or HII region centre <ul style="list-style-type: none"> ρ_0 - radius of the initial Strömgen sphere ρ_1 - distance from the exciting star at which N_{HI} is evaluated ρ_c - average cloud radius ρ_p - present average radius of the HII region
$\Delta\rho$	an increment of ρ
τ	optical depth <ul style="list-style-type: none"> τ_1 - of the background τ_2 - of the gas $\tau(\nu)$ - at ν $\tau(V)$ - at V
ϕ	position angle

ACKNOWLEDGMENTS

I am especially grateful to Dr. R. S. Roger, my supervisor at D.R.A.O., who suggested the observation of IC5146. His willingness to answer questions, make suggestions, and provide explanations was greatly appreciated. Also, thanks to Dr. C. D. Scarfe at the University of Victoria who supervised course work and details of the degree requirements.

Mrs. D. Stewart set up the observations a number of times and Mr. R. Hamilton helped produce photographic prints for the figures. Monica Kulling helped with figures and references and also criticized the text. Mrs. E. Rohner typed the major portion of this thesis.

I would also like to thank the director of D.R.A.O., Dr. J. A. Galt, for allowing me to use the facilities there. This work was financed by the R. M. Petrie Memorial Fellowship from the University of Victoria and the National Research Council.

DEDICATION

And whatever you do in word or
deed do all in the name of the
Lord Jesus, giving thanks through
Him to God the Father.

Colossians 3:17

CHAPTER 1

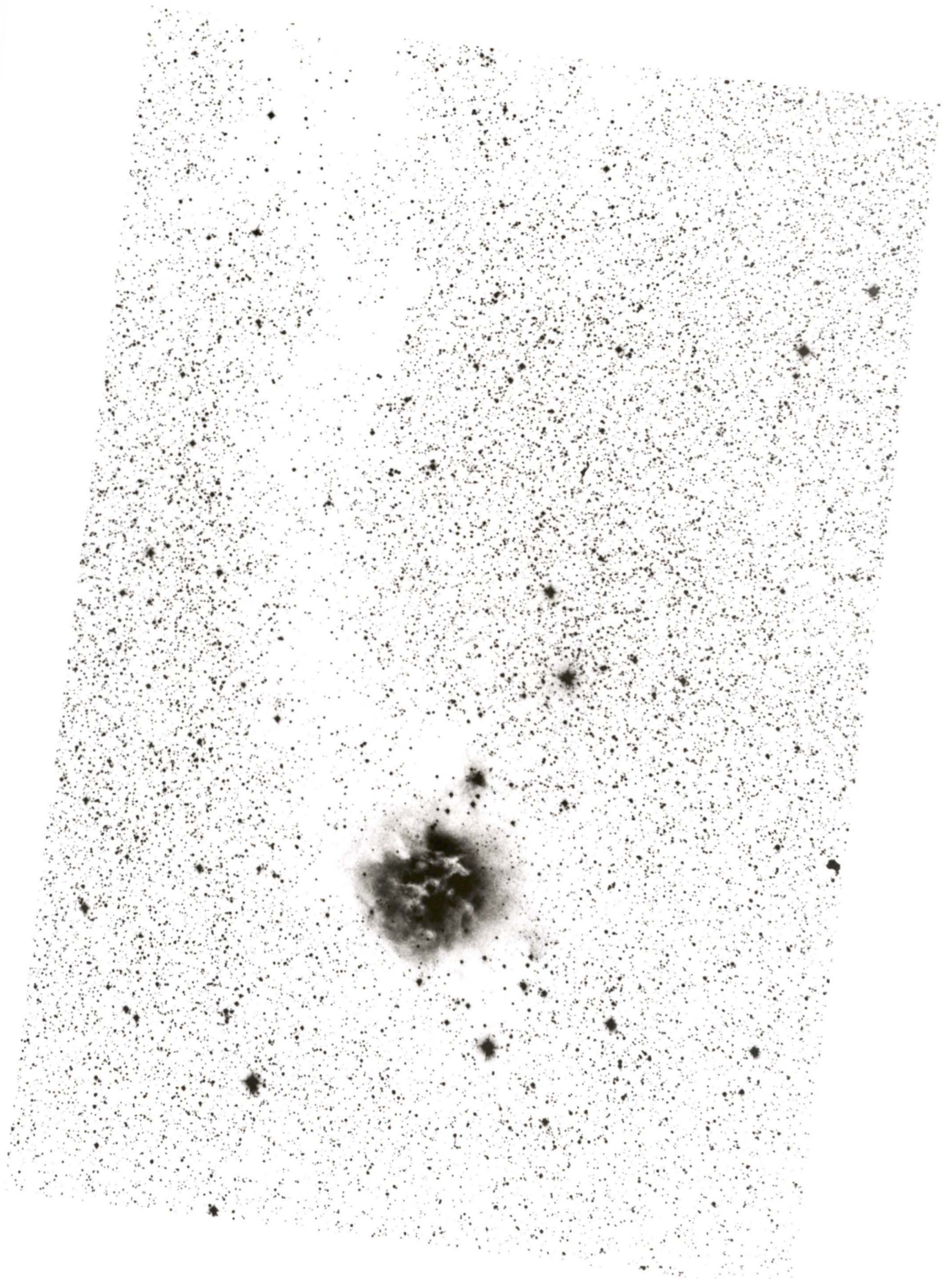
INTRODUCTION

IC5146 (S125) is a well-studied emission nebula (HII region) located in the constellation of Cygnus. It was first observed and photographed as early as 1904 by Max Wolf, who noted that the nebulosity is situated in a 'lacuna', or region in which few stars are visible. He also observed a channel of low stellar emission extending over 2° to the north-west of the nebula. We now know that these features are due to the presence of an obscuring dark cloud, whose dust content absorbs the light from background stars. Figures 1a and 1b are reproductions of the Palomar Observatory Sky Survey prints (O and E plates respectively). IC5146 can clearly be seen as a high emission region at the 'head' of a comet-like dark cloud. Lanes of obscuring matter are visible across the face of the nebula, especially on the O plate. Table I gives the coordinates¹ and angular extent of the optical nebula.

Since its discovery, various observations of IC5146 have been made. Hubble (1922a, b) observed its spectrum, and H α observations have been made a number of times (Minkowski, 1947; Courtès et al., 1968; Miller, 1968; Williamson, 1970; and Georgelin and Georgelin, 1970). Continuum radio observations began with Harris and Roberts (1960) who observed the source as CTA97. Galt and Kennedy (1968) also observed the source as DA567, and other radio continuum observations have

¹All coordinates mentioned in this thesis are for epoch 1950.

Figure 1.1 Reproductions of the Palomar Observatory Sky
Survey prints of IC5146:
a) O-plate (blue): 4.1 arcmin/cm
b) E-plate (red): 4.2 arcmin/cm



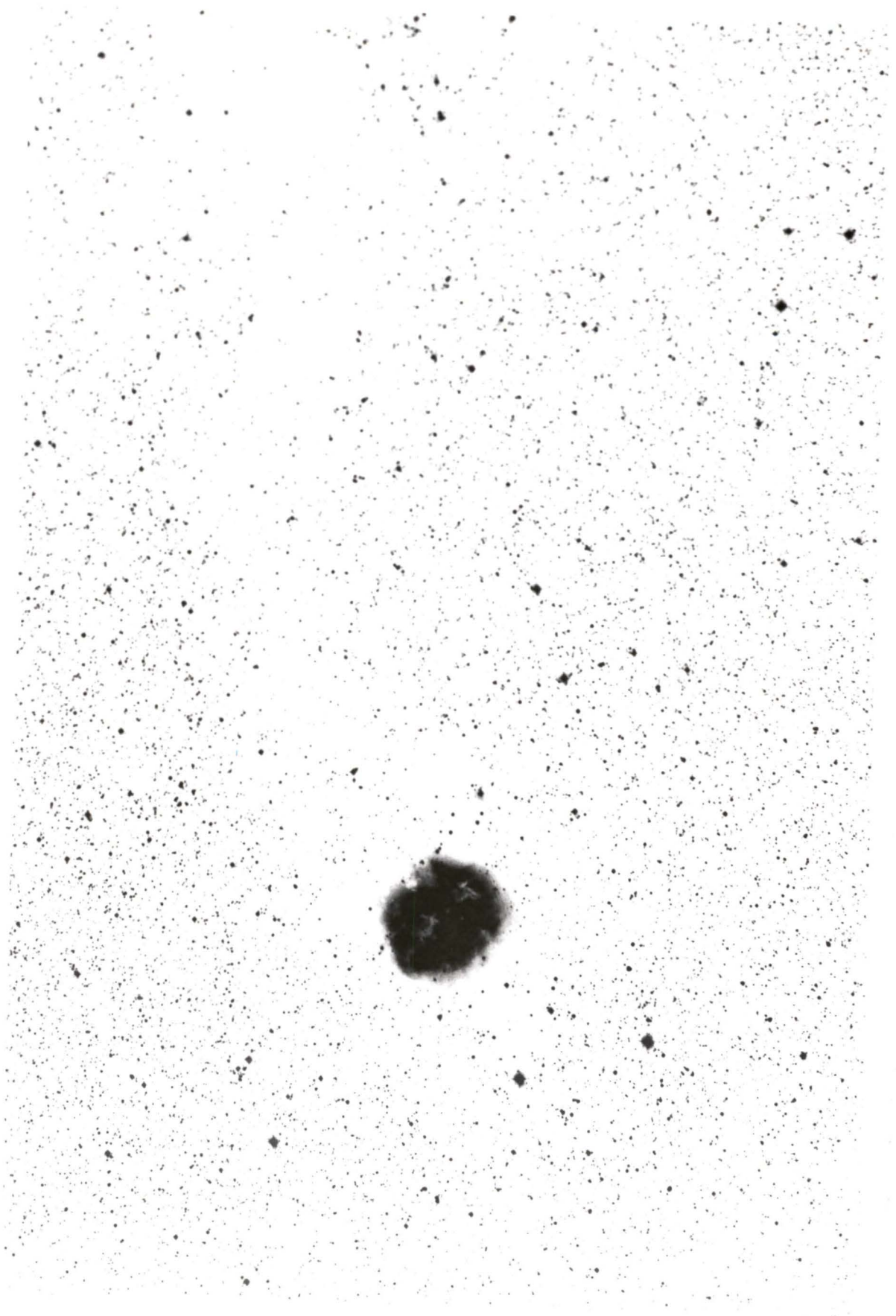


TABLE I

Coordinates and Optical Size of IC5146

l^{II}	b^{II}	α (1950)	δ	Size
94°43	-5°58	21 ^h 52 ^m	47°00'	10' x 10'

been made by Kellerman (1964), Felli and Churchwell (1972), Terzian et al. (1973), Felli et al. (1974), and Israel (1977). Radio recombination line observations in H142 α have also been made by Kuiper et al. (1976).

Associated with IC5146 is a galactic star cluster which is embedded within the nebula and optically obscured. Walker (1959) obtained photoelectric and photographic observations of the cluster, deriving a colour-magnitude diagram. Herbig (1960) detected H α emission from some of the cluster stars. Also, Samson (1976) observed a number of stellar polarization vectors indicating that there is a complex magnetic field in the region. The hottest cluster star is BD+46°3474, located in projection at the centre of the nebula. Crampton and Fisher (1974), have observed its spectrum and have classified it as a B0V star.

The dark cloud associated with IC5146 has been studied by Samson (1975) who plotted contours of equal magnitude extinction in the region. Also, Milman et al. (1975) have observed ^{12}CO and ^{13}CO at a number of positions on the dark cloud.

Observations of atomic hydrogen (HI) around HII regions such as IC5146 are particularly interesting. It is believed that there is a close evolutionary and dynamical relationship between the HII region and surrounding gas (see section 2.2). Much theory has been developed for galactic HII region-cloud

complexes, to explain star formation, the interaction between the nebula and cloud, and the effects of dust in the region. Such theories can only be proven or rejected in the light of observational evidence, including in particular, radio observations both in the continuum and the atomic hydrogen line.

The first and only atomic hydrogen observations of the IC5146 region were made by Riegel (1967), using the 300 ft. paraboloid of the National Radio Astronomy Observatory in Green Bank, West Virginia. He mapped the region with resolutions of $12'.7$, $10'.0$ and $1.06 \text{ km}\cdot\text{s}^{-1}$ in right ascension (α), declination (δ), and velocity²(V), respectively. Of the 27 HII regions which he observed two were notably rich in HI, IC5146 being one of them. Although he observed an HI velocity dispersion for IC5146, the resolution was not sufficient to determine its cause. He has also appealed for higher angular resolution.

At the Dominion Radio Astrophysical Observatory (D.R.A.O.) near Penticton, B.C., resolutions of $2'.0$ (α), $2'.7$ (δ) and $0.66 \text{ km}\cdot\text{s}^{-1}$ (V) can be achieved with the synthesis telescope (section 3.2). The nebula is in a fairly uncomplicated region of sky, and sufficiently large in angular diameter to warrant high resolution mapping. Also, since Riegel's observations, a number of developments have taken place in the theory of HII

² All velocities referred to in this thesis are radial velocities with respect to the local standard of rest (l.s.r.) unless otherwise indicated.

regions associated with dark clouds (section 2.2). For these reasons, the IC5146 region was surveyed in HI and the radio continuum at D.R.A.O. In this study we present new high-resolution continuum and HI maps of the region and attempt an interpretation of the complex.

Chapter 2 deals with basic radio astronomy relationships and presents the general theory for a complex such as IC5146. Chapter 3 covers the observational technique, observing equipment, and data reduction procedures. Chapter 4 contains a study of the continuum emission due to the HII region itself. Chapter 5 presents an analysis of the HI data alone. Chapter 6 considers the dynamic and evolutionary relationships between the HII region and surrounding cloud. Finally, chapter 7 contains a summary of the results and suggestions for future research. All series of maps can be found in the appendices.

CHAPTER 2

GENERAL THEORY

2.1 Emission and Detection of Radiation in the Radio Region of the Spectrum

Maps of the IC5146 region have been made from the present observations, showing the intensity distributions of: (1) continuum radiation due to thermal emission from the ionized hydrogen (HII) region and (2) monochromatic line radiation from the atomic hydrogen (HI) region.

(1) Thermal Emission: When a free electron approaches a free proton a deceleration of the electron takes place. Because of this deceleration, a photon is emitted at a frequency depending upon the closeness of approach, and momentum and charge of each particle (free-free emission). For many electrons and protons within an HII region, a continuous spectrum in the radio region results. The electron velocity distribution is Maxwellian, so the emission is said to be 'thermal'. For thermal emission, the excitation temperature of the gas, defined by the Boltzmann equation, is also the kinetic (electron) temperature, T_e .

(2) Spectral Line Emission: The hydrogen atom emits monochromatic line radiation in the radio region of the spectrum at a wavelength, $\lambda = 21$ cm (a frequency, $\nu = 1420.4$ MHz).

The line results from a hyperfine transition in the ground state of the atom. For an HI gas that is not extremely rarefied (densities $\geq 0.1 \text{ cm}^{-3}$), the excitation (spin) temperature of the gas, T_s , is also equal to the gas kinetic temperature (Kaplan & Pikelner, 1970).

When a source emitting radiation at a frequency, ν , is receding at a velocity, V , with respect to the observer, then the radiation is detected at a frequency which is lower than ν . The amount of shift in ν (Doppler Shift) depends upon the magnitude of V . Thus there is a relationship between the velocity of the source and the frequency of observation. For the present observations a source containing neutral hydrogen which is receding at $10 \text{ km}\cdot\text{s}^{-1}$ is detected at a frequency of 1420.49 MHz. For each velocity increase of $1 \text{ km}\cdot\text{s}^{-1}$ the corresponding decrease in frequency is 4.74 kHz.

It is the monochromatic brightness, $B(\nu)$ (ν can be replaced by V for this and the following quantities), from an area of emission on an extended radio source which is measured at the earth's surface. $B(\nu)$ is the power received per unit collecting area, per unit frequency interval, per unit solid angle, often given in units of $\text{Watts}\cdot\text{m}^{-2}\cdot\text{Hz}^{-1}\cdot\text{sr}^{-1}$.

In the present observations a modified version of $B(\nu)$ was measured, in units of milliJanskys per beam area ($\text{mJy}\cdot\text{ba}^{-1}$); where $1 \text{ Jy} = 10^{-26} \text{ Watts}\cdot\text{m}^{-2}\cdot\text{Hz}^{-1}$. For a black

body (BB) the brightness is given by Planck's law, which, at radio frequencies, is:

$$B(\nu) = \frac{2kT(\nu)\nu^2}{c^2} \dots\dots\dots 2.1$$

where: $k = 1.38 \times 10^{-16}$ erg \cdot $^{\circ}\text{K}^{-1}$ is Boltzmann's constant.

$T(\nu)$ is the temperature of the BB ($^{\circ}\text{K}$).

$c = 3.00 \times 10^{10}$ cm \cdot s $^{-1}$ is the velocity of light.

The brightness temperature of a source, $T_B(\nu)$ is defined as the temperature of a BB which would have the same monochromatic brightness as the observed source. For the present observations $1 \text{ mJy} \cdot \text{ba}^{-1} \equiv 3.70 \times 10^{-2} \text{ }^{\circ}\text{K}$ brightness temperature.

A cloud of particles in space has a certain degree of opacity depending upon the amount and nature of the absorbing particles. The degree of opacity is described by the optical depth, $\tau(\nu)$, defined by:

$$\tau(\nu) = \int_0^d \kappa_{\nu}(s) ds$$

where: s is the line of sight coordinate (cm).

d is the distance through the cloud (cm).

κ_{ν} is the absorption coefficient (cm^{-1}) at a point along the line of sight.

For a single absorbing and emitting cloud, the brightness

temperature, $T_B(\nu)$, is related to the cloud temperature, T_e or T_s , through $\tau(\nu)$ and is:

$$T_B(\nu) = T_c (1 - e^{-\tau(\nu)}) \quad \text{°K..... 2.2}$$

where: $T_c = T_s$ (line radiation)

$T_c = T_e$ (continuum radiation)

When the cloud is 'optically thin', $\tau(\nu) \ll 1$ and equation 2.2 becomes:

$$T_B(\nu) = T_c \tau(\nu) \quad \text{°K..... 2.3}$$

When the cloud is 'optically thick', the brightness temperature just becomes the cloud temperature:

$$T_B(\nu) = T_c \quad \text{°K..... 2.4}$$

Therefore, if the brightness distribution of an extended source at a number of velocities is known, equations 2.1 and 2.2 can be used to investigate the properties and dynamics of the source itself.

2.2 Astrophysics and Evolution of a Galactic Cloud Complex and HII region

In this section we wish to describe something of the

evolutionary sequence and physical processes of a 'typical' galactic complex like IC5146 and its associated features. Only those topics which are particularly relevant to the IC5146 complex will be dealt with and the extent to which IC5146 fits the model described will be looked at in chapter 6 and section 7.1.

Most interstellar gas is invisible at optical wavelengths and is in the form of atomic hydrogen (HI) or molecular hydrogen (H_2). Molecular hydrogen, in particular, is an important constituent of the interstellar medium, and especially of dark clouds such as the one around IC5146. Thus it is of interest to examine molecular hydrogen, and clouds containing molecular hydrogen.

H_2 , however, is not directly detectable from the earth's surface because it has no observable transition in either the radio or optical region of the spectrum. One indirect method of detecting the presence of H_2 is by observing the 'tracer', carbon monoxide (CO) (Encrenaz et al., 1975). Because collisions with H_2 are the most important source of CO excitation (Goldreich and Kwan, 1974; Scoville and Solomon, 1974), the distribution of CO usually implies the distribution of H_2 . The ratio of the column density of ^{13}CO , $N_{^{13}\text{CO}}$, to the column density of H_2 , N_{H_2} , is believed to be relatively constant and equal to about 2×10^{-6} in dark clouds (Elmegreen and Lada, 1978). Thus N_{H_2} can be obtained from ^{13}CO observations. CO fails to be a tracer for H_2 when $n_{H_2} \leq 100 \text{ cm}^{-3}$ because in

such a rare medium CO will neither form nor survive (Thaddeus, 1977).

How is molecular hydrogen formed and destroyed? The H_2 molecule, being homonuclear, contains no electric dipole moment and consequently no electric dipole radiation is produced from transitions between vibrational and rotational levels in any one electronic state. For this reason, radiative association of two hydrogen atoms in their ground states cannot readily form a hydrogen molecule. Instead, H_2 is believed to be formed on the surface of dust grains (Gould and Salpeter, 1963): Perhaps $1/3$ of all atoms which collide with dust grains 'stick' to the surface (Hollenbach and Salpeter, 1971) after which they migrate across the surface, collide with another H atom and form a molecule. Since dust is a catalyst for the reaction, regions of high dust concentration will be regions of molecular hydrogen. The destruction of H_2 takes place by a two-step process: First, H_2 is excited when ultraviolet (UV) radiation is absorbed in its Lyman and Werner bands. Then there is a downward transition to the vibrational continuum of the ground state where the molecule dissociates into two hydrogen atoms (Stecher and Williams, 1967). About 11% of all excited hydrogen molecules result in a dissociation (Jura, 1975).

It is the incident UV flux, and the gas and dust densities which determine the formation and destruction rates of H_2 .

These rates in turn affect the relative abundances of H_2 and HI in molecular clouds (for details see Hollenbach, Werner and Salpeter, 1971; Jura, 1974). At present the relative abundances of HI and H_2 in interstellar clouds cannot be known without observations of the cloud in question.

Stars are believed to form within dense molecular clouds (for example: Strom et al., 1975; Grasdalen et al., 1973). Instabilities within the cloud lead to fragmentation and gravitational collapse (Von Hoerner, 1975). If the newly formed star (or stars) is of spectral type earlier than B5, then it will emit UV radiation in the Lyman continuum, L_C ($\lambda < 912 \text{ \AA}$), with enough energy to ionize the hydrogen around it and form an HII region. It is well known that dense molecular clouds are associated with HII regions, and usually have masses greater than the mass of everything else (i.e. stars, HI, CO, dust, etc.) in the region (Thaddeus, 1977). We will now look at the formation and evolution of an HII region, first within a cloud of atomic hydrogen (since this is the case treated extensively in the literature) and then in a molecular hydrogen environment.

When a star suddenly 'turns on' (i.e. instantaneously reaches its maximum photon flux) in an infinite homogeneous medium of HI, then an ionization front (I-front) forms about the star as the gas surrounding the star is ionized. The I-front is very thin, roughly the mean free path length of a

'typical' ionizing L_c photon (Strömgren, 1939). It advances outward so rapidly that no mechanical effect is made upon the neutral gas (Kahn, 1954). Eventually the I-front slows down until the volume of the ionized sphere (the initial Strömgren sphere) is such, that photoionizations are in equilibrium with recombinations. The time it takes for the HII region to reach this stage is called the 'formation time' of the nebula. In real situations a star does not turn-on instantaneously. For a star initially in a medium of density $> 10 \text{ cm}^{-3}$, the HII region formation time is just the turn-on time of the star: typically, 10^4 years.

After formation, HI and HII densities are approximately equal, but the temperature in the HII region is much higher than that of the HI. This produces a strong pressure gradient across the I-front ($P_r \propto nT$; P_r the pressure, n the density, T the temperature) causing the I-front to expand outward (Savedoff and Green, 1955). A shock wave forms and precedes the I-front into the neutral gas at a velocity roughly equal to the sound velocity in the ionized gas, c_{II} (typically $\approx 10 \text{ km} \cdot \text{s}^{-1}$). The neutral gas accelerates as the shock wave passes through (Kahn, 1954) causing HI to pile up and compress between the shock front (S-front) and I-front. As the shocked HI density increases, the pressure gradient decreases. The HII region stops expanding when dynamical equilibrium is established, and this occurs when the shock velocity, v_s , equals the sound speed in the neutral gas, c_I (typically

$\approx 1 \text{ km} \cdot \text{s}^{-1}$).

Observations have been made of HI around HII regions and in a number of cases expanding shells have been suspected (Davies and Tovmassian, 1963; Wade, 1958; Raimond, 1966; Girstein and Rohlif, 1964). If these are indeed expanding shells then the thickness of the shells is much greater than theory predicts. Various effects have been proposed to account for the discrepancy (Lasker, 1966a, b, 1968; McPherson, 1974) but the observations are not yet completely understood.

We will now consider an exciting star initially in a completely molecular hydrogen environment. An HII region will again form from UV radiation of $\lambda < 912 \text{ \AA}$. However, radiation of $\lambda = 912 \text{ \AA}$ to $\lambda = 1108 \text{ \AA}$ can also dissociate hydrogen molecules, so an HI-H₂ transition region, or dissociation front (D-front) will be formed as well. Mendis (1968a, b) first considered this situation, and found that the I-front and D-front are virtually combined. Although he did not include dissociation by the 2-step process described earlier, his results are valid for the formation time of the nebula. Recently Hill and Hollenbach (1978) have also investigated HII regions expanding into molecular clouds. They find the following: During the expansion stage of the HII region, the D-front moves ahead of both the I-front and the S-front. It becomes extremely broad, as wide as the region of dissociated H₂ (i.e. HI region) and is better referred to as a 'dissocia-

tion wave' (D-wave). As the atomic hydrogen approaches equilibrium the D-wave slows down at a faster rate than the S-front, broadens even more, and is finally overtaken by the S-front. For models in which the initial gas density is $10^3 - 10^4 \text{ cm}^{-3}$, the S-front passes through the centre of the D-wave when $v_s \approx 3-4 \text{ km}\cdot\text{s}^{-1}$ and $t \approx 7 \times 10^4 \rightarrow 2 \times 10^5$ years after stellar turn-on. The D-wave is then 'trapped' between the I and S-fronts. Typical post-shock column densities are predicted to be $\approx 10^{21} \text{ cm}^{-2}$ during the nebula expansion stage.

CHAPTER 3OBSERVATIONS AND REDUCTIONS3.1 Earth-Rotation Aperture Synthesis

The resolution of a circularly symmetric aperture (such as a paraboloidal antenna) of diameter, L , is proportional to λ/L . At a wavelength of 21 cm, this means that antennas with diameters of the order of 1 km are required for a resolution of ≈ 1 arcmin. However, the engineering of such large antennas is not feasible, and instead, two small moveable antennas (dishes) can be used. By obtaining observations of a source at various hour angles and dish separations (baselines), and by keeping track of the correlated power from the antennas, the brightness distribution of a source can be reconstructed (Fomalont, 1973). Because observations are necessary over a period of time, this technique can only be used for sources whose brightness distributions do not vary within the observing period.

The rotation of the earth can be used to alter the orientation of the baseline as projected on the sky. Consider two antennas along an east-west track at an intermediate latitude separated by L and observing a source at the north celestial pole (NCP). As viewed from the NCP, one dish will trace out a circle of radius, L , around the other over a 24 hour period. If the dish separation is changed another circle of different radius will be traced out. Observations can be

made at all radii from zero out to some finite separation until the source has been observed from all positions within a circular aperture (i.e. the aperture has been 'filled'). For an observed source at some declination, $\delta < 90^\circ$, the synthesized aperture is an ellipse with the north-south axis shortened to $L \sin \delta$. The projected plane of the telescope aperture as seen from the source is called the UV plane. It turns out, from symmetry considerations, that only 12 hour observations at each separation are necessary to completely fill the aperture in the UV plane.

Two paraboloids used in such a system, comprise an interferometer. Radiation from a point source at a non-zero hour angle (HA) must travel farther to reach one antenna than the other, the path difference depending on HA and L. As HA changes, the path difference also changes, and if the signal voltages from the two dishes are multiplied together, the power output, P, will vary sinusoidally with time. Each paraboloid has a finite beamwidth (or resolution) depending upon its diameter, l, so radiation can only be received from a field of view within the antenna beam. However, the response is not uniform for all positions within the field. The variation of this response with angular displacement, θ , from the field centre is called the polar diagram or power pattern. The polar diagram is circularly symmetric about the axis of the paraboloid. Figure 3.1 shows the normalized power response of an interferometer for a point source which

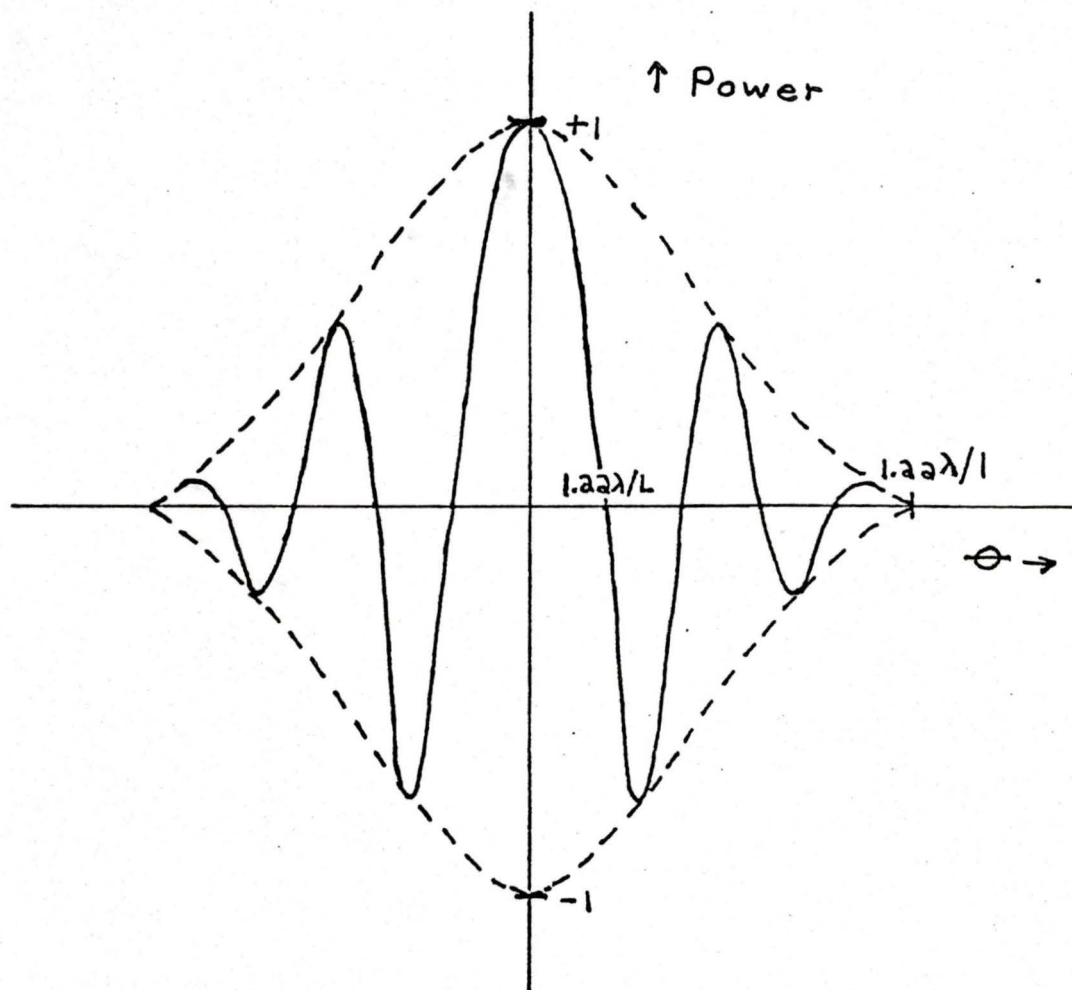


Figure 3.1 Normalized power output of a multiplying interferometer for a point source passing through the centre of the primary beam.

is passing through the centre of the primary beam of an antenna. As the angle of the source changes with time, this 'fringe' pattern is traced out.

The interferometer can be thought of as putting fringes across the field of view, and the orientation of the fringes on the sky changes with time. If an extended source is within the field, then radiation from various positions on the source will add together or cancel to contribute to the 'net' power received by the telescope. The contribution from a particular point on the source depends upon the dish separation, the brightness of the source at that point, and the polar diagram weighting at that point. To put this another way: the power response is proportional to the convolution¹ of the source brightness distribution with the polar diagram of the antenna. The convolution theorem applied to the above, states that the Fourier transform² (F.T.) of the power response is equal to the F.T. of the brightness distribution multiplied by the F.T. of the polar diagram. The convolution theorem is very useful for interferometer observations of this kind, and it turns out that a two-dimensional (2-D) F.T. from the UV plane to the $\alpha - \delta$ plane, reproduces the brightness

¹ The convolution of 2 functions, f and g , is defined by:

$$f(\mu_0) \cdot g(\mu_0) = \int_{-\infty}^{\infty} g(\mu) f(\mu - \mu_0) d\mu$$

² The Fourier transform is defined as follows:

$$f \text{ is the F.T. of } g \text{ if: } f(s) = \int_{-\infty}^{\infty} g(t) e^{2\pi i s t} dt$$

distribution multiplied by the polar diagram. It is then a simple matter to correct for the polar diagram.

3.2 Interferometer Observations and Reductions

Observations were made with the 'supersynthesis' interferometer (Figure 3.2) at D.R.A.O. (Roger et al., 1973) during an observing period from March 28 to June 21, 1977. The interferometer antennas are two 8.6 m steerable parabolic reflectors. Each paraboloid has a half power beam width of 1.7° and the polar diagram of its primary beam can be seen in figure 3.3. This allowed the mapping of a region of sky 2° in diameter with the centre of the field at $\alpha = 21^{\text{h}} 51^{\text{m}} 36^{\text{s}}.0$, $\delta = 47^\circ 01' 56''$ (epoch 1950), also the centre of IC5146. The dishes are equatorially mounted on towers which can be moved along an east-west track 300 m in length. The track is divided into 70 spacings (or stepping intervals), each separated by a distance approximately equal to the dish radius (i.e. 4.286 m). IC5146 was observed at each of 68 spacings, from 3 to 70 (dish separations of 3×4.3 m to 70×4.3 m), the maximum separation corresponding to a resolution of $2' \times 2'$ csc δ at a wavelength of 21 cm. Each observation at a single spacing was twelve hours in length, beginning at an hour angle of 15^{h} and tracking to 3^{h} . During one twelve-hour period, a sample was taken every 3.36 minutes and both tracking and sampling were controlled by a Digital Equipment Corporation PDP-9 computer. The control and data logging programs were written by Dr. C.H. Costain.

Figure 3.2 The supersynthesis interferometer at the Dominion Radio Astrophysical Observatory.



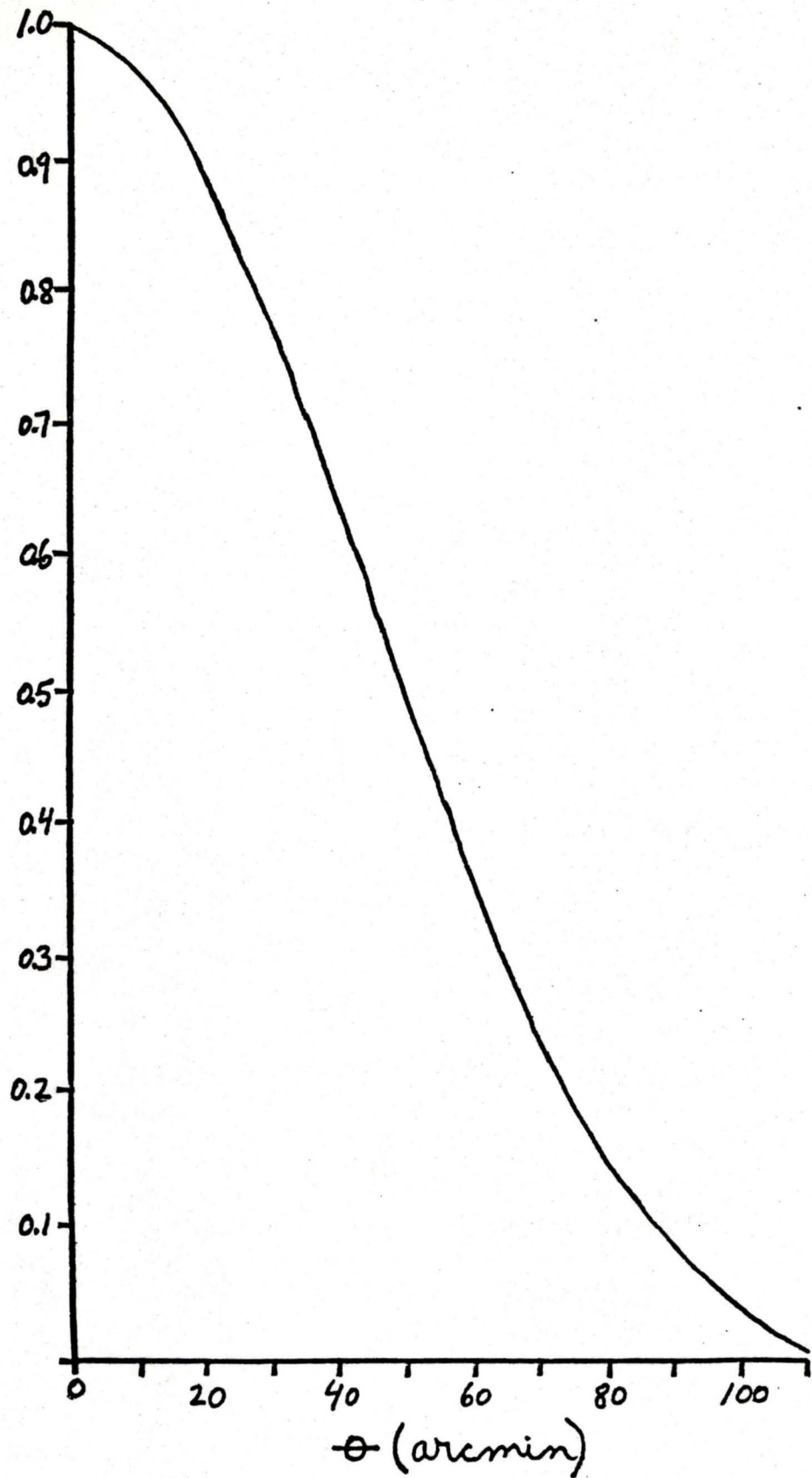


Figure 3.3 Polar diagram weighting of the 8.6 m paraboloid primary beam as a function of the angular distance θ , from the field centre.

The receiving system is described in a block diagram modified from Roger et al. (1973), in Figure 3.4. The incoming signal to both antennas is first amplified and passed through filters which leave a band roughly 35 MHz in width and centred on 1420 MHz. The filter output is then mixed with a phase-controlled local oscillator (LO) signal at 1390 MHz. The LO phase is continually adjusted by computer while the source is being tracked in order to correct for signal phase shifts due to the rotation of the earth, the motion of the earth around the sun and motions with respect to the l.s.r. This 'freezes' the interferometer fringes on the source. The intermediate frequency after mixing is 30 MHz and at this corresponding long wavelength, phase control is trivial. Also, losses in cables are much less at lower frequencies.

A finite path difference between signals received at the two antennas corresponds to different phase shifts for different frequencies across the 35 MHz band. To equalize phase shifts across the band, the signals are passed through a path delay compensator which causes one signal to travel through extra lengths of cable, equalizing the two signal paths. As the source is tracked, the length of extra cable is continually altered by computer for a proper delay correction. In spite of this, slight path (and therefore phase) differences between incoming signals may still occur from day to day, or spacing to spacing. They may be due to small

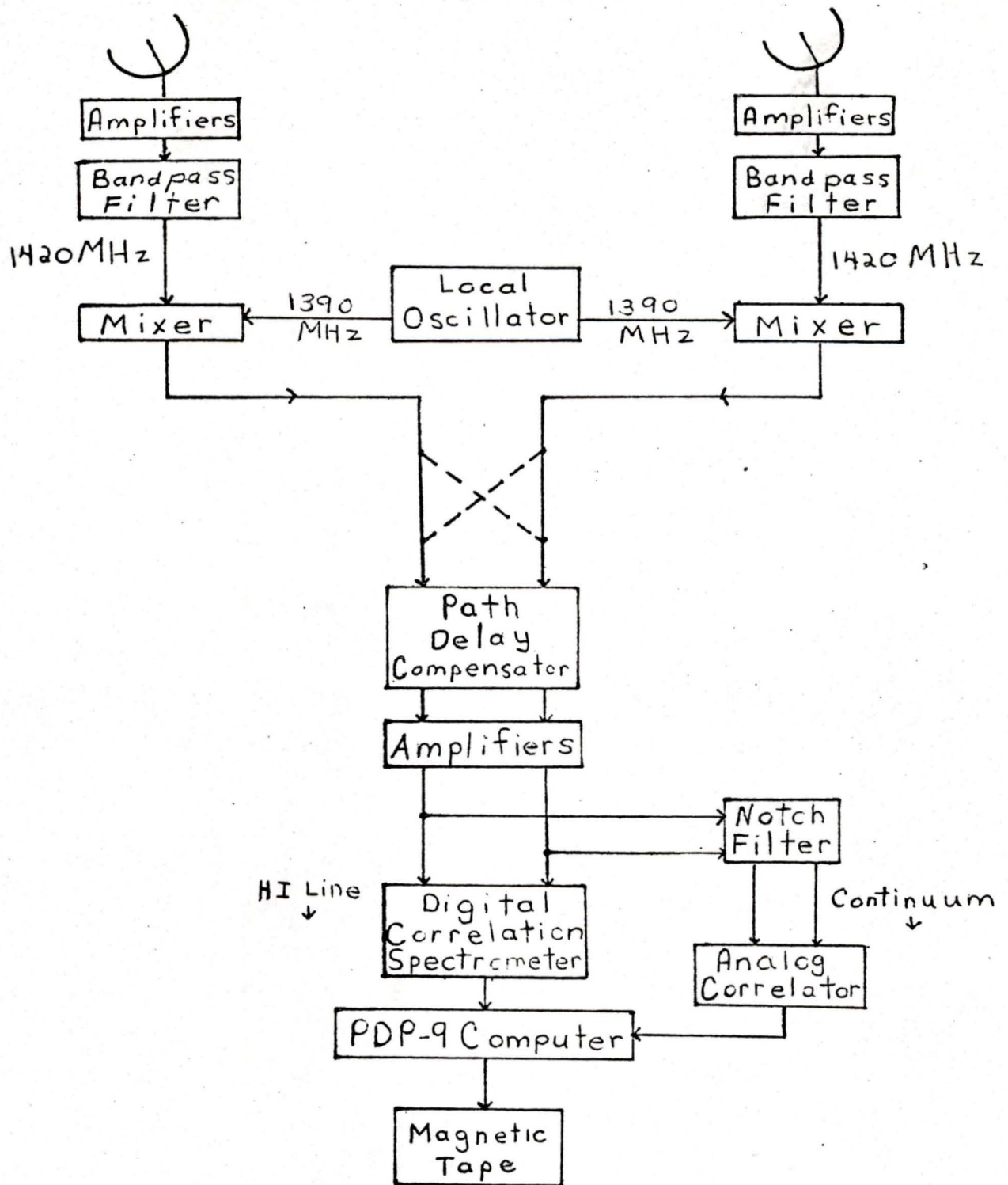


Figure 3.4 Block diagram of the interferometer receiving system.

errors in the position of one dish with respect to the other, or due to slight fluctuations in the receiving system. To keep track of minor phase variations in order to correct for them during data reduction, 20 minute calibrations of the point source 3C147 (a quasar) were made at each spacing. 3C147 was also used to calibrate the flux density scale for the IC5146 observations and was observed at a frequency near 1420 MHz which avoided any absorption features in its spectrum. At 1415 MHz the flux density of 3C147 is $S_{1415} = 22.45 \pm 0.35$ Jy (Fomalont and Moffat, 1971). After path compensation the signals are again amplified and the bandwidth is reduced to 20 MHz.

To obtain continuum data uncontaminated by galactic hydrogen emission, the signal is passed through a notch filter. The filter removes 5 MHz from the centre of the 20 MHz band, leaving 15 MHz over which the continuum can be averaged. The signals are multiplied in an analog correlator and the output is stored on magnetic tape.

Line information is obtained by passing the signal through further mixing and filtering stages which reduce the band to the range $\frac{1}{4}$ to $\frac{1}{2}$ MHz (quasi-baseband conversion). Both the 20 MHz and $\frac{1}{4}$ MHz band responses were measured twice during the survey in order to correct for filter responses. This was done by making 2 hour observations of the strong source, Cygnus A (3C405). Cygnus calibrations also provided

a check on the entire receiving system. Weekly 'cross-talk' calibrations (P. Dewdney, to be published) also allowed the bandshapes to be measured: The dishes are pointed in different directions and twenty minute observations made at a frequency well away from local hydrogen frequencies. Equal small amounts of noise are 'leaked' from one signal path into the other at positions indicated by the dashed lines in Figure 3.4. The noise is then correlated and the $\frac{1}{4}$ MHz bandshape can be measured. A cross-talk also checks the receiving system from the 'leakage-point' onward.

After quasi-baseband conversion, the signals enter a digital correlation spectrometer (Bowers et al. 1973). The time-delay cross-correlation function is stored on magnetic tape, and spectra are obtained by a Fourier transform from the time to the frequency domain. The $\frac{1}{4}$ MHz band is divided into 125 frequencies (channels) which contain HI line information. The channel separation is 1.95 kHz ($\Delta V = 0.41 \text{ km}\cdot\text{s}^{-1}$), and the frequency resolution for the $\frac{1}{4}$ MHz band is 3.13 kHz ($0.66 \text{ km}\cdot\text{s}^{-1}$).

The main reduction programs were written by P. Dewdney and G. Croes and include some subroutines originally written by C. Costain. They are in basically three steps:

- 1) PHASEØ: This constructs a table of all information pertinent to the reductions. Calibration information is reduced to include a minimum amount of data.

- 2) PHASE1 - NTRLUD: This applies the bandshape and phase corrections and scales the data to flux density units (i.e. applies Cygnus, cross-talk and 3C147 calibrations). It also rearranges (or transposes) the data so that a two-dimensional array depicts the UV plane at one frequency.
- 3) PHASE2: This first converts from polar coordinates to rectangular coordinates in the UV plane. It then performs the 2-D Fourier transform employing the fast Fourier transform (FFT) algorithm of Cooley and Tukey (1965).

One continuum map which has been averaged over the 15 MHz band is produced, as well as 125 maps at frequencies within the $\frac{1}{4}$ MHz band centred at 1420.49 MHz. A map is in the form of a 128 x 128 array which covers a $128'$ ($\approx 2^\circ$) square region of sky centred on IC5146. The array elements are in units of $\text{mJy}\cdot\text{ba}^{-1}$ but are still weighted by the polar diagram of the 8.6 m dishes (Figure 3.4). Also, each map containing real emission has a baseline which is depressed below zero. This is because data from spacing zero have not been added to the maps. Consequently each map consists of cosine and sine functions which add up to zero.

3.3 26 m Paraboloid Observations and Reductions

It was physically impossible to obtain interferometer

observations at spacings 0, 1, and 2 (x 4.3 m) along the track because of the closeness of the two dishes. Therefore to supplement the interferometer data, IC5146 was also observed with the 25.6 m paraboloid (Figure 3.5) at D.R.A.O. The half-power beamwidth of this dish is 36' at $\lambda 21$ cm (Locke, Galt and Costain, 1965).

Two minute computer controlled observations were made of 113 positions at 16' intervals within a circular field of view centred on IC5146. The incoming signal was split into two signals and sent through the same receiving system as the interferometer, beginning with and including the path delay compensator (Figure 3.4). To check the receiving system of the 26 m dish and the $\frac{1}{4}$ MHz bandshape, an observation was made of a 'blank' region of sky at a position and velocity where no HI is known to exist. Also, to calibrate the temperature scale, observations were made of the standard source, S6 (Williams, 1973), which has a peak brightness temperature of 51 ± 4 °K.

The data were first Fourier transformed from the time to the frequency domain to give a spectrum for each of the 113 observational points. Spectra were then corrected for the $\frac{1}{4}$ MHz bandshape. At this point the line emission was seen to be superimposed on a positive baseline of continuum emission and receiver noise. The baseline was therefore reduced to zero, leaving only an HI line spectrum for each point. Figure

Figure 3.5 The 25.6 m paraboloid at the Dominion Radio
Astrophysical Observatory.



3.6 shows a sample spectrum revealing a peak due mainly to general background hydrogen in the IC5146 region.

In general, the reduction involved a transform to the UV plane, a filtering off of data equivalent to interferometer spacings ≥ 3 , and a 2-D F.T. back to the sky brightness plane. It was also necessary to correct for the beamshape of the 26 m dish. The result was 125 2° line maps, each containing data for spacings 0, 1, and 2 only. These maps are also in the form of 128 x 128 arrays with elements in units of $^\circ\text{K}$.

3.4 Map Manipulations

The maps were manipulated as follows:

A. Interferometer Maps:

- 1) 125 spectral line maps from the $\frac{1}{4}$ MHz band:

Emission shown on these maps is due to the hydrogen line superimposed on a continuum. Since the continuum map was readily available and in an appropriate format, it was a simple matter to subtract the continuum from each line map.

Each map was also reduced to a 64 x 64 array to cover only a $64'$ ($\approx 1^\circ$) square field centred on IC5146. The root-mean-square (rms) noise was calculated for ten of these maps which show no HI emission, and the average rms noise is 6°K . Thirty maps showing HI emission can be seen in appendix A. Contours have been drawn above the baseline rather than the zero level in these figures and no correction for the polar

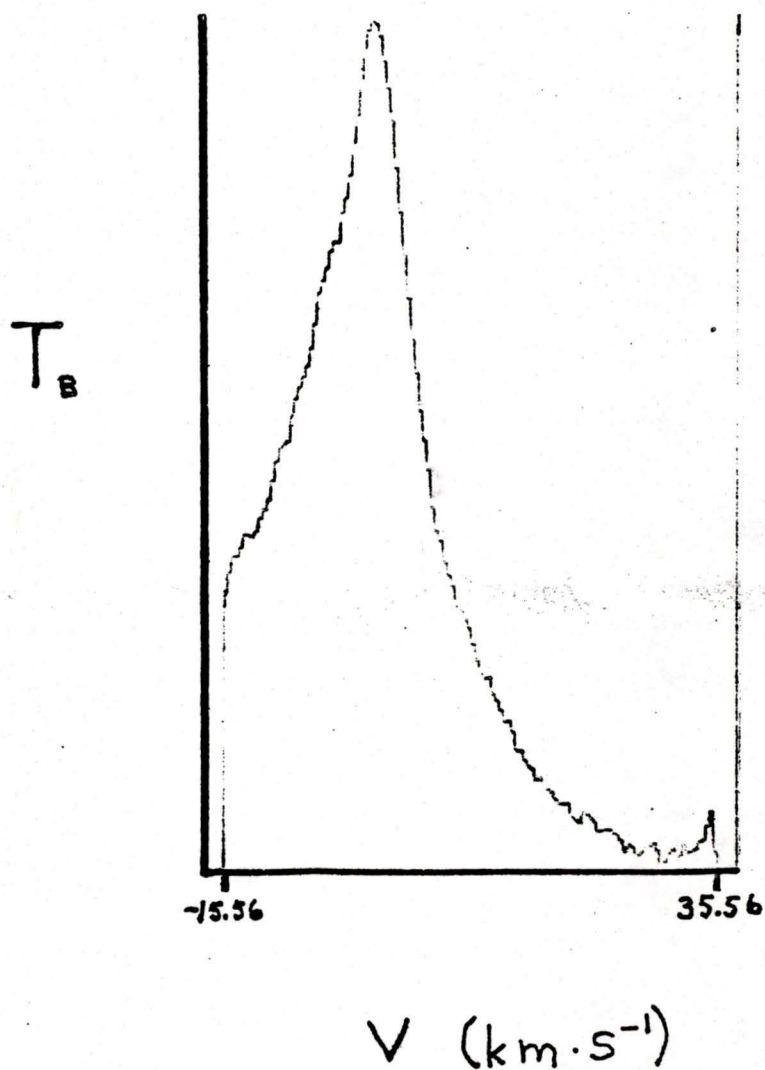


Figure 3.6 Sample spectrum for hydrogen at $\alpha = 21^{\text{h}}49^{\text{m}}33.9^{\text{s}}$, $\delta = 45^{\circ}49.3$, as observed by the 25.6 m paraboloid.

diagram has been made.

From the 1° $\alpha - \delta$ maps, $\alpha - V$ and $\delta - V$ maps were produced over the velocity range $-6.90 \leq V \text{ (km}\cdot\text{s}^{-1}) \leq 19.07$. Selected $\alpha - V$ and $\delta - V$ maps can be seen in appendices B and C respectively. Contours were drawn above the baselines for these maps also.

2) The continuum map from the 15 MHz band:

This map was also reduced to cover only a 1° square region of sky. Since the continuum emission is small in angular extent and low in intensity, the baseline is depressed only slightly to $-2 \text{ mJy}\cdot\text{ba}^{-1}$. Each map point was then increased by $2 \text{ mJy}\cdot\text{ba}^{-1}$ to raise the baseline to zero and the rms noise is $4 \text{ mJy}\cdot\text{ba}^{-1}$ (0.1°K). The map was also corrected for the polar diagram with the maximum correction amounting to an increase of only $1 \text{ mJy}\cdot\text{ba}^{-1}$ or 0.3% of the peak emission. The corrected continuum map can be seen in Figure 4.1.

B. Total Line Maps:

Complete line maps must include all spacings from 0 to 70, corresponding to a completely filled aperture in the UV plane. This required a simple addition of two sets of maps:

1) Spacings 3 - 70: 2° line maps with depressed baselines corrected for the 8.6 m dish polar diagram and converted into units of $^\circ\text{K}$ (section 2.1).

2) Spacings 0, 1, 2: 2° line maps as indicated in section

3.4. Thirty final maps can be seen in appendix D. Noise is evident around the periphery of the map because the polar diagram correction increases the noise at the map edge with respect to the map centre. Background hydrogen is still present in these maps (section 5.2) so in order to emphasize hydrogen from the region near IC5146 only, contours have been set at levels above the background (Figure 5.1). This is equivalent to performing the subtraction in the numerator of equation 5.2 and assuming that the denominator ≈ 1 .

CHAPTER 4
CONTINUUM EMISSION

4.1 Extent of the Continuum Emission

The continuum map has been produced from the interferometer data (section 3.4) and can be seen in Figure 4.1. It shows a smooth increase in intensity to a peak about 1 arcmin to the northwest of map centre. The centre of the continuum emission was assumed to be at the position of this peak. The main emission region is almost circular with a small 'knob' on the north end. Two small regions of emission can also be seen to the north of the main component. Both the knob and smaller northern features have been resolved by Israel (1977) and found to be separate background sources, unrelated to IC5146. In the present survey, it was assumed that these are the only real contributions to the continuum map, other than the emission from IC5146 itself.

To obtain the northern boundary of the continuum emission, map contours were interpolated visually to exclude the knob. The boundary of IC5146 was set at a point where the emission falls to levels within $2 \text{ mJy} \cdot \text{ba}^{-1}$ of the baseline level (within the rms noise level). Slightly different projected radii, R_{ϕ} , can be measured from the centre to the boundary of the emission, depending upon the position angle, ϕ , at which the radius is measured. Table II gives values of R_{ϕ} for a number of directions of measurement. The maximum east-west extent of the continuum emission is

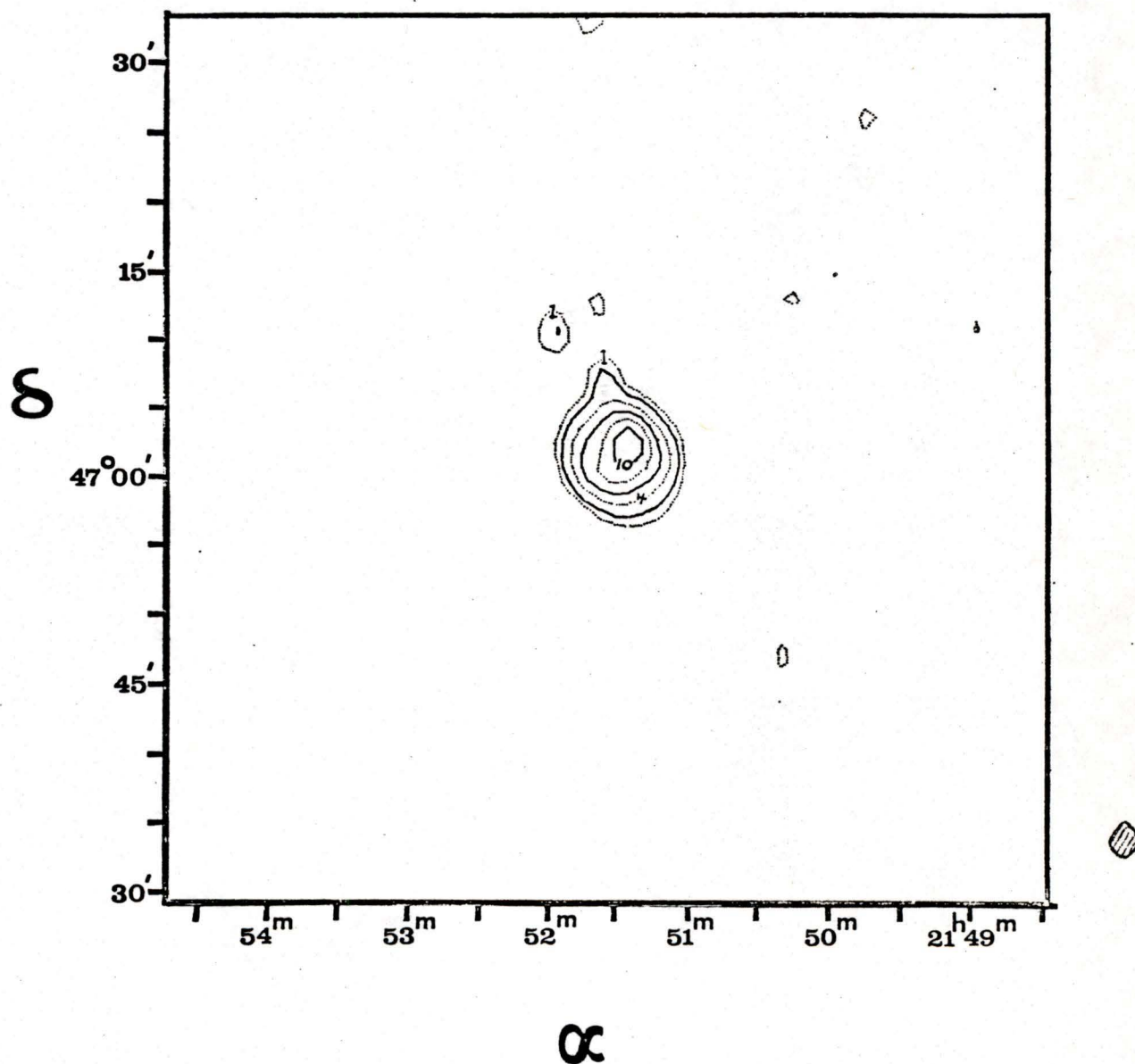


Figure 4.1 Corrected continuum map of IC5146. Contour levels are at brightness temperatures of: 1, 2, 4, 6, 8, and 10 °K, with contours of alternating dotted and solid lines.

TABLE II

Projected Radii of IC5146 Measured
at Various Position Angles

Position Angle, ϕ	R_{ϕ} (arcmin)
West : 270°	5.0
South-west: 225°	6.5
South: 180°	8.0
South-east: 135°	7.0
East : 90°	6.0
North-east: 45°	5.5
North: 0°	5.0
North-west: 315°	5.0

11 arcmin, and the maximum north-south extent is 13 arcmin. The average projected radius is $R_{\text{avg}} = 6$ arcmin which corresponds to 1.68 pc using a distance to the exciting star of $D = 960$ pc (Crampton and Fisher, 1974)¹.

4.2 Flux Density

The flux density of IC5146 is:

$$S_{\nu} = B_p \cdot (1 \times 10^{-3}) \sum_{i=1}^{\ell} \sum_{j=1}^m B_{ij} \quad \text{Jy} \dots \dots \dots 4.1$$

where: i and j are east-west and north-south map coordinates respectively, measured from map centre.

B_{ij} is the brightness at a point, ij , in units of $\text{mJy} \cdot \text{ba}^{-1}$.

$\ell \cdot m$ is the number of points on the map within a rectangle ($13' \times 11'$ in size for the continuum map), over which the sum was obtained.

$B_p = 0.194$ is the number of beam areas occupied by one map point.

If points outside the boundary of IC5146 are included in the above sum, then S_{ν} is altered only slightly, since these points are both positive and negative noise values. Also, the error in the flux density calculated for IC5146

¹ Strictly speaking, a slight correction should be made for the effects of beam broadening, but this correction is not large enough to affect the results found throughout the rest of this thesis.

must be at least as large as the error quoted for the calibration source, 3C147 (section 3.2). From these effects, an error of 2.5% was estimated, yielding a total flux density of: $S_{\nu} = 1.95 \pm 0.05$ Jy.

Table III compares flux densities calculated by various observers. A flux density is often estimated by using only the peak brightness of the source and angular width at half-maximum (HPBW). The present calculation, however, involves an integration of many points over the source. Therefore a more accurate estimate of the true flux density should result.

4.3 Emission Measures

Equation 2.2 relates brightness temperature of the continuum emission to optical depth. The maximum brightness temperature of IC5146 is $\approx 12^{\circ}\text{K}$ compared to electron temperatures of about 10^4 $^{\circ}\text{K}$ (see later). Thus the nebula is optically thin, and equation 2.3 is applicable; that is:

$$T_B = T_e \tau(\nu) \dots\dots\dots 4.2$$

Altenhoff et al. (1960) have formed an approximation to $\tau(\nu)$, and Oster (1961) has derived an exact expression for it. Following Mezger and Henderson (1967), and from equation 4.2, the brightness temperature at a point, $T_{B_{ij}}(\nu)$, depends upon the electron density distribution, $n_{e_{ij}}(s)$, in the following manner:

TABLE III

Flux Density Measurements of IC5146

ν GHz	Designation	HPBW	S_{ν} Jy	Reference
0.958	CTA 97	48'	4.4 \pm 0.6	Kellerman (1964)
0.96	CTA 97	48'	4.5 \pm 0.6	Harris and Roberts (1960)
1.4	DA 567	10'.3 x 11'.1	2.18 \pm 0.06	Bridle et al. (1972)
1.4	S125	10'	2.4	Felli and Churchwell (1972)
1.415	S125	24'.6 x 33'.6	1.6 \pm 0.2	Israel (1977)
1.42	CTA 97	36'	5.1 \pm 2.6	Kellerman (1964)
1.42	DA 567	36'	2.2	Galt and Kennedy (1968)
1.42	IC 5146	2'.0 x 2'.7	1.95 \pm 0.05	present work
2.3	IC 5146	21'	2.2 \pm 0.1	Klein (1975) quoted by Kuiper et al. (1976)
2.695	IC 5146	5'.2	2.0 \pm 0.3	Terzian et al. (1973)
8.3	IC 5146	2'.1	2.50 \pm 0.15	Kuiper et al. (1976)

$$T_{B_{ij}}(\nu) = 8.235 \times 10^{-2} a(\nu, T_e) \left[\frac{T_e}{K} \right]^{-0.35} \left(\frac{\nu}{\text{GHz}} \right)^{-2.1} \int_0^{d_{ij}} \left[\frac{n_{e_{ij}}(s)}{\text{cm}^{-3}} \right]^2 ds \quad \text{°K} \dots\dots\dots 4.3$$

where: s is the line of sight coordinate, in pc, measured from $s = 0$ at the near edge to $s = d_{ij}$ at the far edge of the HII region.

$a(\nu, T_e)$ is the ratio of $\tau(\nu)$ (Oster) to $\tau(\nu)$ (Altenhoff et al.), tabulated as a function of ν and T_e by Mezger and Henderson and can be seen in Table IV.

$$EM_{ij} = \int_0^{d_{ij}} n_{e_{ij}}^2(s) ds \quad \text{pc} \cdot \text{cm}^{-6} \dots\dots\dots 4.4$$

is the emission measure at a point.

Equation 4.3 indicates that the emission measure is directly proportional to the measured radiation intensity and is independent of distance.

For simplicity, and because the emission measure is only weakly dependent upon the electron temperature, T_e is assumed to be constant throughout the HII region. However, this may not strictly be the case, since temperature fluctuations do exist in HII regions (Peimbert, 1967). Seaton (1974) argues, from a theoretical viewpoint, that T_e should increase with increasing distance from the exciting star. Recently, Peimbert and S. Torres-Peimbert

(1977) have observed optical emission lines for 12 regions in the Orion Nebula and have found temperature differences of up to 4000°K . To provide an idea of the errors resulting from an assumption of constant T_e , emission measure calculations were carried out for four different electron temperatures.

Clearly, electron temperature measurements of IC5146 itself are needed. Kuiper et al. (1976) have observed the $\text{H}142\alpha$ recombination line in IC5146 and have obtained an electron temperature of $T_e = 10270 \pm 2100 - 1400^\circ\text{K}$. Considering the line width only, and assuming that the line broadening is thermal, they also find $T_e = 7800^\circ\text{K}$. T_e will be less than 7800°K if other mechanisms are broadening the line. They tentatively adopted a value of $T_e = 9000^\circ\text{K}$. Williamson (1970) has observed IC5146 in $\text{H}\alpha$, and, from line widths, in the same manner as Kuiper et al., find $T_e \leq 5500 \pm 1000^\circ\text{K}$. Four temperatures used for the following continuum calculations were chosen to span the above range, and are: 4000, 6000, 8000, and 10,000 $^\circ\text{K}$.

For points, B_{ij} , in units of $\text{mJy}\cdot\text{ba}^{-1}$, and solving for the emission measure at a point, equation 4.3 becomes:

$$EM_{ij} = C(\nu, T_e) B_{ij}$$

where: $C(\nu, T_e)$ are given in Table IV for each assumed T_e .

Four maps of emission measures were produced, and the peak

TABLE IV

Maximum Emission Measures for Various
Electron Temperatures

T_e °K	$a(1.42, T_e)$	$C(1.42, T_e)$ ($\text{pc} \cdot \text{cm}^{-6} \cdot \text{ba} \cdot \text{mJy}^{-1}$)	EM(max) ($\text{pc} \cdot \text{cm}^{-6} \times 10^4$)
4×10^3	0.9926	17.25	0.550
6×10^3	0.9962	19.81	0.632
8×10^3	0.9964	21.90	0.699
1×10^4	0.9953	23.71	0.756

emission measure from each, $EM(\max)$, can also be seen in Table IV.

4.4 Relation of Continuum Emission to Stellar Characteristics

It is UV radiation in the Lyman continuum ($\lambda < 912 \text{ \AA}$) from the exciting star, which ionizes the hydrogen around it. Therefore, a study of the continuum emission from an HII region will provide information about the central exciting star. The exciting star of IC5146, BD+46°3474, has been classified by Crampton and Fisher (1974) as being of spectral type B0V. It is also highly reddened (Walker, 1959), and Reddish (1967) has suggested that this is due to a surrounding parent globule out of which the star was formed, implying that BD+46°3474 is quite young.

It is now necessary to assume a geometric model for IC5146. Because of the circular symmetry displayed on the continuum map, and from HII region theory (section 2.2) a spherical model is chosen. Assuming an equilibrium situation, the number of Lyman continuum quanta, \mathcal{L} , emitted by the star per second and absorbed within a sphere of volume, \mathcal{V} , must be equal to the number of recombinations to levels of principal quantum number $n > 1$ in the same volume:

$$\mathcal{L} = (\alpha_t - \alpha_1) \frac{4\pi}{3} \left(\frac{U}{\text{cm}^{-1}} \right)^3 \text{ s}^{-1} \dots\dots\dots 4.5$$

where: α_t is the recombination probability to all levels ($\text{cm}^3 \cdot \text{s}^{-1}$).

α_1 is the recombination probability to the first level ($\text{cm}^3 \cdot \text{s}^{-1}$).

From Kaplan and Pikelner (1970):

$$\alpha_t - \alpha_1 = 2.9 \times 10^{-13} \left[\frac{10^4}{T_e} \right]^{0.85} \text{cm}^3 \cdot \text{s}^{-1}$$

U (in $\text{pc} \cdot \text{cm}^{-2}$) is the excitation parameter, given by:

$$\frac{4}{3} \pi U^3 = \int_V n_e^2 dV = C_p \sum_{i=1}^l \sum_{j=1}^m EM_{ij} \dots\dots\dots 4.6$$

where: $C_p = (2.9 \times 10^{-4} D)^2$ is the area occupied by one map point (in pc^2).

The above calculations, however, assume that the nebula is ionization bounded, and since this may not be true on the near side (section 6.1), then both \mathcal{L} and U will be lower limits. Over the temperature range assumed, the present calculations yield:

$$14.6 \leq U \text{ (lower limit)} \leq 16.3$$

$$47.15 \leq \log \mathcal{L} \text{ (lower limit)} \leq 47.35$$

Table V compares excitation parameters and Lyman continuum luminosities found by various observers. Table VI gives predicted relationships between \mathcal{L} , U, and spectral type. Panagia's (1973) predictions for U and $\log \mathcal{L}$ are most consistent with the present calculations and indicate that BD+46°3474 is of spectral type B0V (ZAMS). This result agrees with Crampton and Fisher's classification and

TABLE V

Lyman Continuum Luminosities and Excitation
Parameters Calculated for IC5146

T_e (°K)	\mathcal{L} (s^{-1})	$\log \mathcal{L}$	U ($pc \cdot cm^{-2}$)	Reference
7500			17	Terzian et al. (1973)
9000	$1.7^{+0.5}_{-0.4} \times 10^{47}$	47.23	17.0 ± 1.5	Kuiper et al. (1976)
10,000			16	Israel (1977)
4000	2.25×10^{47}	47.351	14.6	present work
6000	1.83×10^{47}	47.262	15.4	" "
8000	1.58×10^{47}	47.199	15.9	" "
10,000	1.42×10^{47}	47.151	16.3	" "

TABLE VI

Predicted Relationships Between \mathcal{L} , U and Spectral Type

Spectral Type	$\log \mathcal{L}$		U		Reference
	$\Upsilon(\text{ZAMS})$	Υ	$\Upsilon(\text{ZAMS})$	Υ	
B0	47.36	47.63	17.6	21.7	Panagia (1973)
B0.5	46.23	46.50	7.3	9.1	
B1	45.29	45.52	3.5	4.3	
B0	47.62	47.98	24	31	Churchwell and Walmsley (1973)
B0.5	46.65	46.93	11	14	
B1	45.18	45.42	3.5	4	
B0		46.63			Rubin (1968)
B0.5		46.00			

confirms that IC5146 is ionized by a young star.

4.5 Electron Densities and HII Masses

Knowing the emission measures, EM_{ij} , at each point, ij , on the continuum map, the average electron density, $n_e(\text{avg})$, and mass, M_{HII} , of the HII region must be calculated. However, equation 4.4 requires the assumption of an electron density distribution, at least in the line of sight coordinate, s .

In Figure 4.2 the observed brightness distribution (in arbitrary units) of the continuum emission is plotted, showing a decrease in intensity with projected distance from the centre, r . The electron density distribution which is chosen for the calculation of $n_e(\text{avg})$ and M_{HII} must be able to reproduce this observed brightness distribution. For each density model assumed, emission measures (in arbitrary units) were calculated for projected radii, r , using equation 4.4. The resulting predicted distributions were then scaled and compared to the observed distribution.

Two models are now considered:

MODEL #1: Uniform electron density distribution

The simplest choice is a uniform distribution throughout the entire HII region:

$$n_{e_{ij}}(s) = n_e(\text{max}) \quad \text{for all } i,j, \quad 0 \leq s \leq d_{ij}$$

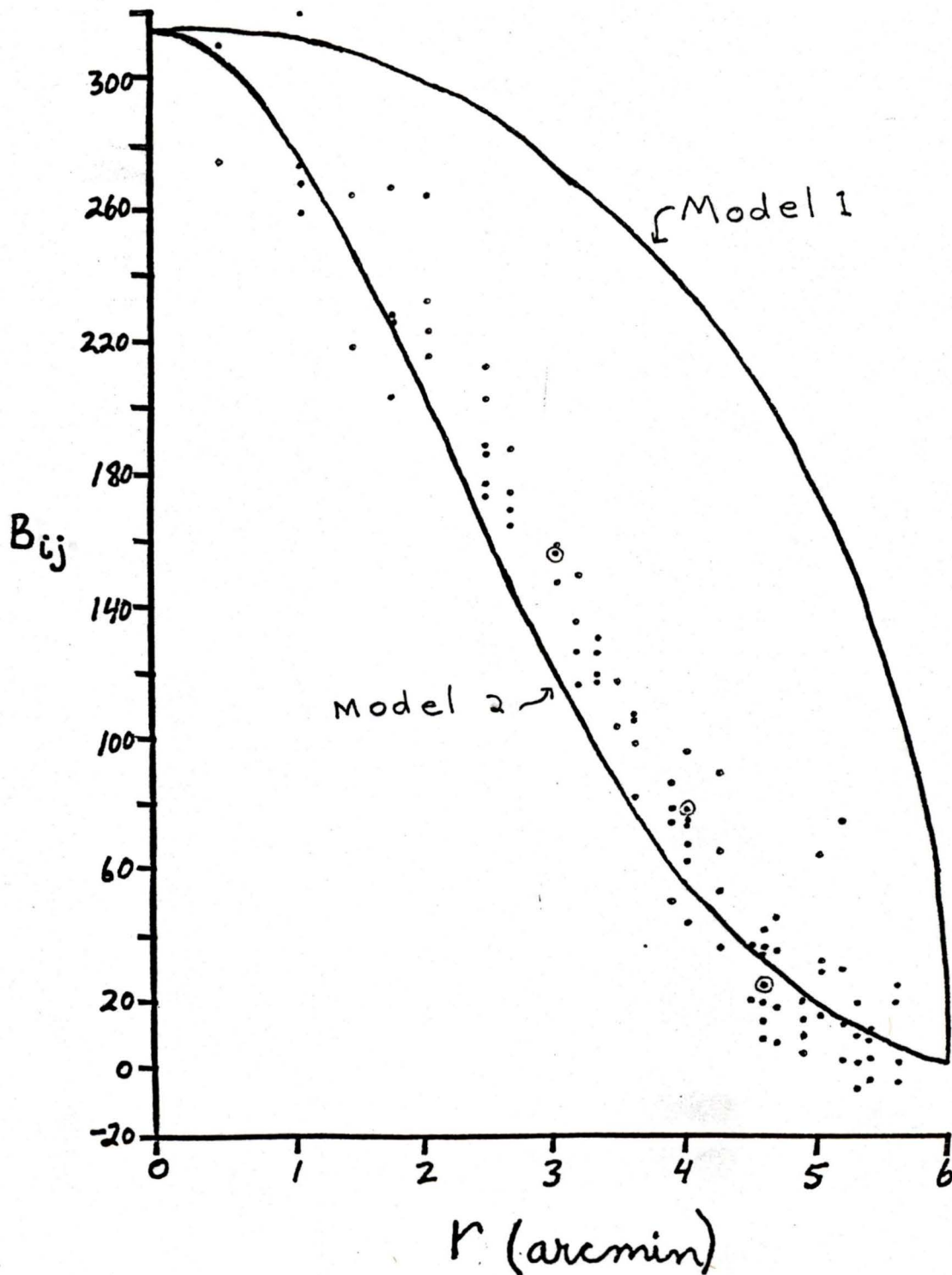


Figure 4.2 Observed brightness distribution of the continuum emission (scatter of points) as a function of angular radius from the centre. If two points occur at the same position, then they are circled. Solid curves are the predicted brightness distributions for:

- Model #1: Uniform electron density
- Model #2: Gaussian electron density distribution in the line of sight.

Previous calculations of M_{HII} have been made by a number of observers (Riegel, 1967; Terzian et al., 1973; Kuiper et al., 1976; Israel, 1977) all of whom have assumed this model. M_{HII} was also calculated from the present data using four electron temperatures and the equation derived by Mezger and Henderson (1967) for a uniform distribution. Results of these calculations can be seen in Table VII.

The predicted brightness distribution expected from a uniform electron density distribution, however, does not adequately represent the data (see Figure 4.2), and a more sophisticated model is required.

MODEL #2: Gaussian distribution in the line of sight

Figure 4.2 also shows the predicted brightness distribution expected from a Gaussian density distribution of the form:

$$n_e(\rho) = n_e(\text{max}) \exp \left[\frac{-1.9 \rho^2}{R_{\text{avg}}^2} \right] \quad \text{cm}^{-3} \quad \dots \quad 4.7$$

where: $n_e(\text{max})$ is the electron density at the centre.

ρ is the distance from the centre of the HII region.

(ρ and R_{avg} in appropriate units)¹

This was the model which was chosen, since it resulted in a reasonable fit to the data, and it indicates that there

1. Units are occasionally omitted from equations where they can be easily inferred from the context.

TABLE VII

Electron Densities and HII Masses Calculated for IC5146

T_e (°K)	n_e (max) (Centre of HII region) cm^{-3}	n_e (avg) cm^{-3}	n_e (min) (at the I-front) cm^{-3}	M_{HII} Model 1 (M_{\odot})	M_{HII} Model 2 (M_{\odot})	Reference
7500		29*		18		Terzian et al. (1973)
9000		100*		6		Kuiper et al. (1976)
10,000				20†		Riegel (1967)
10,000				7		Israel (1977)
4000	60.1	23.6	9.0	12.7	11.1	present work
6000	65.1	25.4	9.7	13.6	11.8	" "
8000	68.4	26.7	10.2	14.3	12.5	" "
10,000	71.2	27.8	10.6	14.9	13.0	" "

* These are the only listed electron densities which have been determined assuming a uniform density model (Model 1).

† Riegel used the flux density of Kellerman (1964) to calculate M_{HII} .

is indeed a decrease in electron density from the centre of the HII region outward.

Since the density distribution need only be assumed in the line of sight, then at a point, ij:

$$n_{e_{ij}}(s) = n_{e(\max)_{ij}} \exp \left[-1.9 \left(\frac{r_{ij}^2 + s^2}{R_{\phi}^2} \right) \right] \text{ cm}^{-3} \dots 4.8$$

$$0 < s \leq d_{ij}$$

where: $n_{e(\max)_{ij}}$ is the maximum electron density at a map point.

From equations 4.4 and 4.8:

$$n_{e(\max)_{ij}} = \sqrt{\frac{EM_{ij}}{G_{ij}}} \text{ cm}^{-3}$$

(for EM_{ij} in cm^{-5})

where:

$$G_{ij} = 2 \int_0^{d_{ij}/2} \exp \left[-3.8 \frac{r_{ij}^2 + s^2}{R_{\phi}^2} \right] ds \text{ cm}$$

Then the total number of electrons along a line of sight at a point, ij, are:

$$N_{ij} = 2 \cdot C_p \int_0^{d_{ij}/2} n_{e_{ij}}(s) ds$$

(for C_p in cm^2)

The average electron density of the HII region is:

$$n_e(\text{avg}) = \frac{\sum_{i=1}^l \sum_{j=1}^m N_{ij}}{V} \text{ cm}^{-3} \dots \dots \dots 4.9$$

where: $V = 5.55 \times 10^{56} \text{ cm}^3$ is the volume occupied by the HII region.

Assuming that the number of electrons equals the number of protons within the nebula, then the total mass of the HII region, in solar mass units, is:

$$M_{\text{HII}} = \frac{m_{\text{HI}}}{M_{\odot}} \sum_{i=1}^l \sum_{j=1}^m \mathcal{N}_{ij} \dots\dots\dots 4.10$$

where: $m_{\text{HI}} = 1.674 \times 10^{-24} \text{ g}$ is the mass of the hydrogen atom.

$M_{\odot} = 1.989 \times 10^{33} \text{ g}$ is the mass of the sun.

The results of these calculations for four electron temperatures can be seen in Table VII. Over the temperature range it is found that:

$$60.1 \leq n_e(\text{max}) \leq 71.2$$

$$23.6 \leq n_e(\text{avg}) \leq 27.8$$

$$9.0 \leq n_e(\text{min}) \leq 10.6$$

$$11.1 \leq M_{\text{HII}} \leq 13.0$$

Figure 4.3 shows the dependence of M_{HII} on assumed electron temperature for models 1 and 2. Model 2 represents M_{HII} to the extent that a Gaussian density distribution in the line of sight reproduces the observed brightness distribution shown in Figure 4.2. An estimate of the error introduced from choosing model 2, was obtained by repeating the calculations assuming a uniform density in

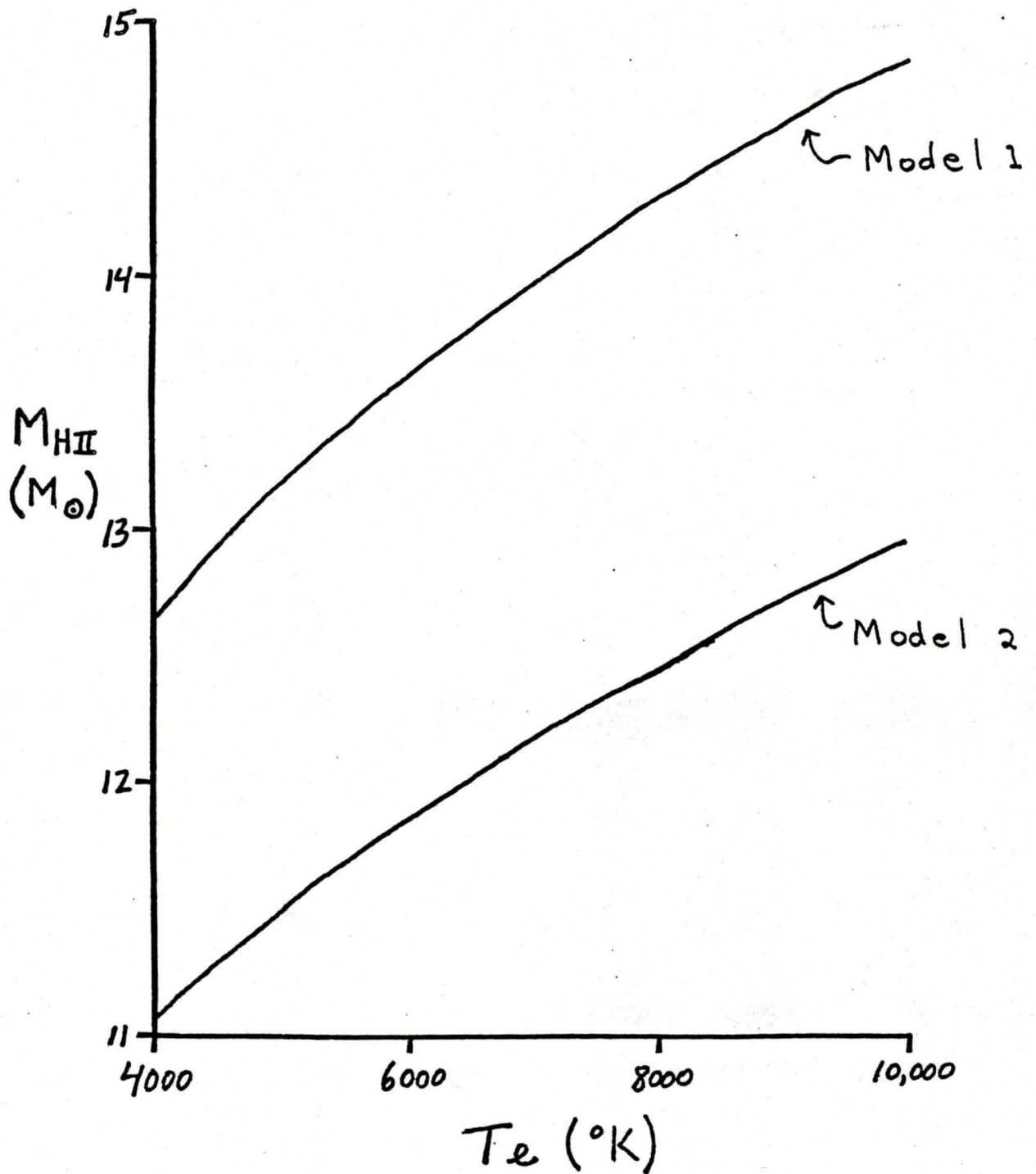


Figure 4.3 Dependence of HII mass on the assumed electron temperature for models 1 and 2.

the line of sight. In this case, M_{HII} is increased by only 6%.

The two measured temperatures for IC5146 (section 4.3) span a temperature range over which the HII mass varies about $1 M_{\odot}$. These two temperatures average to 7250°K . Also, Churchwell and Walmsley (1975), using data of Reifenstein et al. (1970), have investigated the dependence of electron temperatures in HII regions, on their distances from the galactic centre, D_G . They find that, for HII regions in the range $9 \leq D_G \leq 11$ kpc, and of low emission measures ($\leq 10^5 \text{ pc}\cdot\text{cm}^{-6}$), an average electron temperature is 6600°K . Thus, $T_e = 7000^{\circ}\text{K}$ has been chosen as the most probable electron temperature for IC5146, from which the HII mass is:

$$M_{\text{HII}} = 12.2 \pm 1 M_{\odot}$$

CHAPTER 5

ATOMIC HYDROGEN LINE EMISSION

5.1 Fine Structure and Broad Structure

Two sets of HI maps were initially produced (sections 3.2, 3.3) and it was sometimes helpful to consider them separately: those made from the interferometer data (Appendix A) which include source structure $\leq 28'$ in extent (fine structure), and those made from the 26 m paraboloid data which only include source structure $> 28'$ in extent (broad or extended structure). Thus, it is the use of two different radio telescopes which separates broad from fine structure. However, it will be shown (section 5.3.2) that there is some justification from the HI emission itself, for a separation of components near $28'$.

Both fine and broad structure maps were investigated for the presence of atomic hydrogen over the observed velocity range: $-15.56 \leq V \text{ (km}\cdot\text{s}^{-1}) \leq 35.56$. Each fine structure map has a depressed baseline, provided the map contains real positive emission. It was found that fine structure HI extends from $V_1 = 1.76 \text{ km}\cdot\text{s}^{-1}$ to $V_2 = 13.71 \text{ km}\cdot\text{s}^{-1}$: the velocity range over which depressed baselines are detected. Broad structure HI in the region does not extend beyond V_1 or V_2 . Therefore $V_1 \leq V \leq V_2$ is the velocity range chosen for the total atomic hydrogen maps (Appendix D).

5.2 Background Brightness Temperature Correction

Background atomic hydrogen can be seen in the vicinity of IC5146, and will contribute to the observed brightness temperature near the HII region. The brightness temperature of the background, $T_{B_1}(V)$ ($V_1 \leq V \leq V_2$), was measured from each of the total HI line maps by averaging points over a reference region well away from the main emission. Figure 5.1 shows the measured background brightness temperature as a function of velocity.

The observed brightness temperature near IC5146, with a background contribution is:

$$T_{B_{12}}(V) = T_{B_1}(V) e^{-\tau_2(V)} + T_{B_2}(V) \quad ^\circ\text{K} \dots\dots 5.1$$

where: $T_{B_1}(V)$, $T_{B_2}(V)$ are given by equation 2.2.

$T_{B_2}(V)$ is the brightness temperature of the gas itself without a background contribution.

$\tau_2(V)$ is the optical depth of the gas.

Rearranging, and applying equation 2.2 yields:

$$T_{B_2}(V) = \frac{T_{B_{12}}(V) - T_{B_1}(V)}{\left[1 - \frac{T_{B_1}(V)}{T_{s_2}} \right]} \quad ^\circ\text{K} \dots\dots\dots 5.2$$

where: T_{s_2} is the spin temperature of the gas

Equation 5.2 gives the brightness temperature correction for a gas with a background contribution. Note

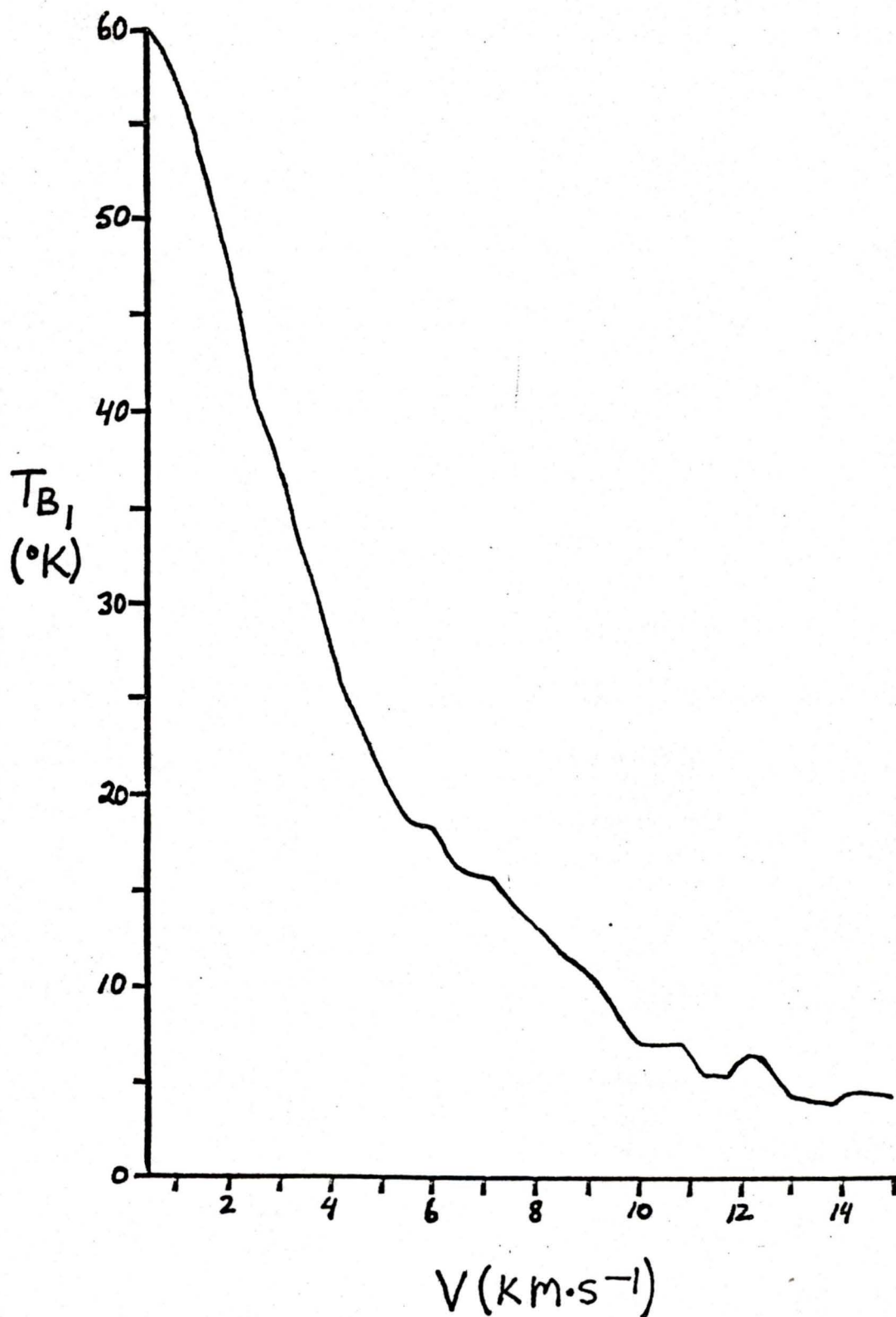


Figure 5.1 Background brightness temperature spectrum in the velocity range: $1.76 \leq V$ ($\text{km}\cdot\text{s}^{-1}$) ≤ 13.71 .

that $T_{B_2}(V)$ does not depend upon the spin temperature of the background, T_{S_1} . For an optically thin gas, T_{S_2} is high with respect to $T_{B_1}(V)$ and $T_{B_2}(V)$. The denominator of equation 5.2 becomes 1, and a simple subtraction of $T_{B_1}(V)$ is required to correct for the background.

5.3 Spin Temperatures

5.3.1 Calculation of T_{S_2}

Allen (1973) gives the relationship between the full width at half maximum of a hydrogen line which is purely thermally broadened, ΔV_D , and the spin temperature of the gas, T_{S_2} . It is modified here as:

$$T_{S_2} = 21.69 \left[\frac{\Delta V_D}{\text{km} \cdot \text{s}^{-1}} \right]^2 \text{ } ^\circ\text{K} \dots\dots\dots 5.3$$

The width of an observed line profile will be greater than ΔV_D if any other broadening mechanism is affecting the line (e.g. turbulence, pressure broadening, or other unresolved random or non-random motions). Thus, a measured line width, ΔV_m , will yield an upper limit to T_{S_2} by equation 5.3, and a minimum upper limit is obtained by selecting and measuring the narrowest line profiles. Broad structure HI can be neglected from the measured profiles since it occupies a large volume in space and therefore has greater turbulence and random motions within it. Three narrow line profiles were measured for ΔV_m . These profiles were observed from points situated at the edge of the fine

structure HI emission (marked with crosses in Figure 5.4). Using equation 5.3, they indicate a minimum upper limit to the spin temperature and standard deviation of 100 ± 4 °K.

When the gas is optically thick, $T_{B_2}(V) = T_{s_2}$ (equation 2.4), but $T_{B_2}(V)$ (and $T_{B_{12}}(V)$) cannot be greater than T_{s_2} . However, at a number of velocities there are a few points of emission near map centre where $T_{B_{12}}(V) > 100$ °K, with the highest of these equal to ≈ 115 °K. Therefore, temperature variations exist within the fine structure HI, with $T_{s_2} \leq 100$ °K right at the edge of the emission, and $T_{s_2} \geq 115$ °K at the centre.

5.3.2 The Two-Component Model

In order to calculate column densities at each map point (section 5.4) and eventually the atomic hydrogen mass (section 5.5), the spin temperature of the gas must be assumed constant (see equation 5.4). Although we have seen that T_{s_2} is not constant over the entire HI emission, it may be almost constant over a smaller region. Figure 5.2 shows the integrated hydrogen map. During integration, the observed brightness temperatures at each velocity ($T_{B_{12}}(V)$) were corrected for background HI, without a spin temperature assumption (i.e. using equation 5.2 for the optically thin case). Then the map was investigated for an indication of some region over which T_{s_2} could be considered constant. Intensity scans in declination across the map were

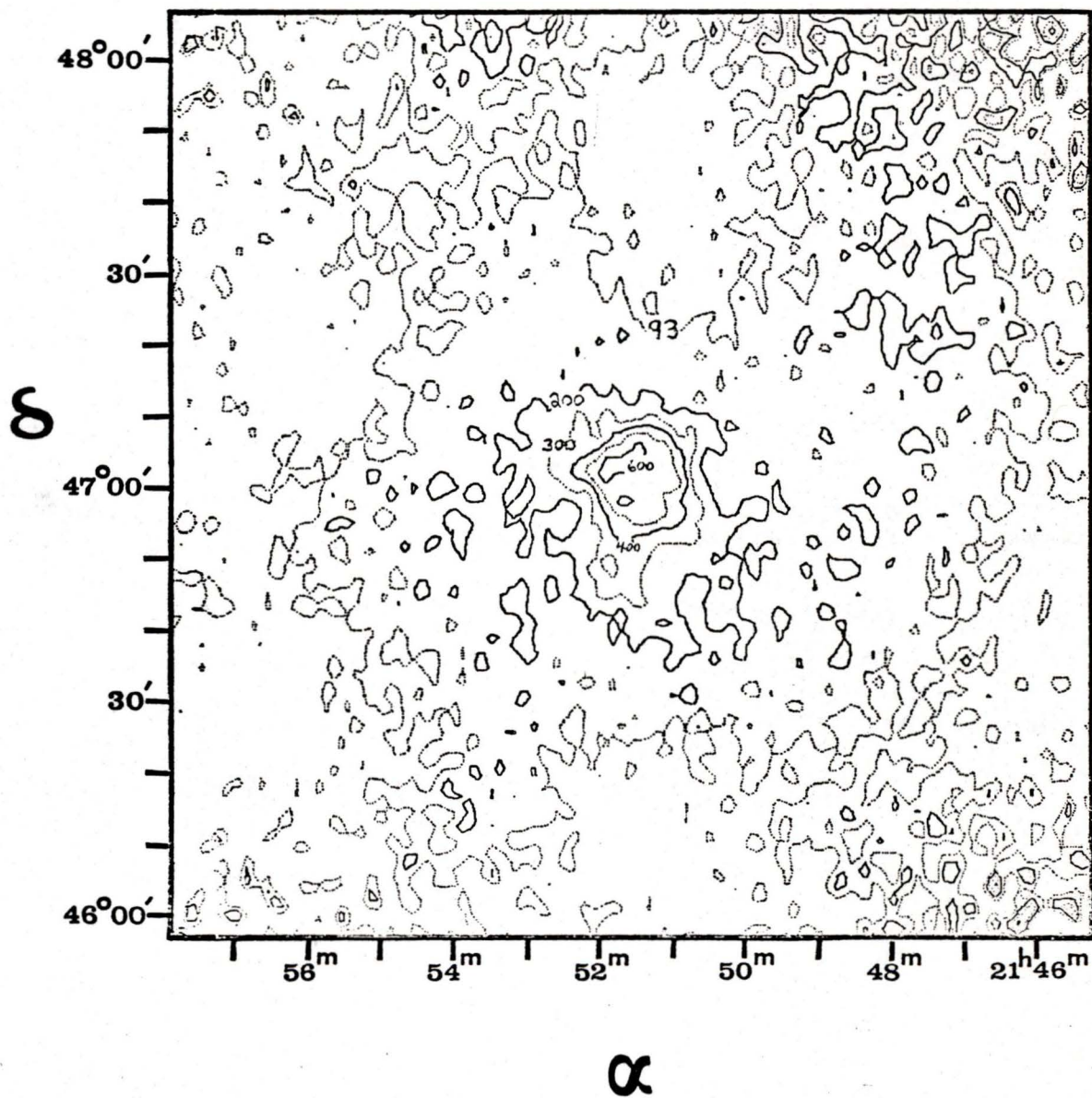


Figure 5.2 Total hydrogen map integrated over the velocity range: $1.76 \leq V \text{ (km} \cdot \text{s}^{-1}) \leq 13.71$. Contour levels are at: 93 (the rms noise), 200, 300, 400, 500, and $600 \text{ }^\circ\text{K} \cdot \text{km} \cdot \text{s}^{-1}$, with contours of alternating dotted and solid lines.

obtained for a number of points in right ascension (Figure 5.3). In general they show a central peak superimposed on a broad weaker feature. We therefore consider that the atomic hydrogen around IC5146 forms two components:

Component #1: This is the stronger central emission. It is assumed to be fine structure HI (see Appendix A for fine structure maps), with a spin temperature of 120 °K.

Component #2: This is the weaker extensive emission. It is assumed to be broad structure HI with a spin temperature of 100 °K.

5.4 Column Densities

Following Van de Hulst et al. (1954) and Lang (1974) the column density along a line of sight is given by:

$$N_{\text{HI}} = 1.823 \times 10^{18} T_{s_2} \int_{V_1}^{V_2} \tau_2(V) d\left(\frac{V}{\text{km}\cdot\text{s}^{-1}}\right) \text{ cm}^{-2} \dots 5.4$$

For points, ij , on a map of atomic hydrogen emission, at a velocity, V ($V = V_1, V_1 + \Delta V, V_1 + 2\Delta V, \dots V_2$), and applying equations 2.2 and 5.2, equation 5.4 becomes:

$$N_{\text{HI}}_{ij} = 7.51 \times 10^{17} T_{s_2} \sum_{V=V_1}^{V_2} - \ln \left\{ 1 - \frac{[(T_{B_{12}}(V))_{ij} - T_{B_1}(V)]}{T_{s_2} - T_{B_1}(V)} \right\} \text{ cm}^{-2} \dots 5.5$$

where: $\Delta V = 0.41 \text{ km}\cdot\text{s}^{-1}$ is the velocity separation between maps (section 3.2).

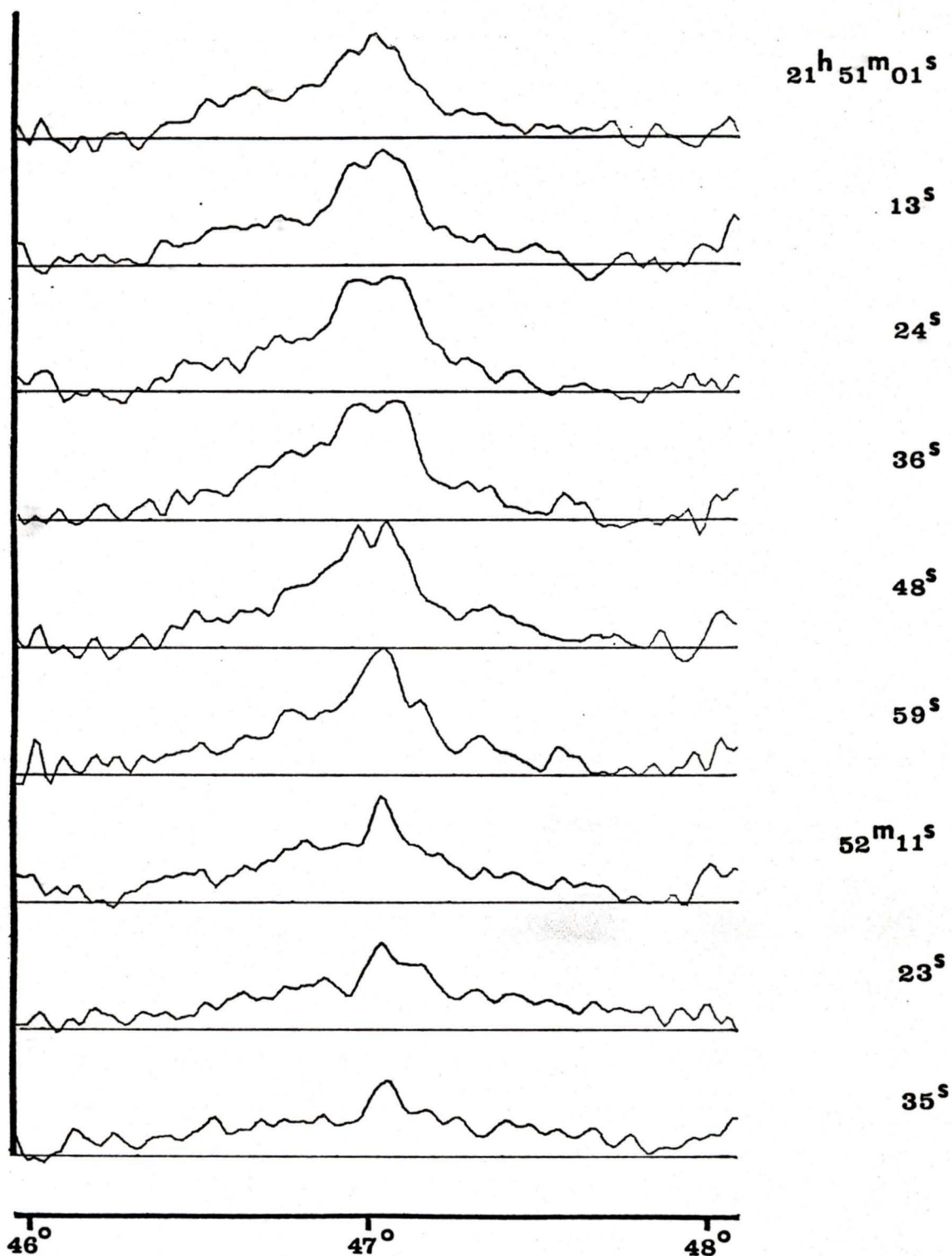


Figure 5.3 Declination scans of the integrated hydrogen map (Figure 5.2) for nine positions in right ascension. The ordinate axis scale is $325 \text{ }^\circ\text{K}\cdot\text{km}\cdot\text{s}^{-1}$ per centimetre.

Column densities were then calculated at all map points for each component separately:

Component #1 (Fine Structure): Fine structure HI maps

(Appendix A) were added together using equation 5.5 which was modified to correct for depressed baselines. Using

$T_{S_2} = 120 \text{ }^\circ\text{K}$ a map of column densities was produced (Figure 5.4) with $N_{\text{HI}}(\text{max}) = 1.6 \times 10^{21} \text{ cm}^{-2}$. The lowest map contour is twice the rms noise ($1.8 \times 10^{20} \text{ cm}^{-2}$) as calculated from a region immediately surrounding the main emission.

Around the map edges, the noise is amplified at least three-fold because of the polar diagram correction. One main emission feature centred on IC5146 can be seen, with weaker emission extending to the south-west. No extension is apparent in the direction of the dark cloud (Figure 1.1 a,b).

Component #2 (Broad Structure): Broad structure maps alone were not used to calculate column densities for the extended component because these maps contain beam broadening effects and raised baselines which are difficult to correct for.

Instead, the total hydrogen maps (Appendix D) were used.

However, Component #1 also contributes to each total HI

map. Therefore, all high brightness temperatures (at velocity, V) were truncated to the level of the maximum brightness temperature of the broad structure HI (at the same velocity). Column densities were then calculated (Figure

5.5) using $T_{S_2} = 100 \text{ }^\circ\text{K}$ in equation 5.5. The maximum column density is $N_{\text{HI}}(\text{max}) = 8.6 \times 10^{20} \text{ cm}^{-2}$ and twice the rms

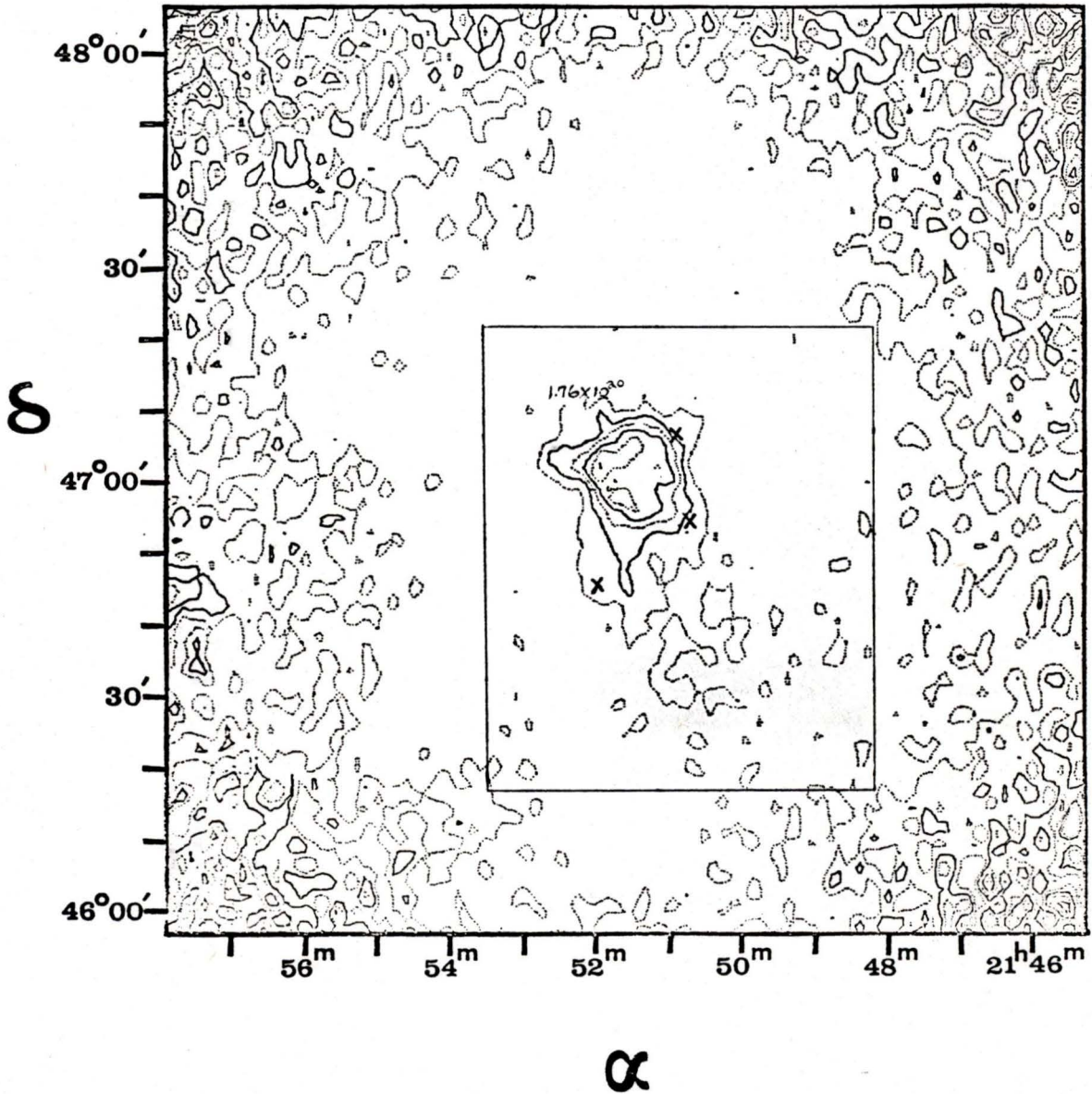


Figure 5.4 Column density map of fine structure hydrogen. Contour levels are at column densities of: 1.76×10^{20} (twice the rms noise), 4.14×10^{20} , 6.53×10^{20} , 8.91×10^{20} , 1.13×10^{21} , and $1.37 \times 10^{21} \text{ cm}^{-2}$, with contours of alternating dotted and solid lines. Crosses mark the positions where HI line widths were measured, and the rectangle encloses the area over which the mass was calculated.

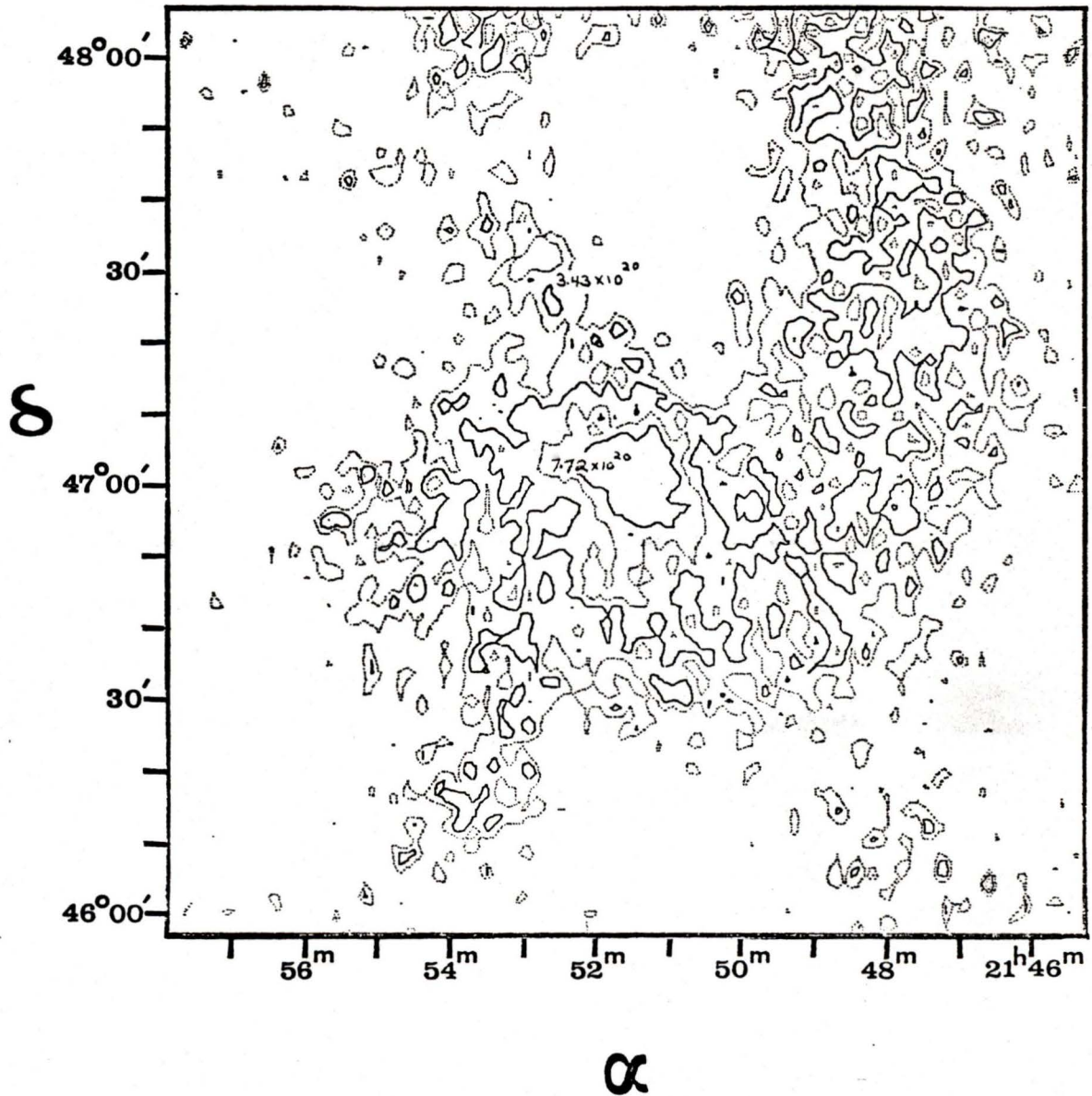


Figure 5.5 Column density map of broad structure hydrogen. Contour levels are at column densities of: 3.43×10^{20} (twice the rms noise), 4.29×10^{20} , 5.15×10^{20} , 6.01×10^{20} , 6.86×10^{20} , and $7.72 \times 10^{20} \text{ cm}^{-2}$, with contours of alternating dotted and solid lines.

noise is $3.4 \times 10^{20} \text{ cm}^{-2}$ (again the lowest map contour). Emission can be seen over most of the map with an 'arm' of emission extending north right to the map boundary. Other fainter features can also be seen east of this arm and to the south of the main emission region.

5.5 Mass of Atomic Hydrogen

The HI mass is given by:

$$M_{\text{HI}} = \frac{m_{\text{HI}}}{M_{\odot}} C_{\text{P}} \sum_{i=1}^{\ell} \sum_{j=1}^{\pi} N_{\text{HI}_{ij}} \dots\dots\dots 5.6$$

(for C_{P} in cm^2)

Masses were calculated for each component separately:

Component #1 (Fine Structure): A 55' x 65' rectangle drawn on the column density map (Figure 5.4) encloses the area over which M_{HI} was calculated. The mass, so obtained, is:
 $M_{\text{HI}} = 230 M_{\odot}$.

The largest error in M_{HI} results from the uncertainty in the spin temperature, $T_{\text{S}_2} = 120 \text{ }^{\circ}\text{K}$. To see the dependence of M_{HI} on T_{S_2} , an upper limit on T_{S_2} was found by measuring the narrowest line profiles from the centre of the HI emission. The upper limit is $480 \text{ }^{\circ}\text{K}$ (by equation 5.3), but this limit is probably quite high since turbulence and random motions will most certainly be acting to broaden lines at the centre. The calculations were repeated using

$T_{S_2} = 480$ °K to obtain a lower limit on the mass of $M_{HI} = 180 M_{\odot}$. We take this lower limit to represent the error in M_{HI} , giving:

$$M_{HI} = 230 \pm 50 M_{\odot}$$

Component #2 (Broad Structure): The entire 128' x 128' map field was used as the boundary of Component #2. HI emission could extend beyond the field presently investigated, but it may not be directly associated with IC5146. The mass of Component #2 is $M_{HI} = 2410 M_{\odot}$.

Again, uncertainty in the spin temperature is the major source of error. Radhakrishnan et al. (1972) have investigated ≈ 30 emission and absorption features from clouds of cool local HI. They find a mean column density of $3 \times 10^{20} \text{ cm}^{-2}$ (comparable to broad structure column densities; Figure 5.5) and a mean spin temperature of 80 °K from a range of 20 to 200 °K (also comparable to $T_{S_2} = 100$ °K used for Component #2). Since these clouds may be similar to the observed cloud of broad structure HI, $T_{S_2} = 80$ °K was chosen as a lower limit to its spin temperature. The calculations were repeated using $T_{S_2} = 80$ °K to indicate the error in M_{HI} , giving:

$$M_{HI} = 2410 \pm 480 M_{\odot}$$

The total detected hydrogen mass within the field

from 1.76 to $13.71 \text{ km}\cdot\text{s}^{-1}$, is: $M_{\text{HI}} = 2640 \pm 530 M_{\odot}$. Riegel (1967) obtained the only other atomic hydrogen mass for the IC5146 region and found: $M_{\text{HI}} = 670 M_{\odot}$. He assumed that the cloud was optically thin and at only one spin temperature of $125 \text{ }^{\circ}\text{K}$. This has the effect of suppressing broad structure column densities with respect to fine structure column densities (equation 5.5). Consequently, the boundaries chosen to calculate M_{HI} will exclude much of the extended structure leading to a lower mass.

CHAPTER 6

INTERPRETATION OF THE IC5146 COMPLEX

6.1 Dynamics

Appendix D contains the $\alpha - \delta$ HI maps in the velocity range $1.76 \leq V \text{ (km}\cdot\text{s}^{-1}) \leq 13.71$. At $V = 1.76 \text{ km}\cdot\text{s}^{-1}$ the emission is small in angular extent and low in intensity. As V increases the HI emission also increases, both in angular extent and intensity, and begins to show a deficit in HI at the centre. The deficit becomes more obvious at higher V , resembling a 'hole' (for example, at $V = 3.82 \text{ km}\cdot\text{s}^{-1}$). By $V = 5.05 \text{ km}\cdot\text{s}^{-1}$ the southern extension can be seen, and at $V = 7.12 \text{ km}\cdot\text{s}^{-1}$ the emission reaches both its maximum intensity¹ and maximum angular extent with an obvious hole at the centre. At higher velocities ($V \geq 8.76 \text{ km}\cdot\text{s}^{-1}$) the hole disappears, and the emission then decreases in size and intensity. The one degree $\alpha - \delta$ maps (uncorrected for the polar diagram) of fine structure HI only (see Appendix A) also reveal this same trend in the variation of emission with velocity. However, in this case, the peak intensity occurs at $9.18 \text{ km}\cdot\text{s}^{-1}$ rather than $7.12 \text{ km}\cdot\text{s}^{-1}$. Appendices B and C contain $\alpha - V$ and $\delta - V$ maps respectively, produced from the 1° fine structure HI maps. For these maps

¹ Maps in the appendices may show an intensity peak at a slightly different velocity than that mentioned in the text. This is because the appendix maps have been corrected for the background according to equation 5.2 with the denominator assumed equal to 1, and no such assumption has been made in the text.

the deficit in HI can be seen at velocities which are lower than velocities where the bulk of the emission occurs.

A number of points related to the dynamics of the complex will now be investigated:

1. Does the 'hole' correspond to the HII region?

The hole can be seen from $V = 1.76 \text{ km}\cdot\text{s}^{-1}$, the lowest velocity at which HI is first detected, to $V = 8.35 \text{ km}\cdot\text{s}^{-1}$: a range of $6.59 \text{ km}\cdot\text{s}^{-1}$. However, if HI emission occurred at velocities $< 1.76 \text{ km}\cdot\text{s}^{-1}$, then perhaps a deficiency would also be seen at these low velocities. Table VIII shows the velocities and ranges in velocity found for IC5146 by various observers. Using these data, the average velocity and maximum velocity range for the HII region are $2.3 \text{ km}\cdot\text{s}^{-1}$ and $20 \text{ km}\cdot\text{s}^{-1}$ respectively. Clearly, the observed hole is seen at velocities consistent with the HII region. Figure 6.1 shows an $\alpha - \delta$ contour plot of fine structure hydrogen integrated over the velocities at which the hole is seen. An outline of the continuum emission is superimposed upon this map and coincides with the hole. Therefore, there is a definite lack of atomic hydrogen at both the position and velocity of the HII region.

2. Where is the HII region physically situated with respect to the cloud?

TABLE VIII

Velocities and Velocity Ranges of IC5146

Observation	Peak Velocity ($\text{km}\cdot\text{s}^{-1}$)	Range ($\text{km}\cdot\text{s}^{-1}$)	Reference
H α	2.4	-3.6 \rightarrow 8.4	Miller, 1968
H α	2.7 \pm 1.3	-3.3 \rightarrow 12.4	Williamson, 1970
H142 α	1.9 \pm 0.7	-7.6 \rightarrow 11.4	Kuiper et al. 1976
HI (hole)		\leq 1.76 \rightarrow 8.35	Present Work

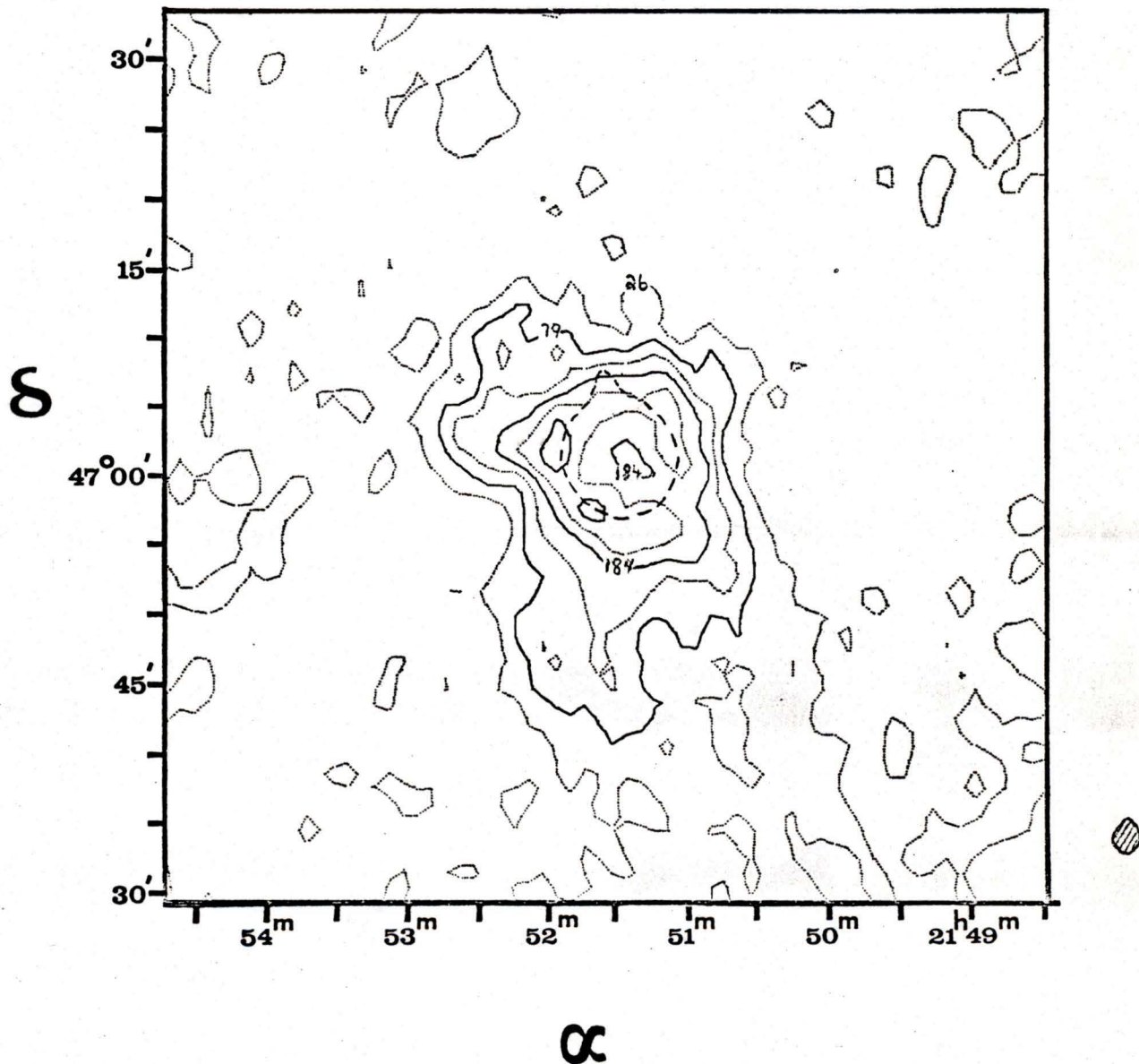


Figure 6.1 Map of fine structure hydrogen integrated over the velocity range, $1.76 \leq V \text{ (km}\cdot\text{s}^{-1}) \leq 8.35$, and weighted by the 8.6 m paraboloid polar diagram. Contour levels are at: 26, 79, 132, 184, 237, and $290 \text{ }^\circ\text{K}\cdot\text{km}\cdot\text{s}^{-1}$, with contours of alternating dotted and solid lines. The dashed curve is the continuum emission 2°K contour.

Israel (1976) has indicated that the HII region is located on the near side of the neutral cloud. There is also optical evidence for this (Figure 1.1 a, b) since the HII region is easily visible on the dark cloud and only a few dust lanes can be seen across its face. An HII region is associated with motions of expansion in the neutral gas around it (section 2.2). Also, as we have seen, there is virtually no HI emission at lower velocities than IC5146. Therefore the present observations also place the nebula on the near side. In fact, it is typical of HII regions which are related to dark clouds to be on the edge of the cloud rather than embedded within it. Well known examples of this include: Ori A (Zuckerman, 1973), Ori B (Tucker, Kutner and Thaddeus, 1973), M17 (Lada and Chaisson, 1975) and M8 (Lada et al., 1976).

3. What is the 'systemic velocity' of the cloud?

We take 'systemic velocity', V_s , to mean the initial velocity of the cloud at the time of star formation. A massive HI cloud in which most of the gas has been left dynamically unaffected by an HII region would be expected to peak in intensity and angular extent at the systemic velocity. Furthermore, the maximum intensity should occur at V_s for projected positions both within the boundary of the HII region and toward the outer boundary of the HI emission. The present observations show that these conditions are met for $V_s = 7.12 \text{ km} \cdot \text{s}^{-1}$. This is close to

the velocity of $7.6 \text{ km}\cdot\text{s}^{-1}$ found by Milman et al. (1975) for ^{12}CO at a position near the HII region. Also, a star which has formed out of the cloud should be travelling at V_s . BD+46°3474 has a velocity of $5.8 \pm 4.2 \text{ km}\cdot\text{s}^{-1}$ (Crampton and Fisher, 1974), a value which agrees with the initial cloud velocity (although the error is large).

4. What is the significance of the fine structure HI intensity peak at $9.18 \text{ km}\cdot\text{s}^{-1}$?

The $\alpha - V$, $\delta - V$ maps (Appendices B, C) show that fine structure HI emission peaks in intensity (though not in angular extent) at $9.18 \text{ km}\cdot\text{s}^{-1}$. The peak emission curves around the hole toward lower velocities (like a bright 'rim'), and the maximum angular extent is still seen at about the systemic velocity of $7.12 \text{ km}\cdot\text{s}^{-1}$. Behavior like this is just what would be expected from a shell of HI which is expanding away from the HII region. Furthermore on the total atomic hydrogen maps (Appendix D) a hole in the emission is still visible at the systemic velocity. This indicates that the brightest part of the rim directly behind the nebula is no longer travelling at $7.12 \text{ km}\cdot\text{s}^{-1}$ and therefore must have had a velocity imparted to it. We suggest, then, that the fine structure HI peak at $9.18 \text{ km}\cdot\text{s}^{-1}$ and the above indicate the existence of an expanding HI shell around the HII region (at a velocity of $\approx 2 \text{ km}\cdot\text{s}^{-1}$). Such a shell is probably caused by the passage of a shock wave through the neutral gas (section 2.2).

5. What is the motion of the ionized gas on the near side of the nebula?

An HII region which is density bounded on the near side would be expected to expand freely on that side. The $\alpha - V$ and $\delta - V$ maps indicate that IC5146 is probably not completely density bounded on the near side since some low intensity contours do 'close' at lower velocities than the HII region. However, the neutral hydrogen density is probably very low on the near side, allowing a high expansion velocity there. IC5146 is observed at $2.3 \text{ km}\cdot\text{s}^{-1}$: a velocity negative with respect to the systemic velocity of $7.12 \text{ km}\cdot\text{s}^{-1}$. Therefore $5 \text{ km}\cdot\text{s}^{-1}$ appears to be the average 'free expansion' velocity of the ionized gas on the near side.

Israel (1978) has listed 77 sources for which he finds HII - CO velocity differences. For visible HII regions he finds an average blue-shift with respect to the cloud, of $3.4 \pm 0.4 \text{ km}\cdot\text{s}^{-1}$ from a range of -12.7 to $+6.5 \text{ km}\cdot\text{s}^{-1}$. The expected blue-shift is 5 to $15 \text{ km}\cdot\text{s}^{-1}$, and he contributes the discrepancy to geometrical effects and large errors in the data. The present value of $5 \text{ km}\cdot\text{s}^{-1}$ agrees well with the expected expansion velocity, and is consistent with the presence of very low density foreground neutral gas.

6.2 The Dissociation Model

An attempt was made to model the HI density distribution at increasing distances from the nebular boundary. Hill and Hollenbach (1978) (hereafter HH) have developed an expression relating the total (HI and H₂) column and volume densities, N_t and n_t , to the molecular hydrogen column and volume densities, N_{H_2} and n_{H_2} . Their expression applies to an HII region surrounded by hydrogen in which H₂ dissociations, due to UV radiation from the exciting star, are in equilibrium with molecular reformations on the surface of dust grains. It is applicable to any stage in the evolution of the system as long as such an equilibrium has been established. The expression, modified by Roger (1978, private communication) is:

$$\mathcal{R} n_t (n_t - 2n_{H_2}(\rho)) = I_0 \left(\frac{\rho_p}{\rho}\right)^2 \beta (N_{H_2}(\rho))^{-\frac{1}{2}} e^{-KN_t(\rho)} n_{H_2} \quad 6.1$$

where: \mathcal{R} is the molecular reformation rate ($\text{cm}^3 \cdot \text{s}^{-1}$).

I_0 is the initial unshielded dissociation rate at the boundary of the HII region (s^{-1}).

ρ_p is the present radius of the HII region (cm).

ρ is the distance from the exciting star at which the equation is evaluated (cm).

β is a constant equal to $4.2 \times 10^5 \text{ cm}^{-1}$.

K is the dust coefficient (cm^2).

The left-hand side of equation 6.1 is the reformation rate

per unit volume ($s^{-1} \cdot \text{cm}^{-3}$) and depends upon both the grain density ($\propto n_t$) and the atomic hydrogen density ($\propto n_t - 2n_{\text{H}_2}$). The right-hand side is the dissociation rate per unit volume and depends on the molecular hydrogen density (n_{H_2}) and the dust absorption ($e^{-KN_t(\rho)}$). The term, $\beta(N_{\text{H}_2}(\rho))^{-\frac{1}{2}}$ is unitless and accounts for the fact that the square-root portion of the curve of growth is applicable to the absorption of dissociating radiation: that is, the cloud is not optically thin and the absorption lines are strong enough that natural line broadening is important. Solving for $n_{\text{H}_2}(\rho)$, equation 6.1 becomes:

$$n_{\text{H}_2}(\rho) = \frac{\mathcal{R} n_t^2}{2\mathcal{R} n_t + I_0 \left(\frac{\rho_p}{\rho}\right)^2 \left[\frac{\beta}{(N_{\text{H}_2}(\rho))^{\frac{1}{2}}} \right] e^{-KN_t(\rho)}} \quad \text{cm}^{-3} \quad 6.2$$

Furthermore:

$$\left. \begin{aligned} n_t &= n_{\text{HI}}(\rho) + 2n_{\text{H}_2}(\rho) \\ N_{\text{H}_2}(\rho) &= n_{\text{H}_2}(\rho) \Delta\rho \\ N_{\text{HI}}(\rho) &= n_{\text{HI}}(\rho) \Delta\rho \\ N_{\text{HI}} &= \sum_{\rho=\rho_p}^{\rho_1} N_{\text{HI}}(\rho) \end{aligned} \right\} 6.3$$

where:

$\Delta\rho$ is the increment chosen in ρ .

ρ_1 is the distance from the exciting star at which N_{HI} is evaluated.

Given an initial total hydrogen density, n_t , $n_{H_2}(\rho)$ can be evaluated for increasing distances, ρ , from the exciting star. Since $N_{H_2}(\rho_p)$ is initially zero at the I-front, the first H_2 density is calculated using equation 6.2 for the optically thin case in which $\mathfrak{B}(N_{H_2}(\rho))^{-\frac{1}{2}} \approx 1$ (Jura, 1974). Then column and volume densities can be calculated at progressively increasing values of ρ using equations 6.2 and 6.3. At some distance from the exciting star, no more dissociating radiation can penetrate into the molecular cloud, so $N_{HI}(\rho)$ tends to zero and the accumulated column density, N_{HI} , will level off to some finite value.

To apply this model we will consider broad structure and fine structure HI separately:

1. Broad Structure: Broad structure (or diffuse) HI covers a region of large angular extent in the sky (Figure 5.5). At positions off the optical dust cloud in this diffuse component, no obscuration is visible (Samson, 1975). Therefore little or no dust must be available on which H_2 can form. At the same time, general interstellar UV radiation may also be preventing the formation of molecules. No CO is detected in these regions (Roger, McCutcheon and Dickman, 1978; private communication), so if molecular hydrogen is indeed present in the extended feature, its density cannot be greater than 100 cm^{-3} (section 2.2). For these reasons, the model of HH has not been applied to broad structure HI.

2. Fine Structure: In this case the parameters, \mathcal{R} , K , and n_t were varied in equation 6.2 until the following three observational conditions were reproduced:

- a) The HI column density N_{HI} : The observed column density along a line of sight at the position of the exciting star is $N_{\text{HI}} = 1.6 \times 10^{21} \text{ cm}^{-2}$. The parameters were adjusted until the final calculated column density levelled off at this value.

- b) The cloud radius, ρ_c : The average projected radius of the fine structure HI emission, as measured from the position of the exciting star to twice the rms contour level on the column density map (Figure 5.4) is considered to be the cloud radius, $\rho_c = 3.7 \text{ pc}$. It was assumed that this radius is also the distance from the exciting star along the line of sight at which the HI density dropped to the 10% level. Therefore, the parameters were adjusted until $n_{\text{HI}} = 0.1 n_{\text{HI}}(\text{max})$ at 3.7 pc.

- c) An average HI density, $n_{\text{HI}}(\text{avg})$: An average HI density was calculated from the observations using equation 5.6 for the HI mass, and the volume of a cylinder whose radius is slightly larger than the radius of the HII region. The

observed density, in this way, is $n_{\text{HI}}(\text{avg}) = 157 \text{ cm}^{-3}$. The parameters of equation 6.2 were adjusted until the calculated $n_{\text{HI}}(\text{max})$ and HI density distribution were consistent with an average density of 157 cm^{-3} .

The values given in Table IX are those which reproduce the three conditions listed above. ρ_p and I_0 were considered fixed: ρ_p is the measured radius of the HII region (section 4.1); I_0 was taken from Jura's (1974) value of I for the B0V star, τ Sco, extrapolated (with $I \propto 1/\rho^2$) to a distance, ρ_p , from the star. Equation 6.2 is most sensitive to variations in K , and considerably less sensitive to alterations in \mathcal{R} . The value of \mathcal{R} listed in the table is the reformation rate quoted by HH. Other than the total density, only K needed a slight alteration from HH's value of 10^{-21} . It is possible that other combinations of \mathcal{R} , K and n_t may also describe the observations, but we believe that the parameters listed here, are those which are least changed from the literature values.

Figure 6.2 shows the modelled HI density distribution as a function of ρ . Close to the I-front, n_t is also n_{HI} with the gas completely dissociated. The point at which the gas is half molecular and half atomic is at $\rho = 3.15 \text{ pc}$. We will consider this to be the centre of the

TABLE IX

Parameters of the Dissociation Model

ρ_p pc	I_0 s^{-1}	\mathcal{R} $cm^3 \cdot s^{-1}$	K cm^2	n_t cm^{-3}
1.68	2.9×10^{-8}	3×10^{-17}	1.95×10^{-21}	345

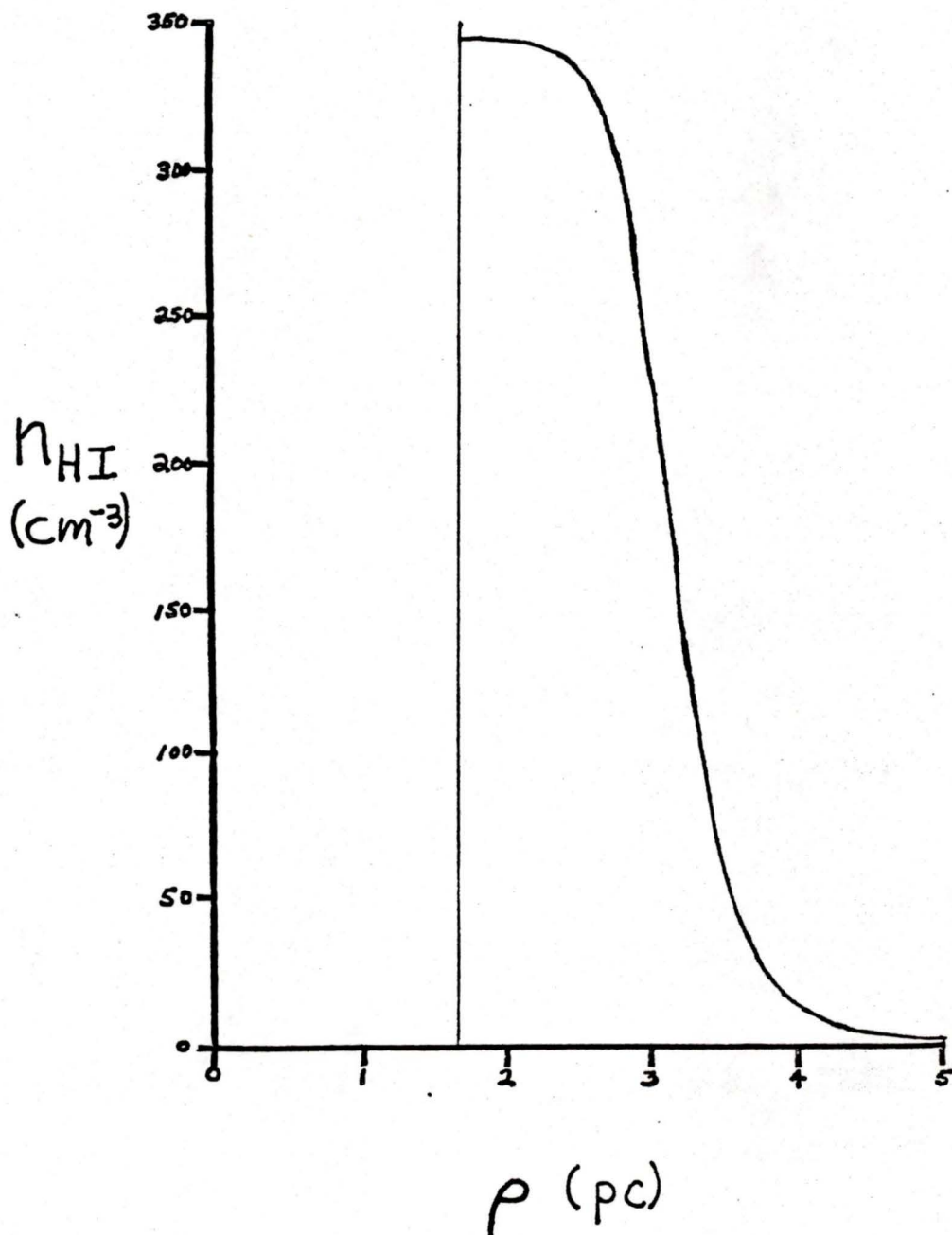


Figure 6.2 Atomic hydrogen density distribution as a function of distance from the exciting star, as predicted by the dissociation model.

dissociation wave.

Finally, we assumed that this model applied for all radial directions from the I-front over 2π steradians, in order to calculate the HI mass. M_{HI} , determined in this way, is $500 M_{\odot}$, about twice as high as the observed mass (section 5.5). This could be accounted for if the total density, n_t , is not uniform within the entire half-sphere. The density is probably the highest (345 cm^{-3}) in regions directly behind the HII region where the nebula is ionization bounded, and lower closer to the near side.

6.3 Evolution

We will now look at a number of points related to the evolution of the HII region and surrounding medium making use of the total density, n_t , derived from the model calculations:

1. Is the HII region still expanding?

The gas pressure on either side of the I-front is given by:

$$P_{r_i} \propto \frac{n_i T_i}{\mu_i} \dots\dots\dots 6.4$$

where: i represents either the HII side of the boundary ($i = 2$) or the HI side of the boundary ($i = 1$).
 μ_i is the mean molecular weight.

The following values were used in equation 6.4: $T_2 = T_e = 7000 \text{ }^\circ\text{K}$, $n_2 = n_e(\text{min}) = 10 \text{ cm}^{-3}$ (section 4.5), $\mu_2 \approx \frac{1}{2}$, $T_1 = T_s = 120 \text{ }^\circ\text{K}$ (section 5.3.2), $n_1 = n_t = n_{\text{HI}}(\text{max}) = 345 \text{ cm}^{-3}$, and $\mu_1 \approx 1$. This gives $P_{r_2}/P_{r_1} \approx 3$, showing that there is a pressure difference across the I-front. Therefore the HII region should still be expanding into the neutral cloud.

2. What is the expansion velocity?

Elmegreen and Lada (1978) give an expression for the expansion velocity of an HII region into a cloud which bounds it on one side:

$$v_{\text{exp}} = \left[\frac{3kT_2 n_2}{m_{\text{HI}} n_1} \right]^{\frac{1}{2}} \dots\dots\dots 6.5$$

where: k is Boltzmann's constant ($\text{erg} \cdot \text{K}^{-1}$).

m_{HI} is the mass of the hydrogen atom (g).

For IC5146, $v_{\text{exp}} = 2.24 \text{ km} \cdot \text{s}^{-1}$.

3. What was the initial density of the cloud?

To estimate this, we assumed that the initial cloud radius is the same as the present cloud radius (i.e. $\rho_c = 3.7 \text{ pc}$). For a cloud in which an HII region forms and then expands, we assumed that the total number of particles in the cloud remains constant. Setting the number of particles in the cloud before expansion, equal to the number of particles in the cloud at the present time,

then for a sphere or half-sphere:

$$n_o \rho_c^3 = n_e(\text{avg}) \rho_p^3 + (\rho_c^3 - \rho_p^3) n_t \quad \dots\dots\dots 6.6$$

where, for IC5146:

$n_e(\text{avg}) = 26 \text{ cm}^{-3}$ is the average density of the HII region (section 4.5).

The initial density, $n_o = 316 \text{ cm}^{-3}$ by equation 6.6, and this is only about 8% lower than the present density of neutral hydrogen, n_t . Since n_o has only been estimated, it is virtually equal to n_t (i.e. $n_o \approx n_t = 345 \text{ cm}^{-3}$). Therefore, at the present time, little or no compression of the neutral gas is observable.

4. What was the radius of the initial Strömgen sphere?

Since equilibrium of photoionizations with recombinations is maintained within the HII region throughout the expansion stage, the initial radius, ρ_o , at the beginning of expansion is given (from equation 4.6) by:

$$n_o \rho_o^{3/2} = n_e(\text{avg}) \rho_p^{3/2} \quad \dots\dots\dots 6.7$$

For IC5146, $\rho_o = 0.30 \text{ pc}$.

5. What is the age of the nebula?

Walker (1959) has given the age of the galactic cluster to be 3×10^6 years. However, the HII region may be somewhat younger than this. Elmegreen and Lada (1978)

provide an expression for the age of a nebula bounded on one side:

$$t = \frac{4 \rho_p}{7 \sqrt{2}} \left[\frac{m_{\text{HI}}}{1.5kT_2} \right]^{\frac{1}{2}} \left[\left(\frac{\rho_p}{\rho_o} \right)^{3/4} - \frac{\rho_o}{\rho_p} \right] \quad \text{seconds 6.8}$$

This gives an age of $t = 2.45 \times 10^5$ years for IC5146, considerably less than the cluster age.

6. What has been the average expansion velocity of the I-front?

The average expansion velocity, V_{avg} , is simply calculated by:

$$V_{\text{avg}} = \frac{\rho_p - \rho_o}{t} \quad \text{..... 6.9}$$

This gives $V_{\text{avg}} = 5.51 \text{ km} \cdot \text{s}^{-1}$ compared to the present expansion velocity of $V_{\text{exp}} = 2.24 \text{ km} \cdot \text{s}^{-1}$. V_{avg} is also consistent with an initial expansion velocity of roughly $10 \text{ km} \cdot \text{s}^{-1}$: the sound speed in the ionized gas, c_{II} (section 2.2).

7. What is the geometrical shape of the nebula?

We now have a picture of the HII region in which at the beginning of the expansion stage, gas moves outward in all directions, probably at about $10 \text{ km} \cdot \text{s}^{-1}$. On the far side the dark cloud 'brakes' the expansion until the present velocity of $2.24 \text{ km} \cdot \text{s}^{-1}$ is reached. On the near side a much less dense medium may reduce the

velocity to the present value of $5 \text{ km}\cdot\text{s}^{-1}$. This indicates that in the line of sight, the HII region may be asymmetric, with gas on the near side less dense and extending farther away from the exciting star than gas on the far side.

8. Where is the S-front now?

According to HH, at ages of approximately 7×10^4 to 2×10^5 years, the shock front will overtake the dissociation wave; that is, half the gas which is immediately in front of the shock will be molecular. Since IC5146 is 2.45×10^5 years old, we would expect the shock front to be at the distance of the D-wave centre (3.15 pc) or farther, from the exciting star.

Each of the above calculations have, in some way, made use of $n_t = n_{\text{HI}}(\text{max})$ derived from the model. It should be kept in mind, however, that the complete exclusion of broad structure HI from the model may be a relevant source of error. Therefore we have calculated the expansion velocity, age, and initial Strömgren radius (given by equations 6.5 - 6.8) as functions of $n_{\text{HI}}(\text{max})$ (see Figure 6.3). Note that the age of the nebula is of the order of 10^5 years over a wide range of densities.

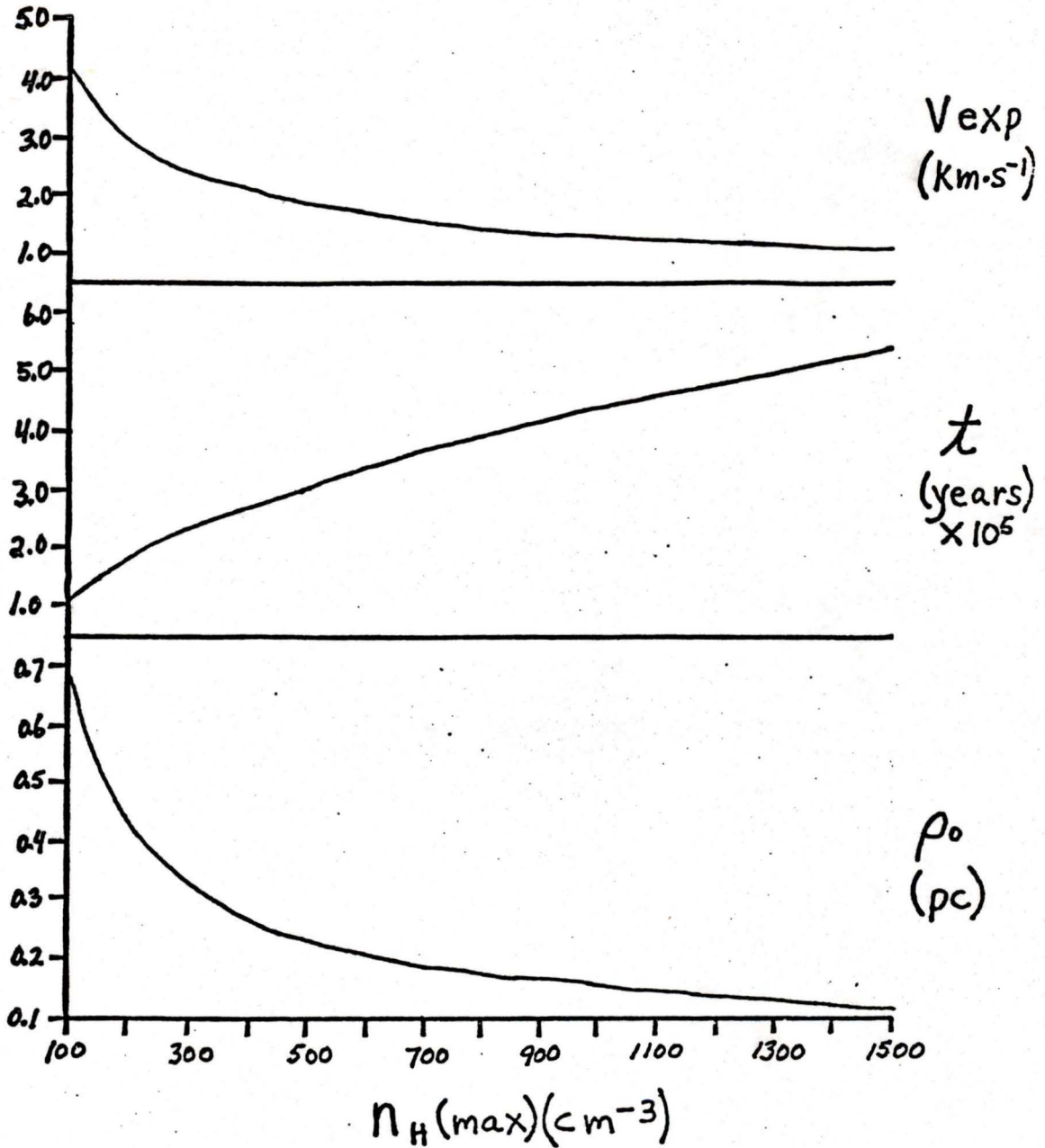


Figure 6.3 Dependence of:
 a) the expansion velocity of IC5146 into the neutral cloud
 b) the age of IC5146
 c) the radius of the initial Strömgren sphere
 - on the maximum density of atomic hydrogen.

CHAPTER 7

SUMMARY

7.1 Comparison of the IC5146 Complex to a Theoretical Complex

Figure 7.1 shows some of the main features associated with IC5146. Outlines of both fine and broad structure HI emission (Figures 5.4 and 5.5 respectively) are shown, as well as those of the continuum emission (Figure 4.1) and dark cloud (Samson, 1975). BD+46°3474 is marked with a cross and appears to be remarkably central to each of the mentioned features.

Hill and Hollenbach's (1978) model for the dissociation of H_2 around an HII region has been applied quite successfully to the IC5146 complex. The observed fine structure in HI around IC5146, can be accounted for by assuming an equilibrium between dissociations due to UV radiation from BD+46°3474 and reformations on dust grains. Clearly, from Figure 7.1, fine structure HI is situated quite neatly within the boundary of the dust cloud, further supporting the dissociation model.

Also, IC5146 appears to fit in well with the theory of expanding HII regions as described in section 2.2, the main difference being that IC5146 is on the near side of the molecular cloud. There is indeed evidence for the

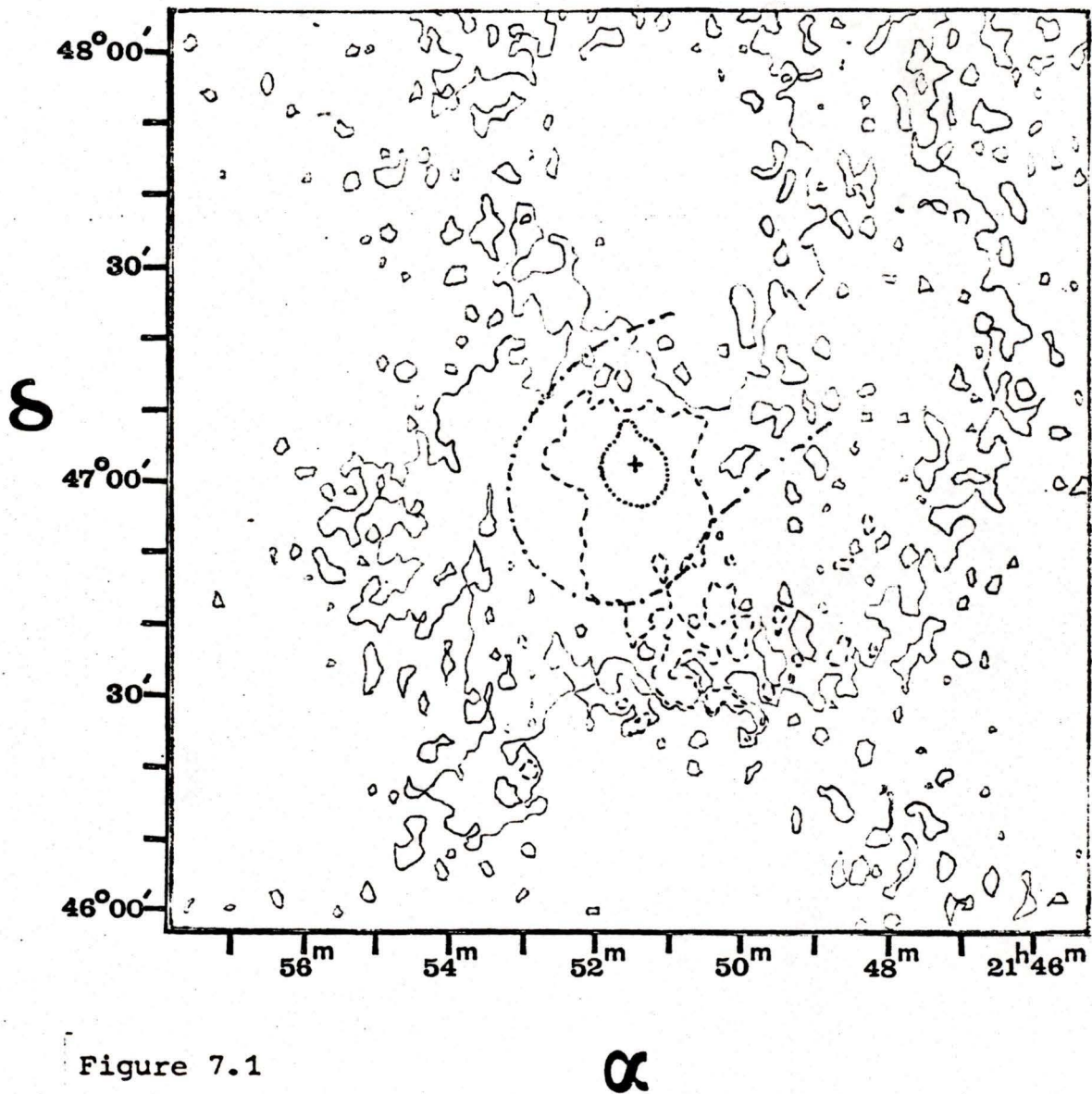


Figure 7.1

Outlines of features associated with IC5146, including:

- $3.43 \times 10^{20} \text{ cm}^{-2}$ broad structure HI column density contour
- $1.76 \times 10^{20} \text{ cm}^{-2}$ fine structure HI column density contour - - - - -
- 1°K continuum emission contour
- 1.5 extinction dark cloud contour (Samson, 1975) - . - . - .

A cross marks the position of BD+46°3474.

existence of an expanding HI shell on the far side of the HII region, but no appreciable compression can be detected (sections 6.1, 6.3). This could well be consistent with the properties and age of IC5146.

7.2 Main Results from Each Chapter

The following is a summary of the observational results and calculations.

Chapter 4: Continuum Emission

1. The average projected radius of IC5146 is $R_{\text{avg}} = 1.68$ pc.
2. The flux density of IC5146 is $S_{1420} = 1.95 \pm 0.05$ Jy.
3. The excitation parameters and Lyman continuum luminosities of IC5146 are consistent with an exciting star of spectral type, B0V (ZAMS).
4. The continuum observations are consistent with an electron density distribution which falls off from the centre in the manner:

$$n_e(\rho) = n_e(\text{max}) \exp \left[\frac{-1.9 \rho^2}{R_{\text{avg}}^2} \right]$$

5. For an electron temperature of $T_e = 7000$ °K, the HII mass is $M_{\text{HII}} = 12.2 \pm 1 M_{\odot}$, and the maximum and average electron densities are $n_e(\text{max}) = 67 \text{ cm}^{-3}$ and $n_e(\text{avg}) = 26 \text{ cm}^{-3}$ respectively.

Chapter 5: Atomic Hydrogen Line Emission

6. HI emission extends over the velocity range, $1.76 \leq$

$$V \text{ (km}\cdot\text{s}^{-1}\text{)} \leq 13.71.$$

7. There is evidence for two HI spin (cloud) temperatures:
 - a) fine structure: $T_{s_2} = 120 \text{ }^\circ\text{K}$
 - b) broad structure: $T_{s_2} = 100 \text{ }^\circ\text{K}$
8. HI masses using the above temperatures are:
 - a) fine structure: $M_{\text{HI}} = 230 \pm 50 M_\odot$
 - b) broad structure: $M_{\text{HI}} = 2410 \pm 480 M_\odot$

Chapter 6: Interpretation of the IC5146 Complex

9. The peak HI intensity and angular extent occurs at $7.1 \text{ km}\cdot\text{s}^{-1}$: considered to be the systemic (and initial cloud) velocity.
10. There is a 'hole' in the HI emission which corresponds in position and velocity to the HII region.
11. On the near side of the HII region, ionized gas is expanding into a rarefied medium. This 'free expansion' velocity is probably about $5 \text{ km}\cdot\text{s}^{-1}$.
12. The HII region is still expanding into the neutral gas on the far side at a velocity of $V_{\text{exp}} = 2 \text{ km}\cdot\text{s}^{-1}$. The average expansion velocity to date is $V_{\text{avg}} = 5.5 \text{ km}\cdot\text{s}^{-1}$.
13. There is evidence, from fine structure HI, for the presence of a half-shell of HI around the HII region, expanding at a velocity of about $2 \text{ km}\cdot\text{s}^{-1}$.
14. According to the dissociation model, the present cloud density is $n_t = 345 \text{ cm}^{-3}$ which is also an estimate of the initial cloud density.

15. For a cloud density of 345 cm^{-3} , the radius of the initial Strömgren sphere is $\rho_0 = 0.30 \text{ pc}$.
16. For a cloud density of 345 cm^{-3} , the age of the HII region is $t = 2.45 \times 10^5 \text{ years}$.
17. According to the dissociation model, the D-wave centre is at 3.15 pc from the exciting star, and the S-front is probably as far as or farther than this.

7.3 Suggestions for Future Research

Recently, three CO 'hot spots' have been detected at positions on the projected boundary of IC5146 (Roger, McCutcheon and Dickman, 1978; private communication). At one of these spots, CS has also been detected (Dickman, 1978; private communication). In regions where star formation is suspected, CO emission is almost always enhanced and is probably due to heat released from stars or proto-stars rather than an increase in H_2 density (Thaddeus, 1977).

Elmegreen and Lada (1977) have proposed a method of star formation in which pressure from an expanding HII region causes compression and gravitational collapse in the adjacent neutral cloud. They have applied their theory on a small scale to the HII region NGC281 (Elmegreen and Lada, 1978). If sufficient compression of the neutral gas around IC5146 has occurred at some time in the past, then perhaps star formation is going on now, particularly in regions of enhanced CO emission. Infrared

emission from dust in circumstellar clouds can often be detected in regions of star formation. Also, it is known that OH and H₂O masers are associated with the formation of stars (Mezger and Robinson, 1968; Lo, Burke and Haschick, 1975). We therefore suggest that infrared, OH and H₂O observations of IC5146 would provide helpful information on whether star formation is indeed taking place in the neutral gas.

It is believed that carbon in gas which surrounds an HII region can be ionized by radiation from the exciting star at wavelengths of 912 - 1107 Å (Zuckerman and Ball, 1974). Therefore, carbon recombination lines may be observable in a thin shell near the I-front of an HII region. Such CII regions have indeed been observed near other emission nebulae (Pankonin, Thomasson and Barsuhn, 1977; Kuiper and Evans, 1978). A. Pedlar (1978; private communication) observed IC5146 for the presence of carbon recombination lines using the 26 m paraboloid at D.R.A.O. No emission was detected in excess of 0.02 °K. However, beam dilution is appreciable for a 36' beam on a 10' source. We therefore suggest that carbon recombination line observations be made on IC5146 with a higher resolution instrument.

Further work on the diffuse (broad structure) HI component may also be interesting. The present survey could not cover the entire region where diffuse HI is present (Figure

5.5). A more extensive study may locate the boundary and possibly explain the broad 'arm' which extends toward the north on the west side. UV absorption or infrared observations of this feature may also determine if there is any molecular hydrogen present.

REFERENCES

- Allen, C. W. 1973. Astrophysical Quantities, 3rd ed. The Athlone Press, University of London, London, England.
- Altenhoff, W., Mezger, P. G., Wendker, H., and Westerhout, G. 1960. Die Durchmusterung der Milchstrasse und die Quillen-Durchmusterung bei 2, 7 GHz. Veroff. Sternwarte, Bonn. No. 59, 48.
- Bowers, F. K., Whyte, D. A., Landecker, T. L., and Klinger, R. J. 1973. A Digital Correlation Spectrometer Employing Multiple-Level Quantization. Proc. I. E. E. E., 61, 1339.
- Bridle, A. H., Davis, M. M., Fomalont, E. B., and Lequeux, J. 1972. Flux Densities, Positions, and Structures for a Complete Sample of Intense Radio Sources at 1400MHZ. A. J., 77, 405.
- Churchwell, E., and Walmsley, C. M. 1973. Observations of Optical Nebulae at 2695 MHZ. Astr. Ap. 23, 117.
- Churchwell, E., and Walmsley, C. M. 1975. Are the Electron Temperatures of H II Regions a Function of Galactic Radius? Astr. Ap. 38, 451.
- Cooley, J. W., and Tukey, J. W. 1965. An Algorithm for the Machine Calculation of Complex Fourier Series. Math. of Comput. 19, 297.
- Courtès, G., Georgelin, Y. P., Georgelin, Y. M., Monnet, G., and Pourcelot, A. 1968. Optical Study of Ionized Hydrogen. In Interstellar Ionized Hydrogen, edited by Y. Terzian, pp 571-615, W. A. Benjamin, Inc., New York.
- Crampton, D., and Fisher, W. A. 1974. Spectroscopic Observations of Stars in H II Regions. Pub. Dom. Ap. Obs. Victoria. 14, 283.
- Davies, R. D., and Tovmassian, H. M. 1963. Neutral Hydrogen in Galactic Star Clusters. M. N. R. A. S., 127, 45.
- Elmegreen, B. G., and Lada, C. J. 1977. Sequential Formation of Subgroups in OB Associations. Ap. J., 214, 725.
- Elmegreen, B. G., and Lada, C. J. 1978. CO and H₂O Observations of the H II Region NGC281. Ap. J., 219, 467.
- Encrenaz, P. J., Falgarone, E., and Lucas, R. 1975. CO, Dust and H₂ in the Molecular Cloud near ρ Ophiuchi. Astr. Ap., 44, 73.

- Felli, M., and Churchwell, E. 1972. Radio Emission at 1400 MHz from Galactic HII Regions. *Astr. Ap. Suppl.*, 5, 369.
- Felli, M., Tofani, G., and D'Addario, L. R. 1974. A Survey of Fine Structure in Galactic HII Regions. *Astr. Ap.*, 31, 431.
- Fomalont, E. B. 1973. Earth-Rotation Aperture Synthesis. *Proc. I.E.E.E.*, 61, 1211.
- Fomalont, E. B., and Moffat, A. T. 1971. Positions of 352 Small-Diameter Radio Sources. *A. J.*, 76, 5.
- Galt, J. A., and Kennedy, J. E. D. 1968. Survey of Radio Sources Observed in the Continuum near 1420 MHz, Declinations -5° to $+70^{\circ}$. *A. J.*, 73, 135.
- Georgelin, Y. P., and Georgelin, Y. M. 1970. Vitesses Radiales et Distances des Régions HII Galactiques. *Astr. Ap.*, 6, 349.
- Girnstern, H. G., and Rohlf, K. 1964. Die Assoziation 1 Mon Aus Messungen Der 21 CM - linie. *Zs. f. Ap.*, 59, 83.
- Goldreich, P., and Kwan, J. 1974. Molecular Clouds. *Ap. J.*, 189, 441.
- Gould, R. J., and Salpeter, E. E. 1963. The Interstellar Abundance of the Hydrogen Molecule. I. Basic Processes. *Ap. J.*, 138, 393.
- Grasdalen, G. L., Strom, K. M., and Strom, S. E. 1973. A 2 - micron Map of the Ophiuchus Dark-Cloud Region. *Ap. J. (Letters)*, 184, L53.
- Harris, D. E., and Roberts, J. A. 1960. Radio Source Measurements at 960 MC/S. *Pub. A. S. P.*, 72, 237.
- Herbig, G. H. 1960. Emission - Line Stars in IC5146. *Ap. J.*, 131, 516.
- Hill, J. K., and Hollenbach, D. J. 1978. Effects of Expanding Compact HII Regions Upon Molecular Clouds: Molecular Dissociation Waves, Shock Waves, and Carbon Ionization. To be published.
- Hollenbach, D. J., and Salpeter, E. E. 1971. Surface Recombination of Hydrogen Molecules. *Ap. J.*, 163, 155.
- Hollenbach, D. J., Werner, M. W., and Salpeter, E. E. 1971. Molecular Hydrogen in HI Regions. *Ap. J.*, 163, 165.
- Hubble, E. 1922 a. A General Study of Diffuse Galactic Nebulae. *Ap. J.*, 56, 162.

- Hubble, E. 1922 b. The Source of Luminosity in Galactic Nebulae. *Ap. J.*, 56, 400.
- Israel, F. P. 1977. Aperture Synthesis Observations of Galactic HII Regions VI. Several Isolated HII Regions. *Astr. Ap.*, 60, 233.
- Israel, F. P. 1978. HII Regions and CO Clouds: The Blister Model. *Astr. Ap.* (In press).
- Jura, M. 1974. Formation and Destruction Rates of Interstellar H₂. *Ap. J.*, 191, 375.
- Jura, M. 1975. Interstellar Clouds Containing Optically Thin H₂. *Ap. J.*, 197, 575.
- Kahn, F. D. 1954. The Acceleration of Interstellar Clouds. *Bull. Astr. Inst. Netherlands*, 12, 187.
- Kaplan, S.A., and Pikelner, S. B. 1970. The Interstellar Medium. Harvard University Press, Cambridge, Mass.
- Kellerman, K. 1964. Measurements of the Flux Density of Discrete Radio Sources at Decimeter Wavelengths. *A. J.*, 69, 205.
- Kuiper, T. B. H., Knapp, G. R., and Kuiper, E. N. R. 1976. The Radio Spectrum, Electron Temperature and Ionizing Flux of the HII Region IC5146. *Astr. Ap.*, 48, 475.
- Kuiper, T. B. H., and Evans, N. J. 1978. Carbon Recombination - Line Mapping of the Orion Nebula. *Ap. J.*, 219, 141.
- Lada, C. J., and Chaisson, E. J. 1975. Observations of Formaldehyde Toward M17. *Ap. J.*, 195, 367.
- Lada, C. J., Gull, T. R., Gottlieb, C. A., and Gottlieb, E. W. 1976. Optical and Millimeter - Wave Observations of the M8 Region. *Ap. J.*, 203, 159.
- Lang, K. R. 1974. Astrophysical Formulae. Springer - Verlag, New York.
- Lasker, B. M. 1966 a. An Investigation of the Dynamics of Old HII Regions. *Ap. J.*, 143, 700.
- Lasker, B. M. 1966 b. Ionization Fronts for HII Regions with Magnetic Fields. *Ap. J.*, 146, 471.
- Lasker, B. M. 1968. Expansion Stages in the Dynamics of HII Regions. In Interstellar Ionized Hydrogen, edited by Y. Terzian, pp 227 - 243, W. A. Benjamin, Inc., New York.

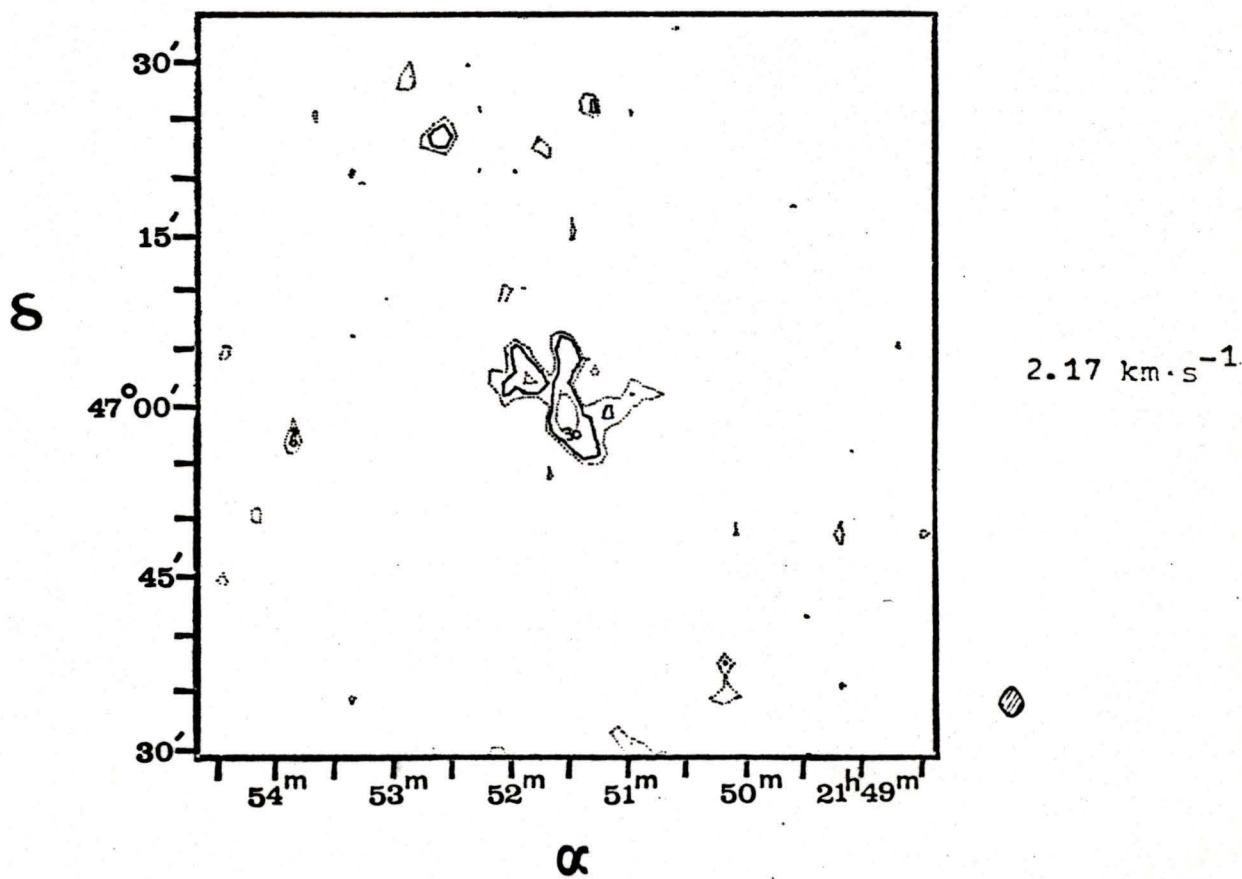
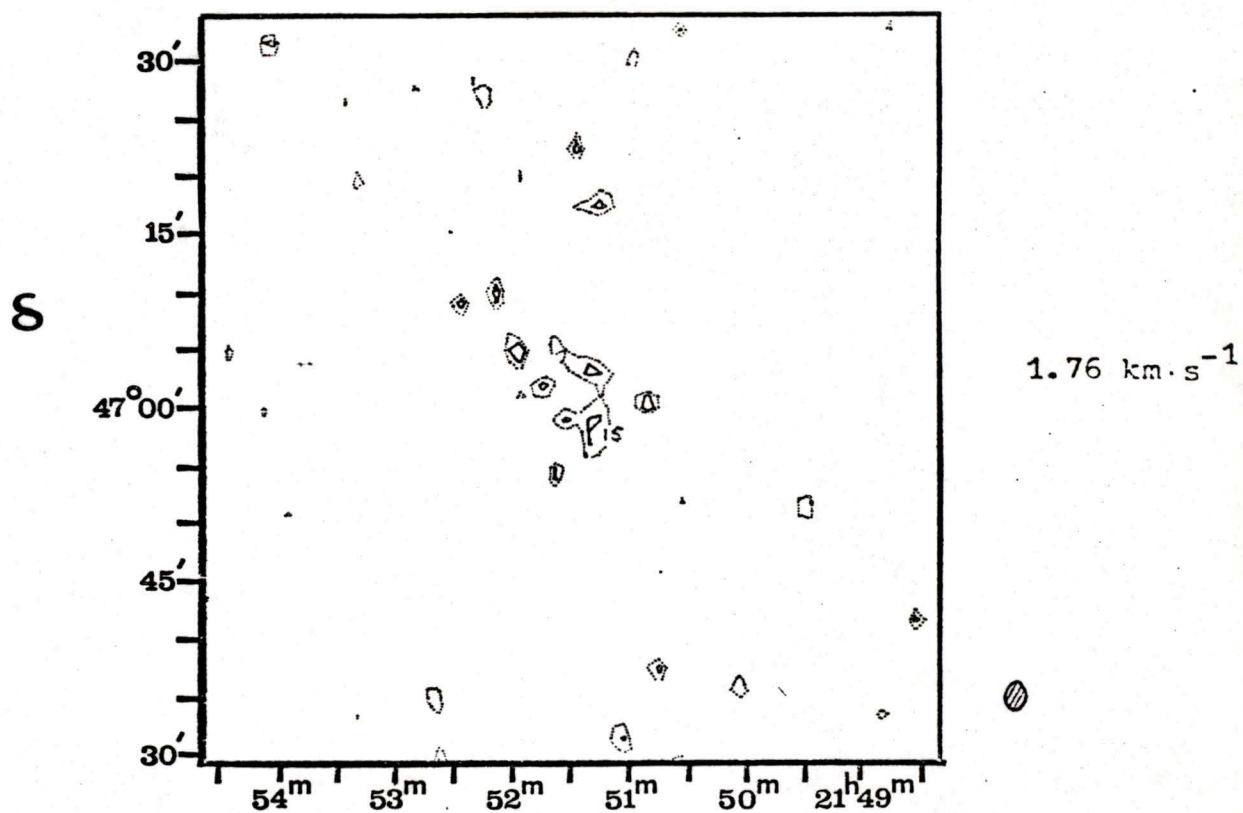
- Lo, K. Y., Burke, B. F., and Haschick, A. D. 1975. H₂O Sources in Regions of Star Formation. *Ap. J.*, 202, 81.
- Locke, J. L., Galt, J. A., and Costain, C. H. 1965. The 1420 MC/S Radio Telescope of the Dominion Radio Astrophysical Observatory. *Pub. Dom. Obs. Ottawa*, 25, 77.
- McPherson, A. K. 1974. The Structure of an HI-HII Boundary. *Ap. J.*, 192, 369.
- Mendis, D. A. 1968 a. Dissociation - Ionization Fronts in Interstellar Gas Clouds - I. *M.N.R.A.S.*, 140, 435.
- Mendis, D. A. 1968 b. Dissociation - Ionization Fronts in Interstellar Gas Clouds - II. *M.N.R.A.S.*, 141, 409.
- Mezger, P. G., and Henderson, A. P. 1967. Galactic HII Regions. I. Observations of their Continuum Radiation at the Frequency 5 GHz. *Ap. J.*, 147, 471.
- Mezger, P. G. 1968. Radio Measurements of Electron Temperatures. In Interstellar Ionized Hydrogen, edited by Y. Terzian, pp 477 - 505, W. A. Benjamin, Inc., New York.
- Mezger, P. G., and Robinson, B. J. 1968. Protostars as Sources of Anomalous OH Emission. *Nature*, 220, 1107.
- Miller, J. S. 1968. Radial Velocities and Kinematics of Galactic HII Regions. *Ap. J.*, 151, 473.
- Milman, A. S., Knapp, G. R., and Knapp, S. L. 1975. Carbon Monoxide Observations of 34 Dust Clouds. *A. J.*, 80, 101.
- Minkowski, R. 1947. New Emission Nebulae (II). *Pub. A. S. P.*, 59, 257.
- Oster, L. 1961. Emission, Absorption, and Conductivity of a Fully Ionized Gas at Radio Frequencies. *Rev. Mod. Phys.*, 33, 525.
- Panagia, N. 1973. Some Physical Parameters of Early-Type Stars. *A. J.*, 78, 929.
- Pankonin, V., Thomasson, P., and Barsuhn, J. 1977. A Survey of Radio Recombination Lines from HI Regions and Associated HII Regions. *Astr. Ap.*, 54, 335.
- Peimbert, M. 1967. Temperature Determinations of HII Regions. *Ap. J.*, 150, 825.
- Peimbert, M., and Torres-Peimbert, S. 1977. Chemical Composition of the Orion Nebula. *M.N.R.A.S.*, 179, 217.

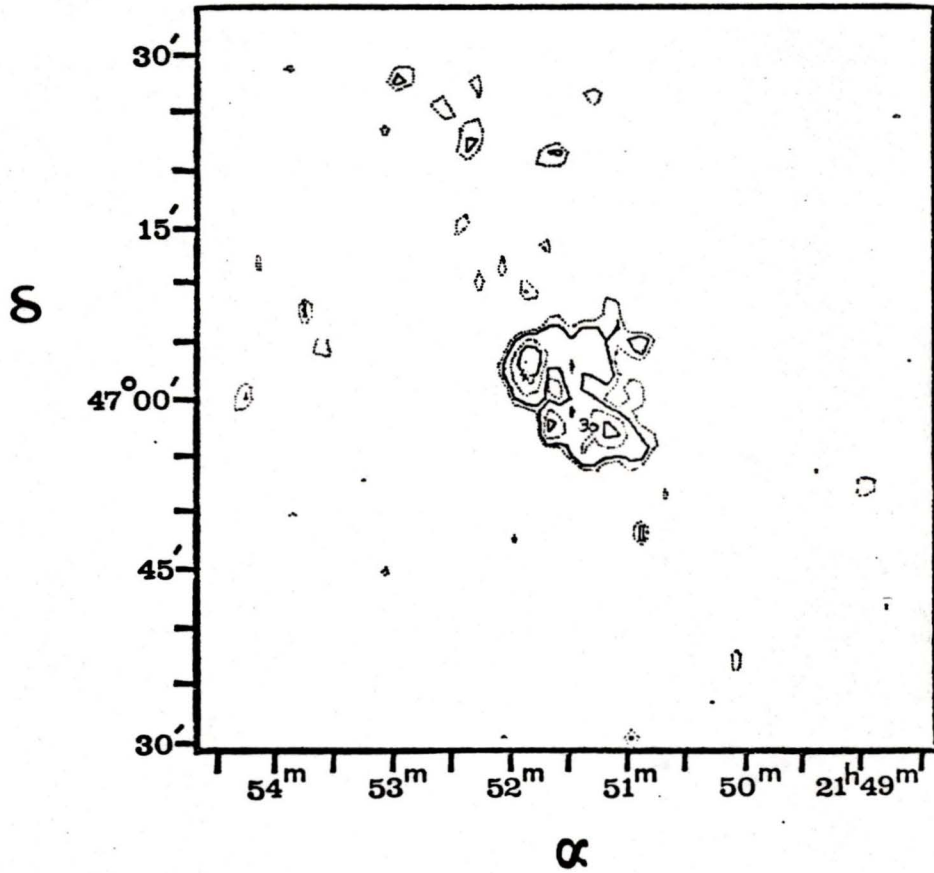
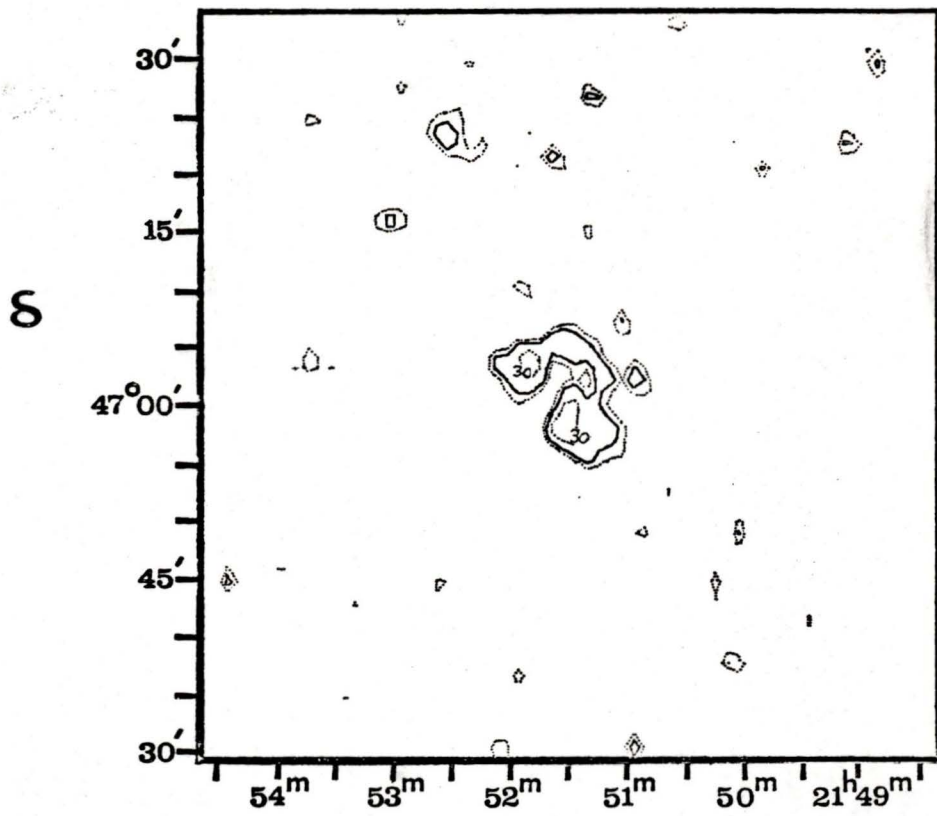
- Radhakrishnan, V., Murray, J. D., Lockhart, P., and Whittle, P. J. 1972. II. Galactic 21 - Centimeter Observations in the Direction of 35 Extragalactic Sources. *Ap. J. Suppl.*, 24, 15.
- Raimond, E. 1966. Hydrogen Connected with Two Stellar Associations in Monoceros. *Bull. Astr. Inst. Netherlands*, 18, 191.
- Reddish, V. C. 1967. The Dependence of Interstellar Reddening on Luminosity Amongst O and B Stars. *M.N.R.A.S.*, 135, 251.
- Reifenstein III, E. C., Wilson, T. L., and Burke, B. F. 1970. A Survey of H109 α Recombination Line Emission in Galactic HII Regions of the Northern Sky. *Astr. Ap.*, 4, 357.
- Riegel, K. W. 1967. 21 - CM Line Observations of Galactic HII Regions. *Ap. J.*, 148, 87.
- Roger, R. S., Costain, C. H., Lacey, J. D., Landecker, T. L., and Bowers, F. K. 1973. A Supersynthesis Radio Telescope for Neutral Hydrogen Spectroscopy at the Dominion Radio Astrophysical Observatory. *Proc. I.E.E.E.*, 61, 1270.
- Rubin, R. H. 1968. A Discussion of the Sizes and Excitation of HII Regions. *Ap. J.*, 154, 391.
- Samson, W. B. 1975. The Distribution of Interstellar Matter in IC5146. *Ap. Space Sci.*, 34, 377.
- Samson, W. B. 1976. The Polarization of Starlight in NGC654 and IC5146. *Ap. Space Sci.*, 44, 217.
- Savedoff, M. P., and Greene, J. 1955. Expanding HII Regions. *Ap. J.*, 122, 477.
- Scoville, N. F., and Solomon, P. M. 1974. Radiative Transfer, Excitation, and Cooling of Molecular Emission Lines (CO and CS). *Ap. J. (Letters)*, 187, 167.
- Seaton, M. J. 1974. Temperatures of Gaseous Nebulae - a Decade of Depression. *Quart. J.R.A.S.*, 15, 370.
- Stecher, T. P., and Williams, D. A. 1967. Photodestruction of Hydrogen Molecules in HI Regions. *Ap. J. (Letters)*, 149, L29.
- Strom, K. M., Strom, S. E., Carrasco, L., and Vrba, F. J. 1975. M78: An Active Region of Star Formation in the Dark Cloud Lynds 1630. *Ap. J.*, 196, 489.
- Strömberg, B. 1939. The Physical State of Interstellar Hydrogen. *Ap. J.*, 89, 526.

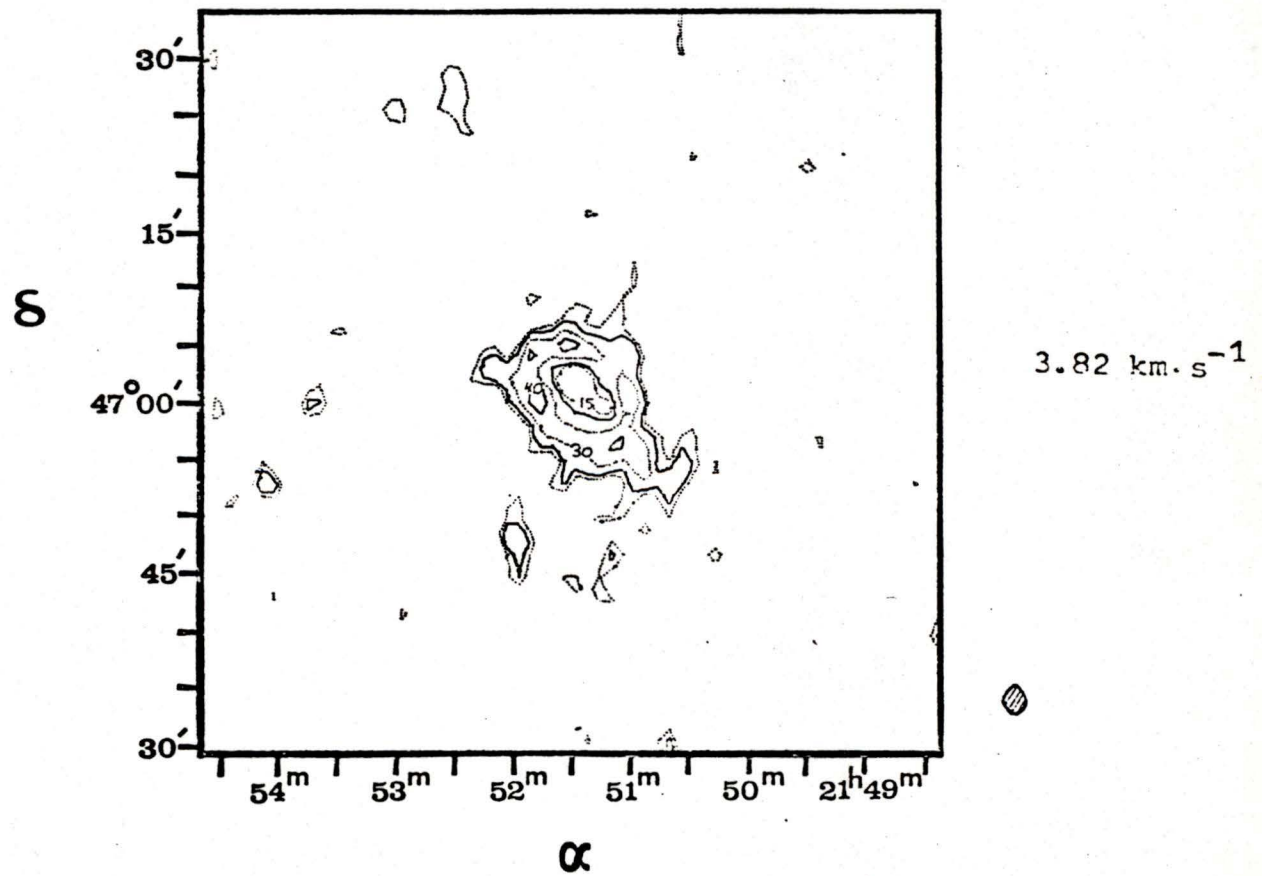
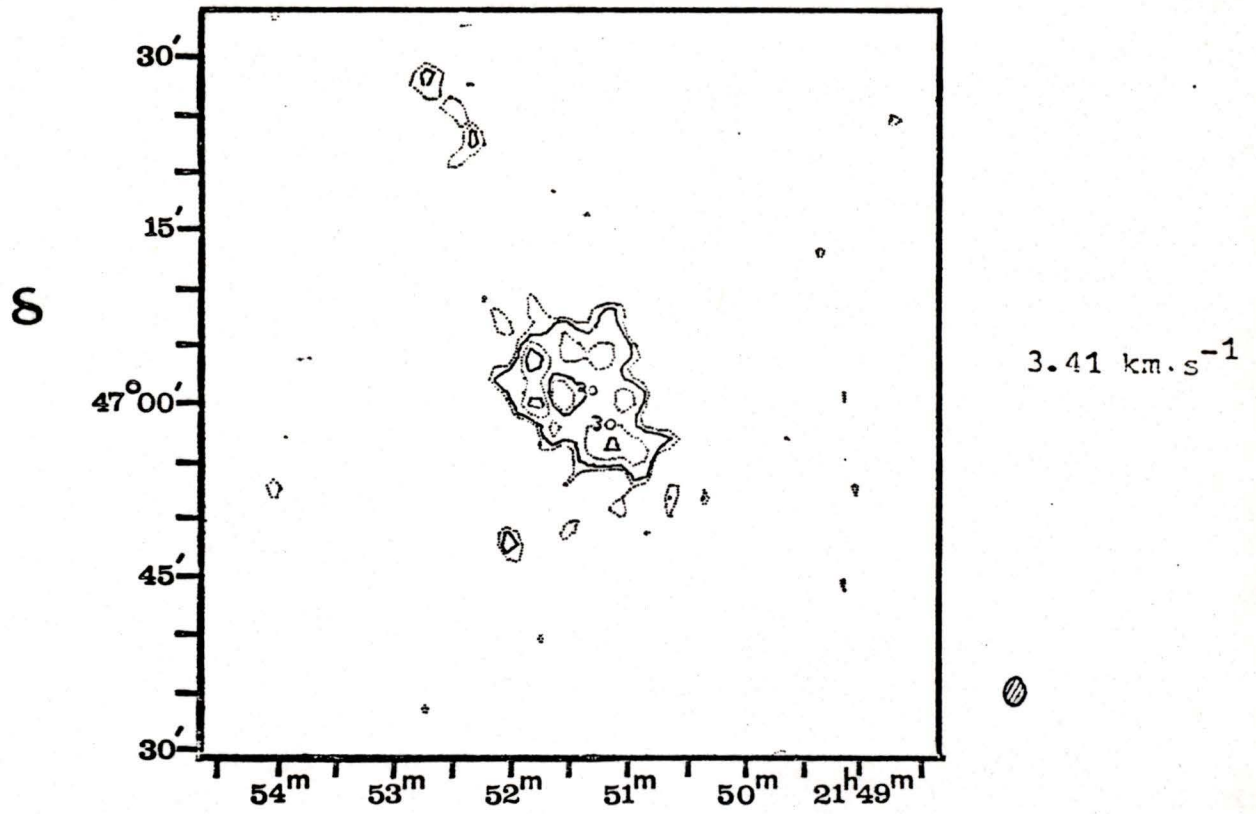
- Terzian, Y., Dennison, B., and Balick, B. 1973. The Nature of Small HII Regions Deduced From Their Radio Emission. *Pub. A.S.P.*, 85, 806.
- Thaddeus, P. 1977. Molecular Clouds. In *Star Formation*, I.A.U. Symps., 75, edited by T. de Jong, and A Maeder, pp 37 - 67, D. Reidel Publishing Co., Boston, Mass.
- Tucker, K. D., Kutner, M. L., and Thaddeus, P. 1973. A Large Carbon Monoxide Cloud in Orion. *Ap. J. (Letters)*, 186, L13.
- Van de Hulst, H. C., Muller, C. A., and Oort, J. H. 1954. The Spiral Structure of the Outer Part of the Galactic System Derived from the Hydrogen Emission at 21CM Wavelength. *Bull. Astr. Inst. Netherlands*, 12, 117.
- Von Hoerner, S. 1975. A Review of Star Formation. In *Lecture Notes in Physics 42: HII Regions and Related Topics*, edited by J. Ehlers, K. Hepp, H. A. Weidenmüller, J. Zittartz, and W. Beiglböck, pp 53 - 78, Springer-Verlag, New York.
- Wade, C. 1958. Discussion. *Rev. Mod. Phys.*, 30, 946.
- Walker, M. F. 1959. Studies of Extremely Young Clusters. III. IC5146. *Ap. J.*, 130, 57.
- Williamson, R. A. 1970. Internal Radial Velocities of Some Selected Small Diameter HII Regions. *Ap. Space Sci.*, 6, 45.
- Williams, D. R. W. 1973. Studies of Four Regions for Use as Standards in 21 - CM Observations. *Astr. Ap. Suppl.*, 8, 505.
- Wolf, M. 1904. A Remarkable Nebula in Cygnus Connected with Starless Regions. *M.N.R.A.S.*, 64, 838.
- Zuckerman, B. 1973. A Model of the Orion Nebula. *Ap. J.*, 183, 863.
- Zuckerman, B., and Ball, J. A. 1974. On Microwave Recombination Lines from HI Regions. *Ap. J.*, 190, 35.

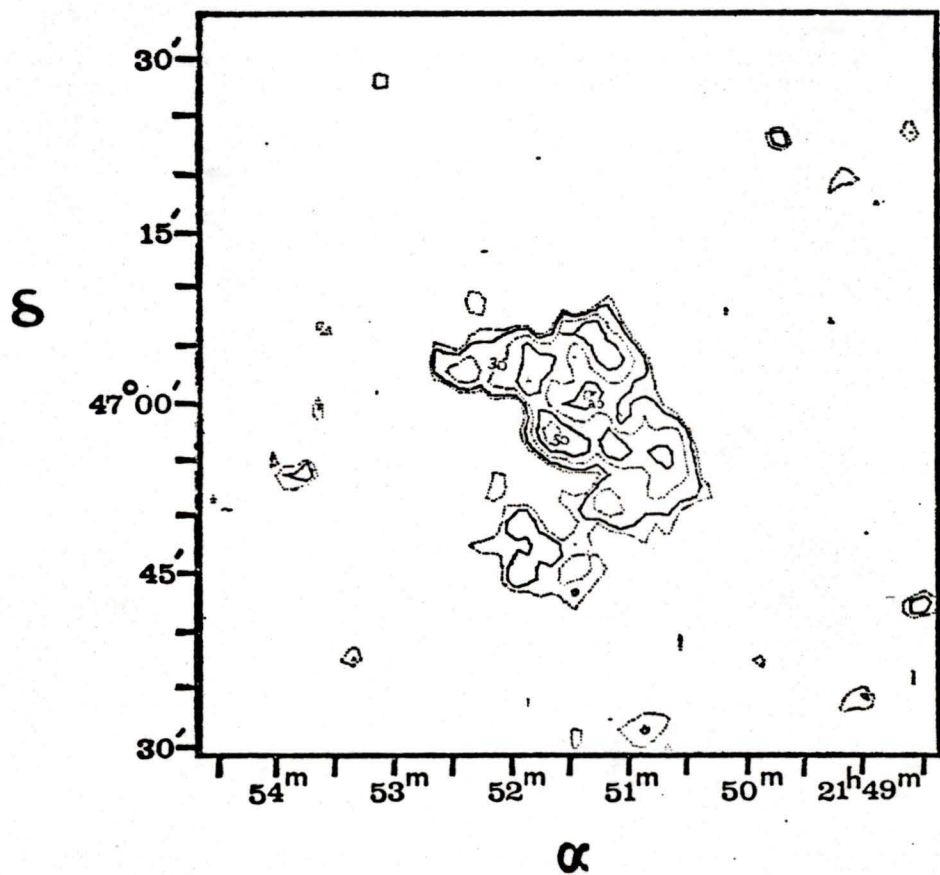
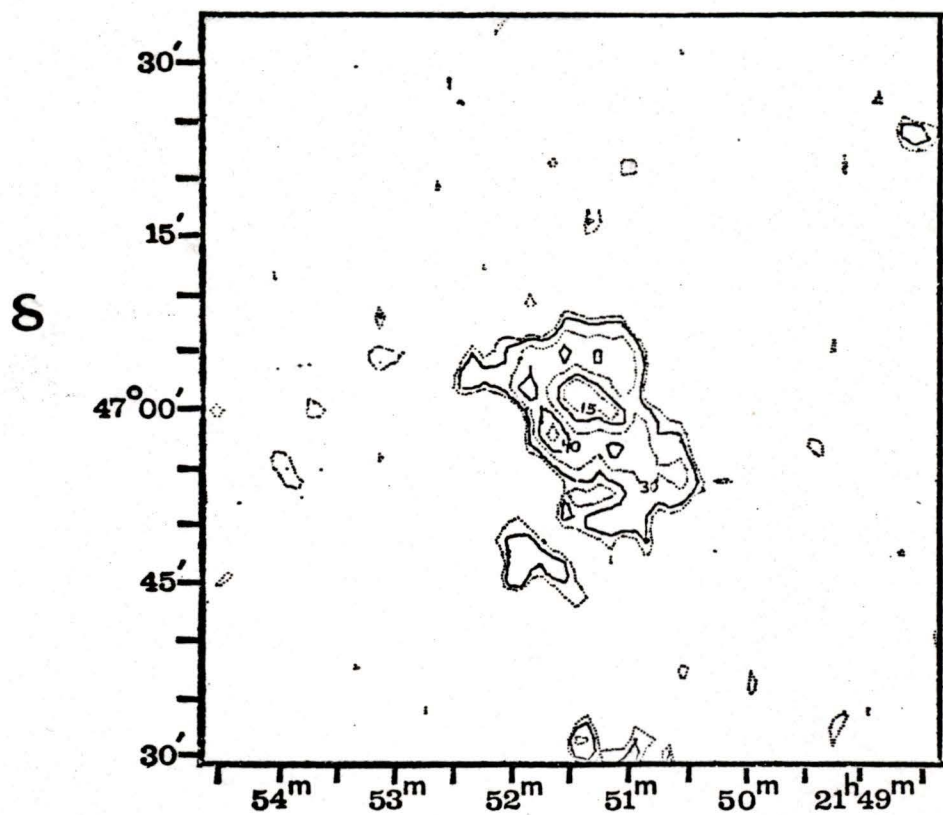
APPENDIX A

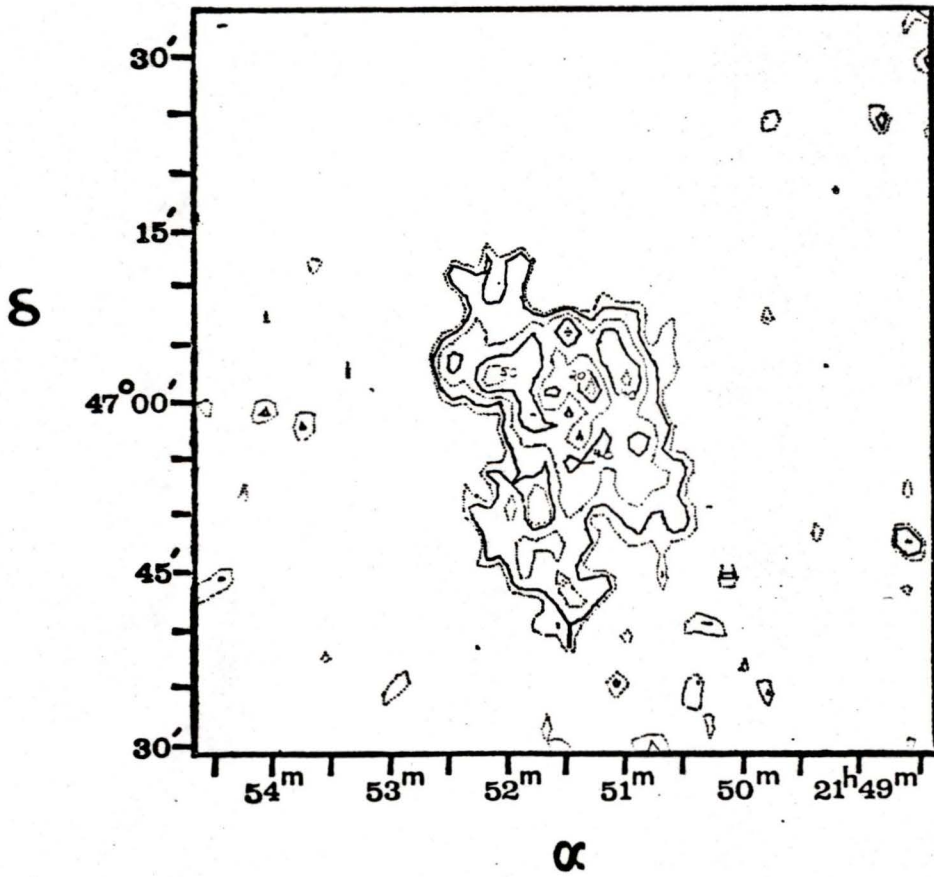
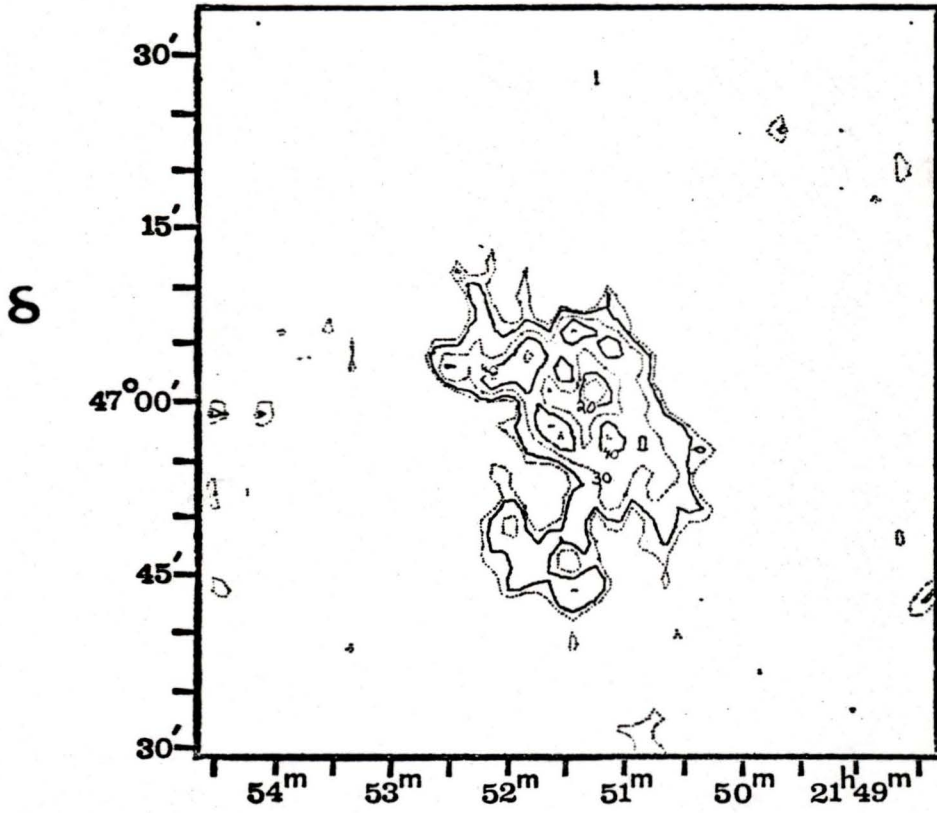
Thirty $1^\circ \alpha - \delta$ HI maps which cover the velocity range $1.76 \leq V \text{ (km}\cdot\text{s}^{-1}) \leq 13.71$ are presented here. All maps contain interferometer data only and are weighted by the polar diagram of the 8.6 m paraboloids. Contours have been set at the following brightness temperatures above the map baseline: 15, 20, 30, 40, 50, 60, 70, and 80 °K, with the contours of alternating dotted and solid lines. The dotted line which indicates the maximum extent of the emission is the lowest 15 °K contour. To aid in locating correct contour values above this, some of the contours have been labelled. The synthesized half-power beamshape can be seen at the lower right of each map.

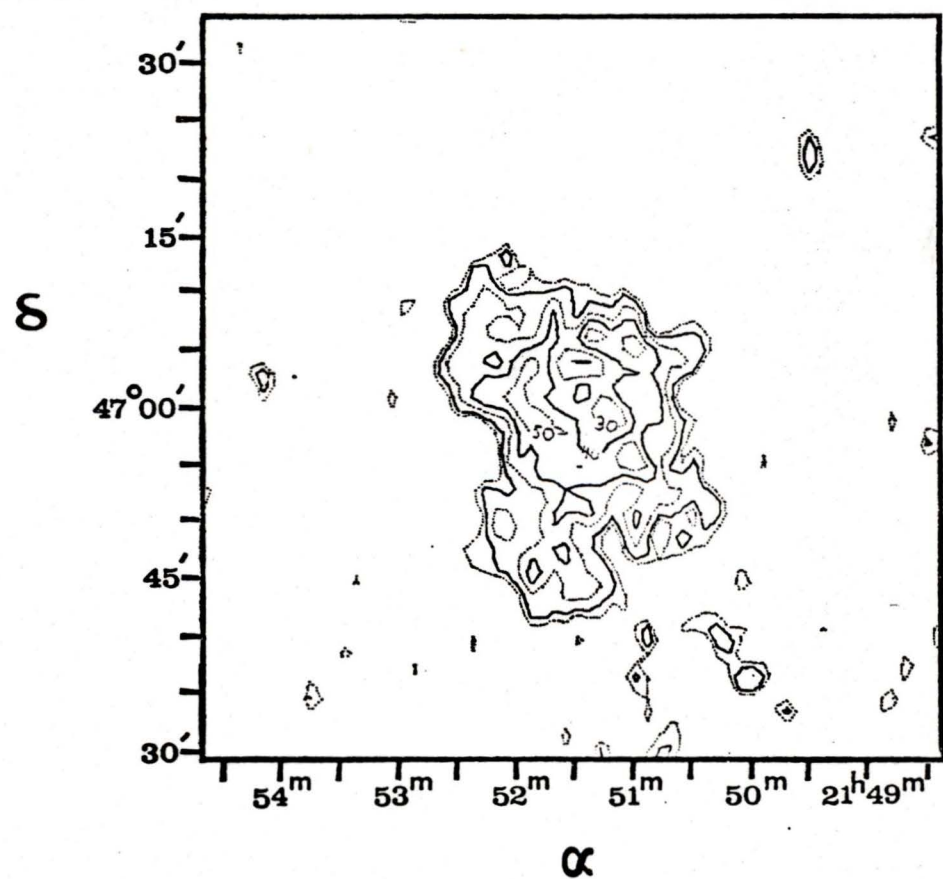
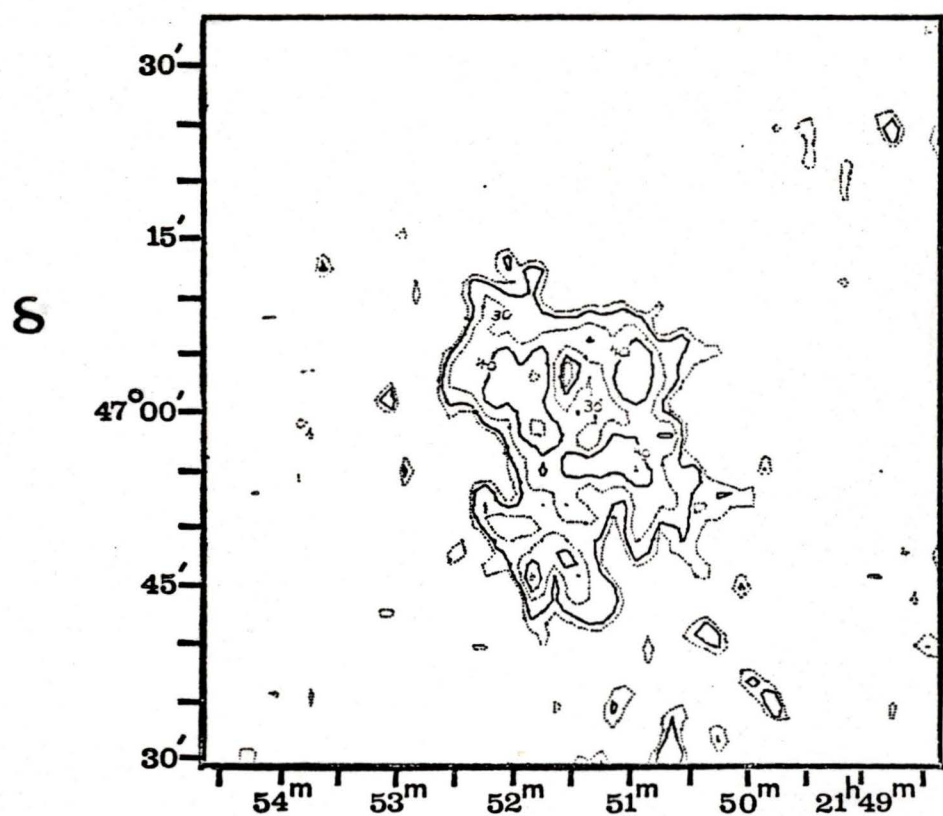


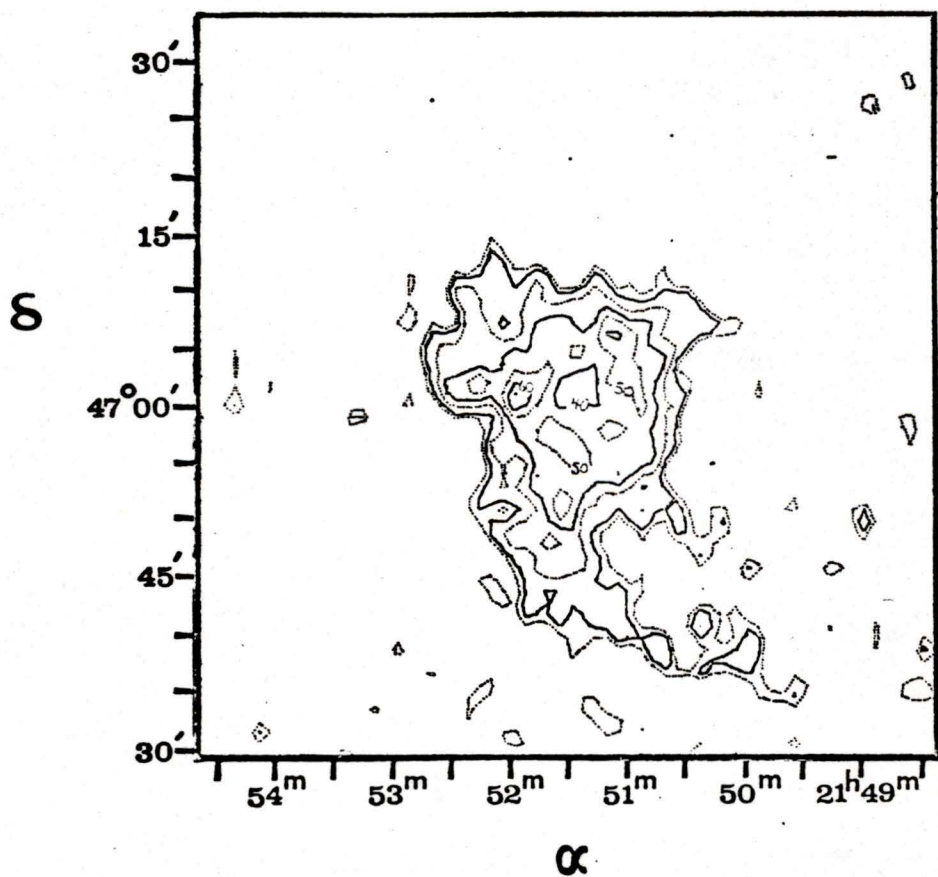
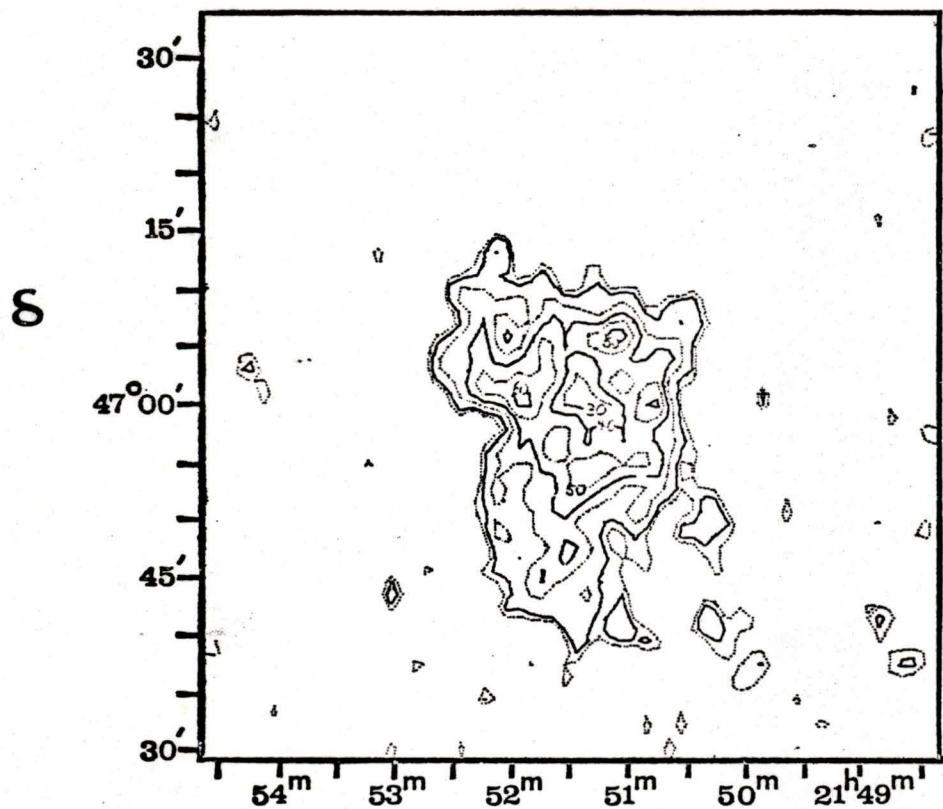


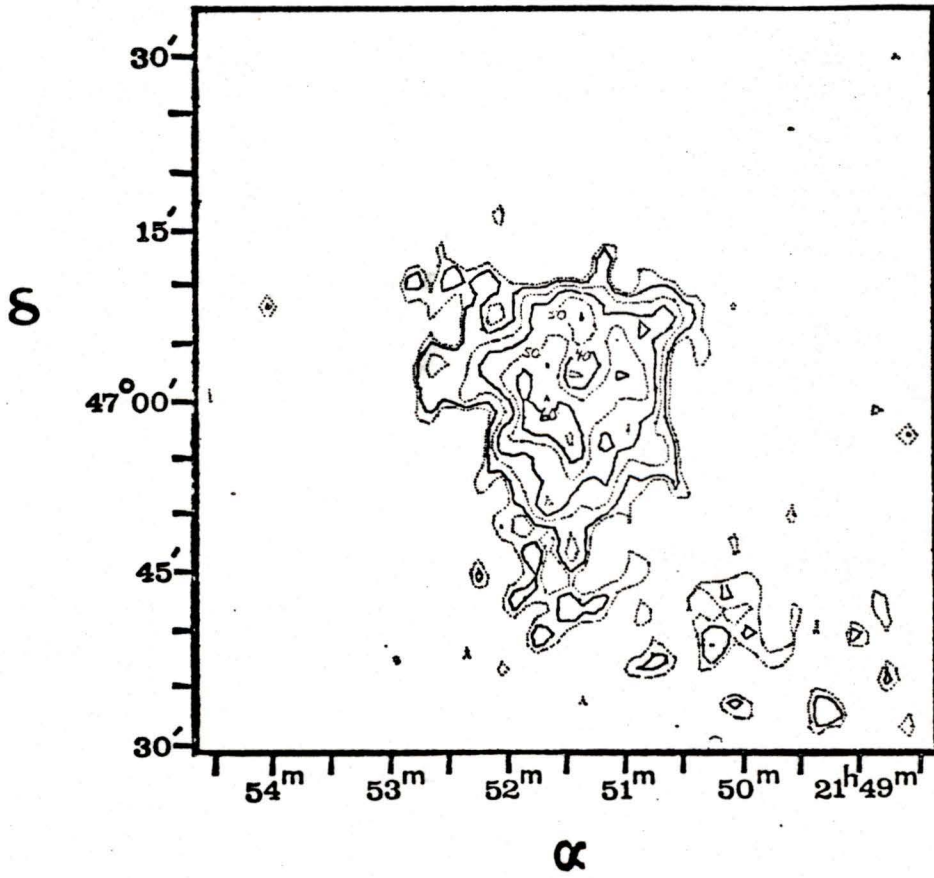
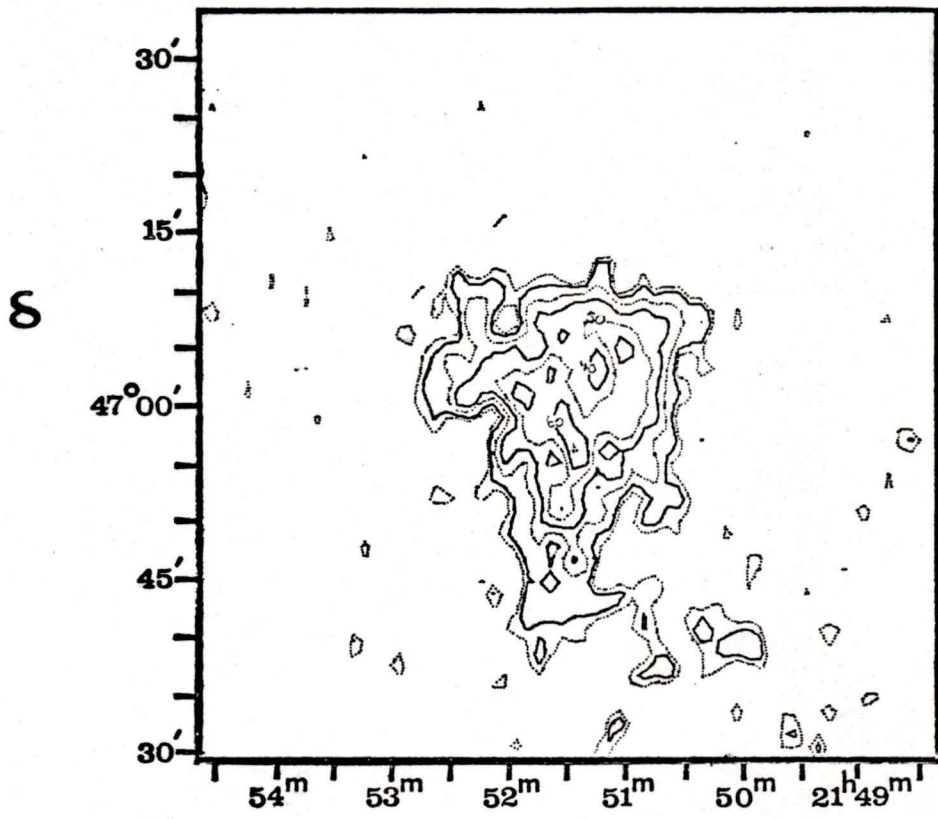


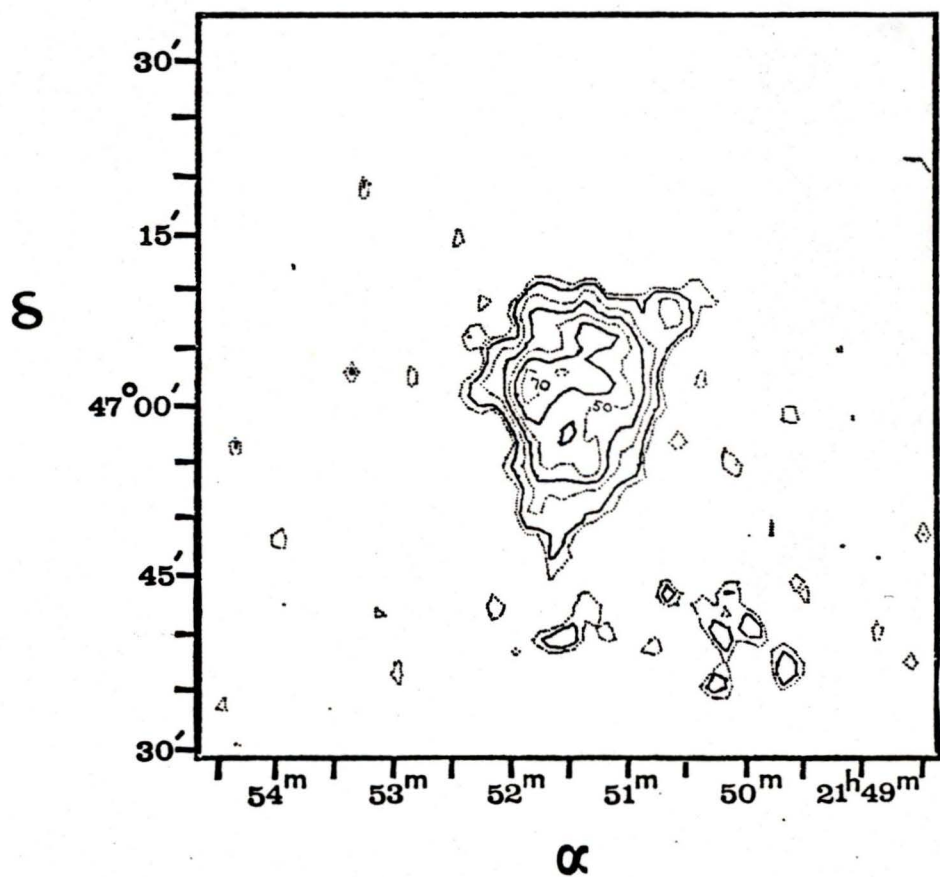
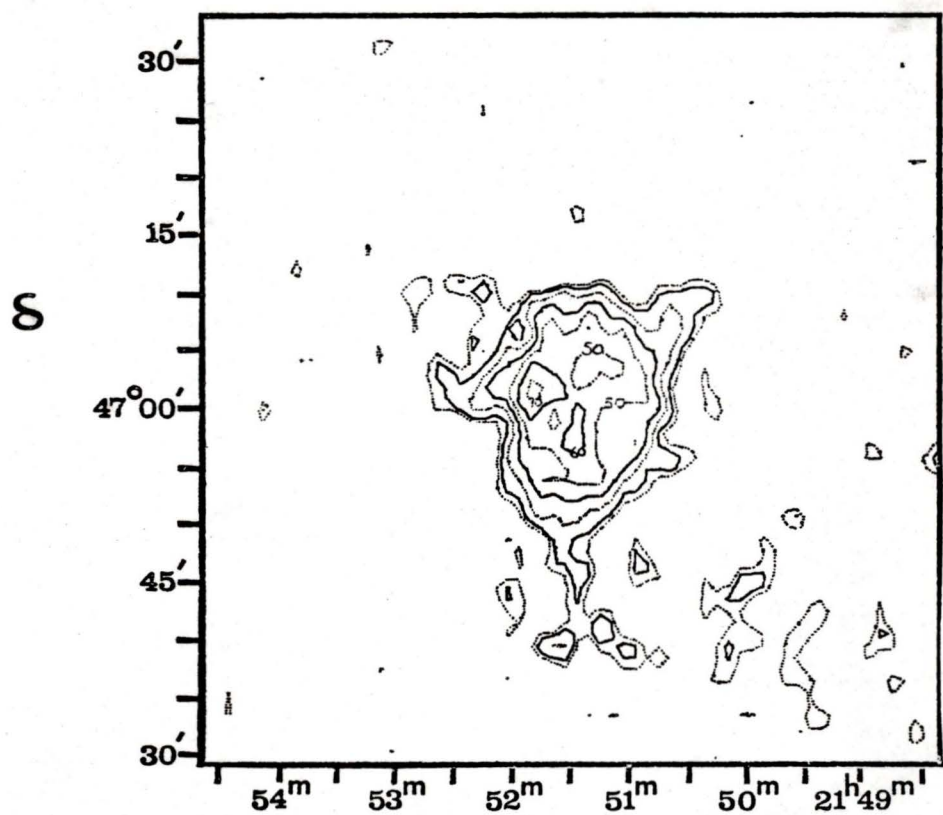


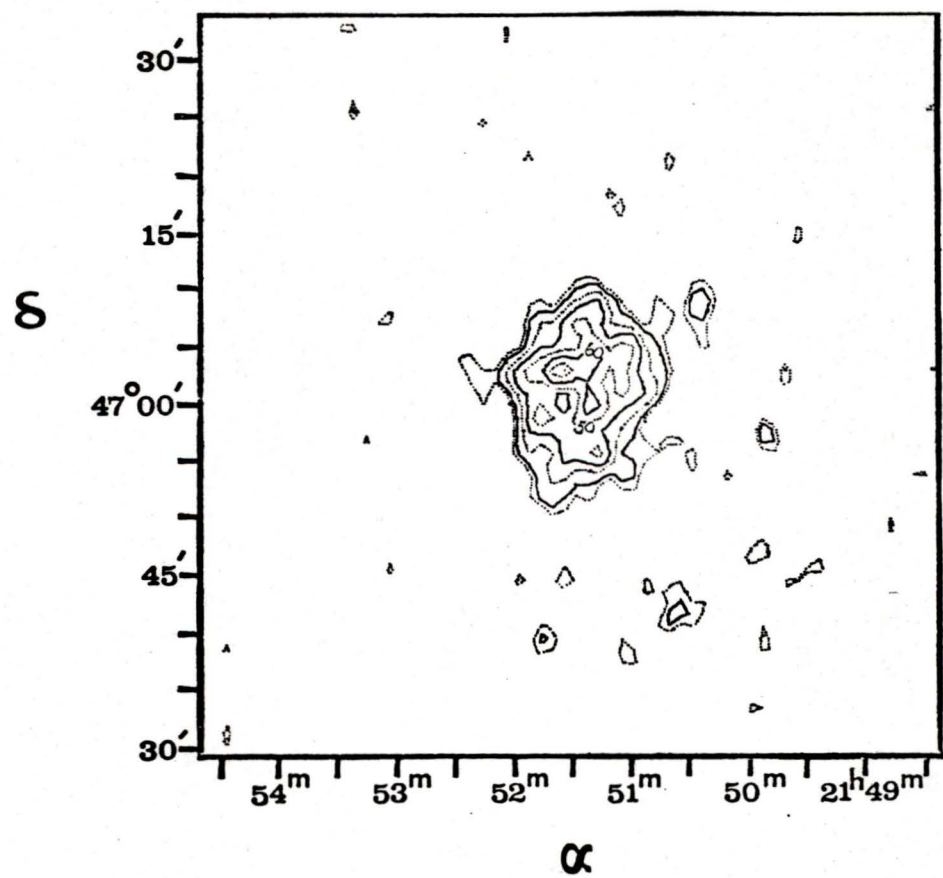
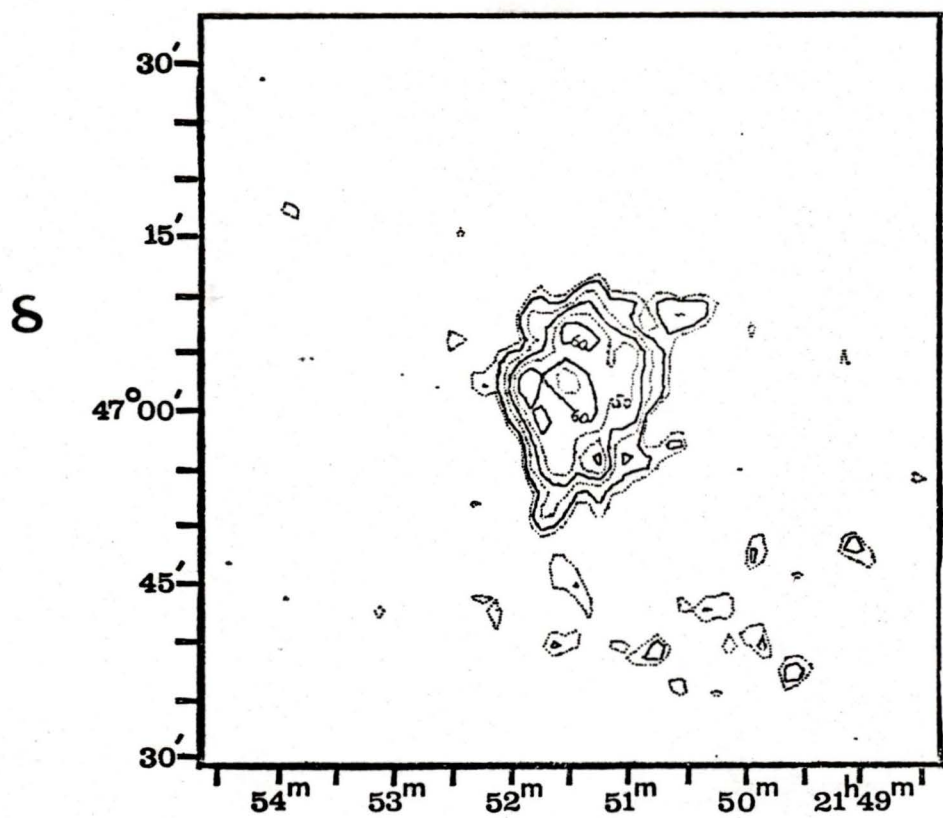


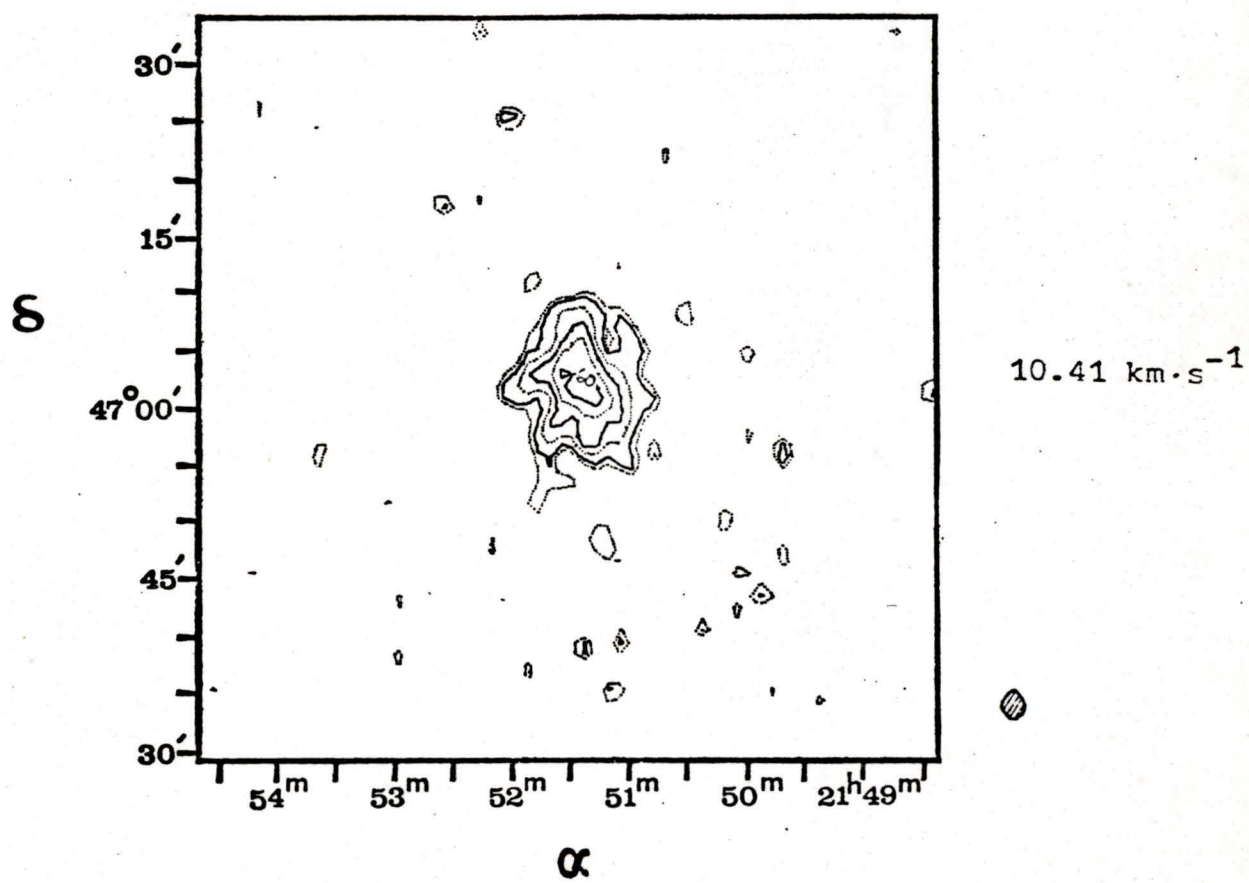
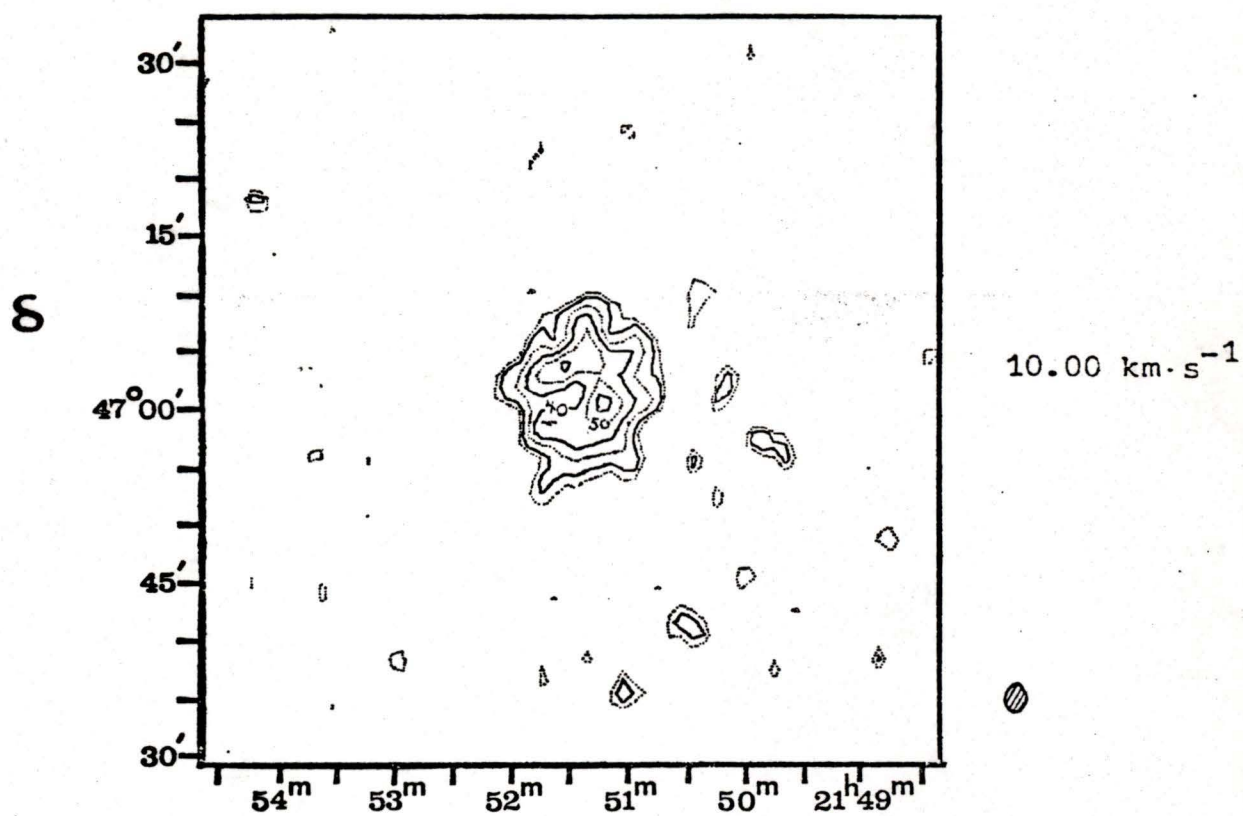


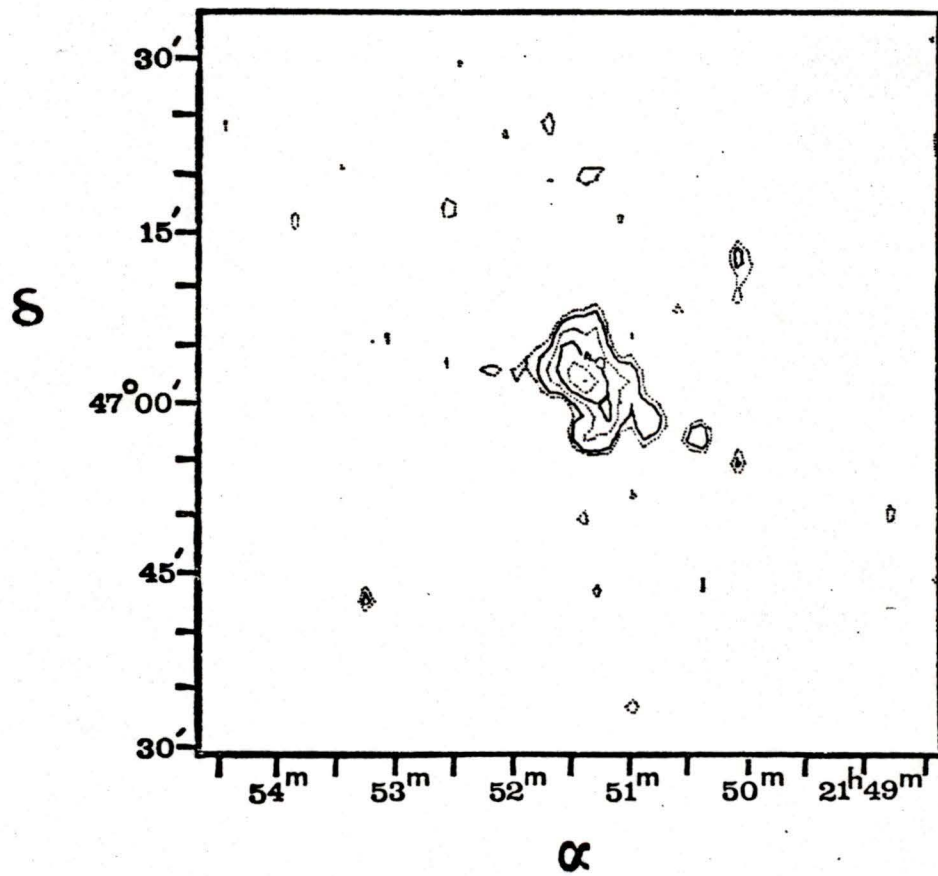
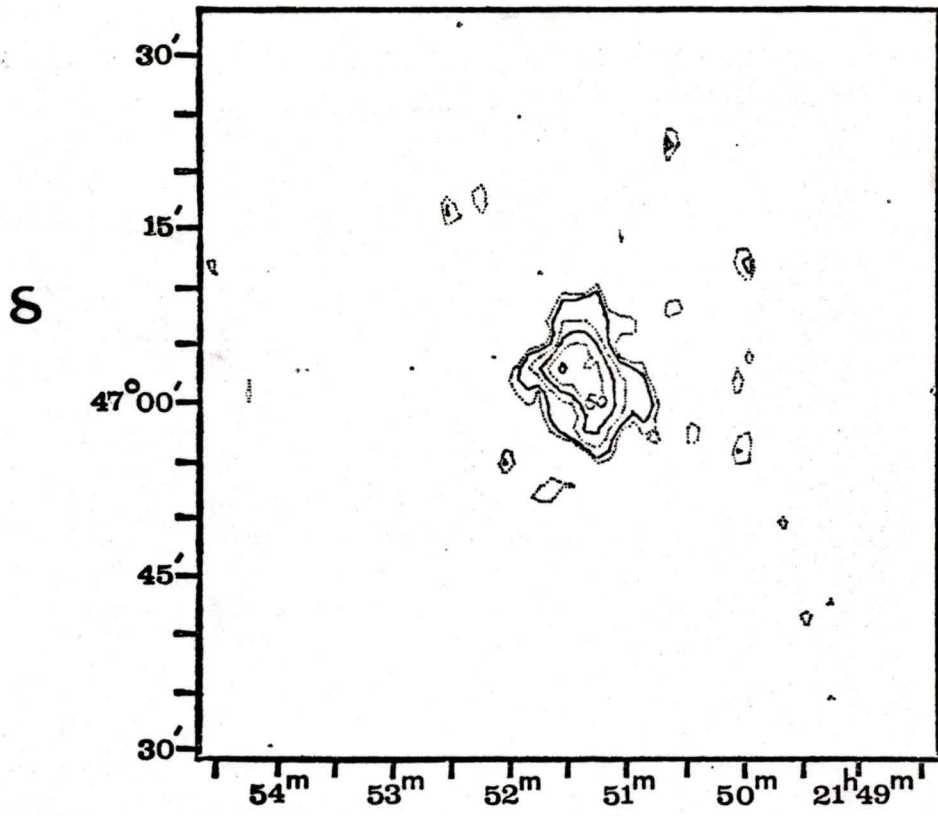


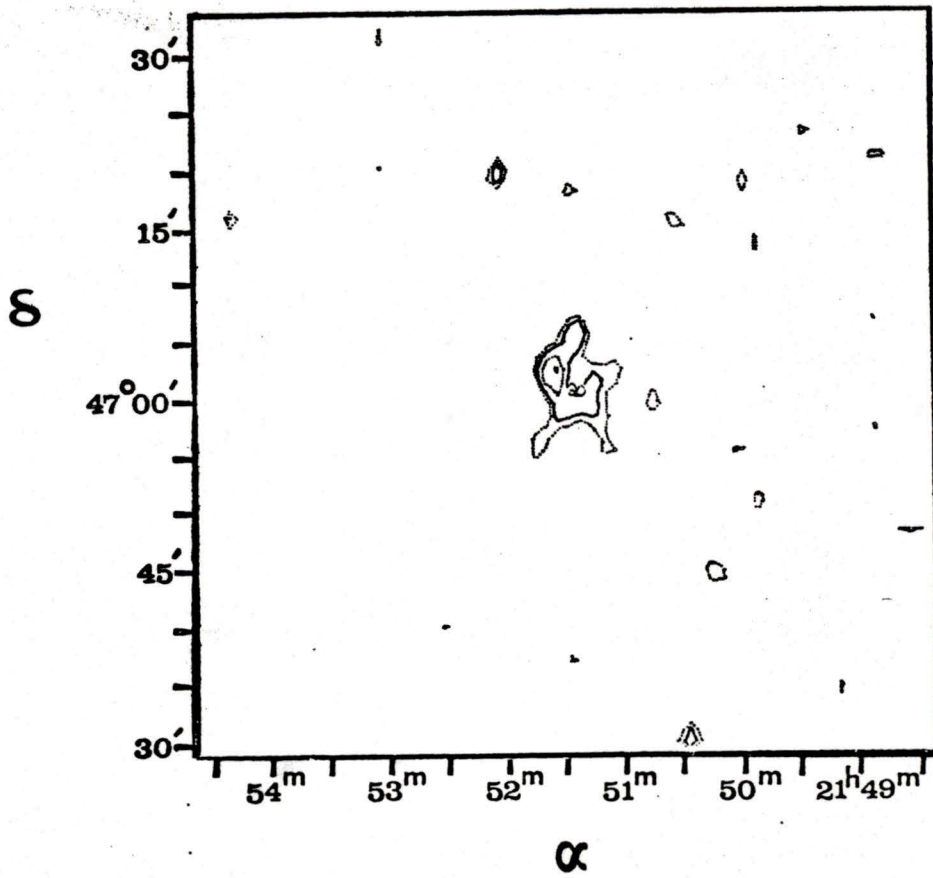
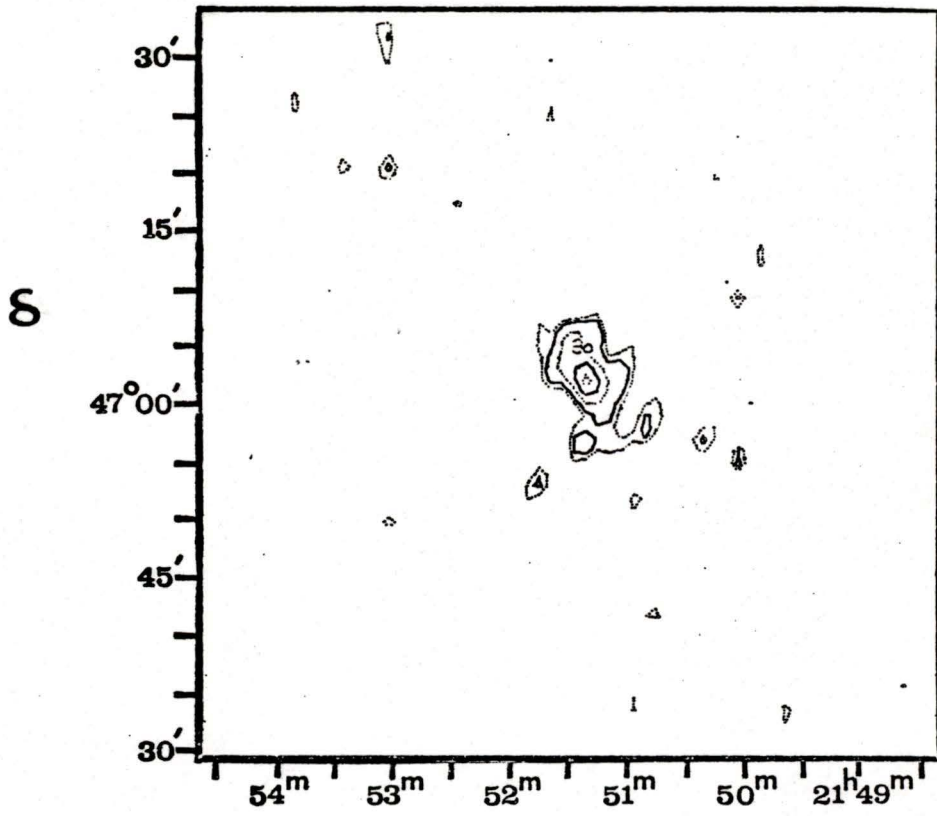


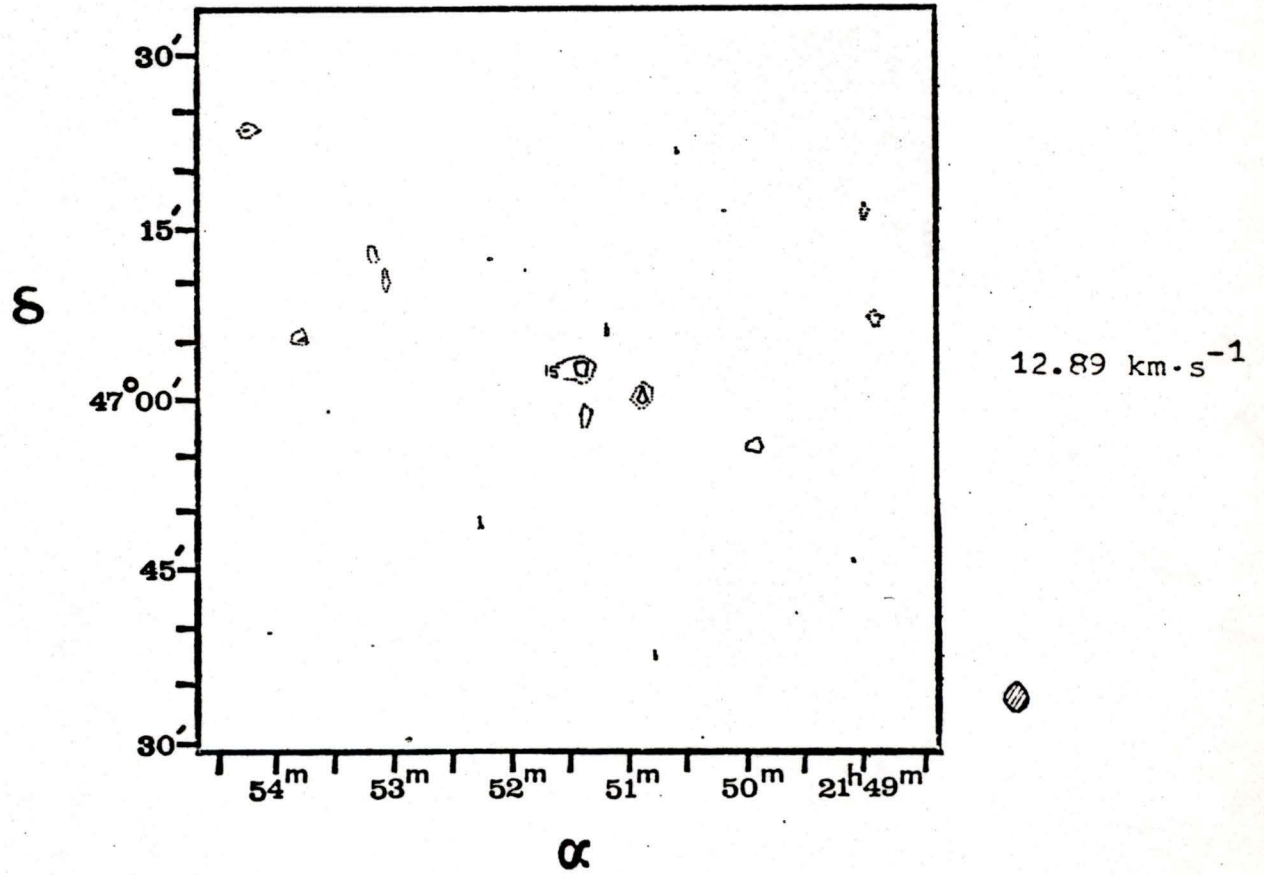
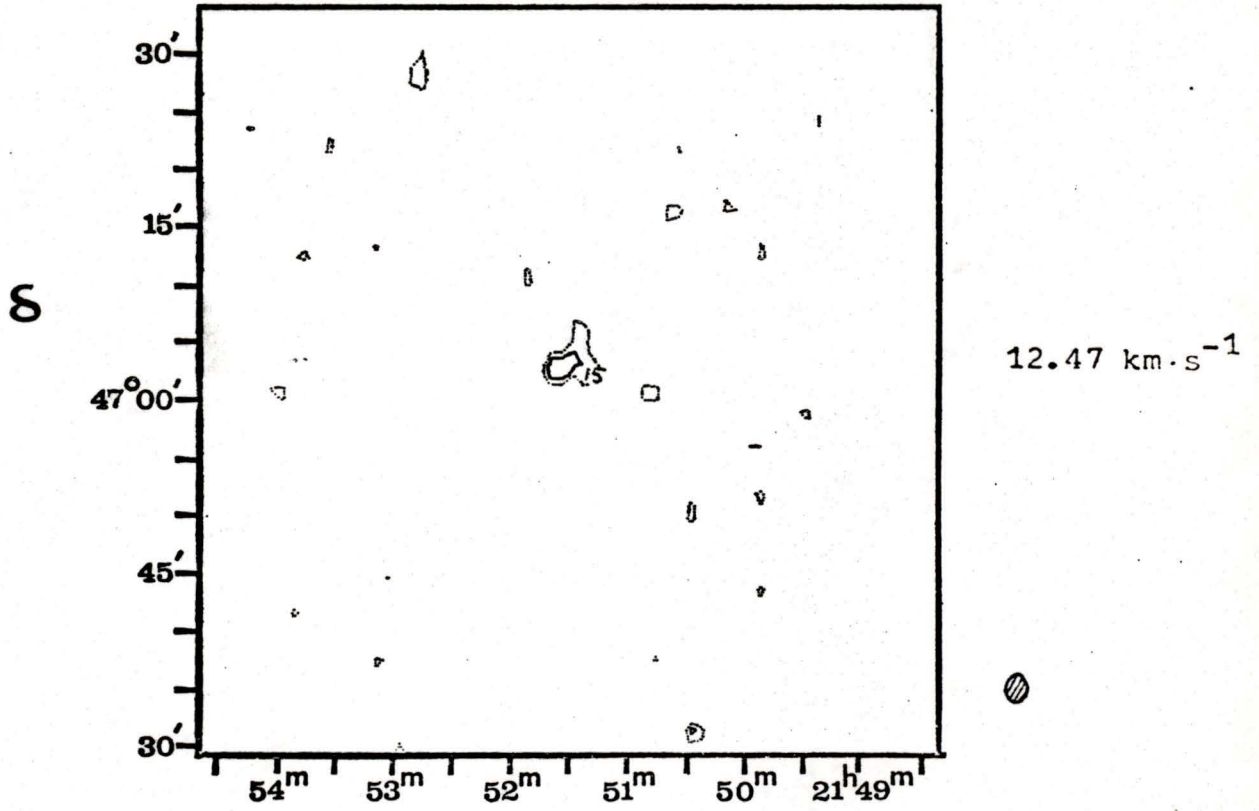


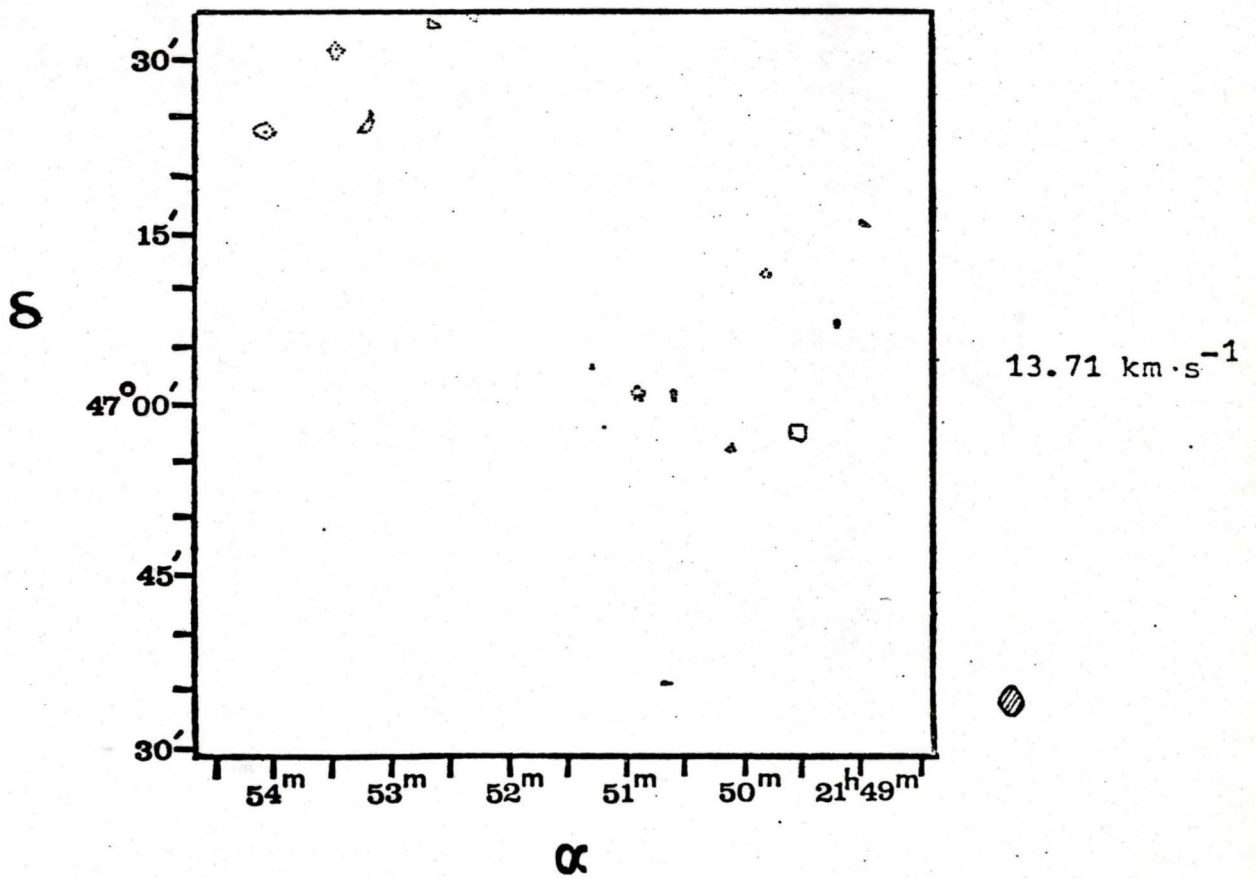
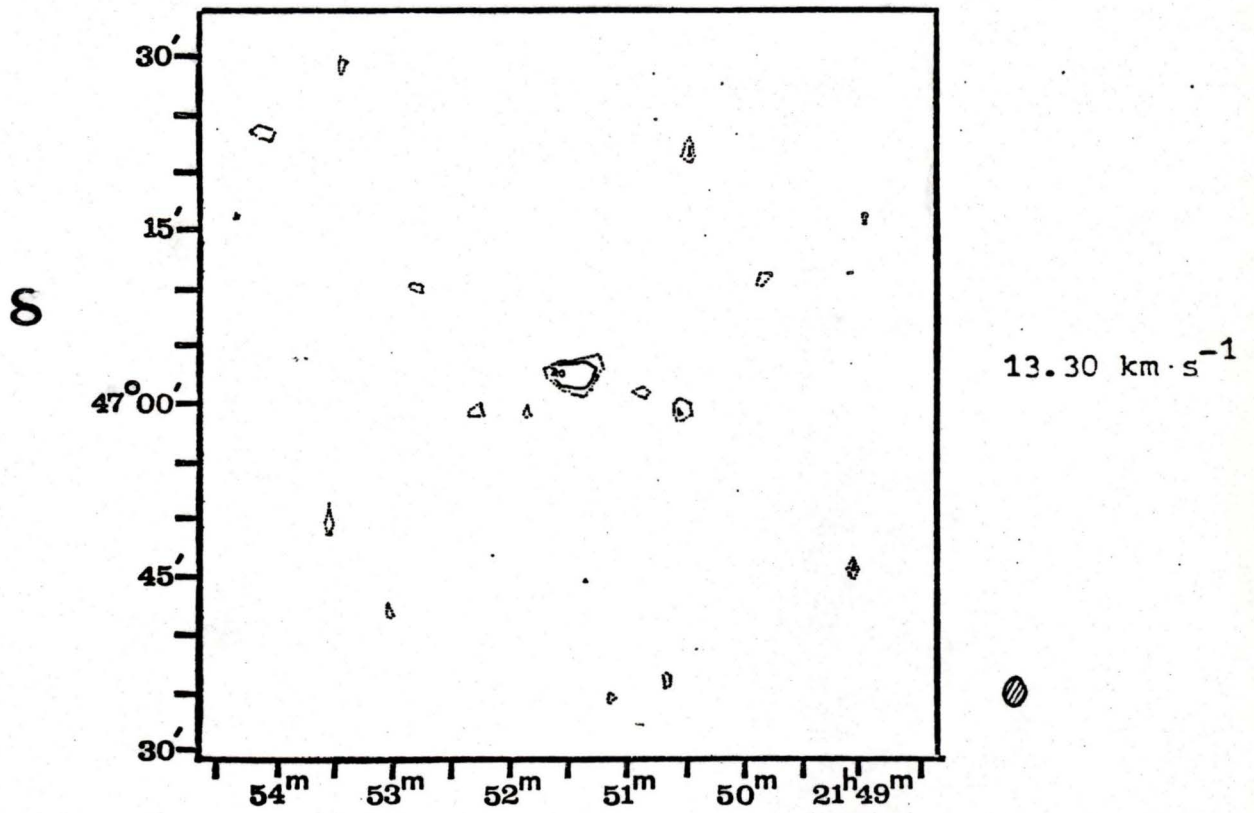






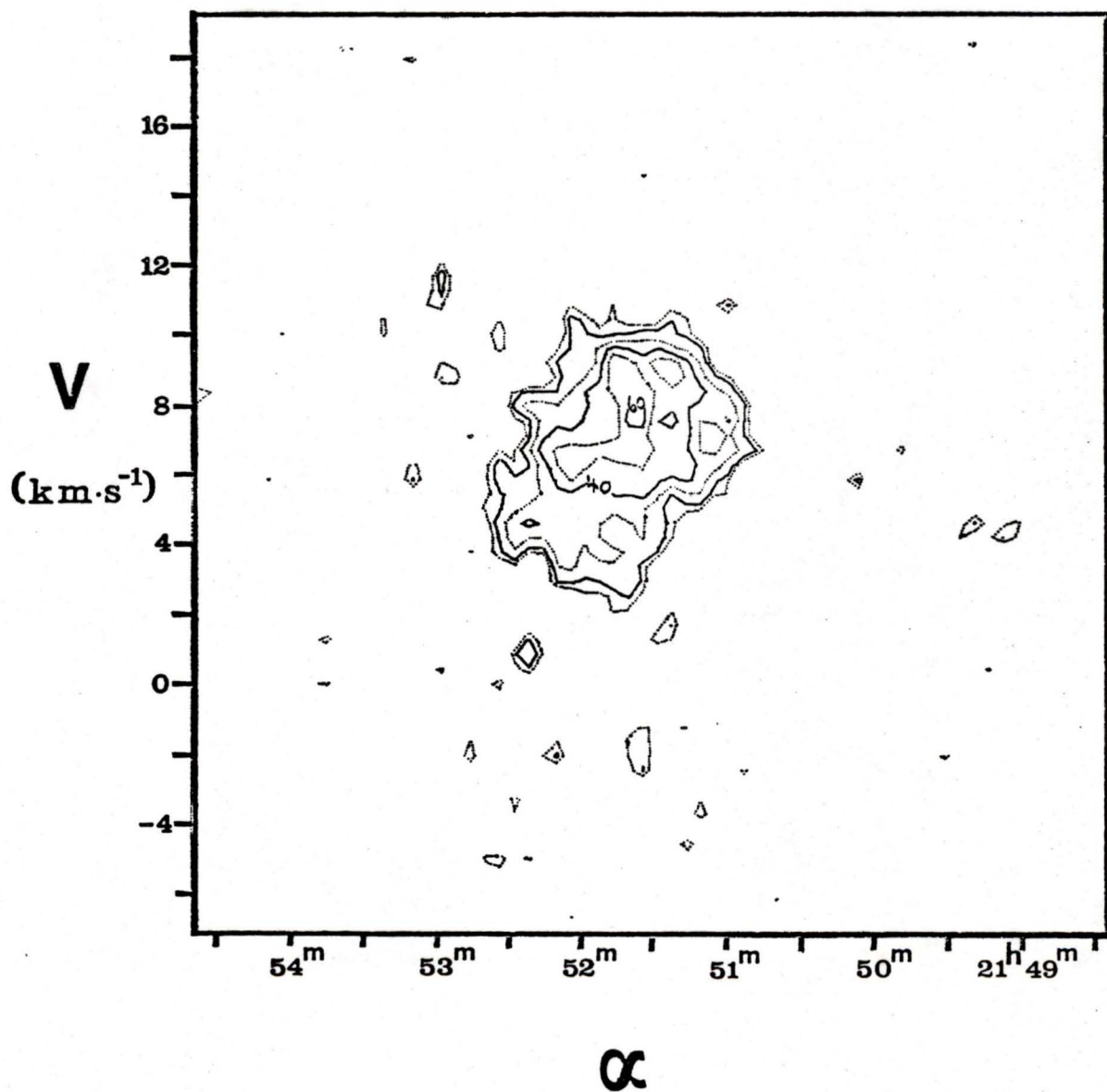


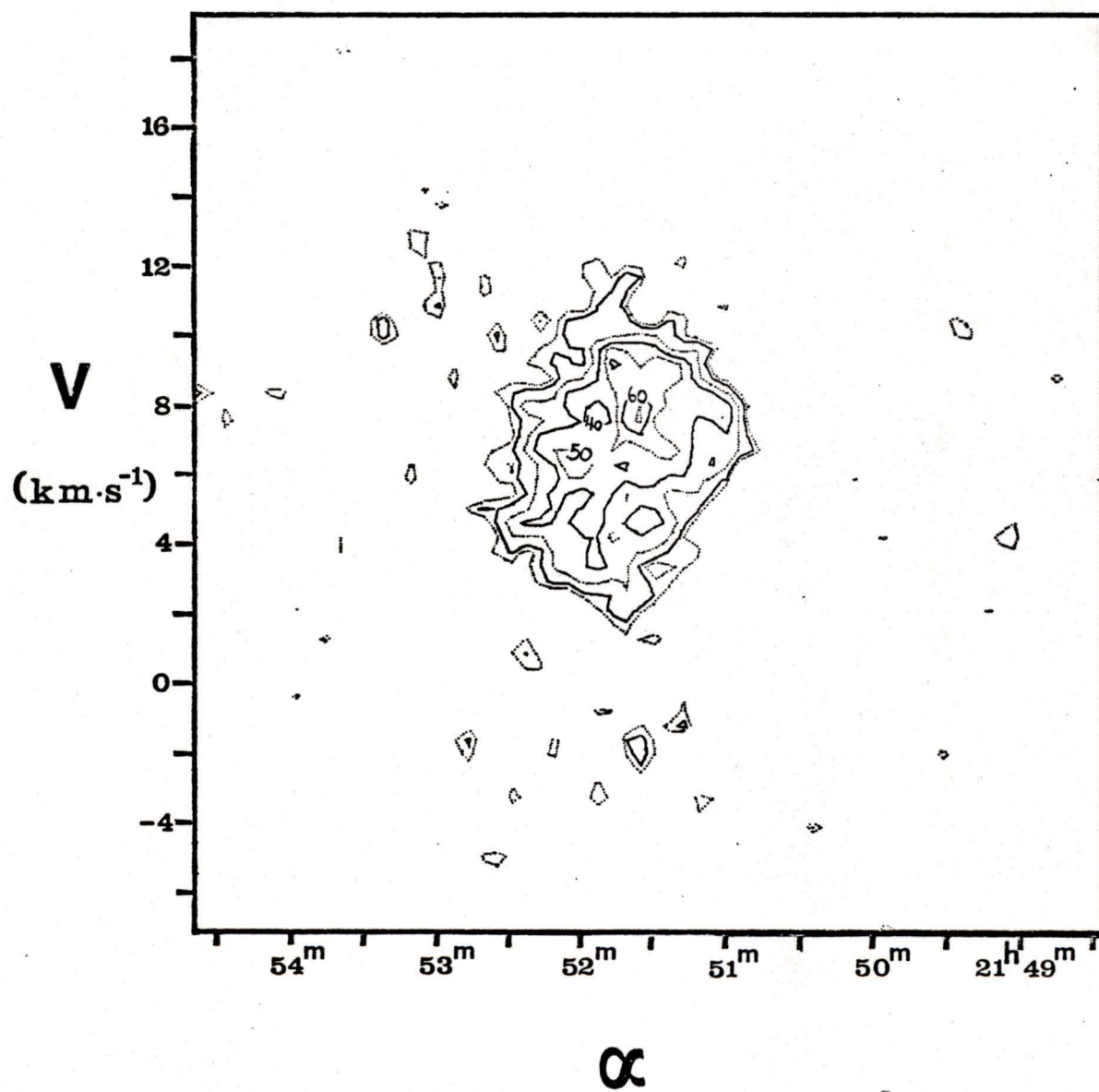


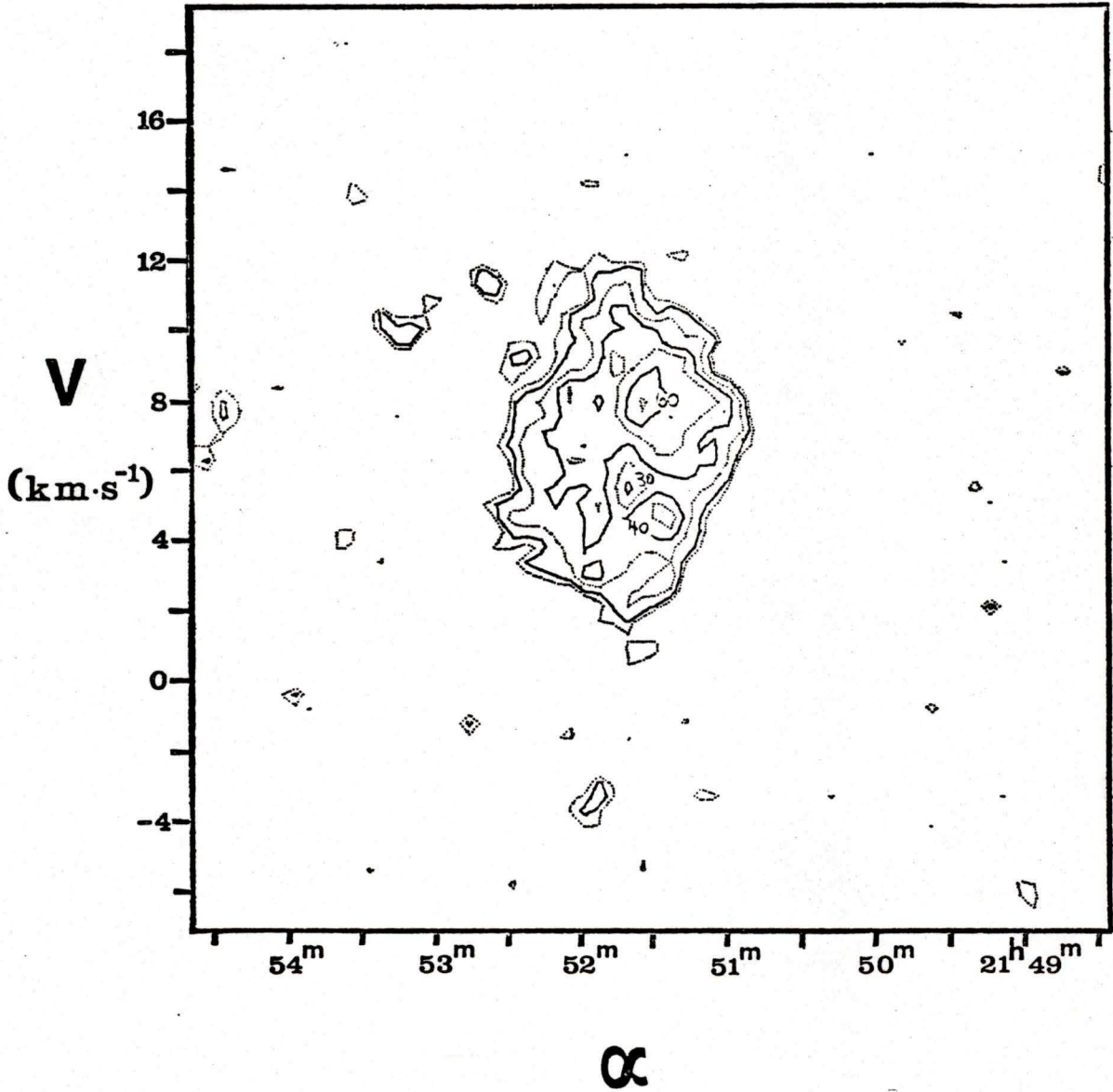


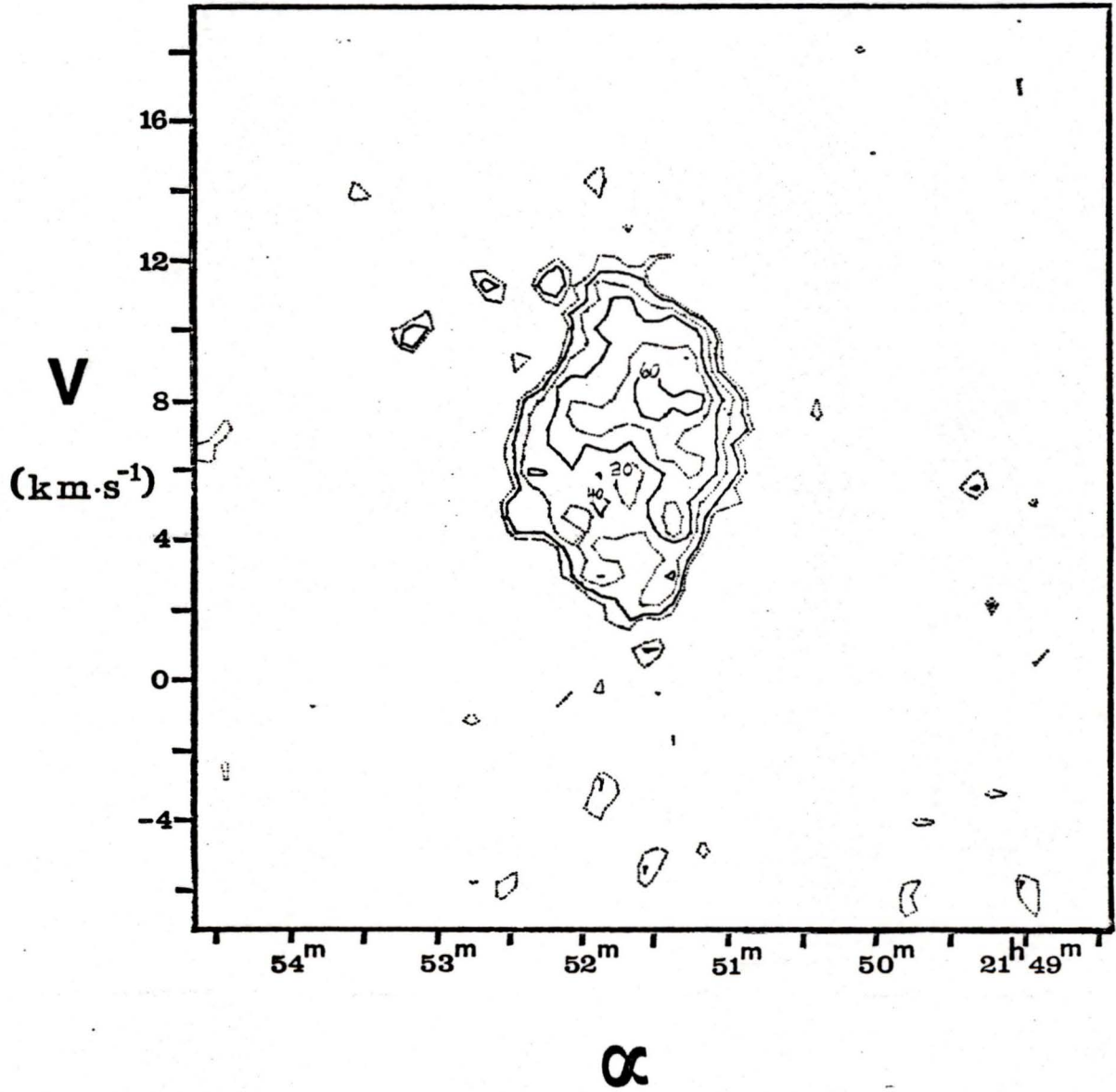
APPENDIX B

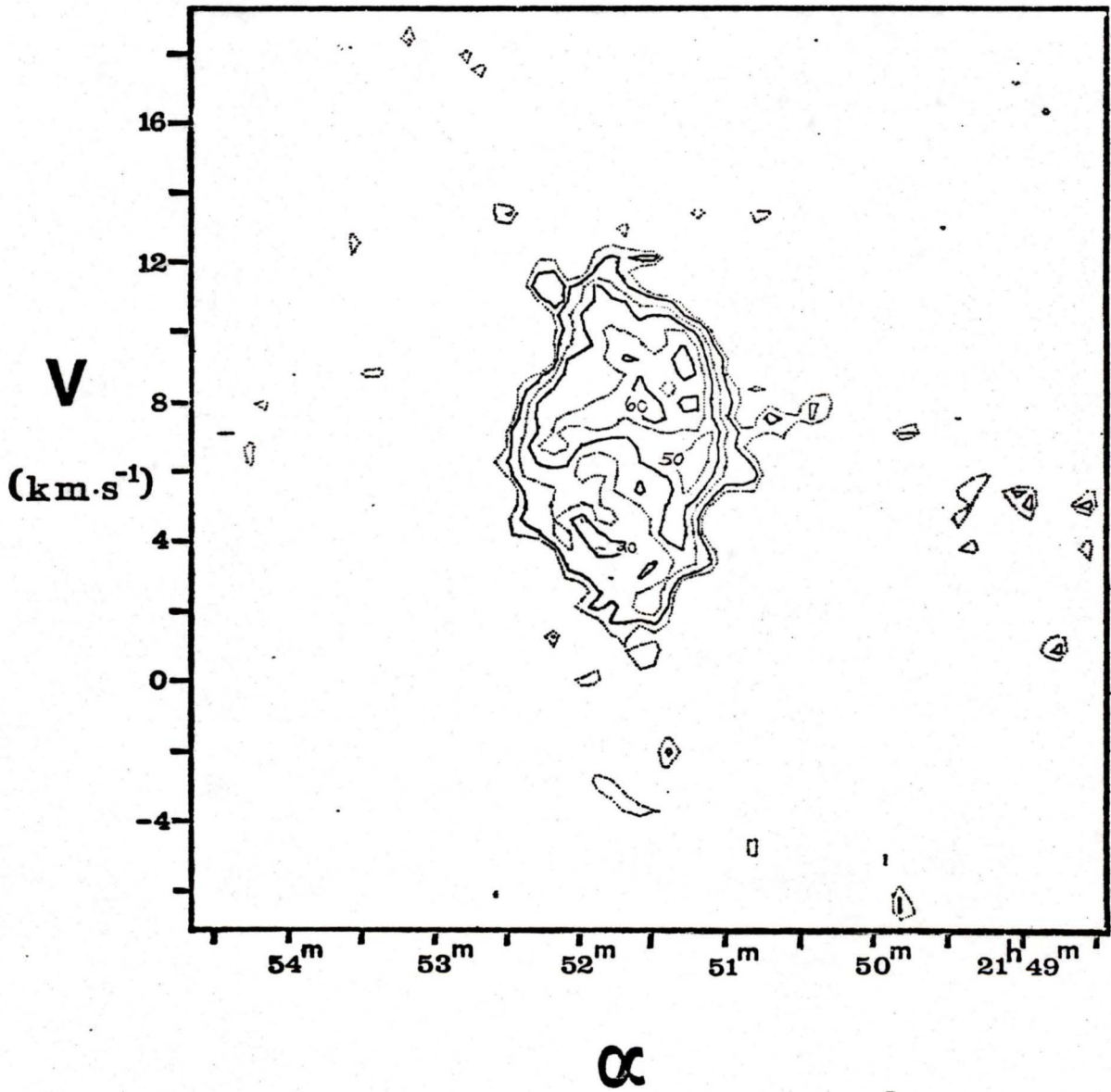
Thirteen α - V HI maps covering the declination range $46^{\circ} 54' 56'' \leq \delta \leq 47^{\circ} 06' 56''$ are presented here. All maps contain interferometer data only and are weighted by the 8.6 m paraboloid polar diagram in the α coordinate. The baseline of each map is at zero, and the following contours have been included: 15, 20, 30, 40, 50, 60, 70, and 80 $^{\circ}$ K (brightness temperature) with contours of alternating dotted and solid lines. Some contours have been labelled.

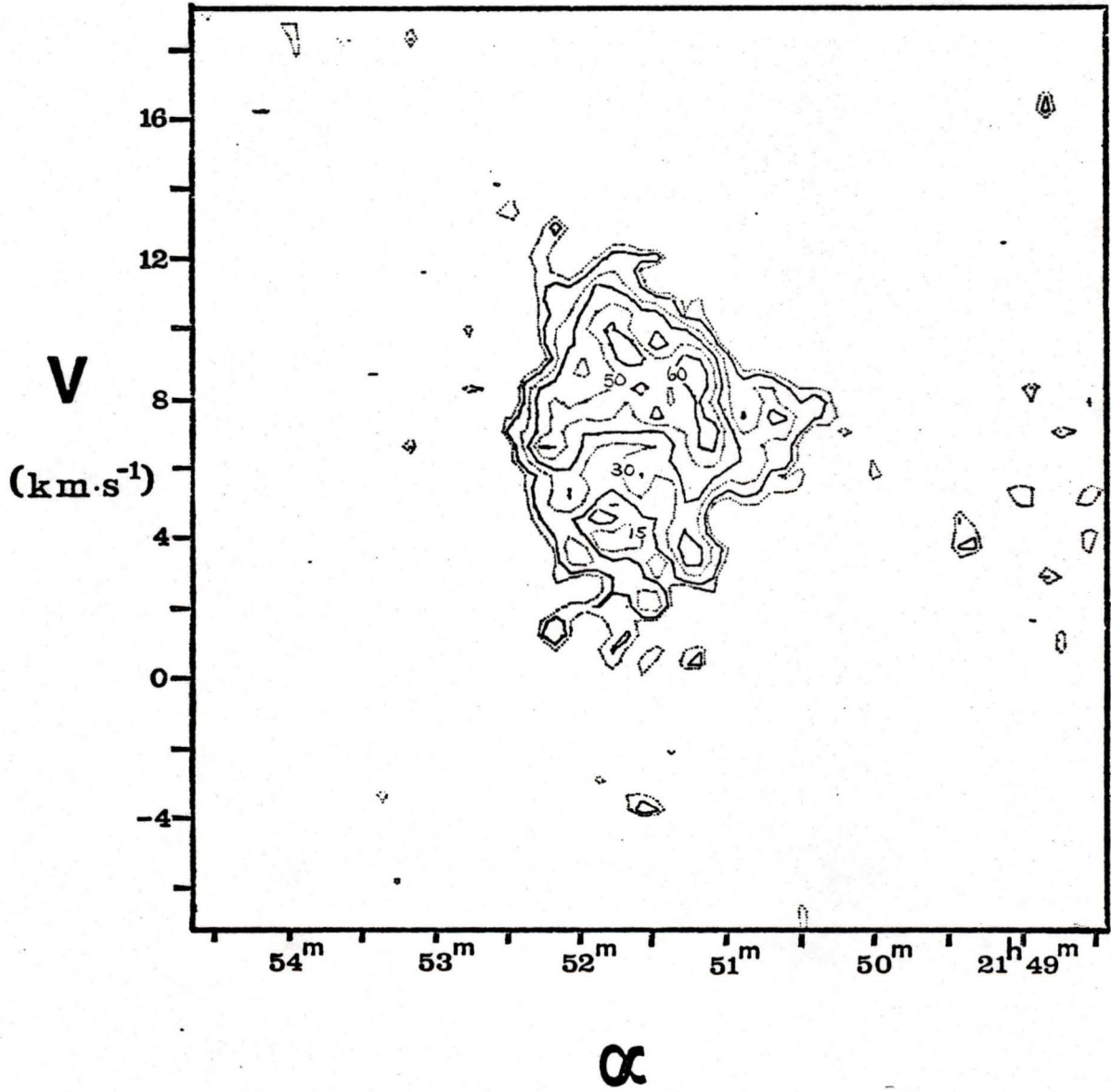
$46^{\circ} 54' 56''$ 

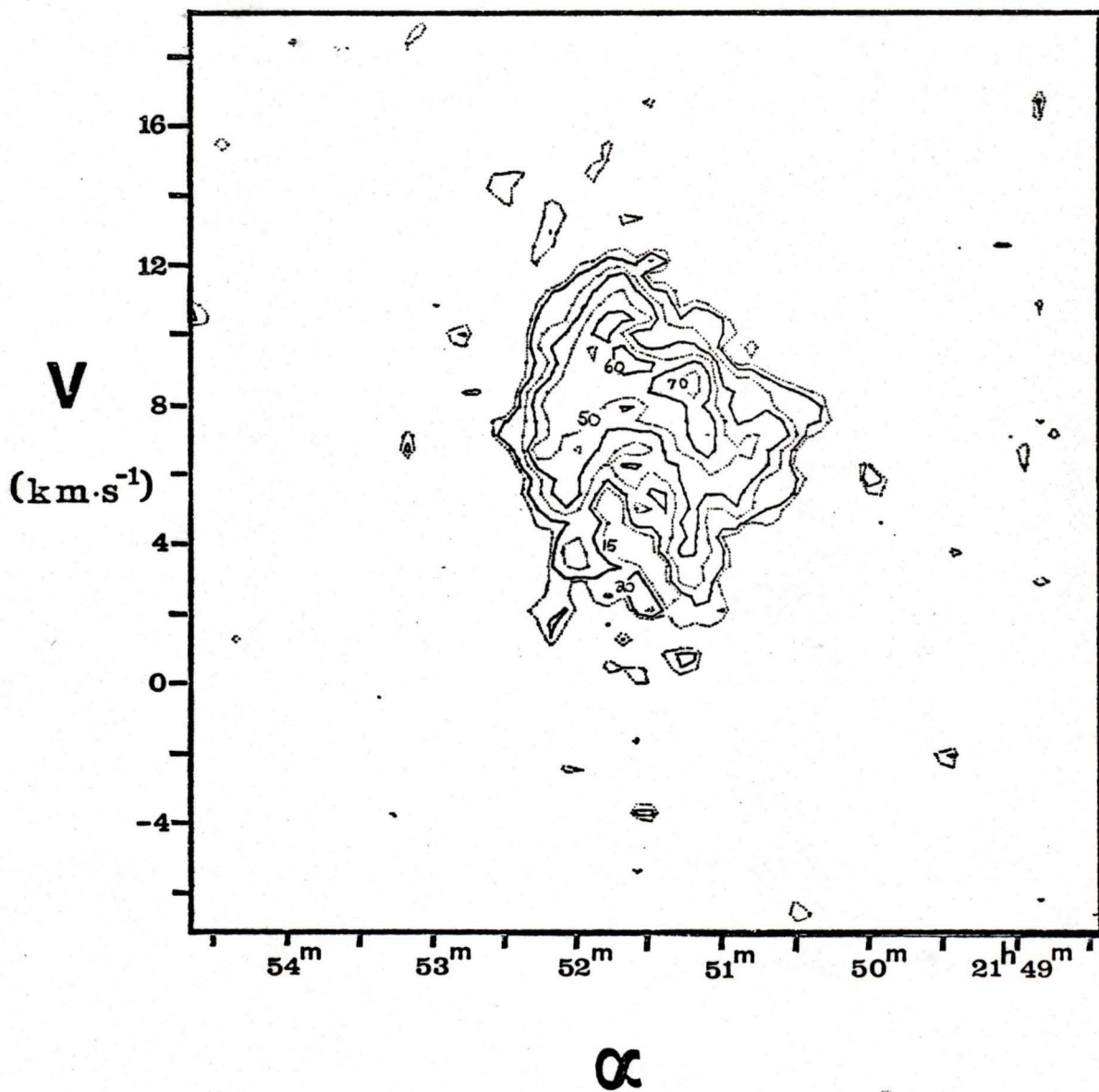
$46^{\circ} 55' 56''$ 

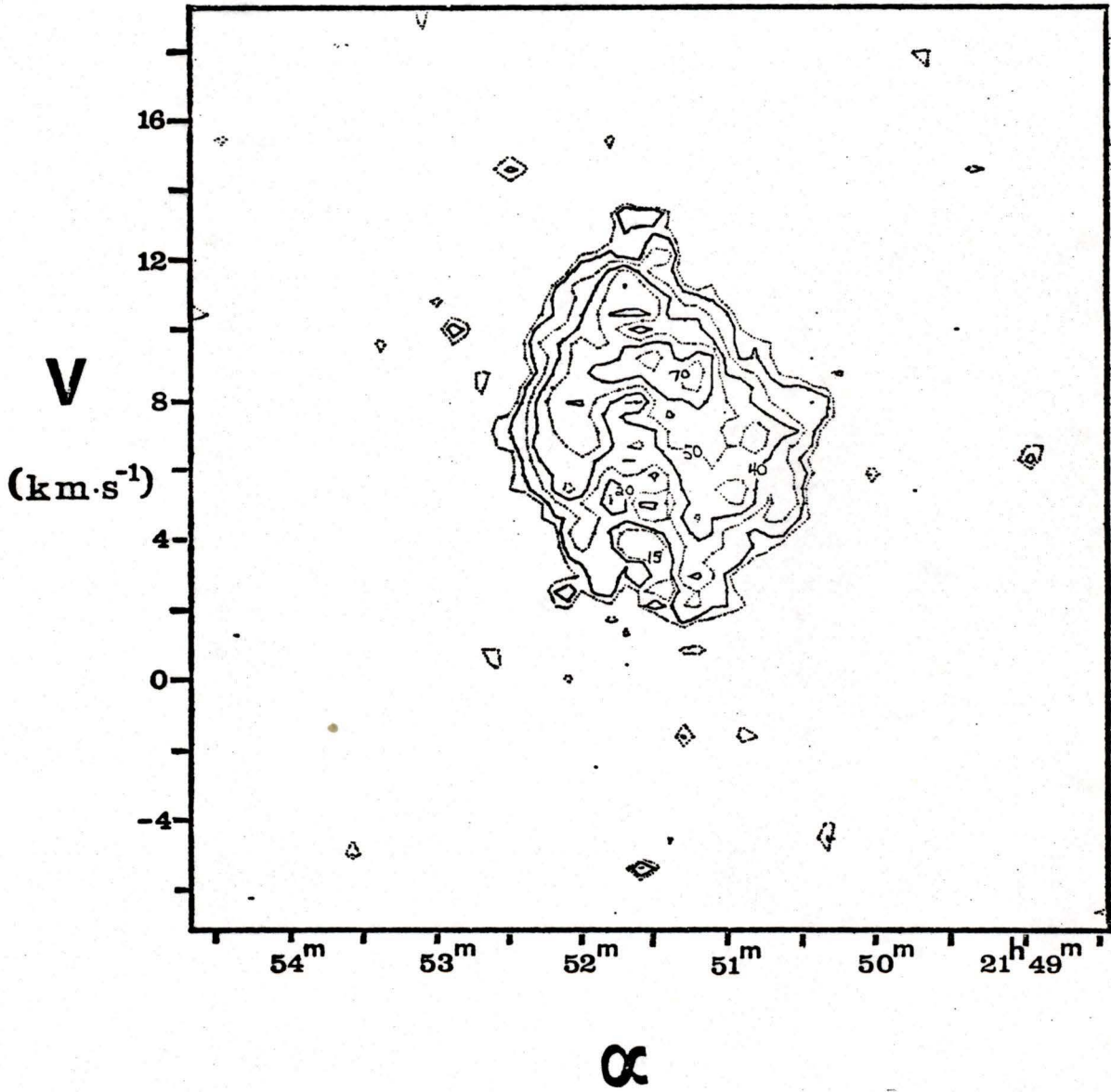
$46^{\circ} 56' 56''$ 

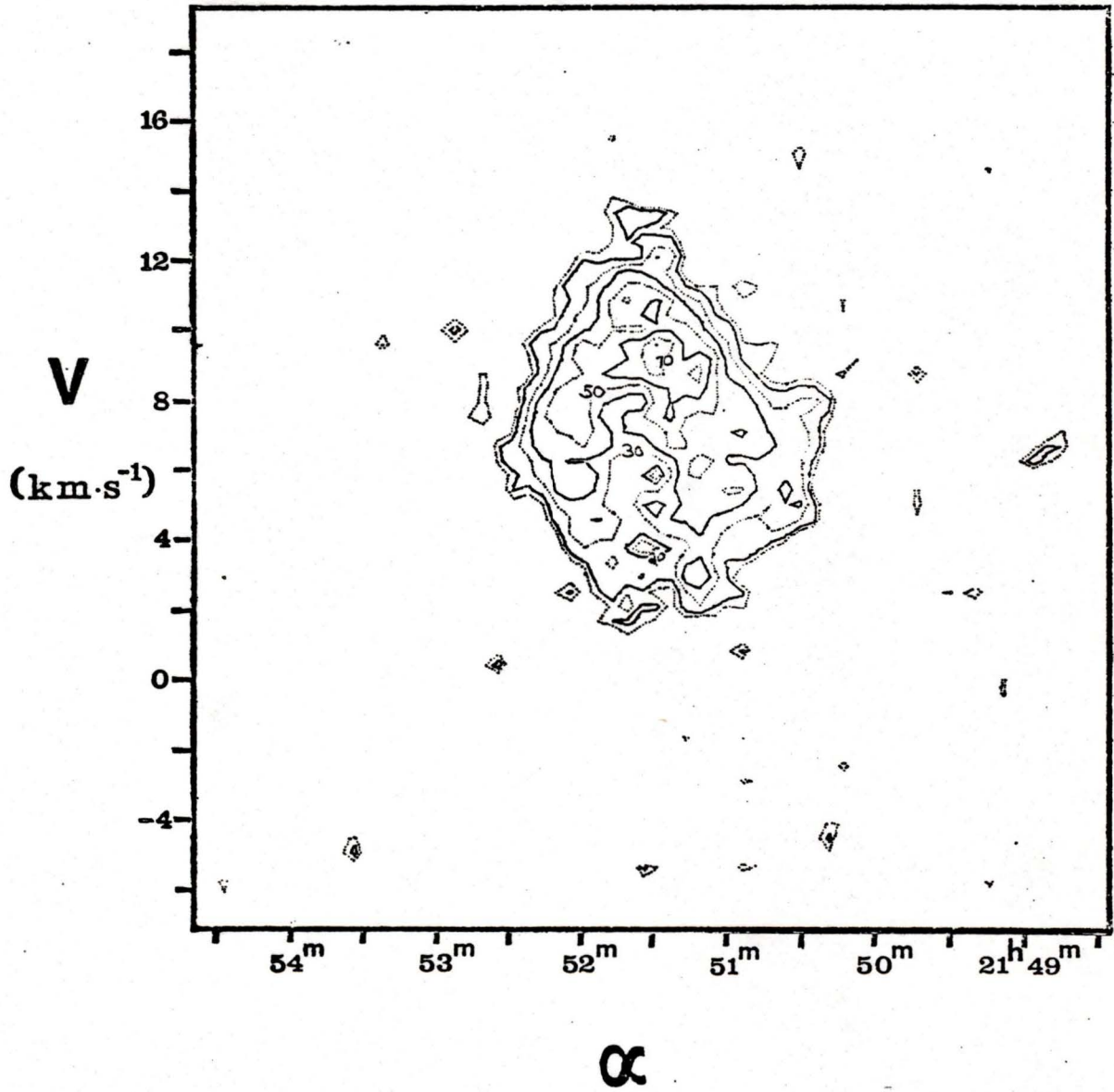
$46^{\circ} 57' 56''$ 

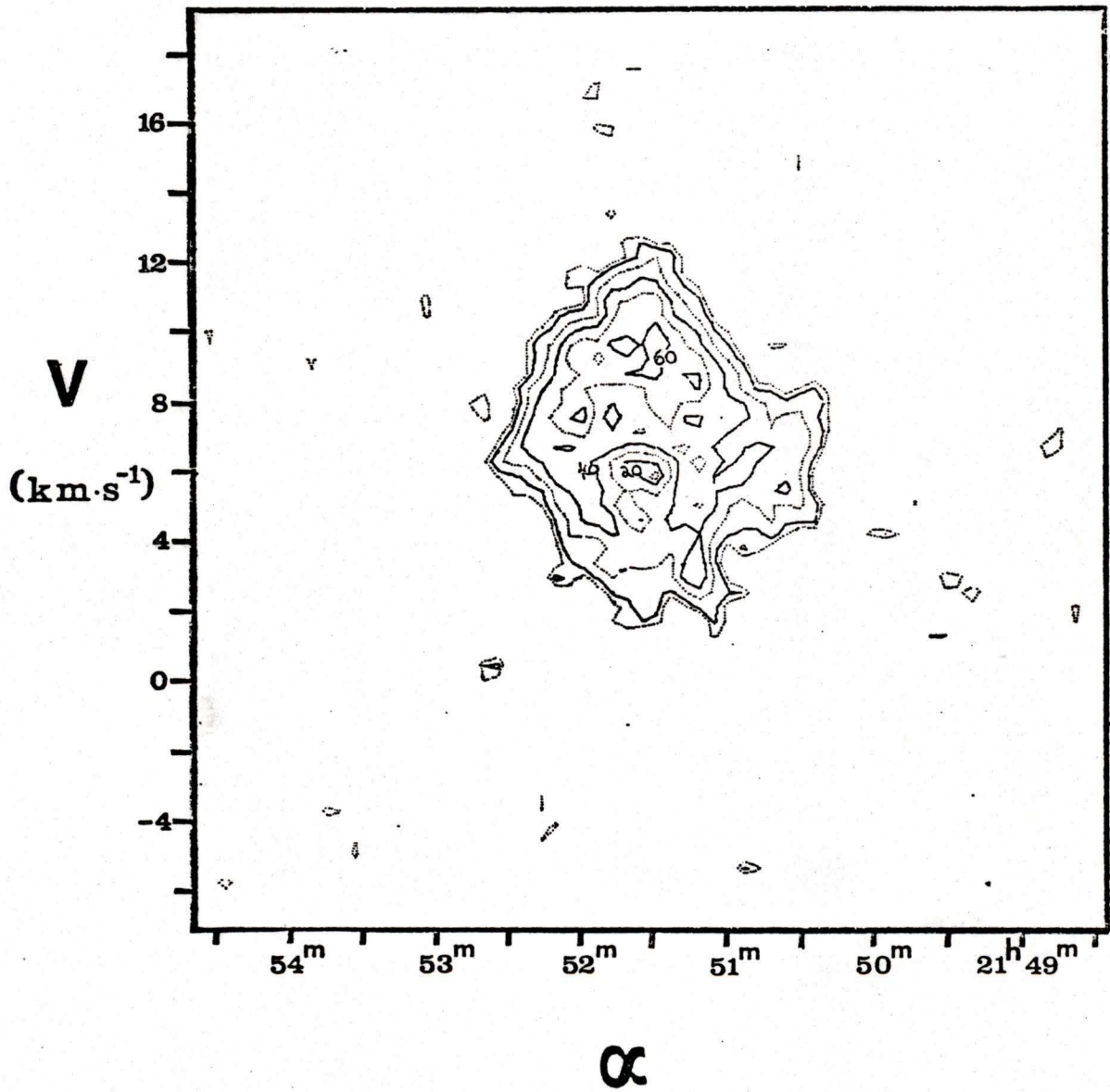
$46^{\circ} 58' 56''$ 

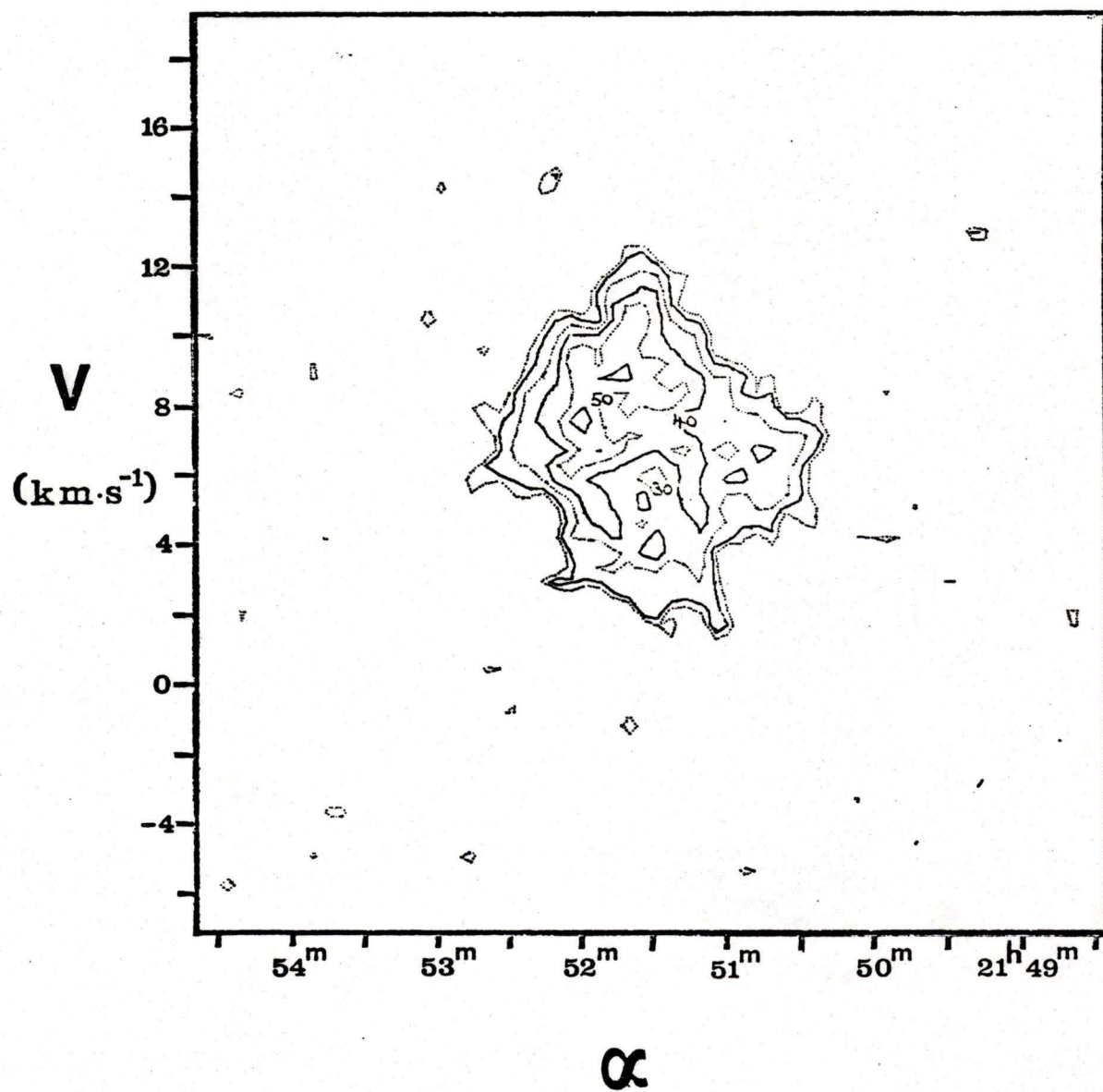
$46^{\circ} 59' 56''$ 

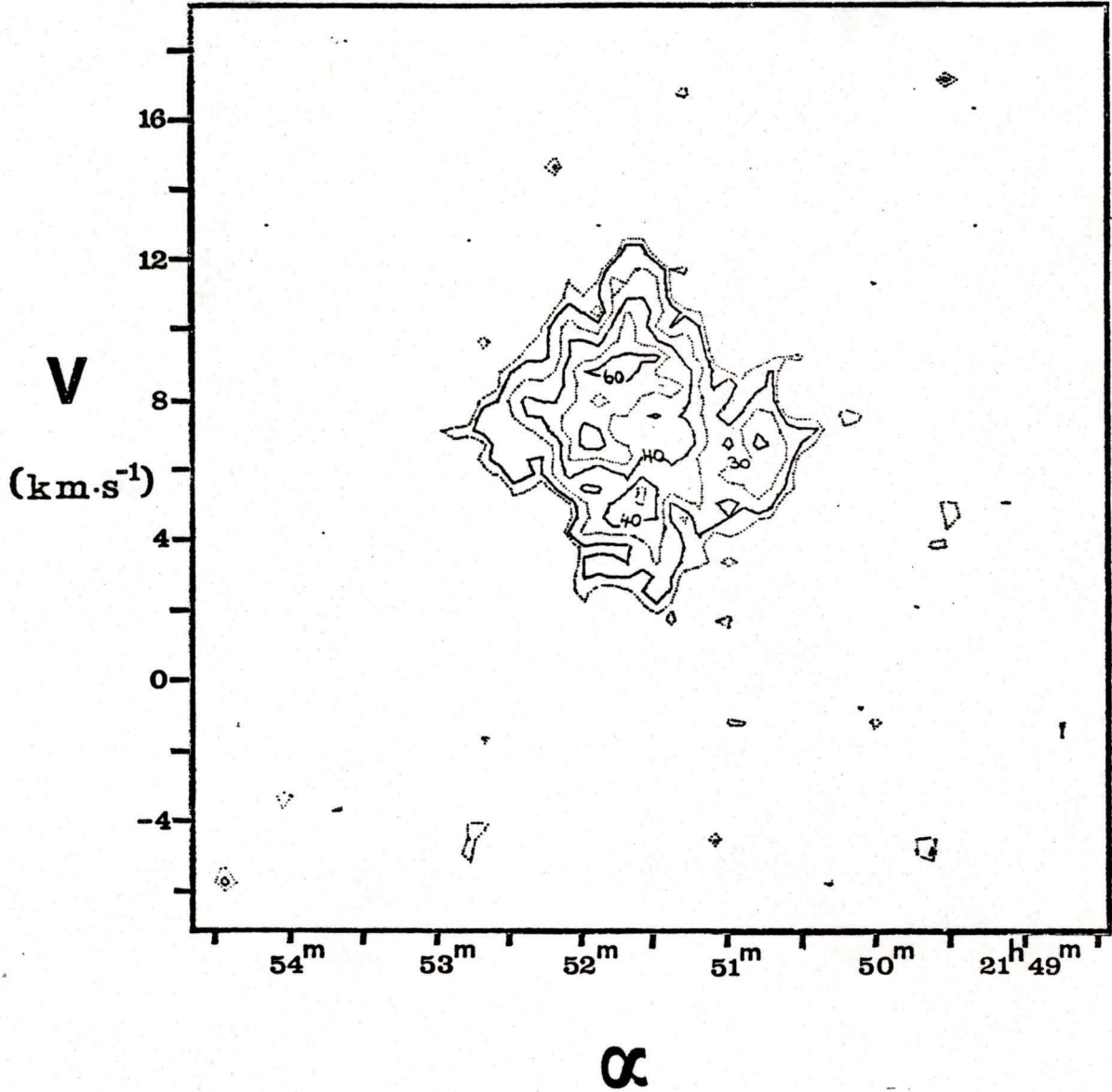
$47^{\circ} 00' 56''$ 

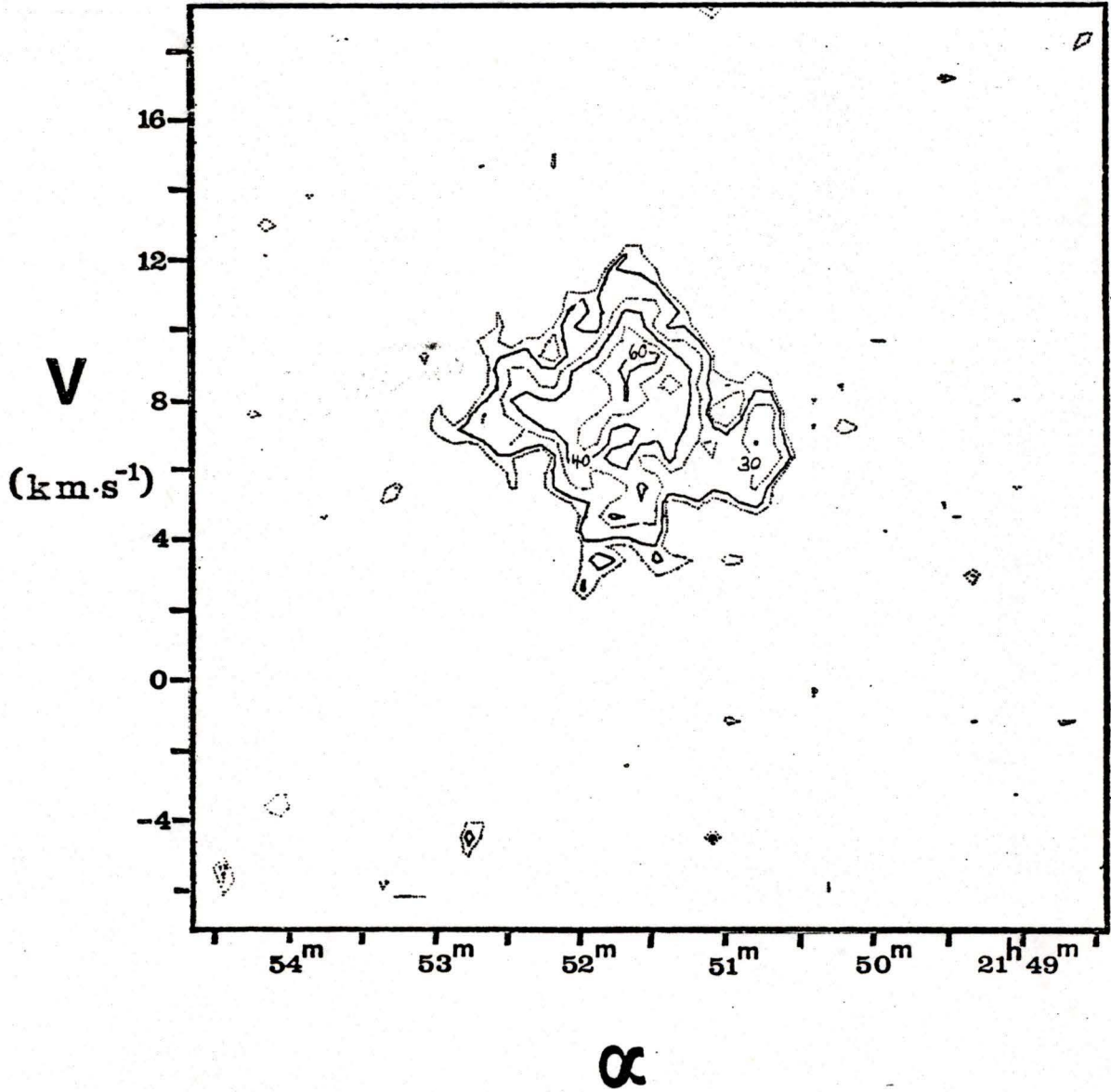
$47^{\circ} 01' 56''$ 

$47^{\circ} 02' 56''$ 

$47^{\circ} 03' 56''$ 

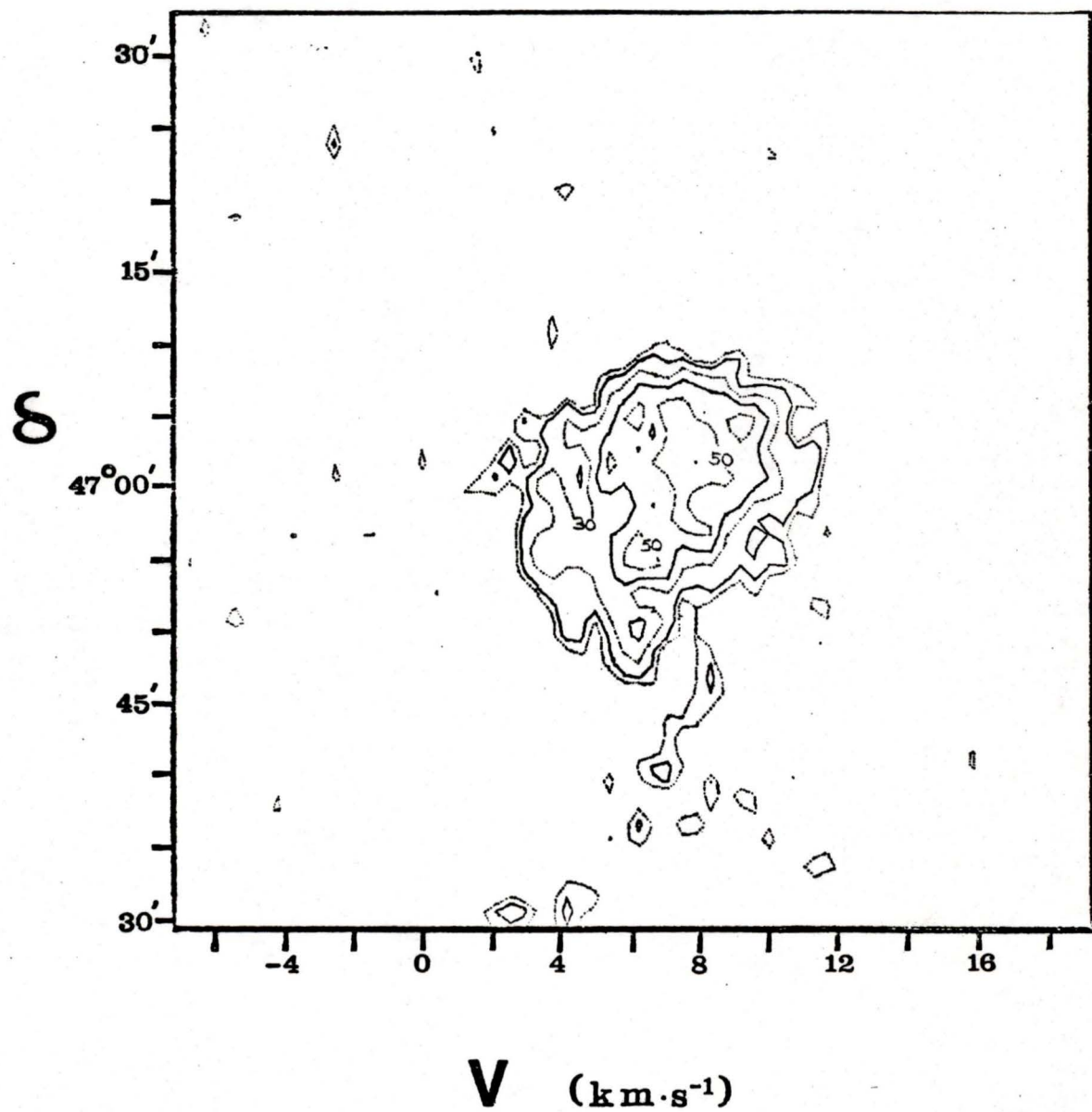
$47^{\circ} 04' 56''$ 

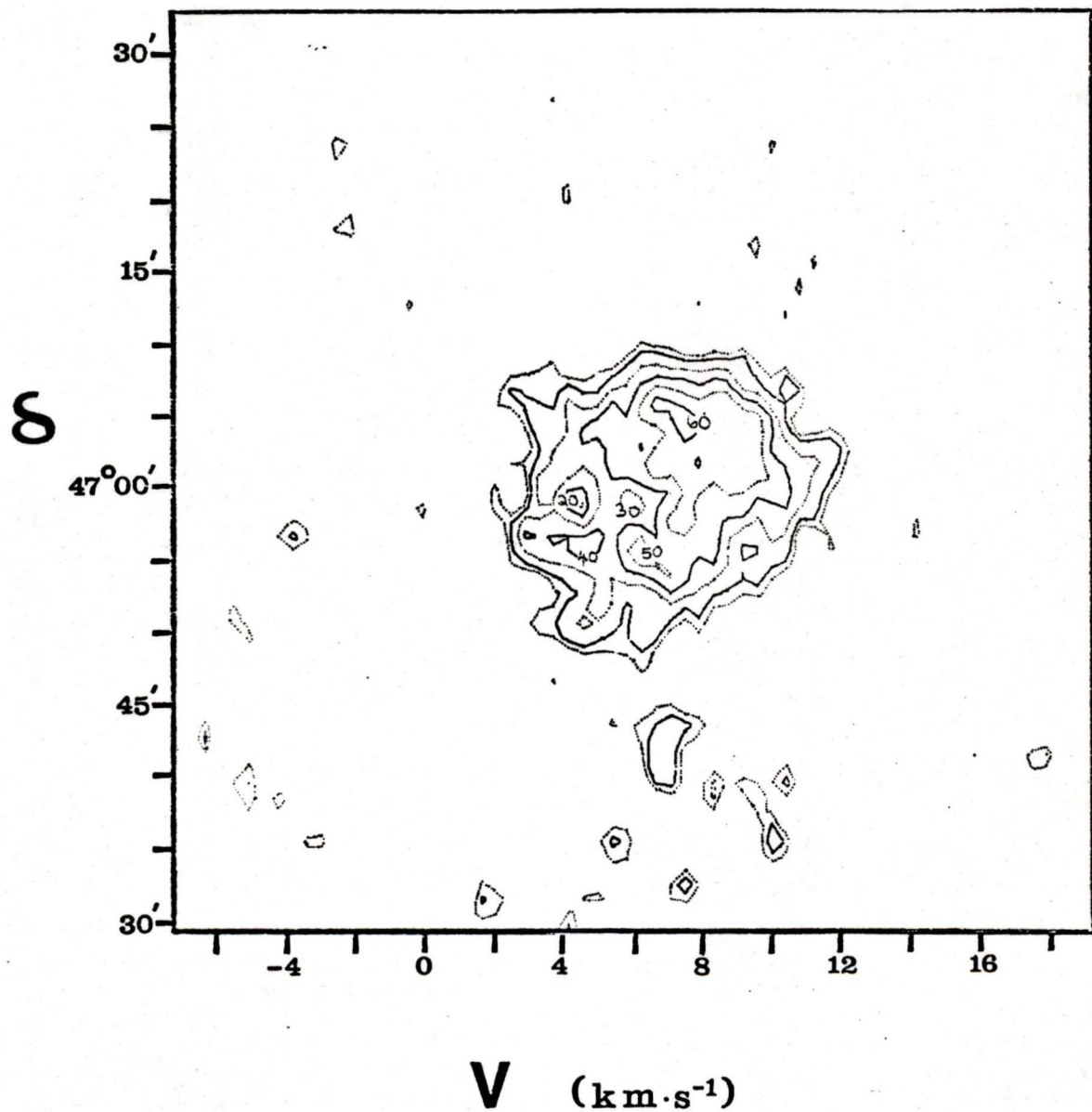
$47^{\circ} 05' 56''$ 

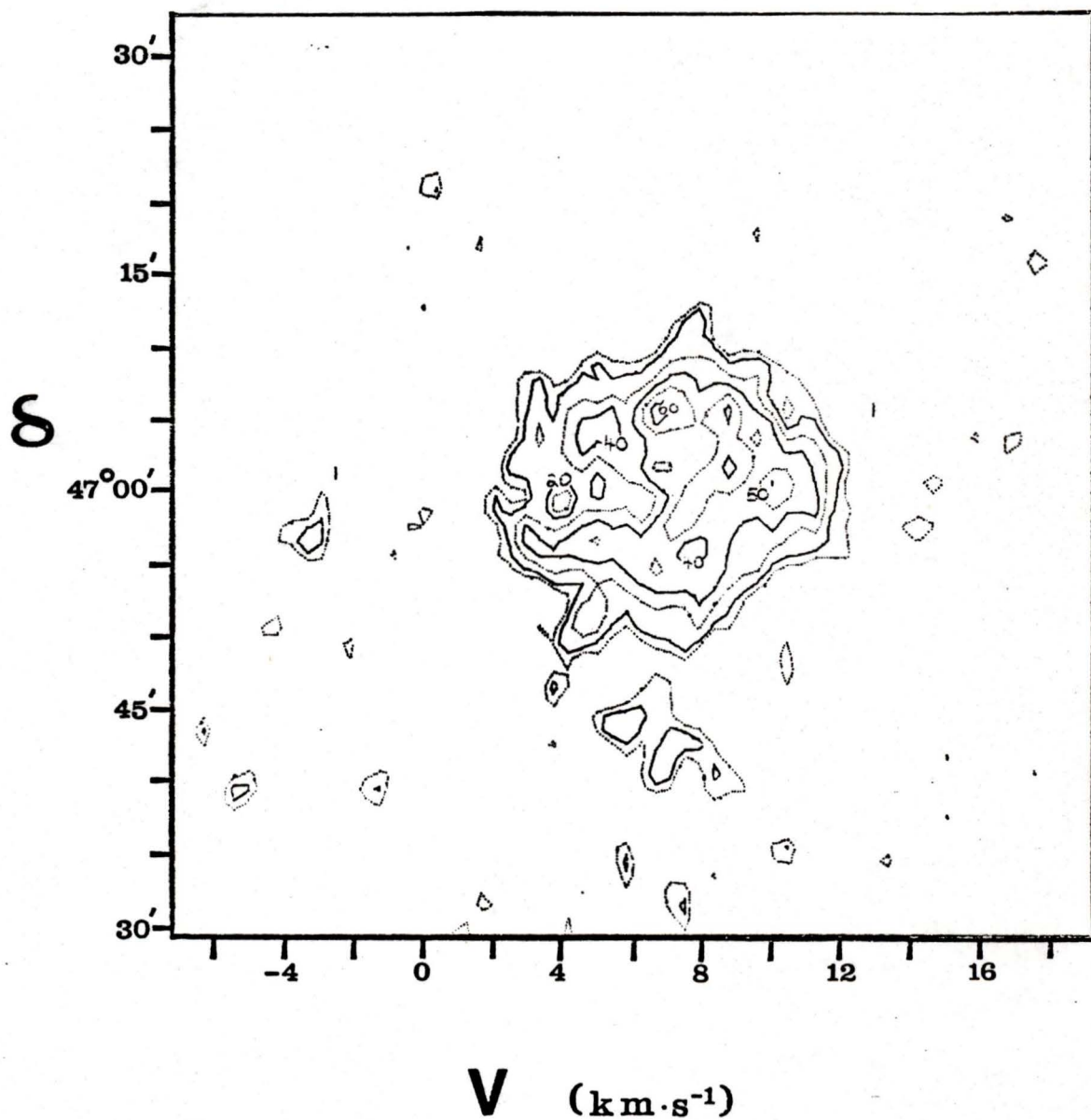
$47^{\circ} 06' 56''$ 

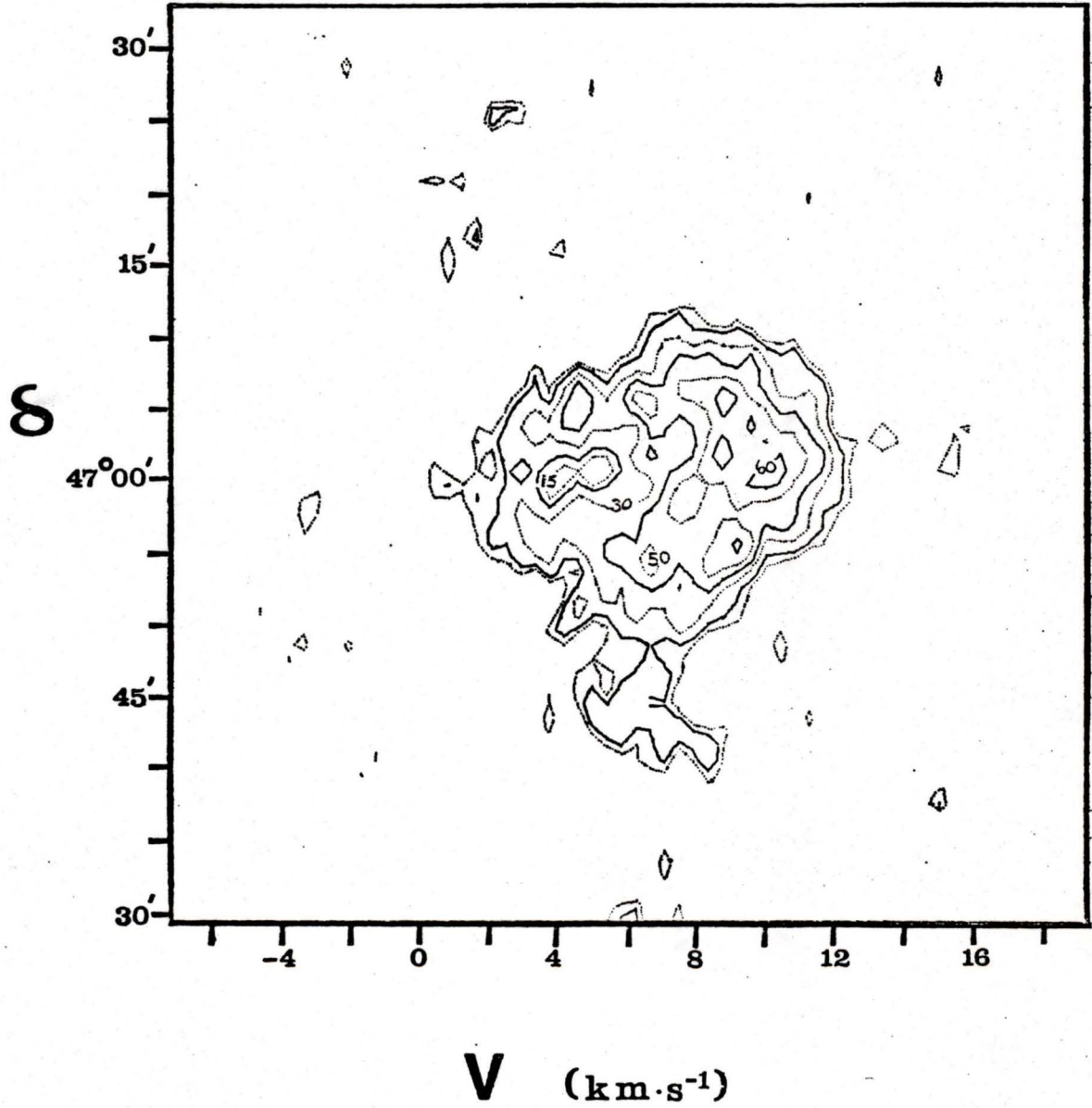
APPENDIX C

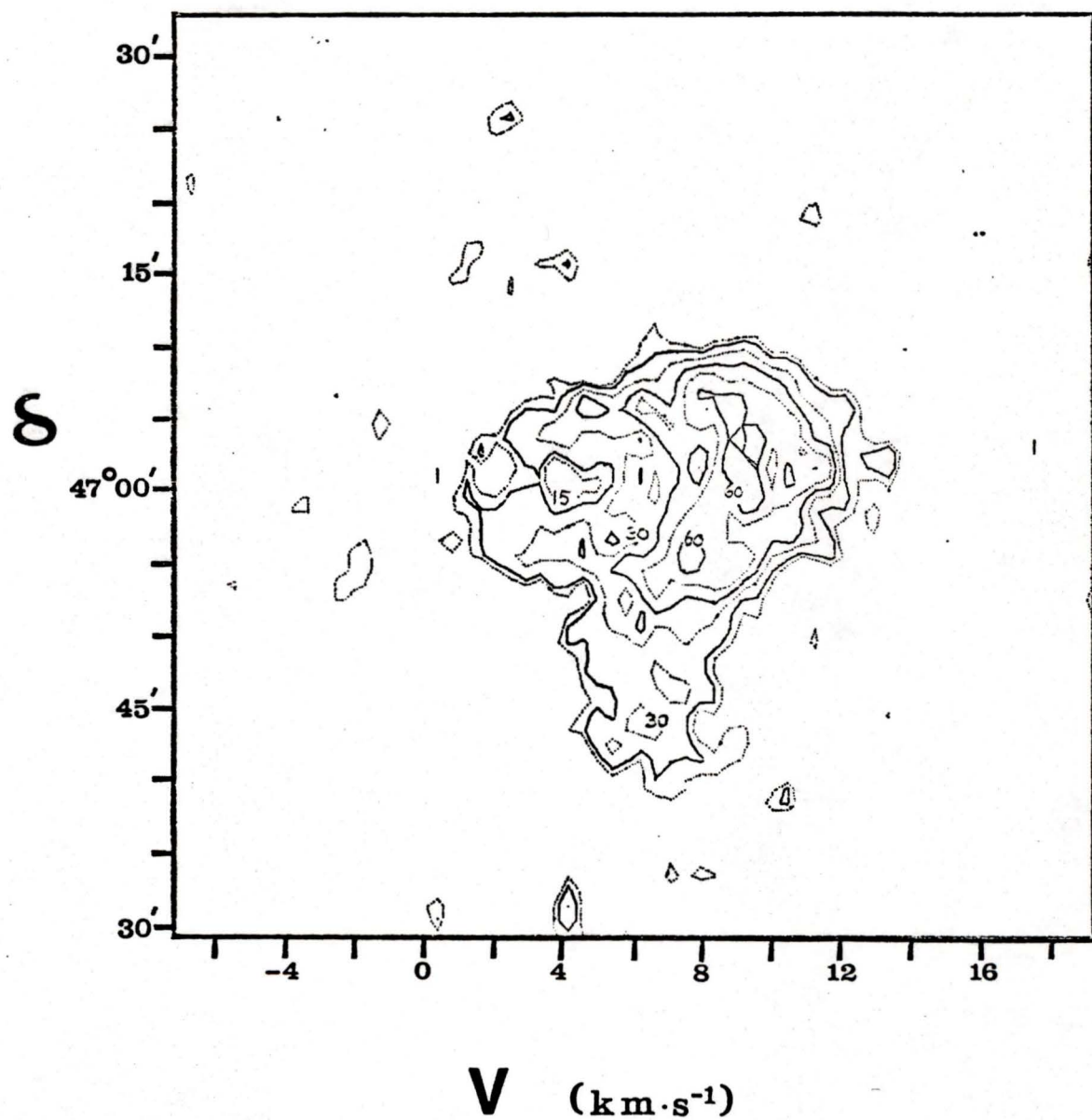
Thirteen δ - V HI maps covering the right ascension range $21^{\text{h}} 51^{\text{m}} 6^{\text{s}}.7 \leq \alpha \leq 21^{\text{h}} 52^{\text{m}} 17^{\text{s}}.1$ are presented here. All maps contain interferometer data only and are weighted by the 8.6 m paraboloid polar diagram in the δ coordinate. The baseline of each map is at zero, and the following contours have been included: 15, 20, 30, 40, 50, 60, 70, and 80 °K (brightness temperature), with contours of alternating dotted and solid lines. Some contours have been labelled.

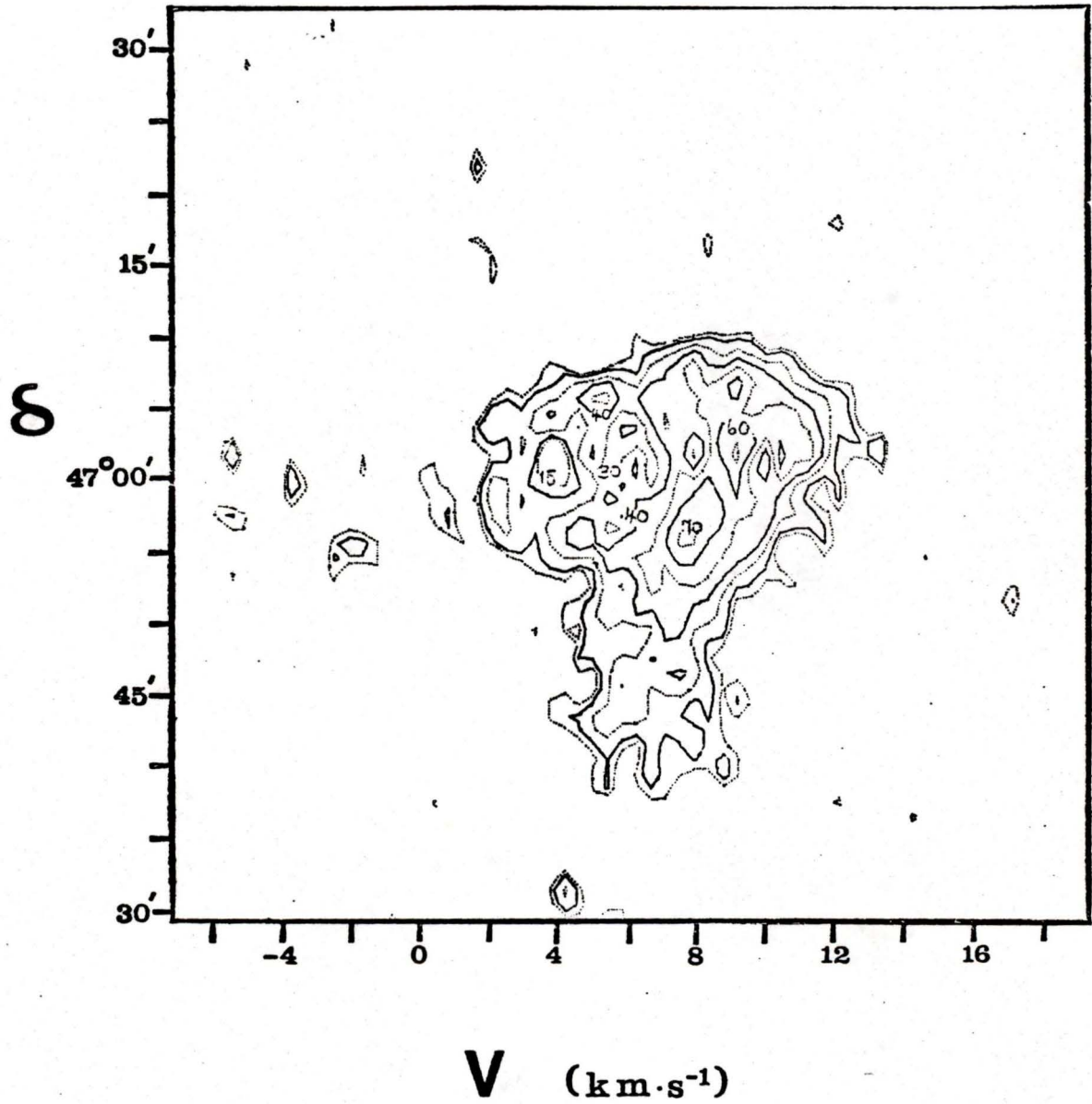
$21^{\text{h}} 51^{\text{m}} 6^{\text{s}}.7$ 

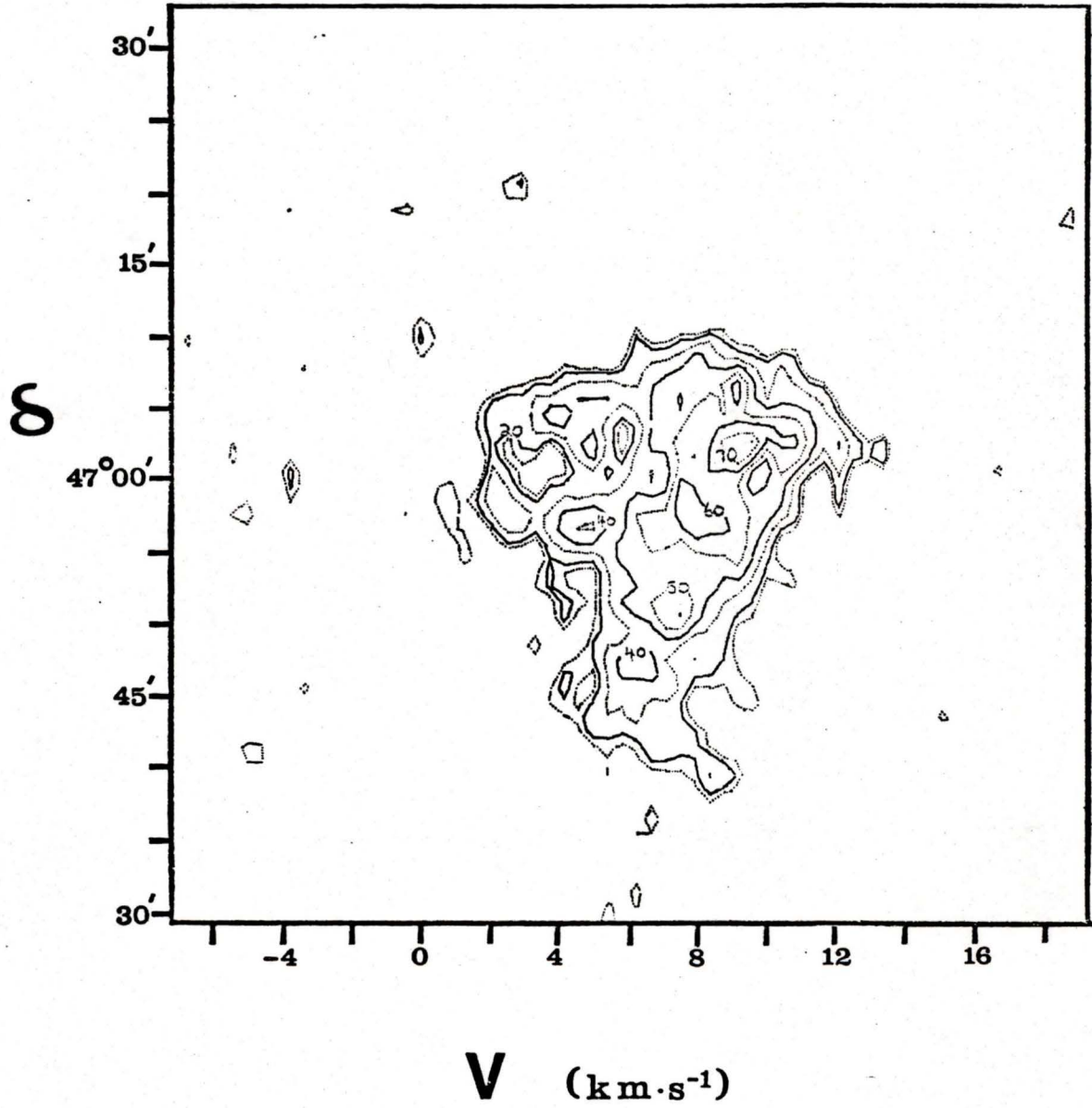
$21^{\text{h}} 51^{\text{m}} 12^{\text{s}.5}$ 

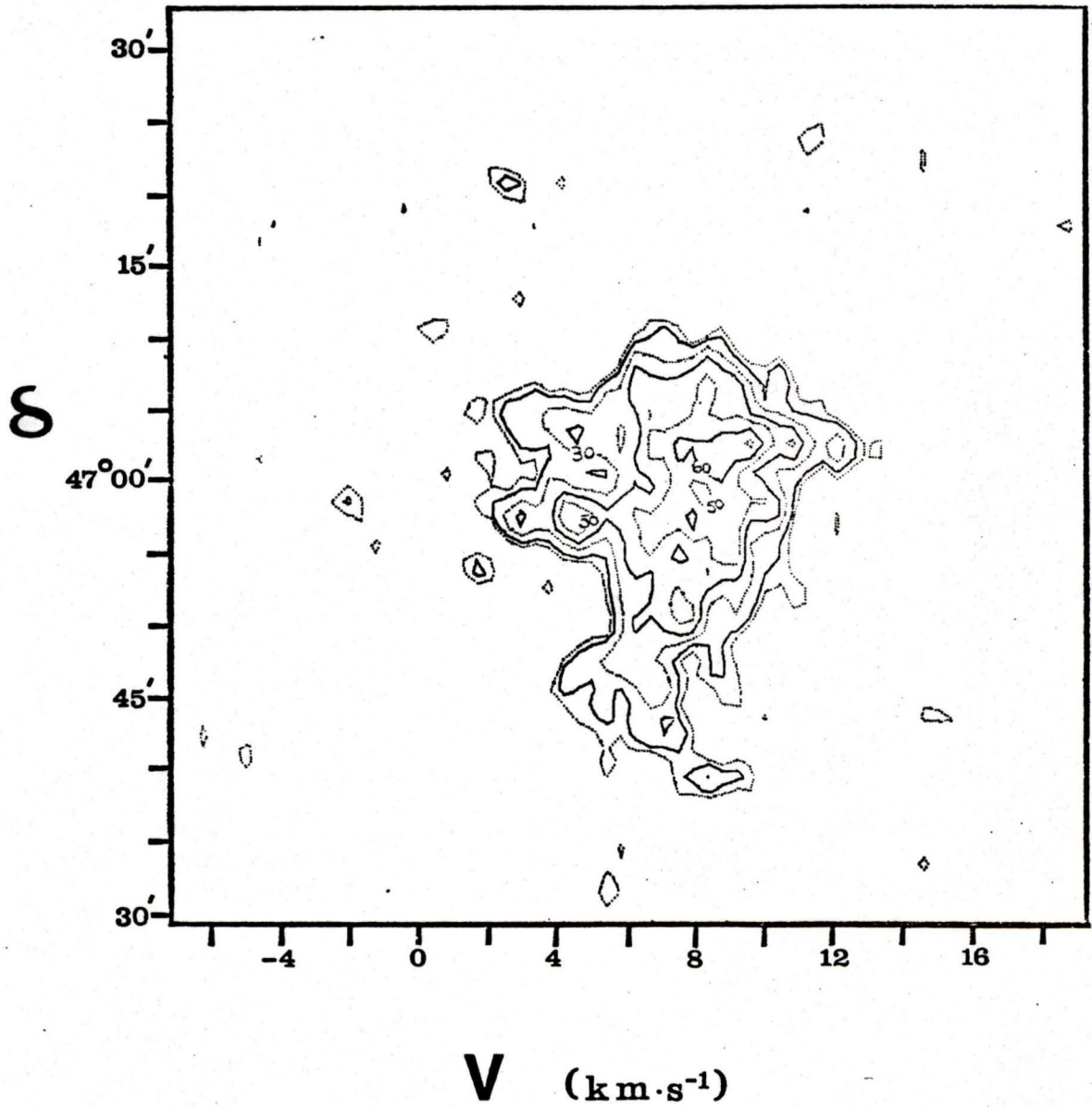
$21^{\text{h}} 51^{\text{m}} 18^{\text{s}}.4$ 

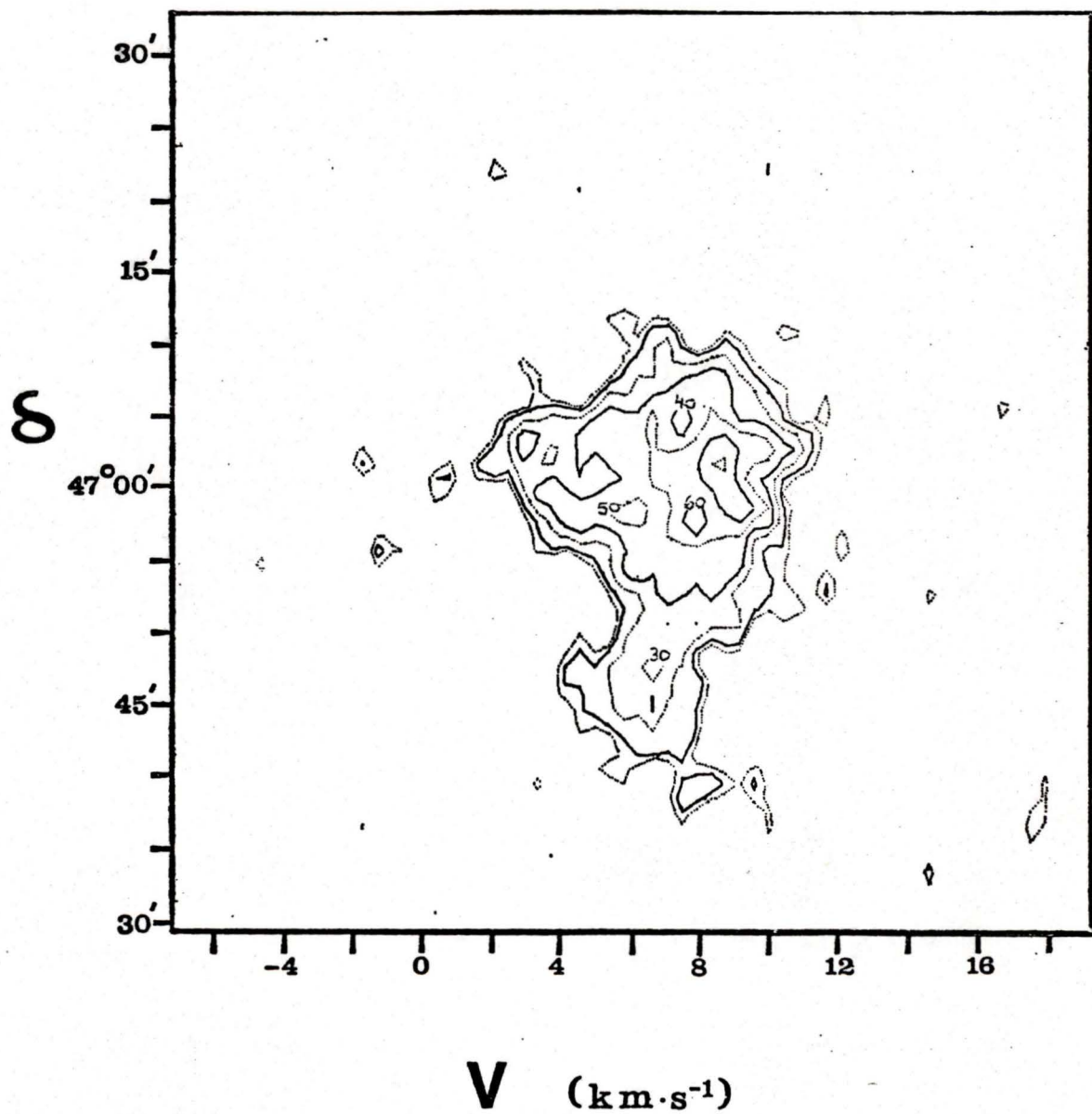
$21^{\text{h}} 51^{\text{m}} 24.3^{\text{s}}$ 

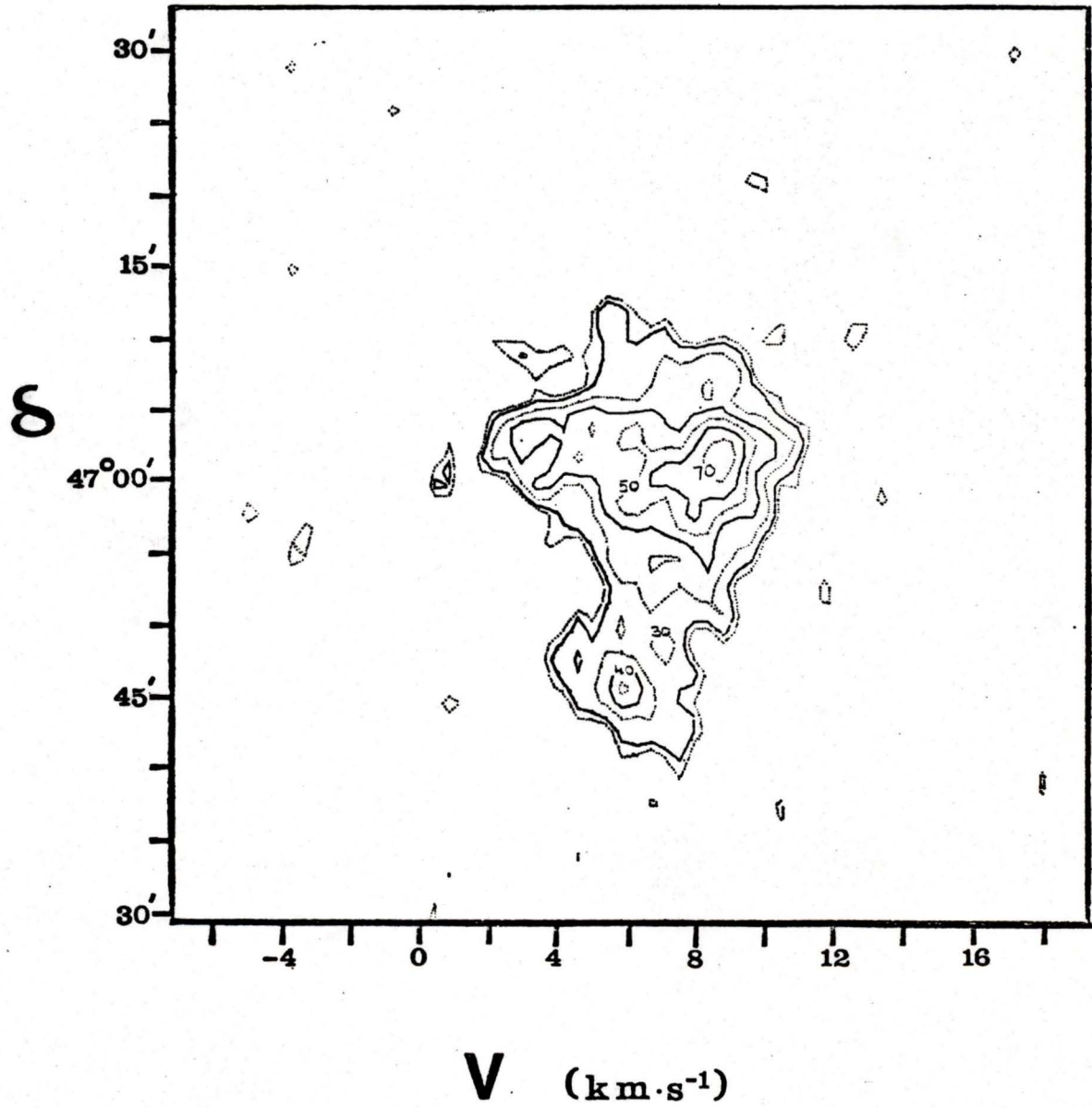
$21^{\text{h}} 51^{\text{m}} 30^{\text{s}}.1$ 

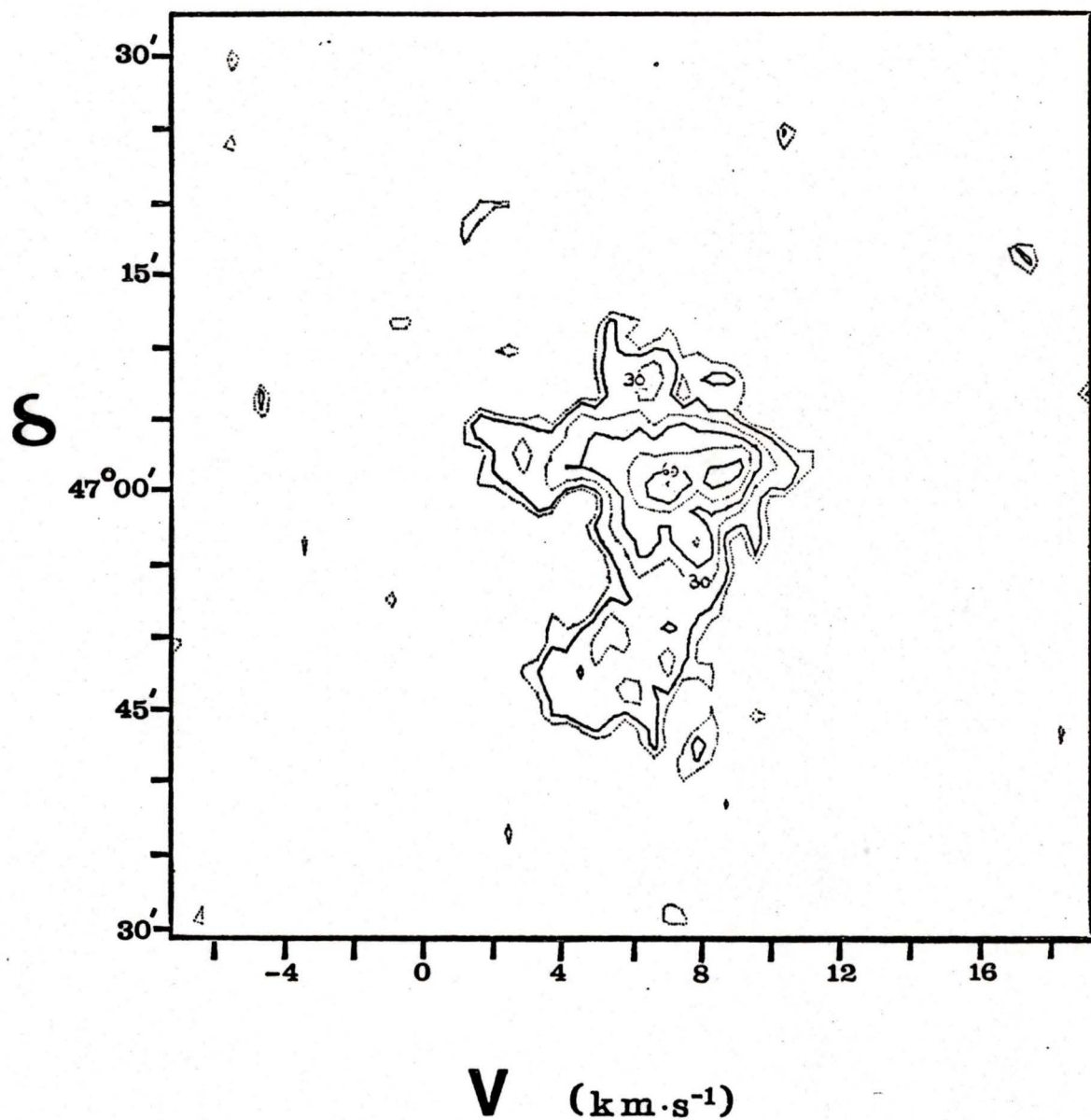
$21^{\text{h}} 51^{\text{m}} 36^{\text{s}}.0$ 

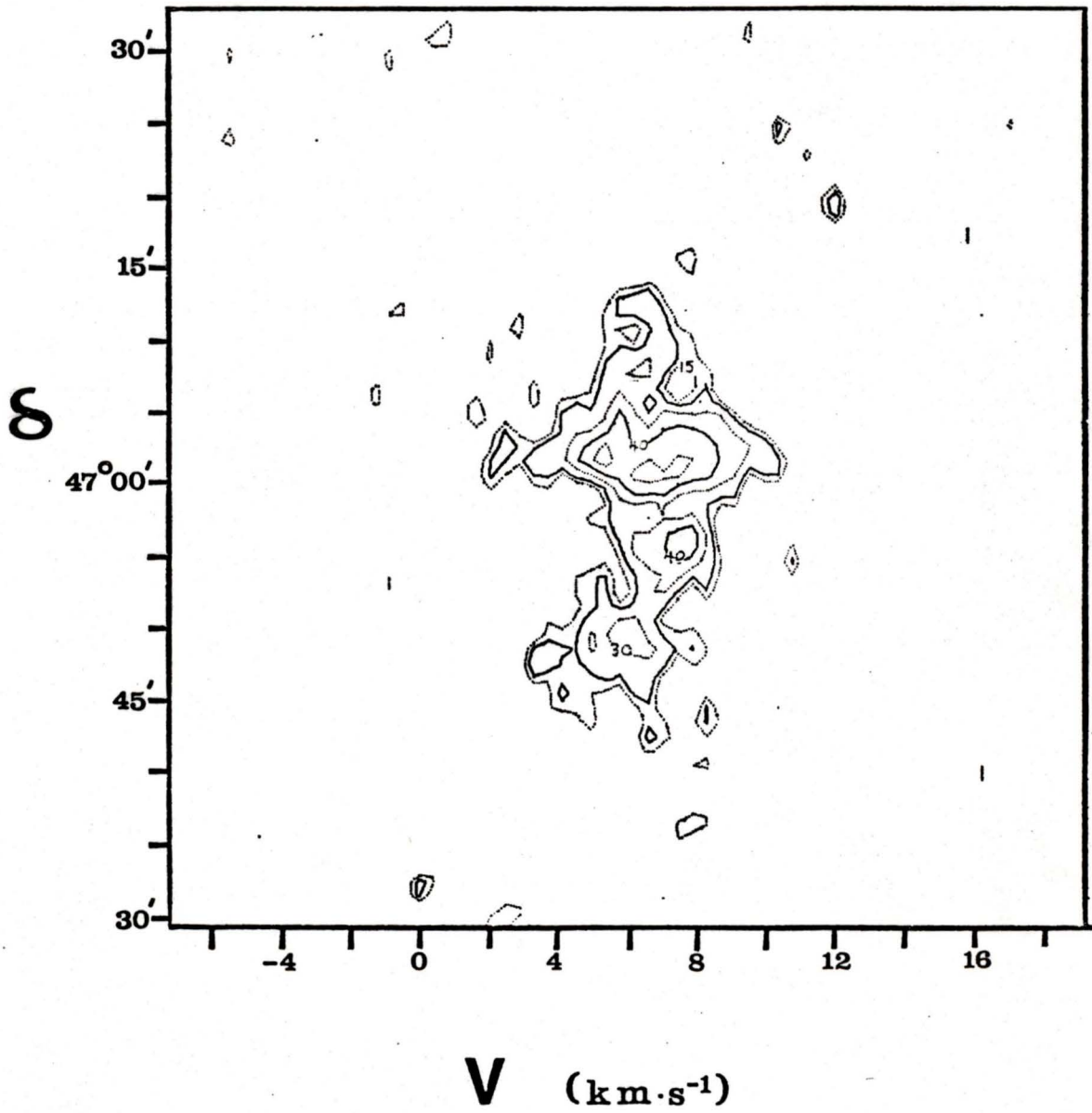
$21^{\text{h}} 51^{\text{m}} 41.59$ 

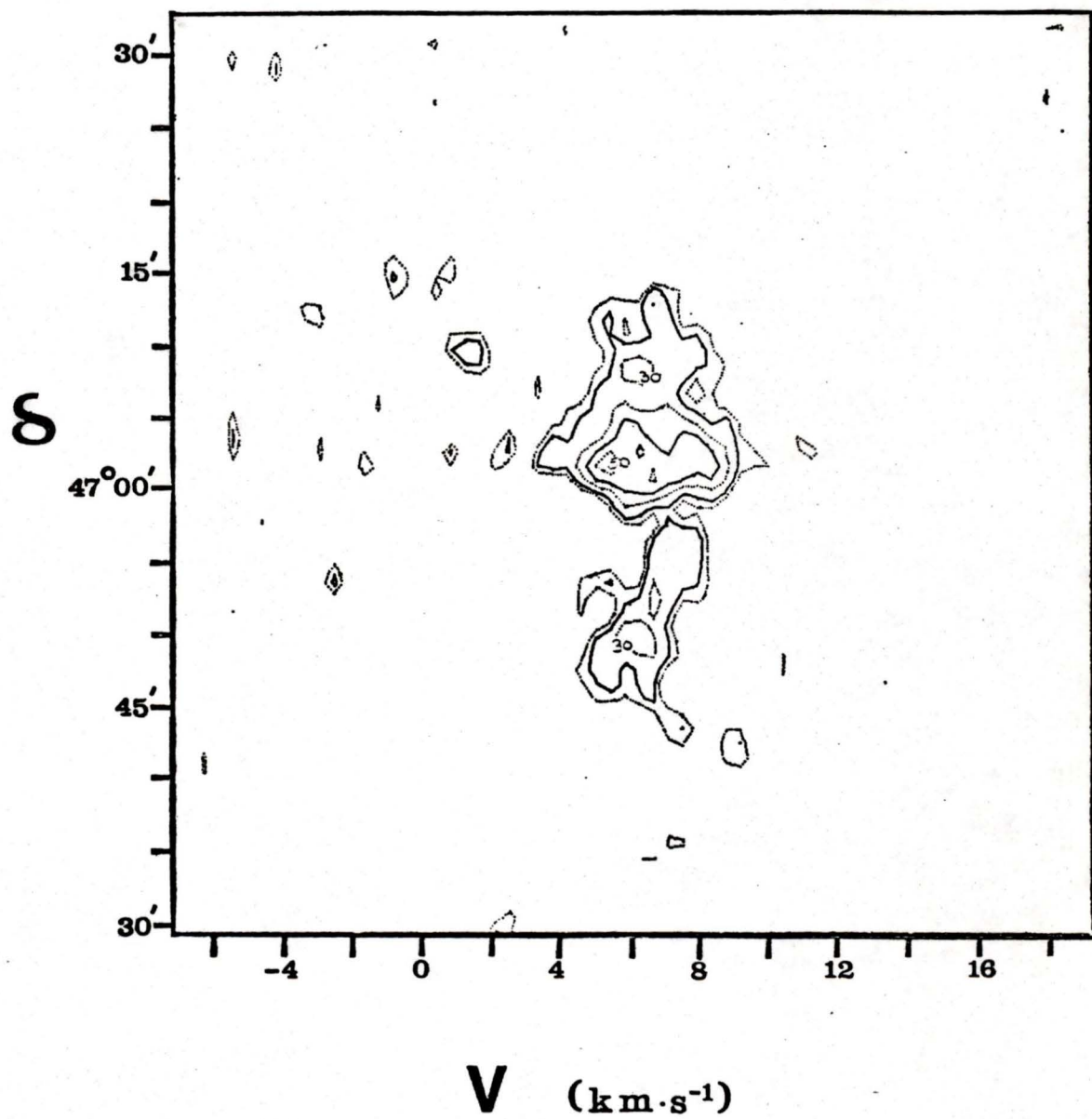
$21^{\text{h}} 51^{\text{m}} 47^{\text{s}}.7$ 

$21^{\text{h}} 51^{\text{m}} 53^{\text{s}}.6$ 

$21^{\text{h}} 51^{\text{m}} 59^{\text{s}.5}$ 

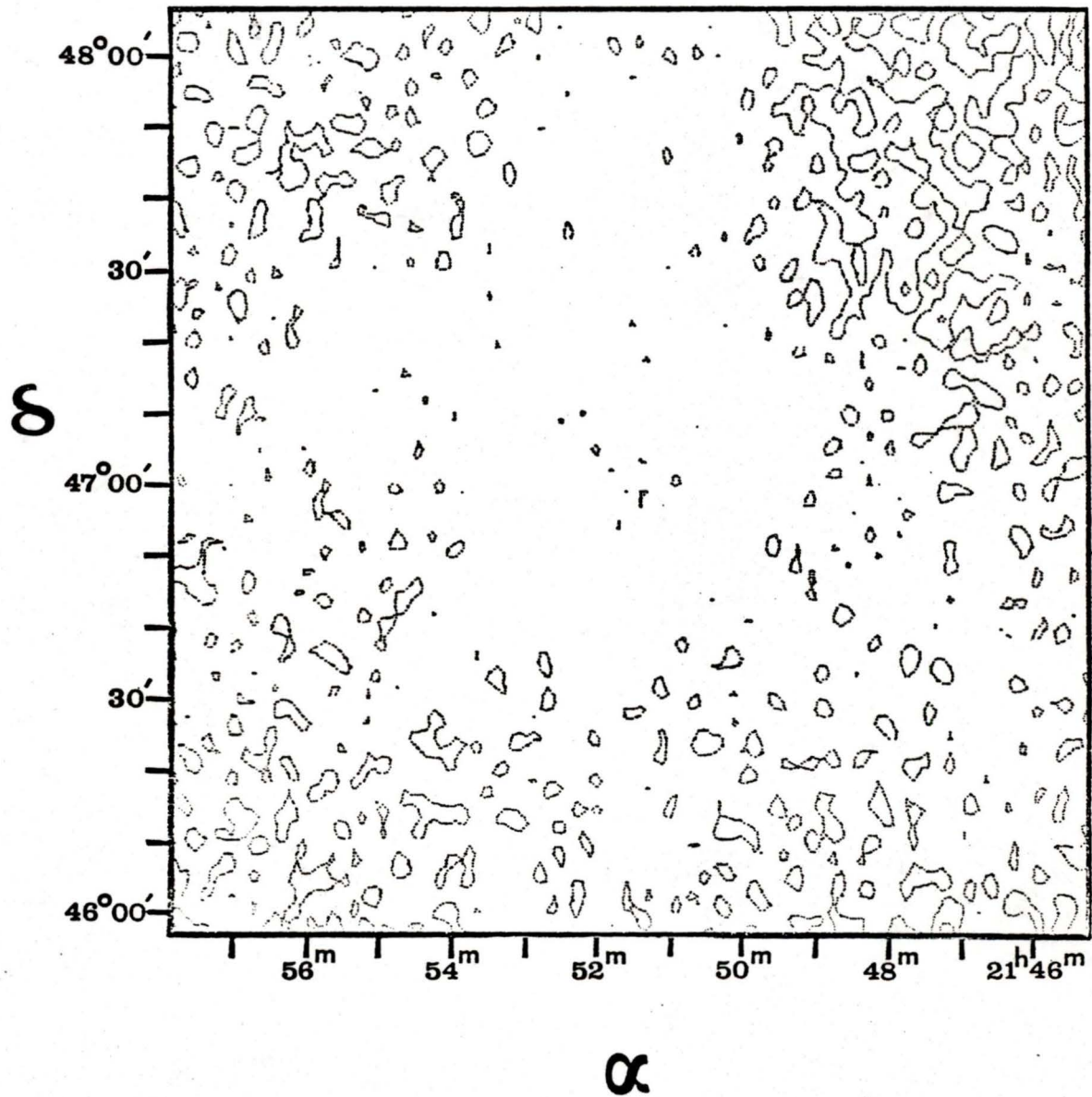
$21^{\text{h}} 52^{\text{m}} 5^{\text{s}}.4$ 

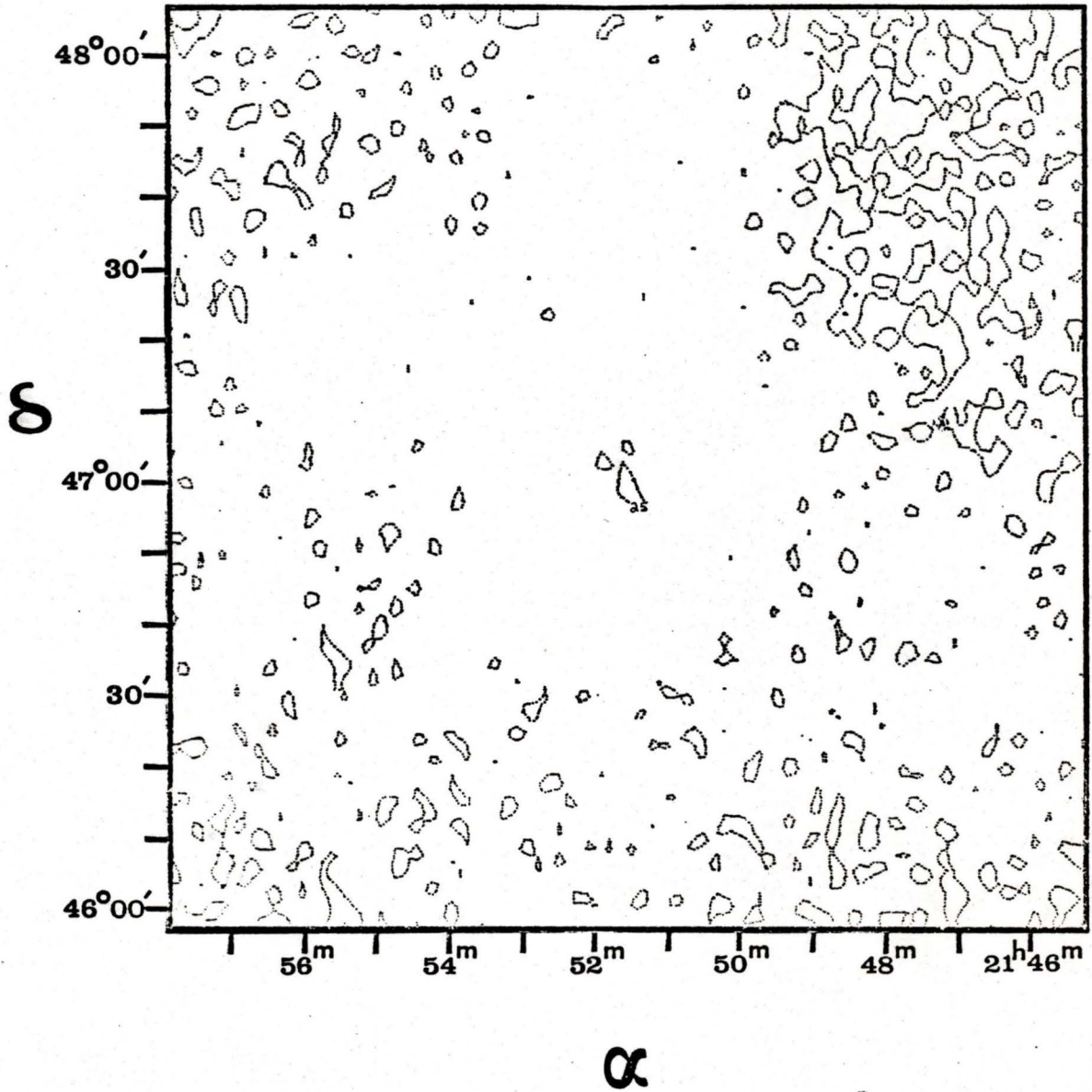
$21^{\text{h}} 52^{\text{m}} 11^{\text{s}}.2$ 

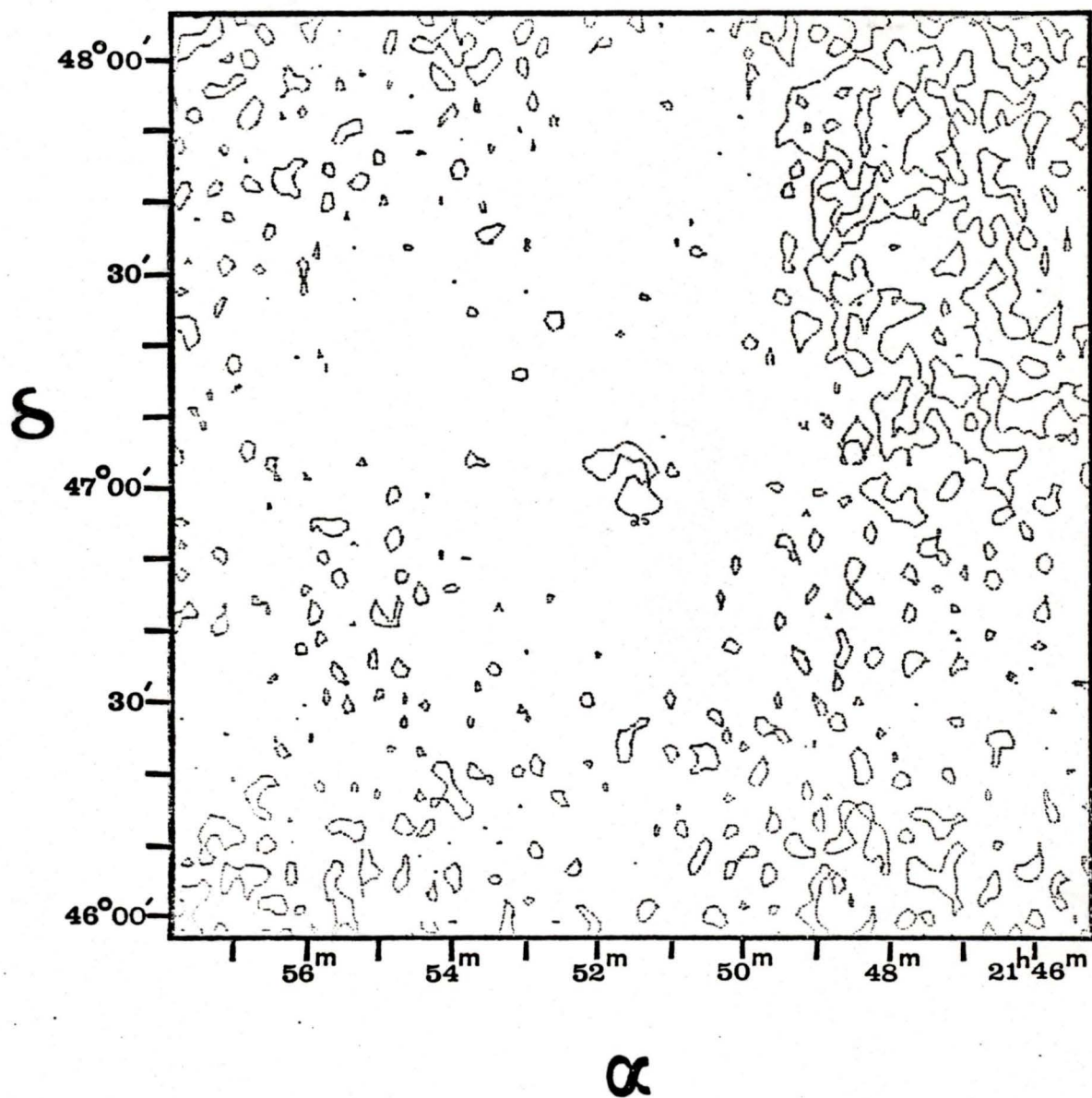
$21^{\text{h}} 52^{\text{m}} 17^{\text{s}}.1$ 

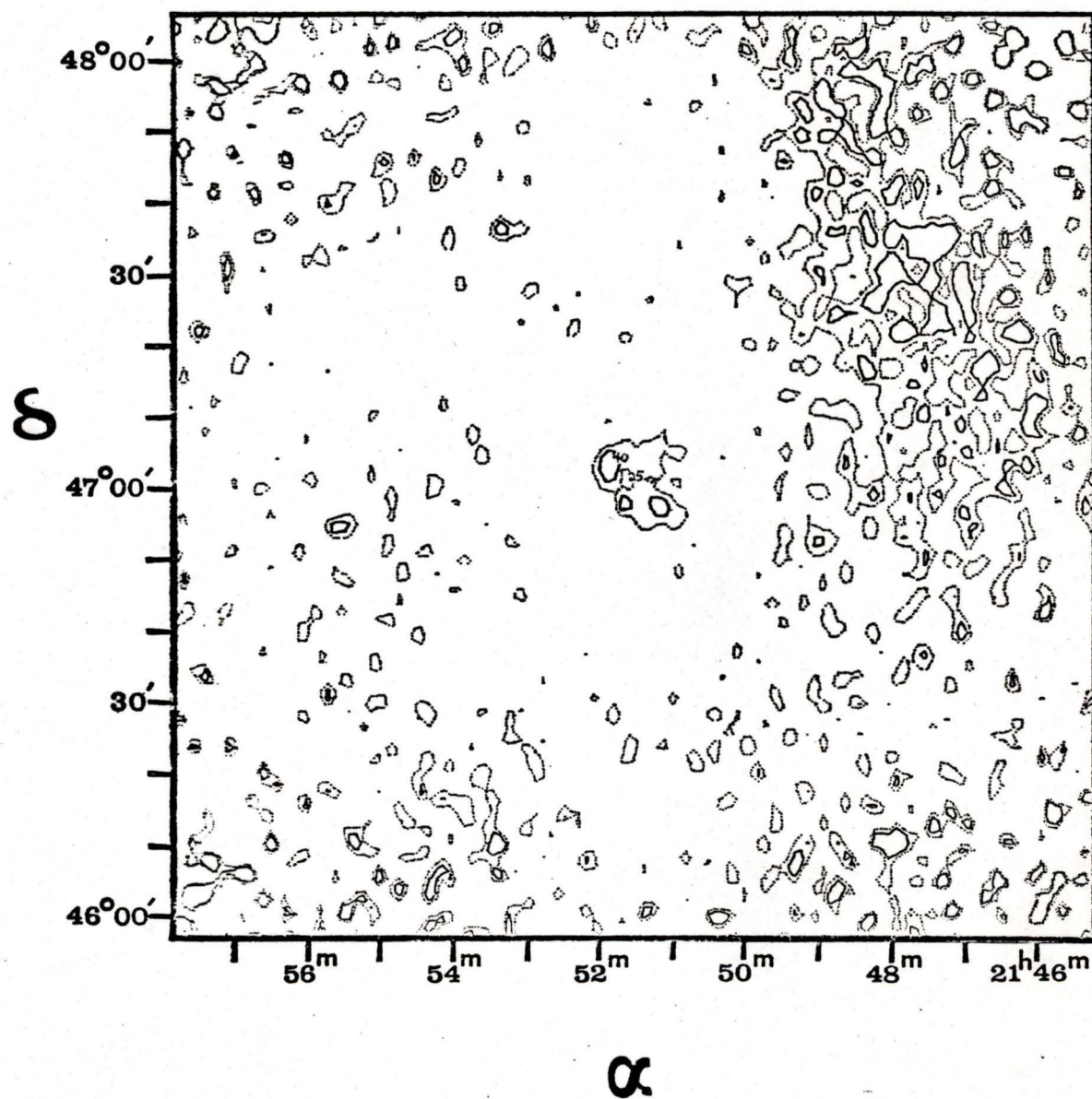
APPENDIX D

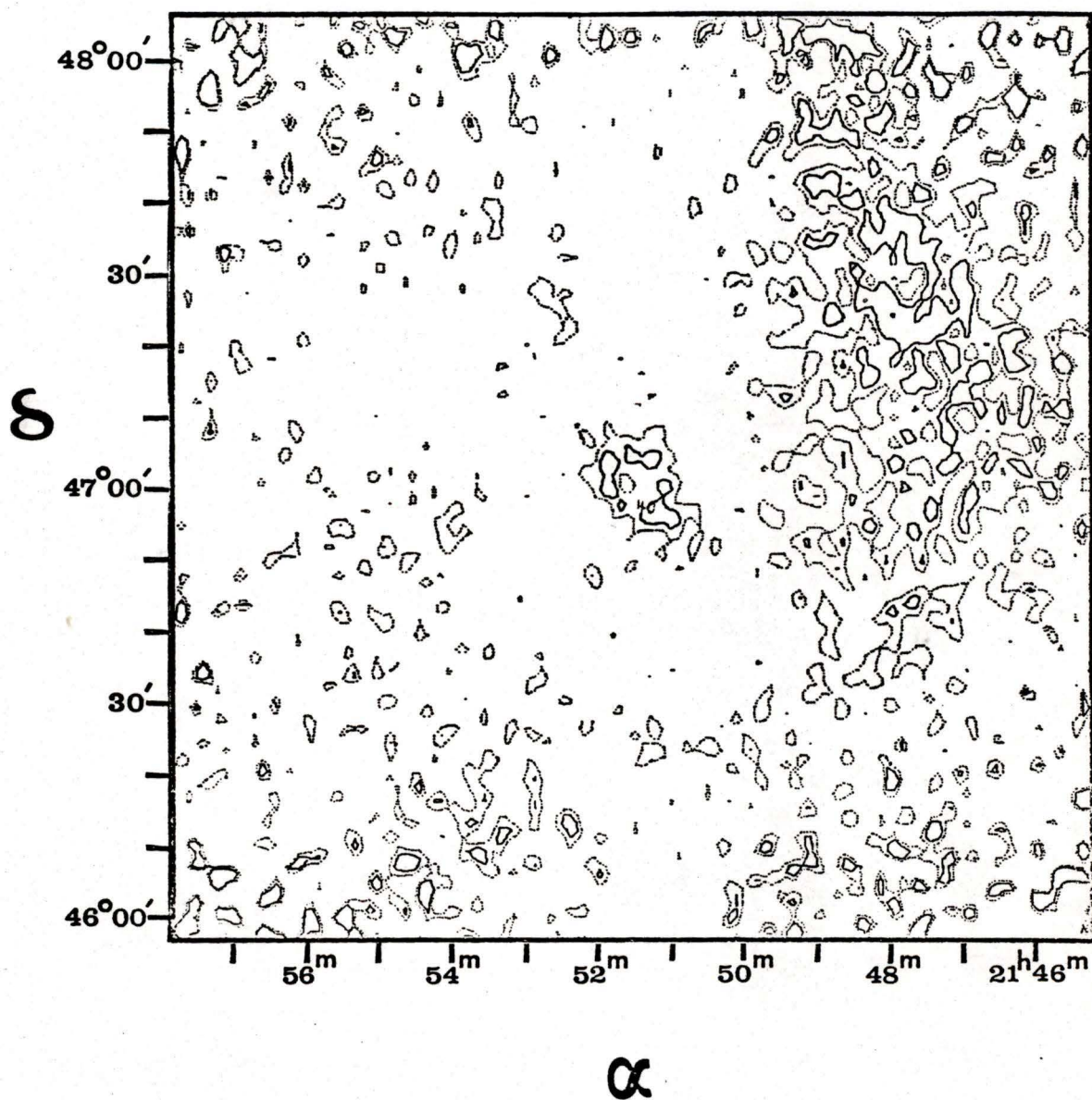
Thirty $2^\circ \alpha - \delta$ HI maps which cover the velocity range $1.76 \leq V \text{ (km}\cdot\text{s}^{-1}) \leq 13.71$ are presented here. Total atomic hydrogen data from all spacings are included in these maps. 'Noisy edges' result from the correction for the 8.6 m paraboloid polar diagram. Contours have been set above the background level as described by Figure 5.1. For maps: $V = 1.76 \text{ km}\cdot\text{s}^{-1}$ and $V = 13.71 \text{ km}\cdot\text{s}^{-1}$ one brightness temperature is displayed at 20°K . For all other maps, contours can be seen at the following brightness temperatures: 25, 40, 55, 70, and 85°K , with the contours alternating between dotted and solid lines. The dotted line which indicates the maximum extent of the central emission feature is the lowest 25°K contour. To aid in locating correct contour values above this, some of the contours have been labelled. The synthesized half-power beamshape can be seen to the lower right of each map.

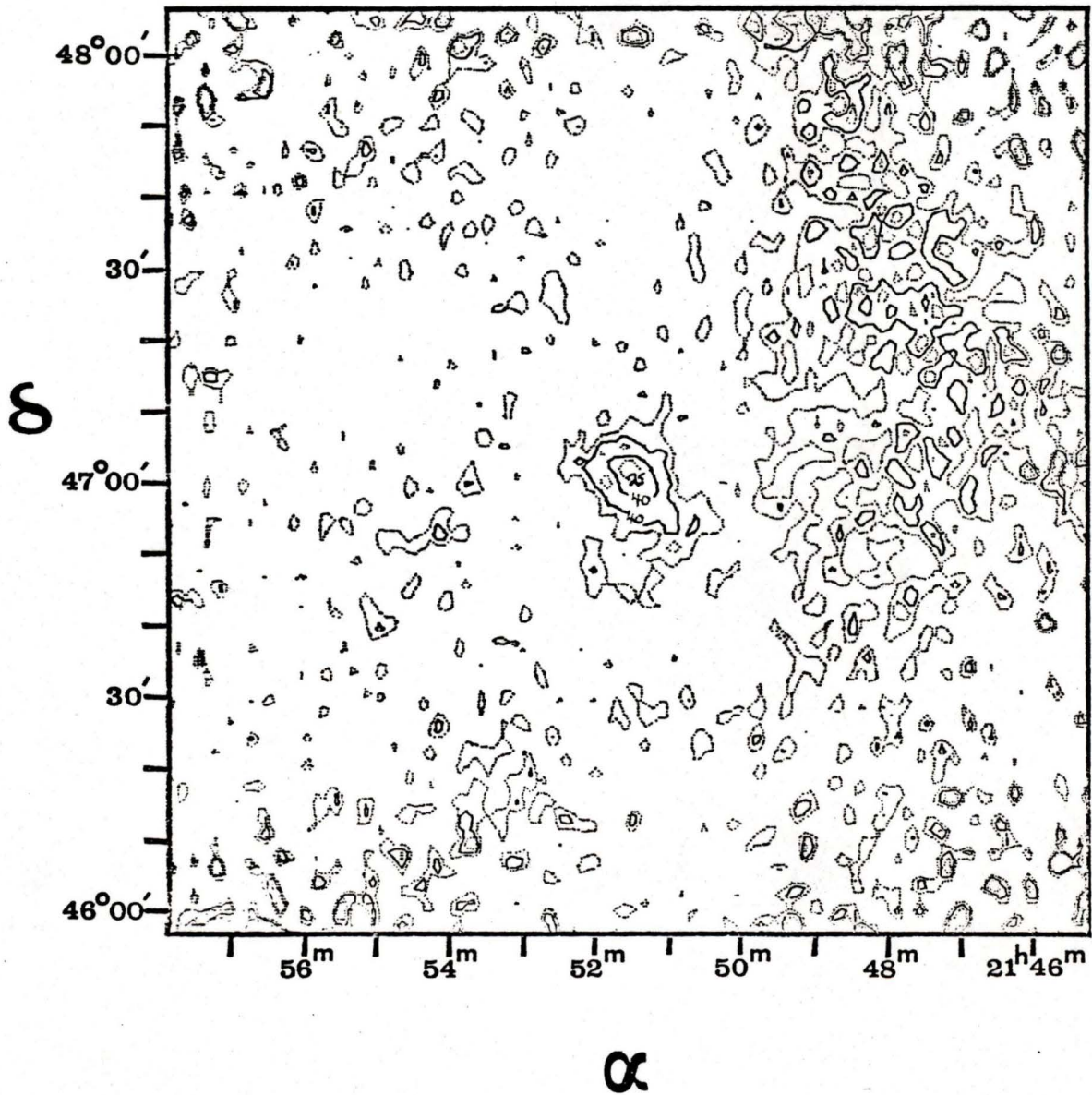
$1.76 \text{ km} \cdot \text{s}^{-1}$ 

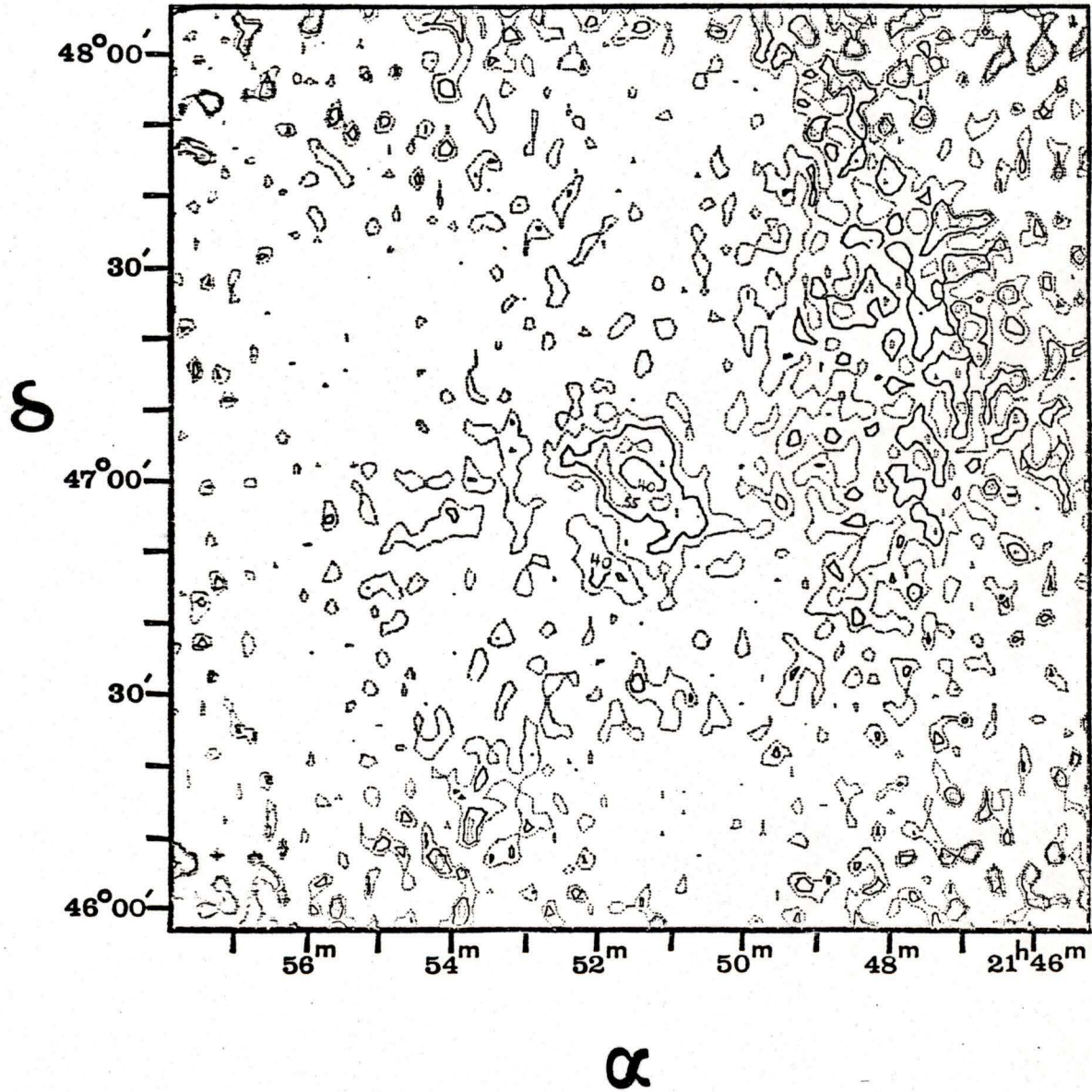
$2.17 \text{ km} \cdot \text{s}^{-1}$ 

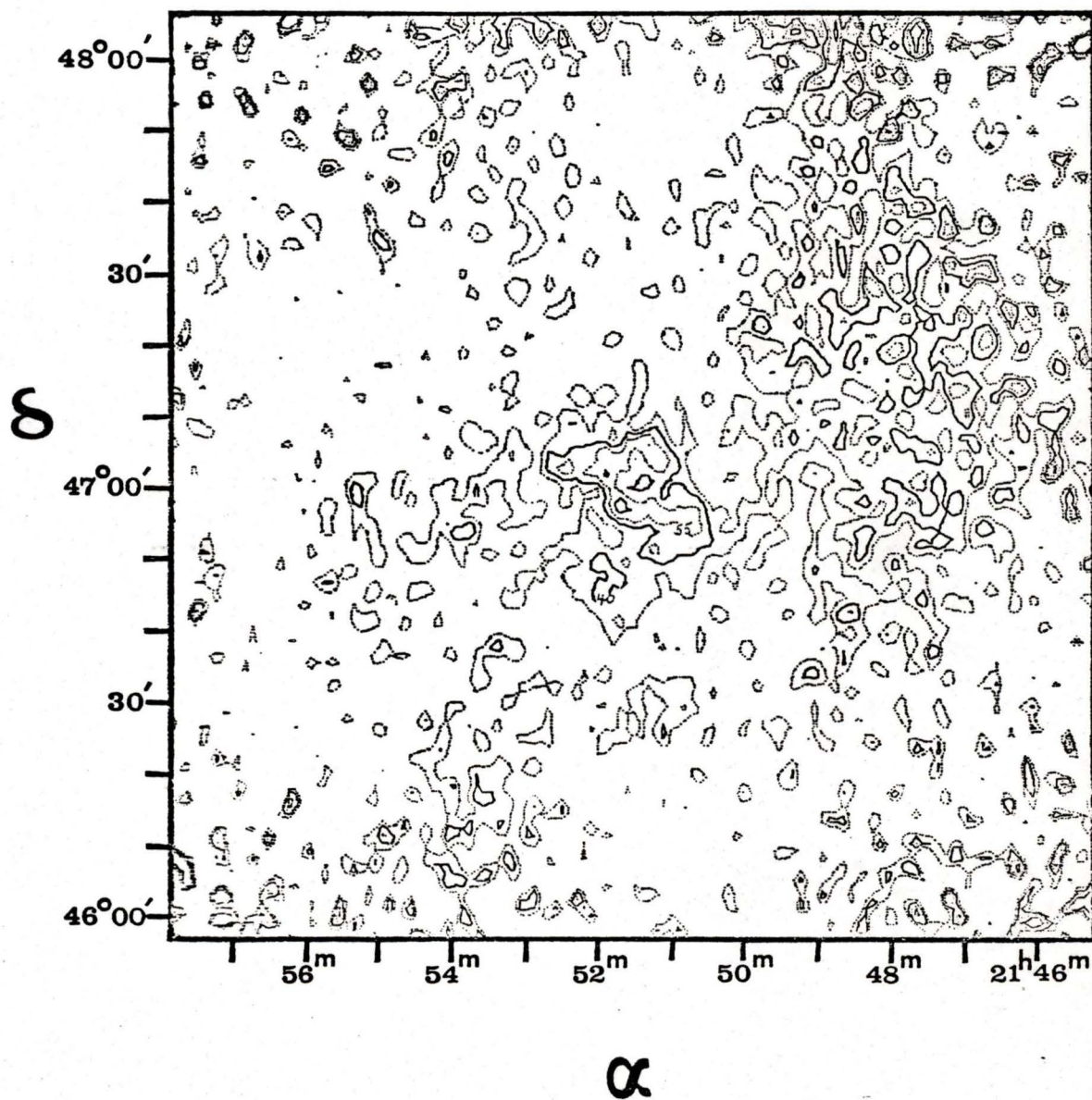
$2.58 \text{ km} \cdot \text{s}^{-1}$ 

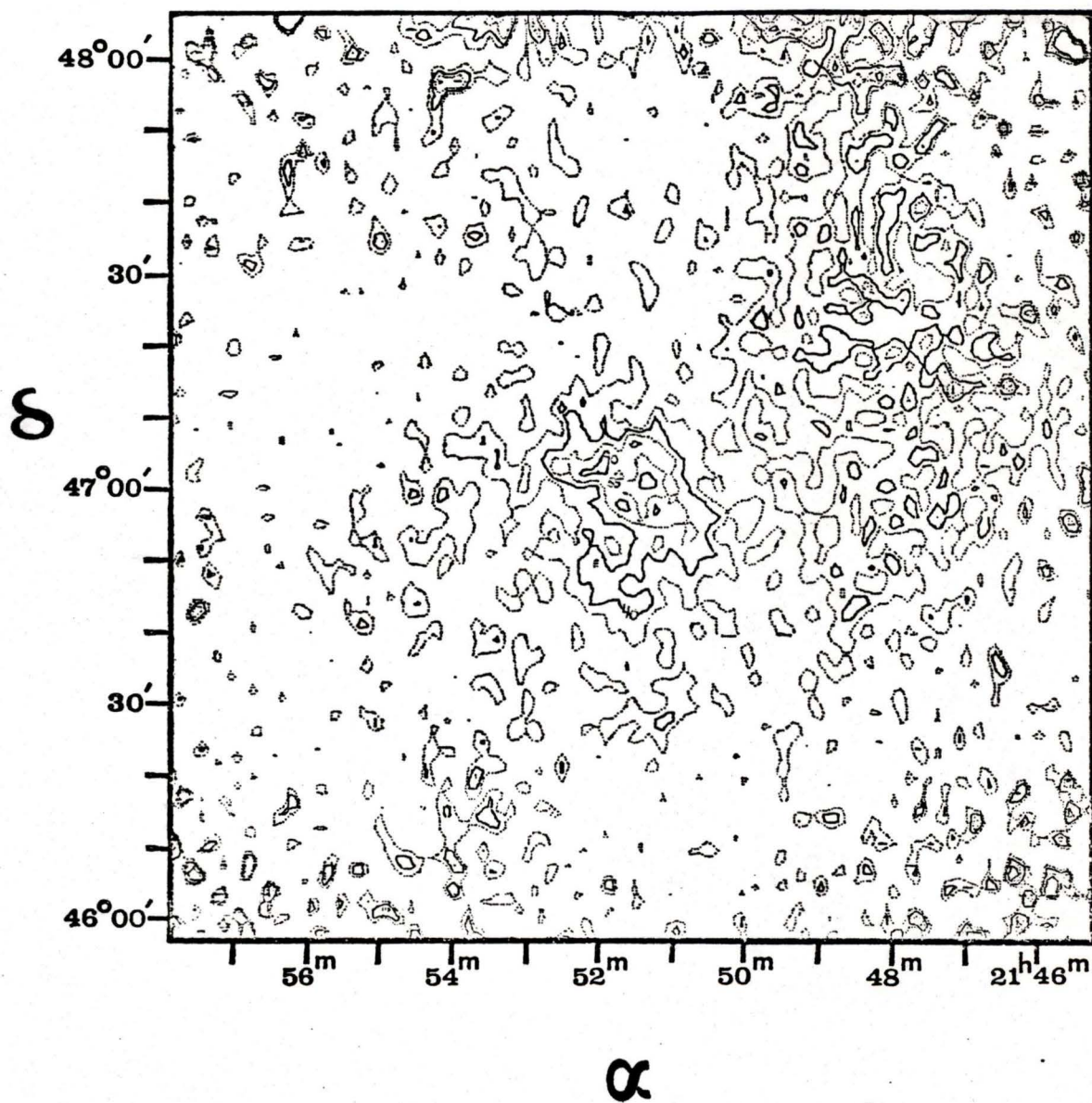
$2.99 \text{ km} \cdot \text{s}^{-1}$ 

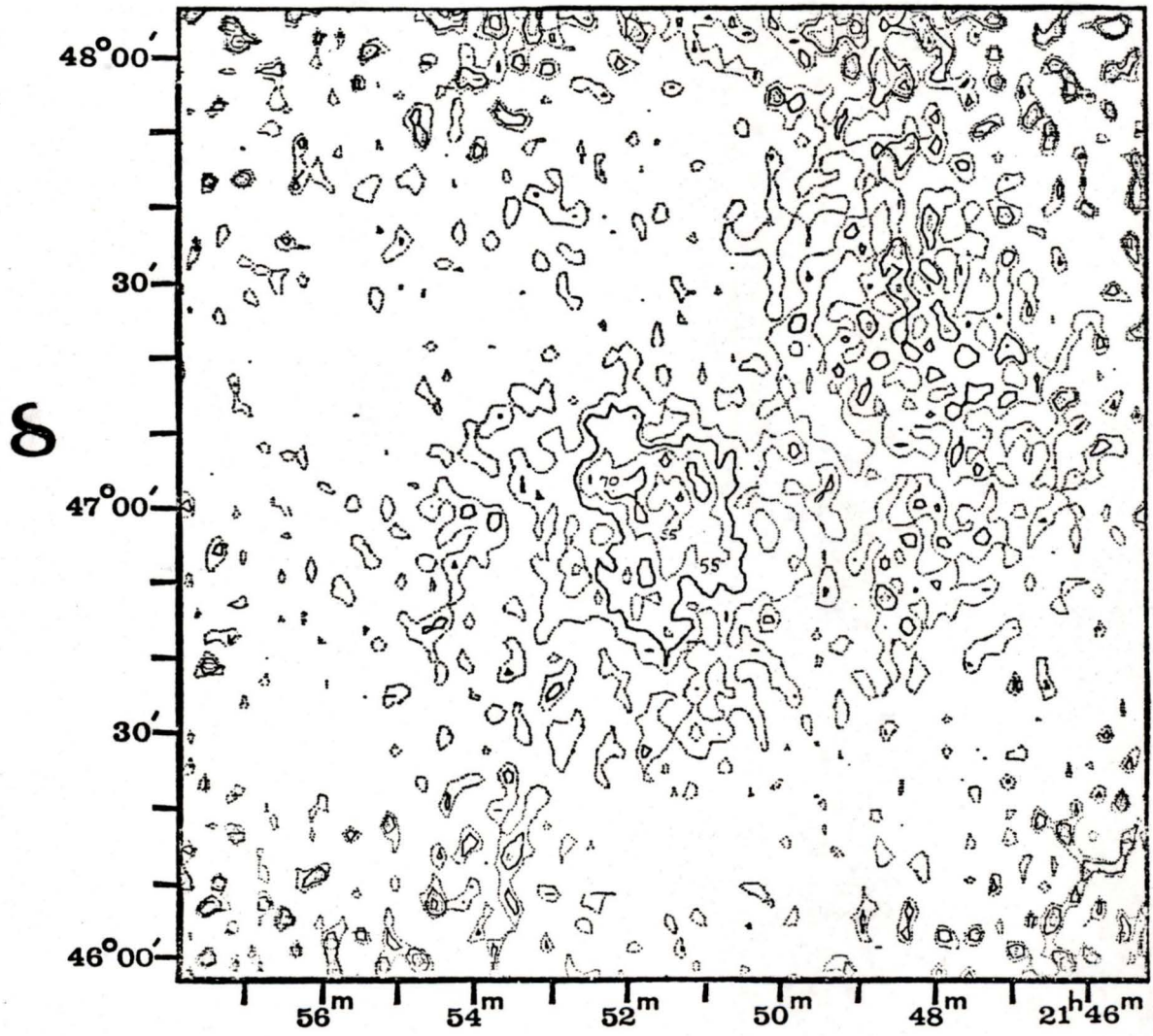
$3.41 \text{ km} \cdot \text{s}^{-1}$ 

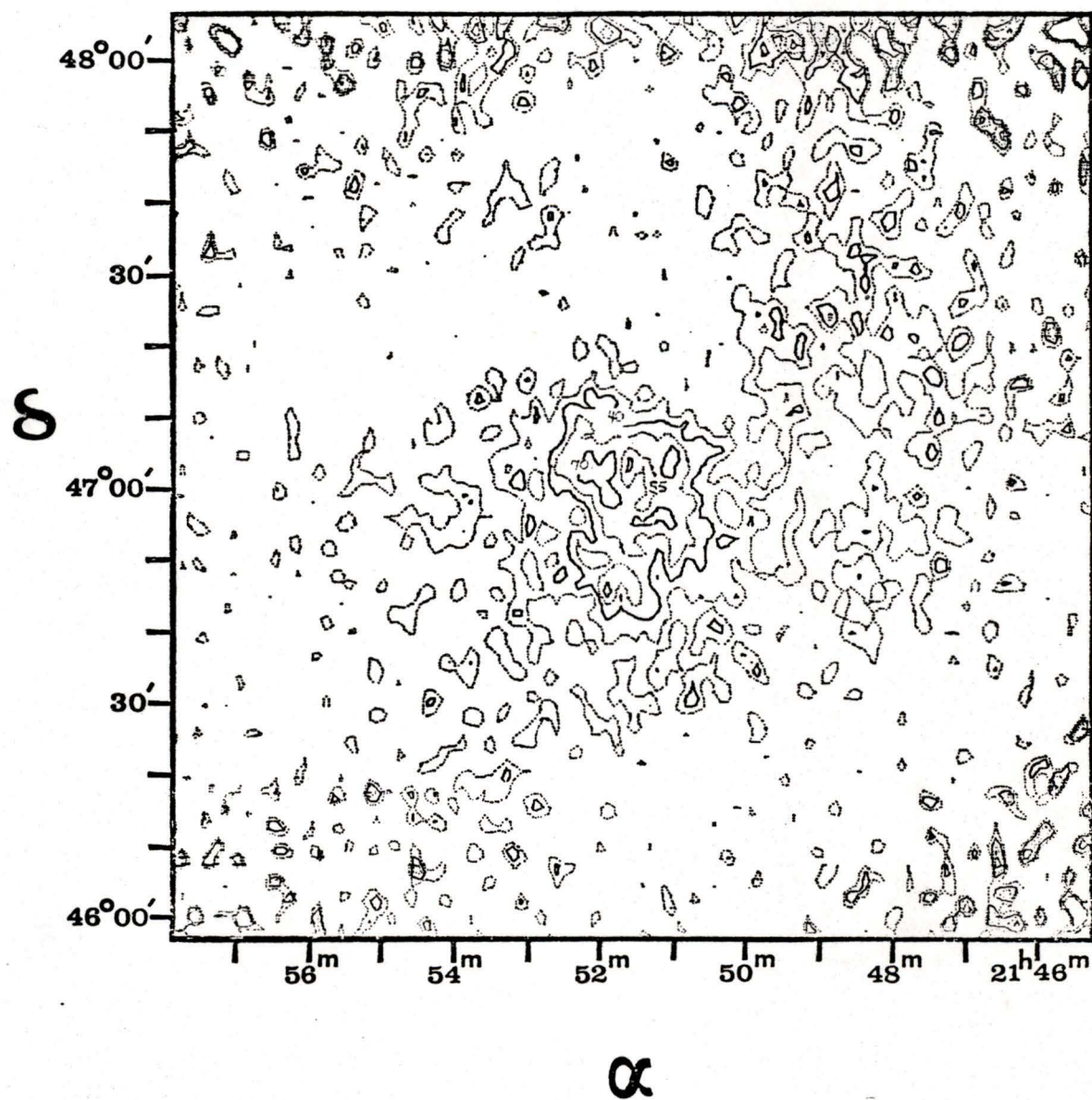
$3.82 \text{ km} \cdot \text{s}^{-1}$ 

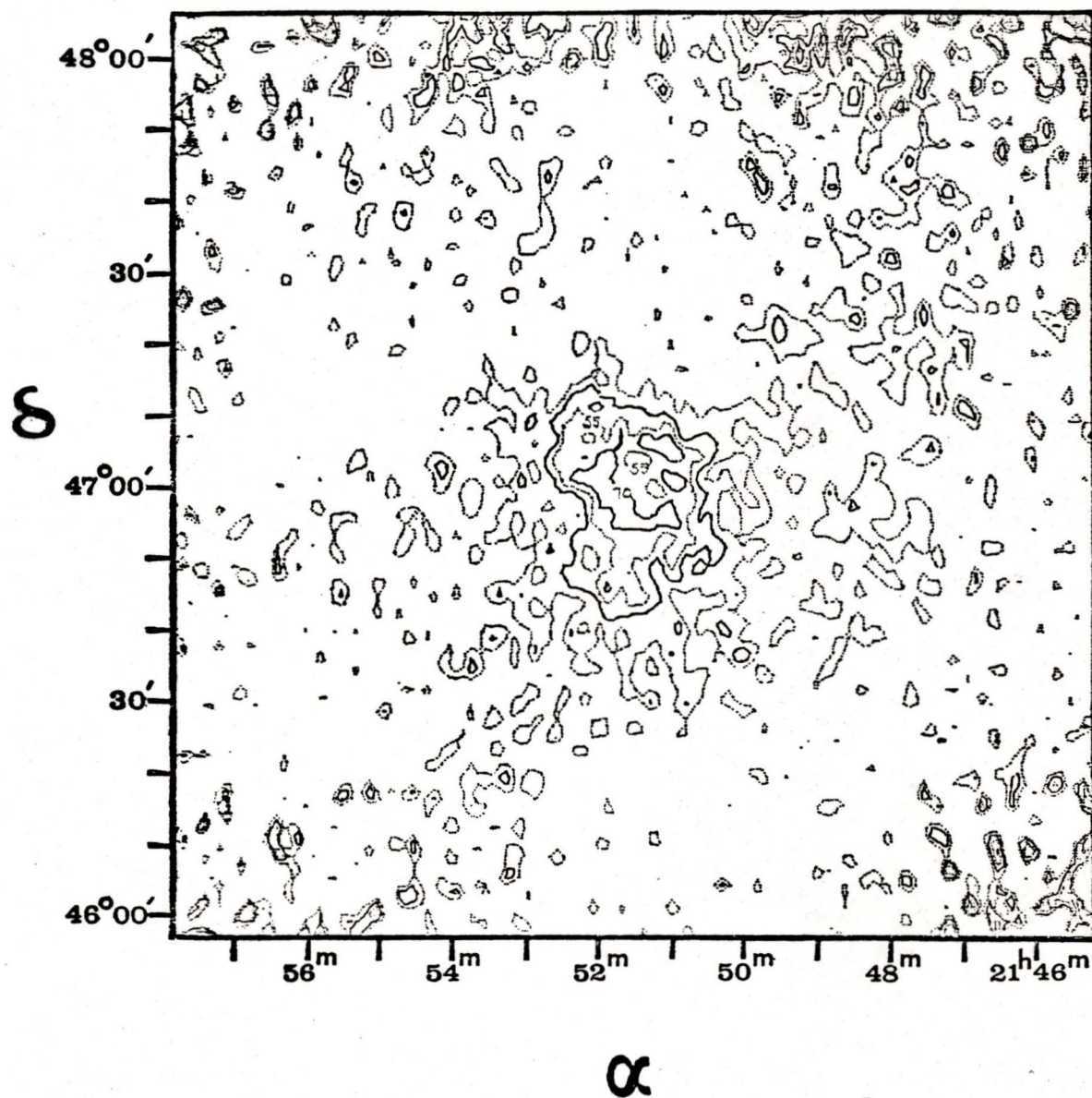
$4.23 \text{ km} \cdot \text{s}^{-1}$ 

$4.64 \text{ km} \cdot \text{s}^{-1}$ 

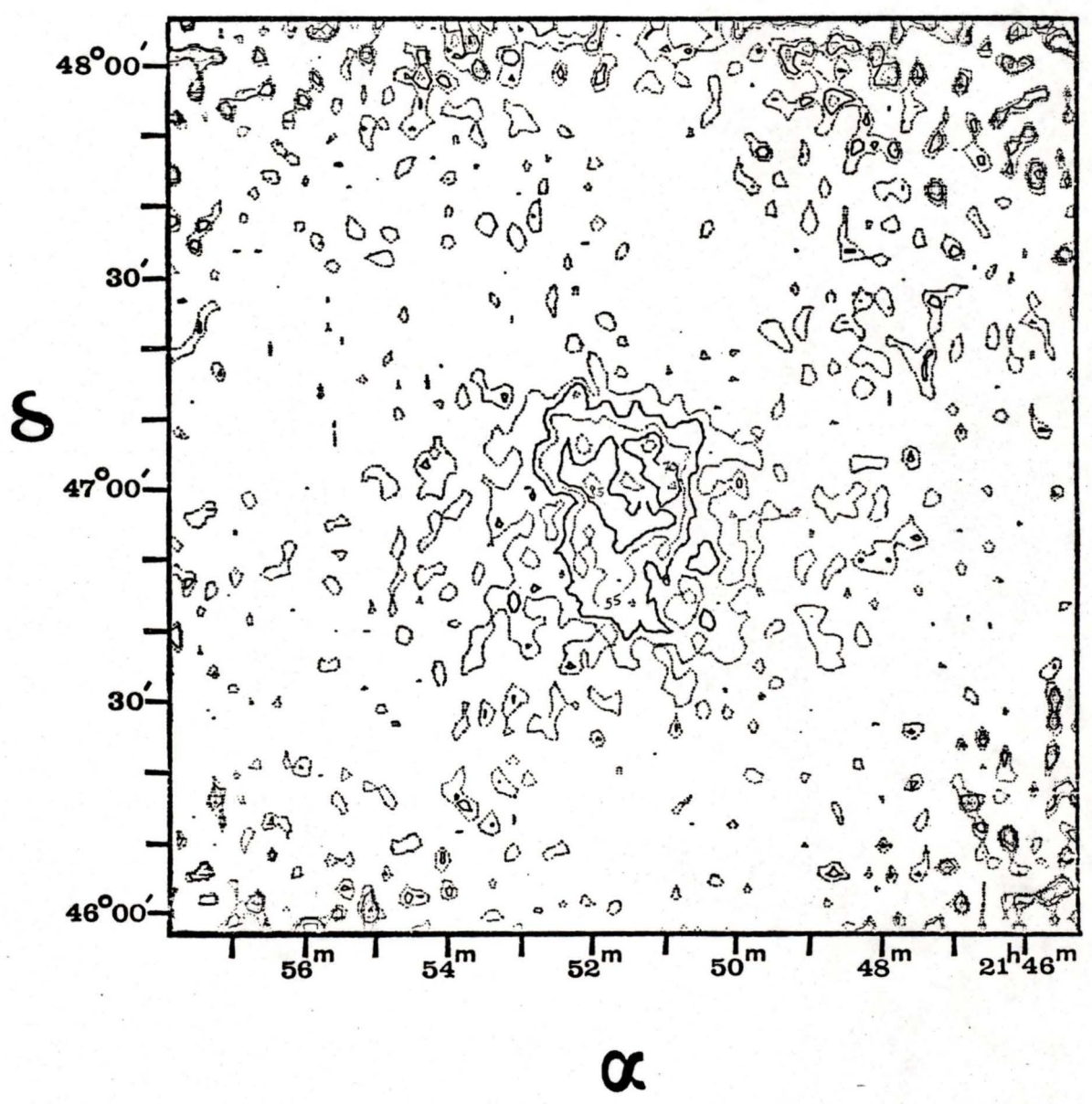
5.05 km s^{-1} 

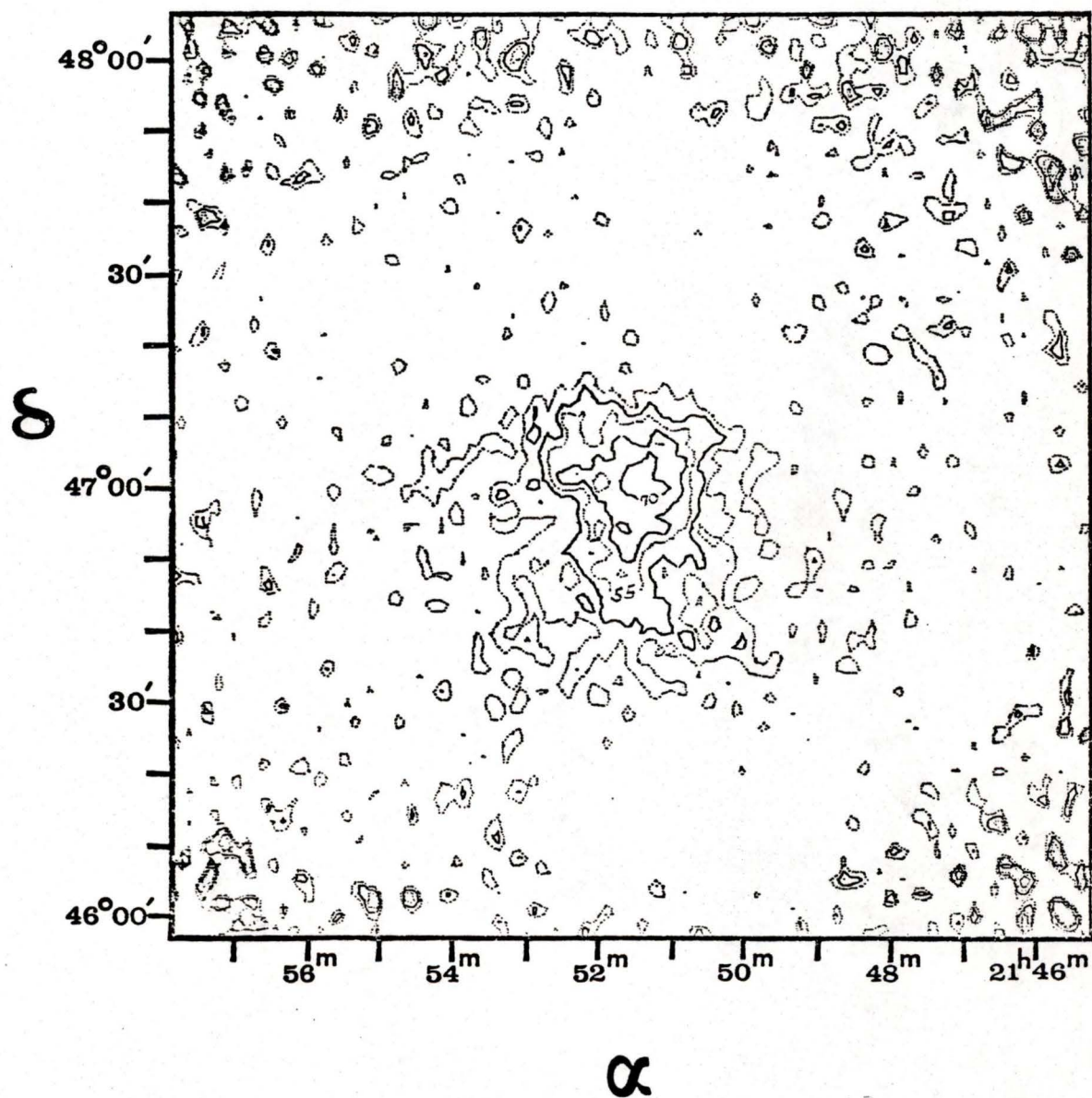
$5.47 \text{ km} \cdot \text{s}^{-1}$  α

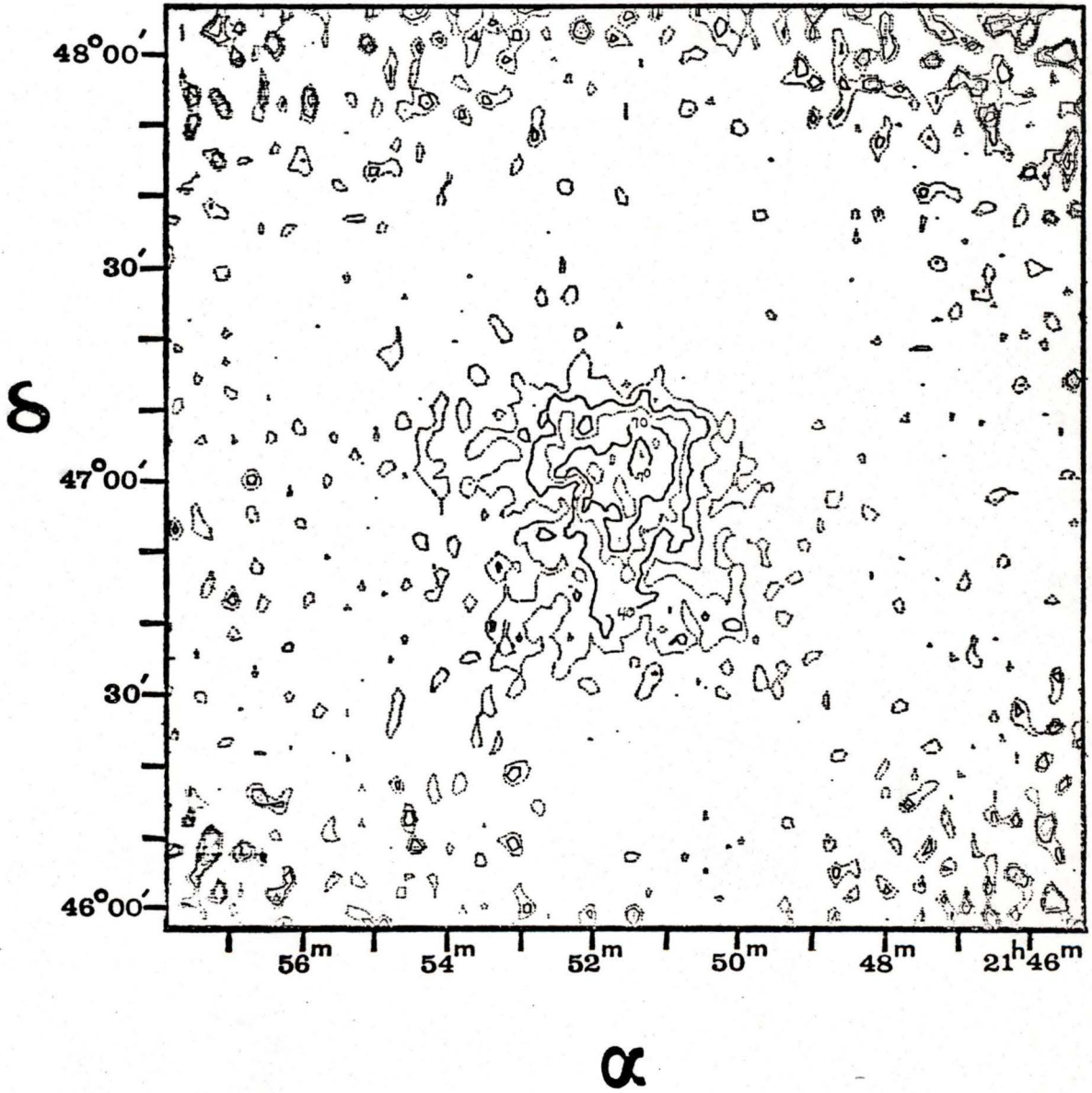
$5.88 \text{ km} \cdot \text{s}^{-1}$ 

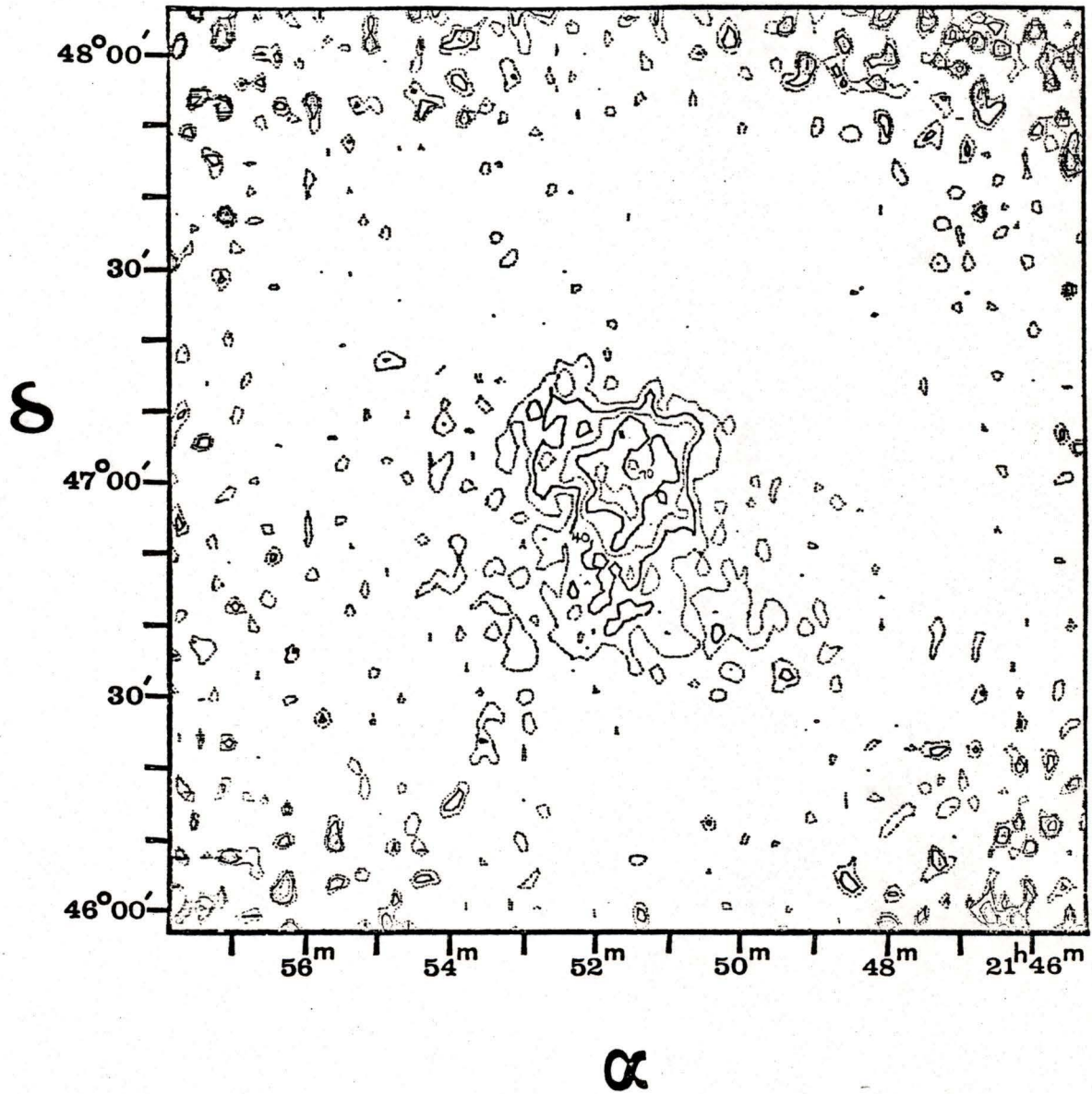
$6.29 \text{ km} \cdot \text{s}^{-1}$ 

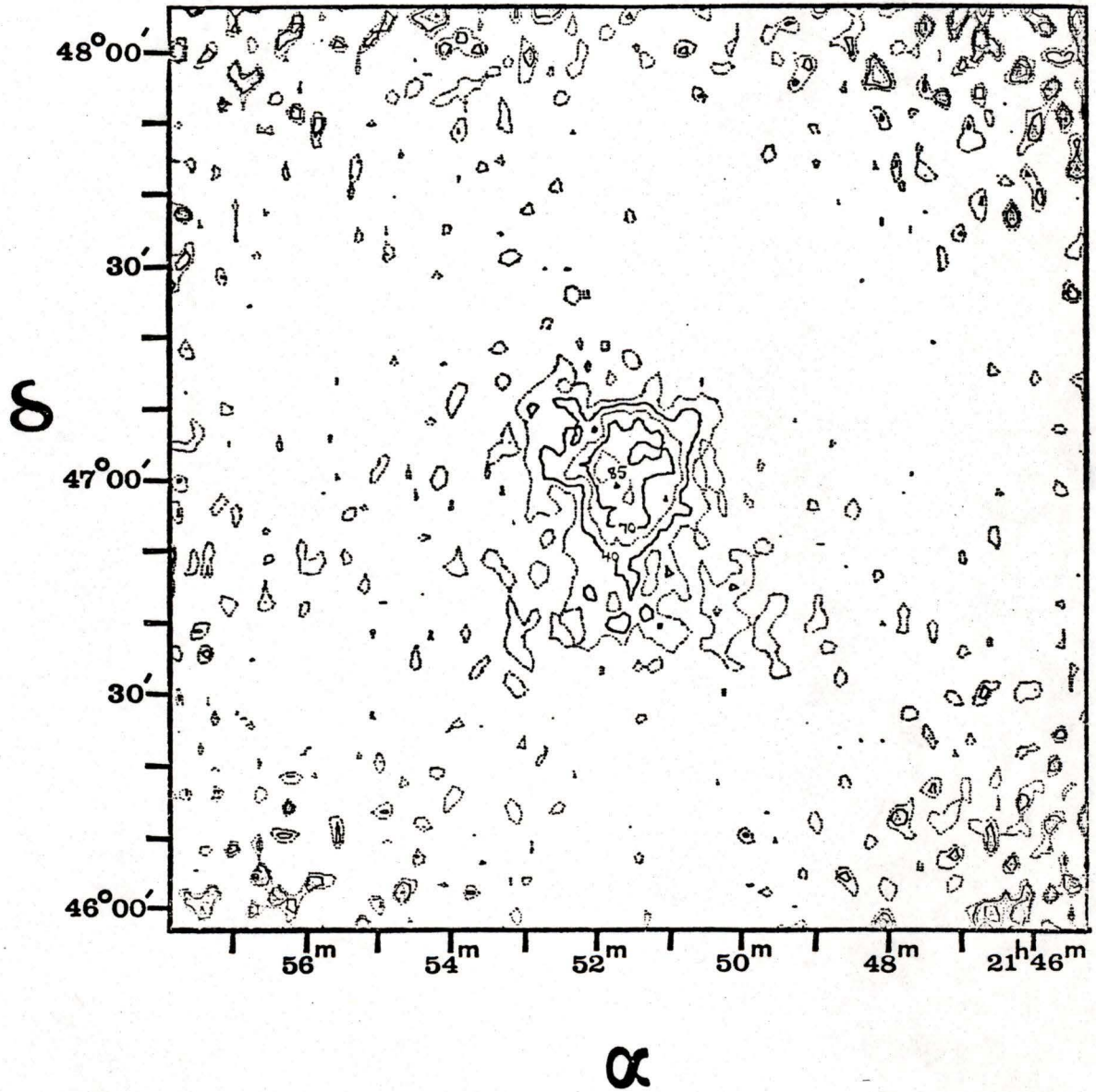
$6.70 \text{ km} \cdot \text{s}^{-1}$

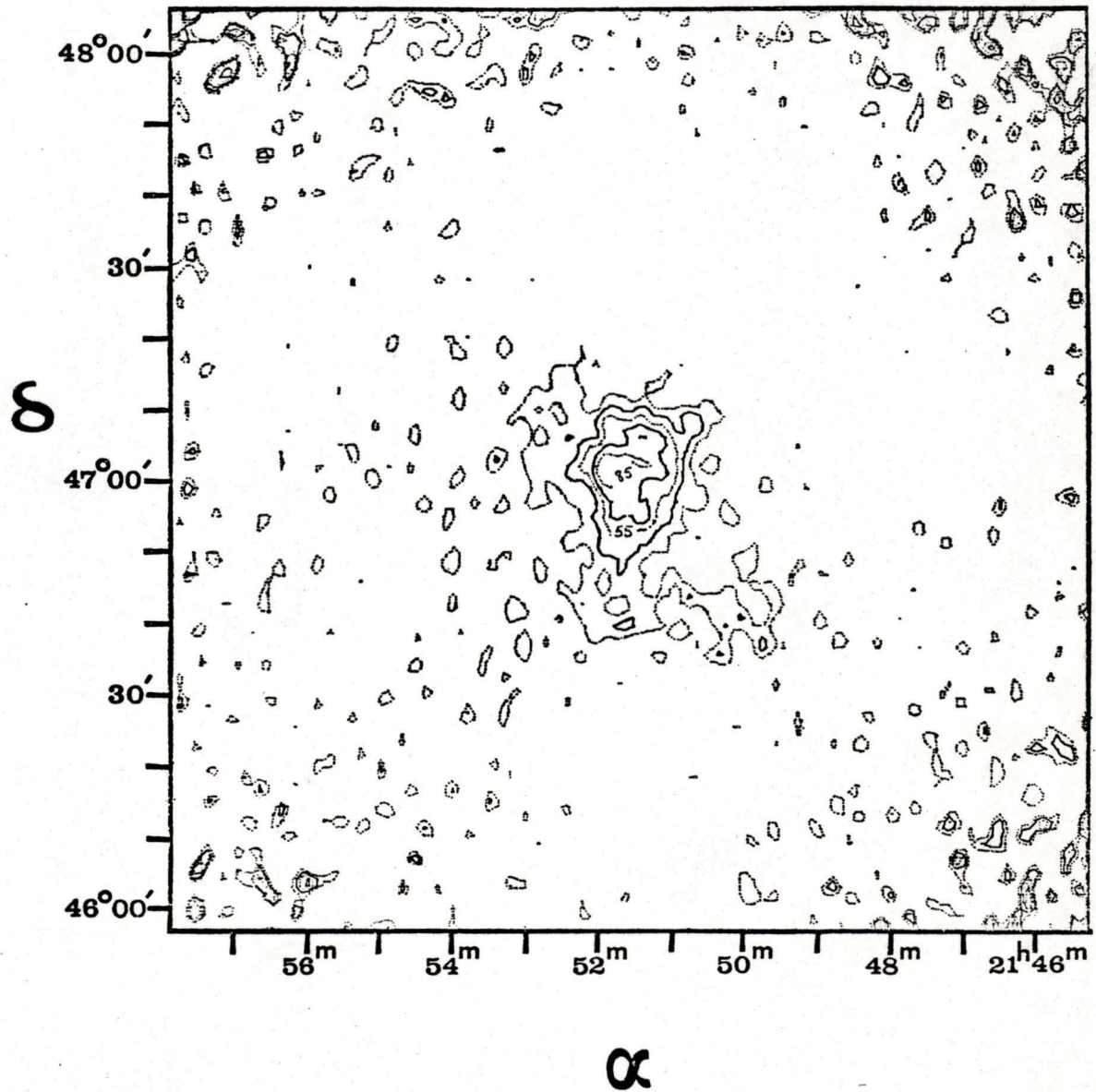


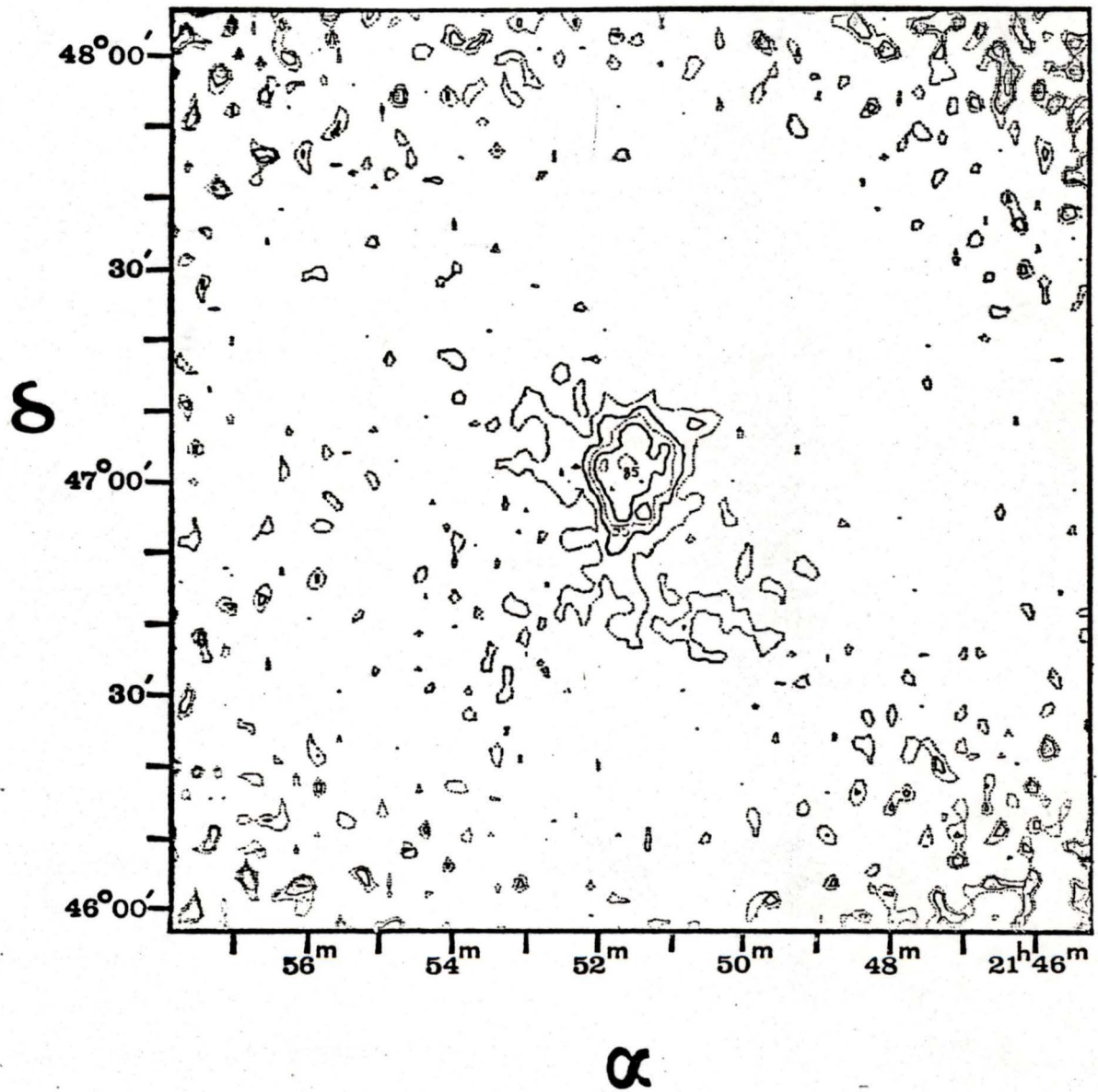
$7.12 \text{ km} \cdot \text{s}^{-1}$ 

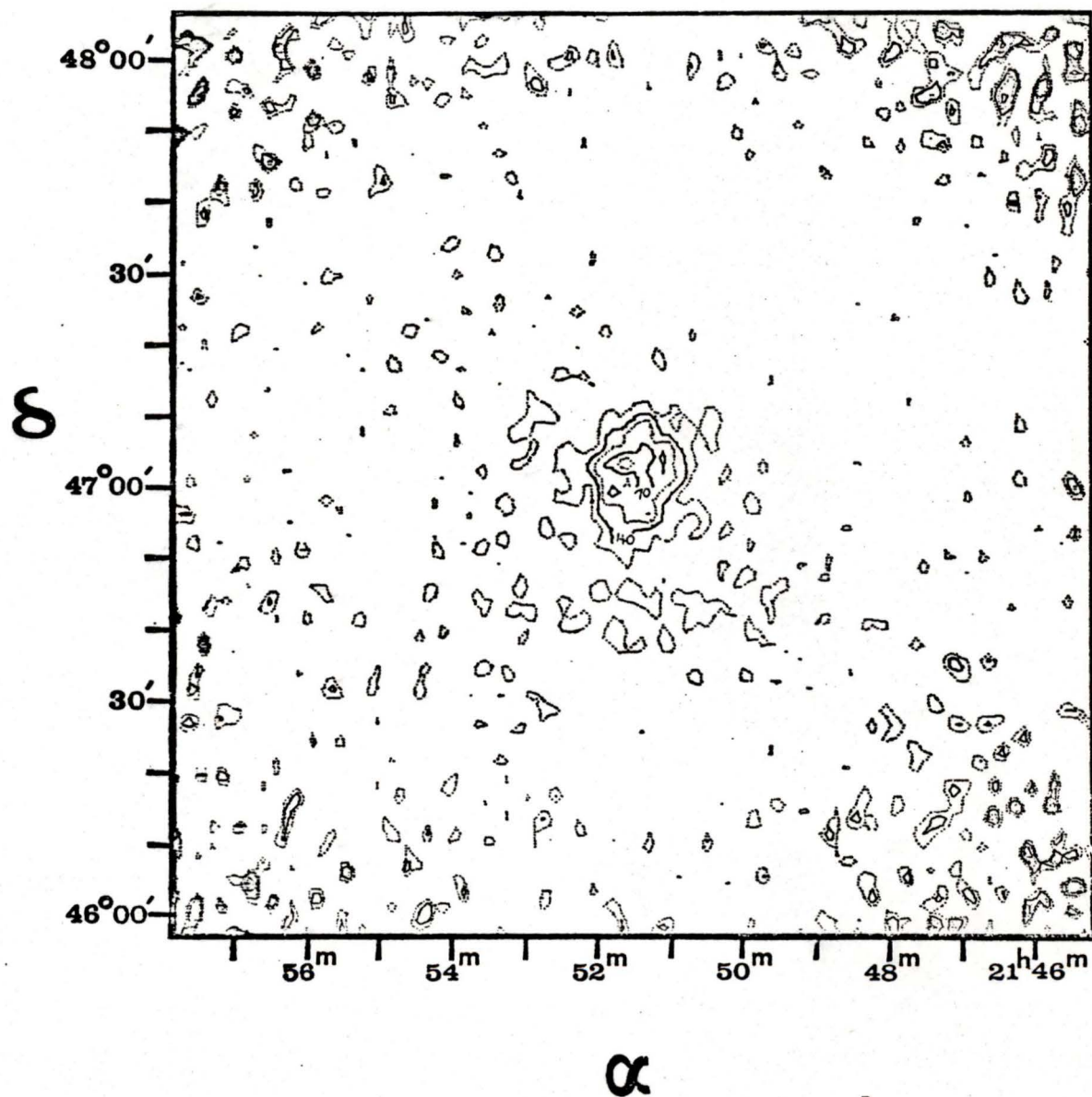
$7.53 \text{ km} \cdot \text{s}^{-1}$ 

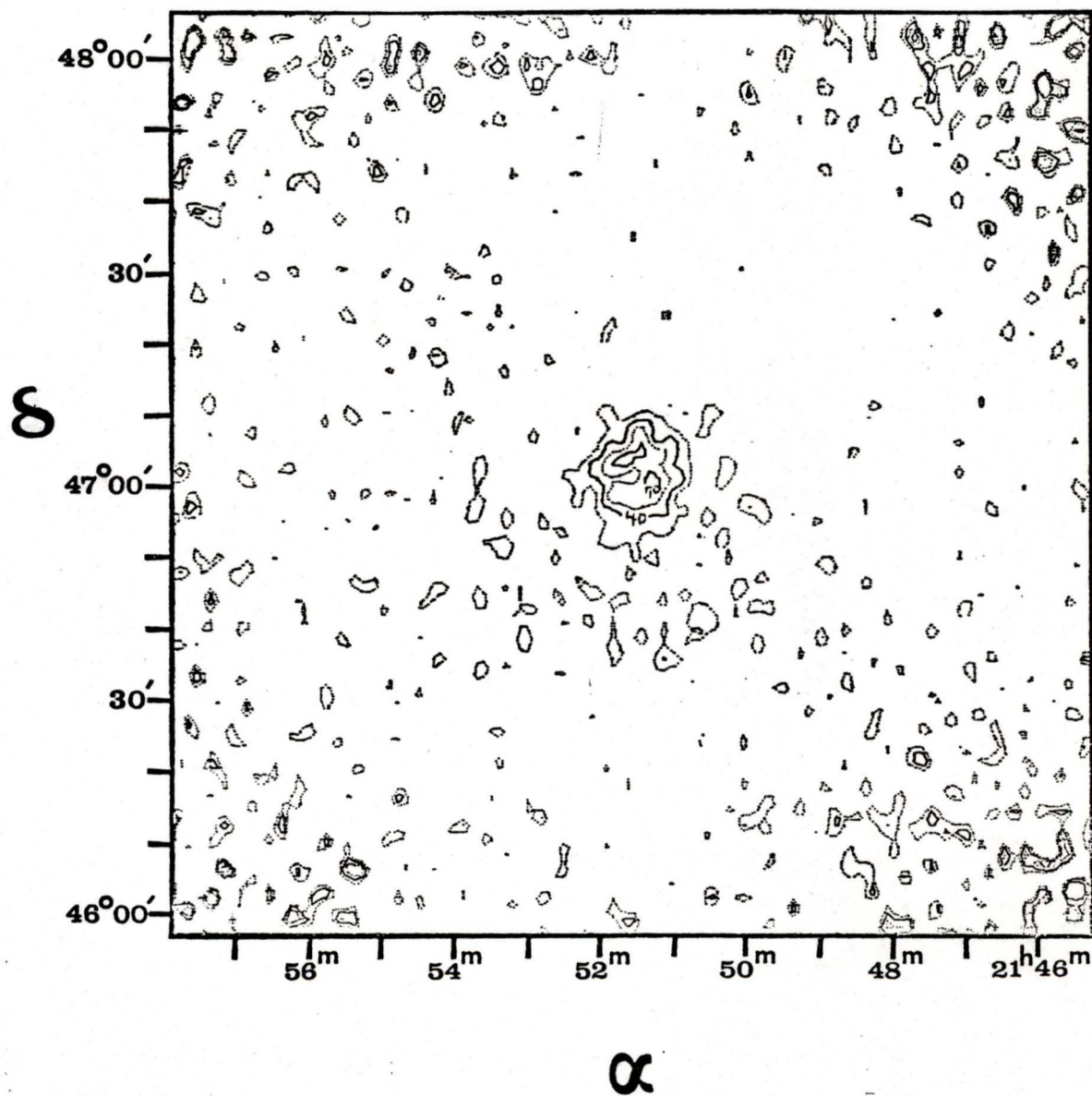
$7.94 \text{ km} \cdot \text{s}^{-1}$ 

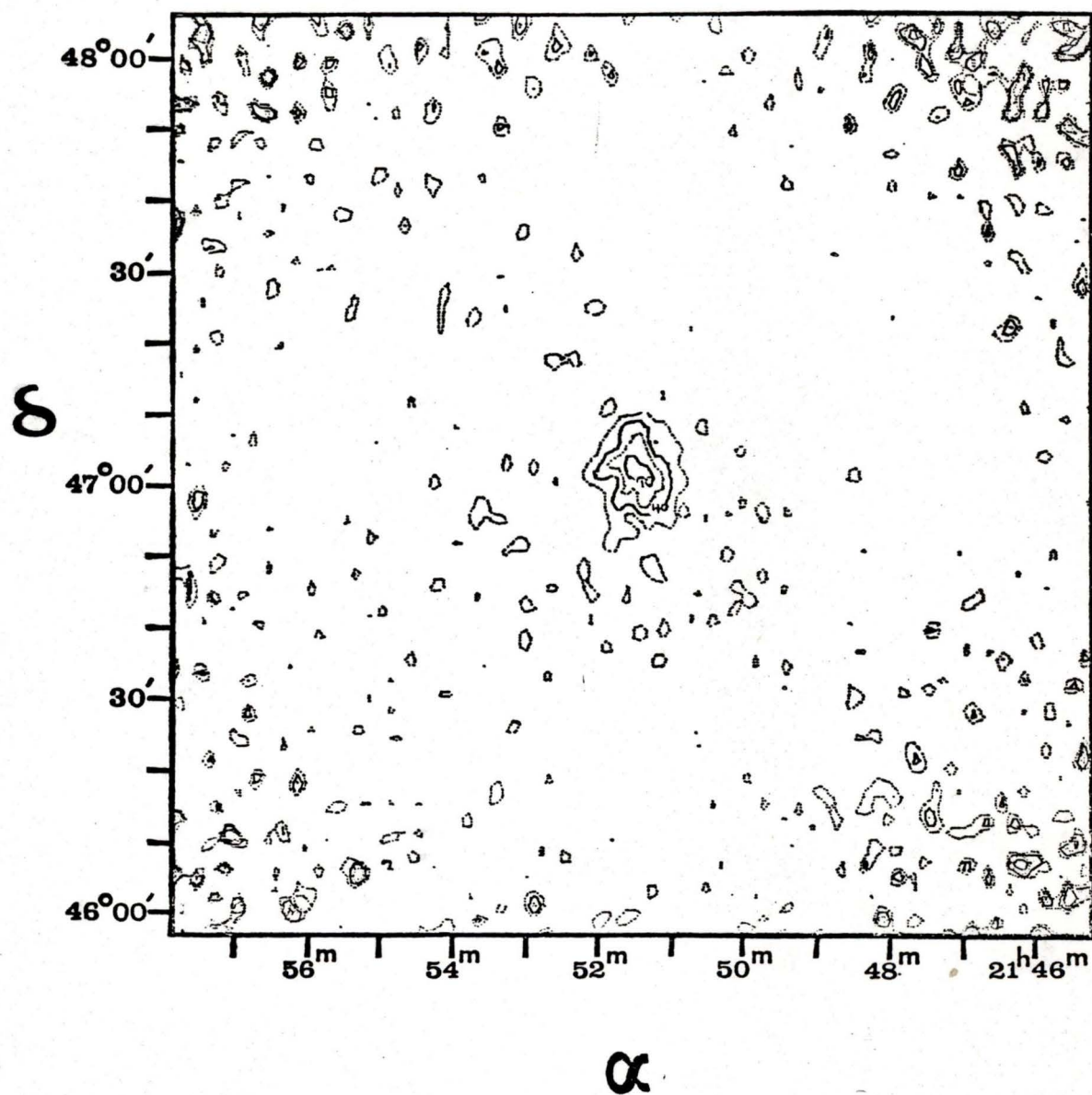
$8.35 \text{ km} \cdot \text{s}^{-1}$ 

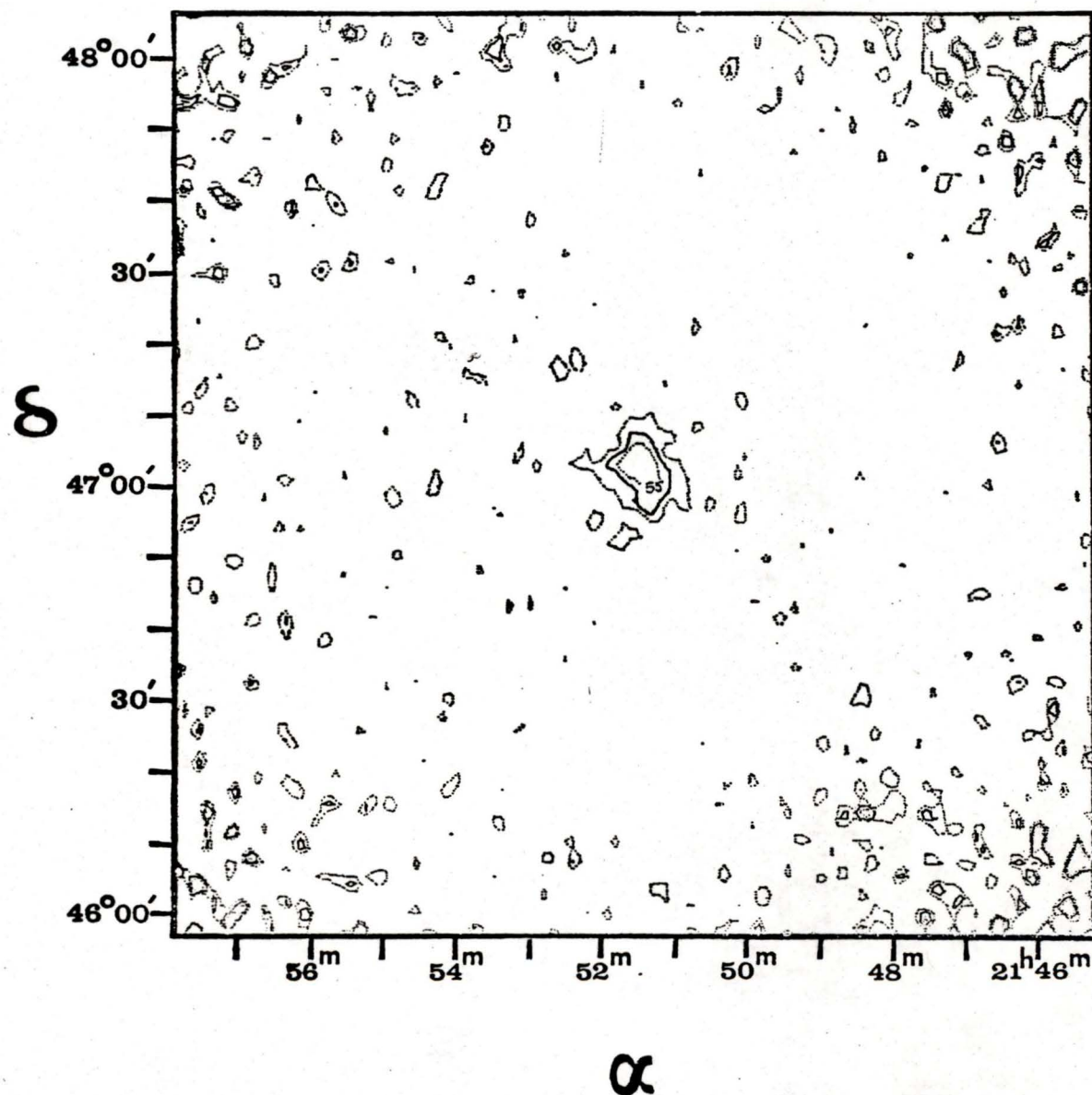
$8.76 \text{ km} \cdot \text{s}^{-1}$ 

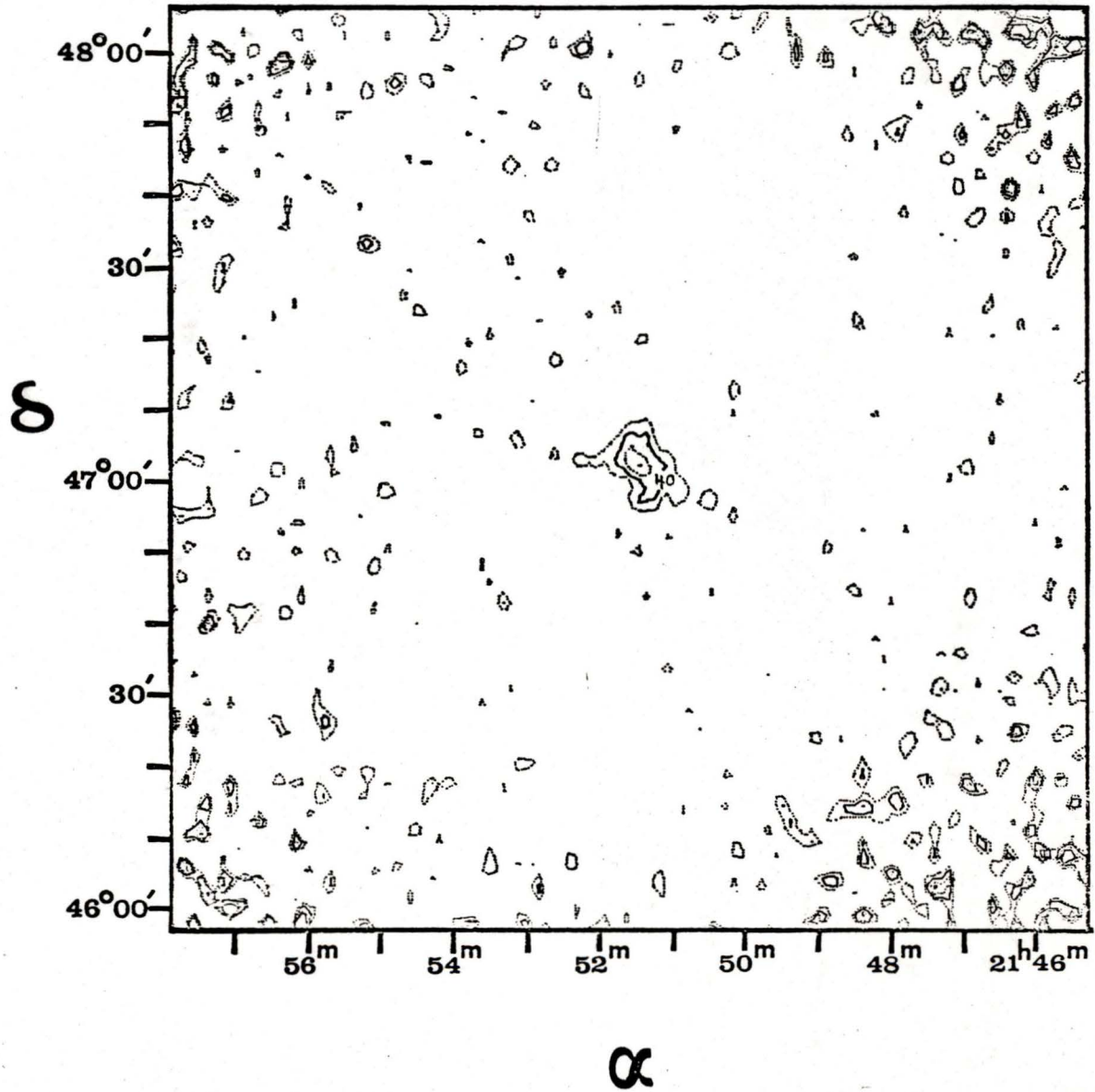
$9.18 \text{ km} \cdot \text{s}^{-1}$ 

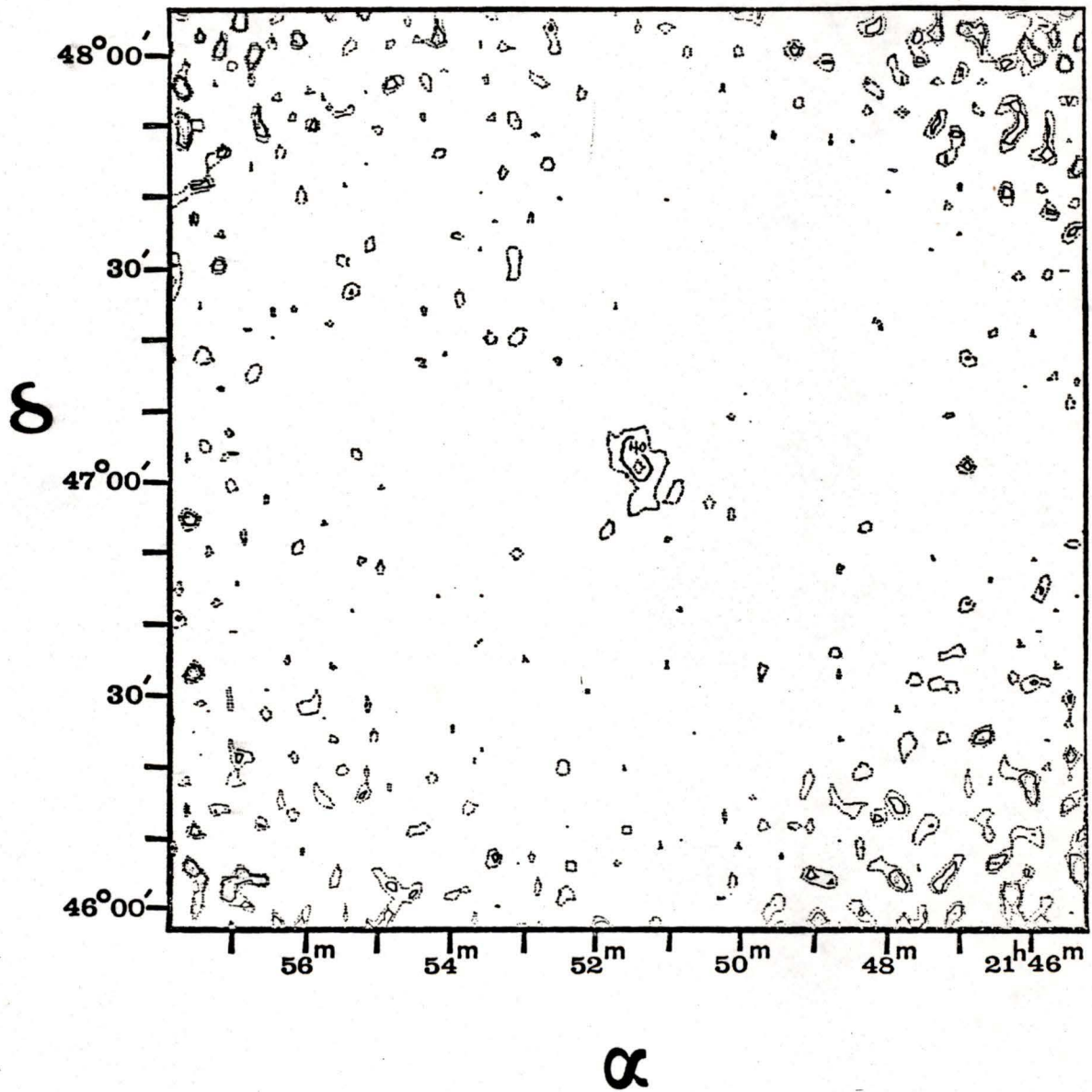
$9.59 \text{ km} \cdot \text{s}^{-1}$ 

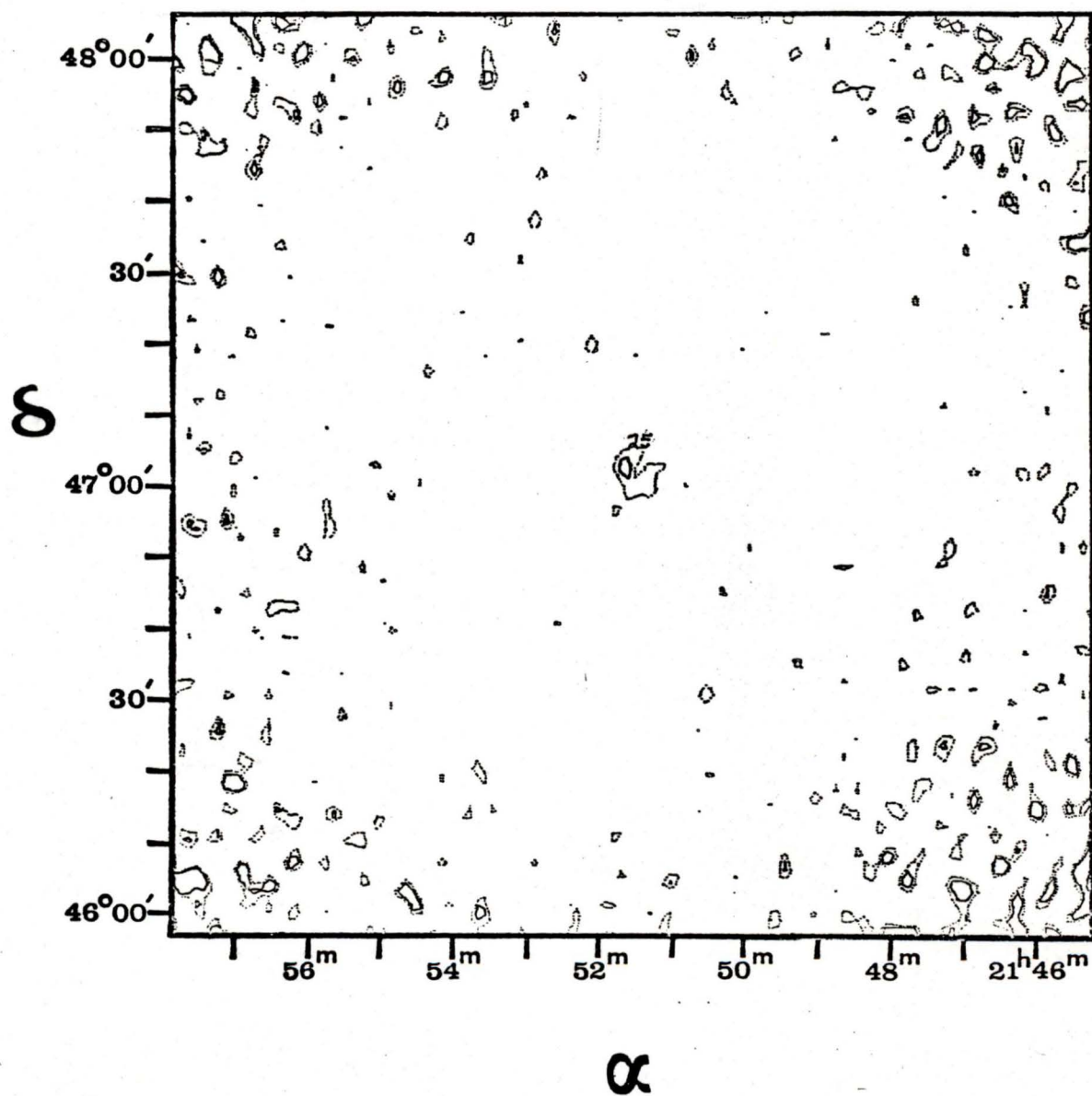
$10.00 \text{ km} \cdot \text{s}^{-1}$ 

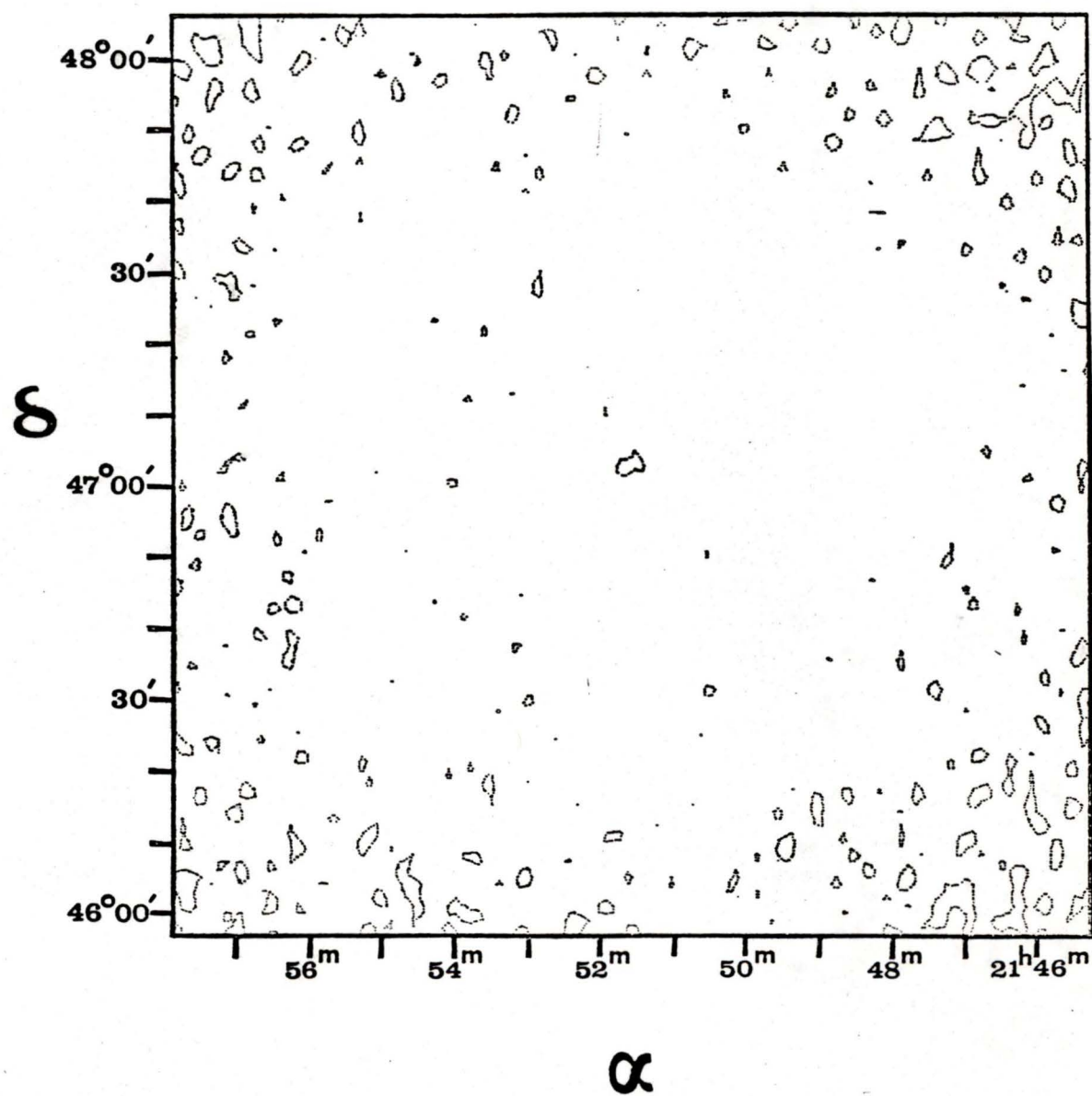
$10.41 \text{ km} \cdot \text{s}^{-1}$ 

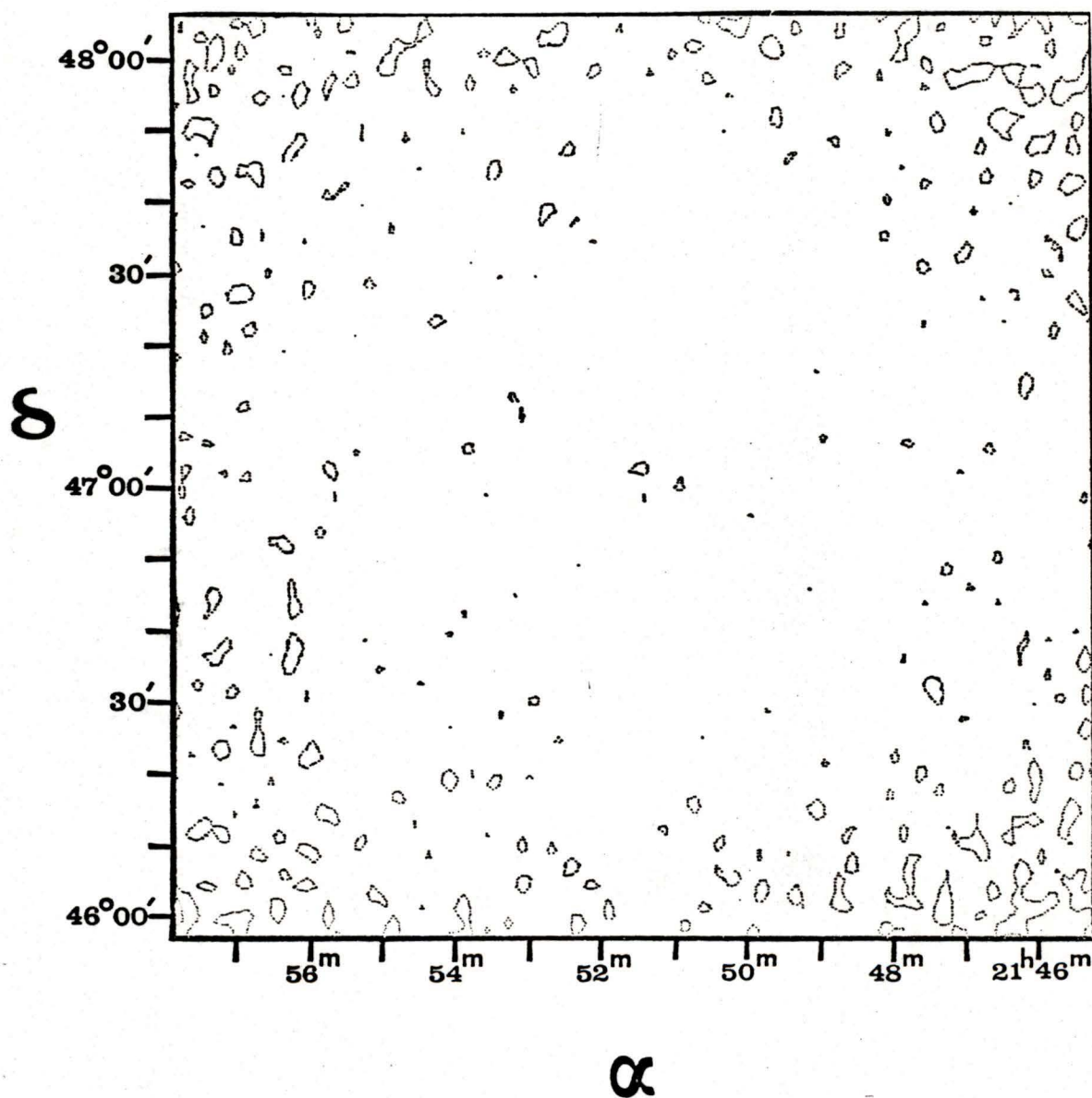
$10.82 \text{ km} \cdot \text{s}^{-1}$ 

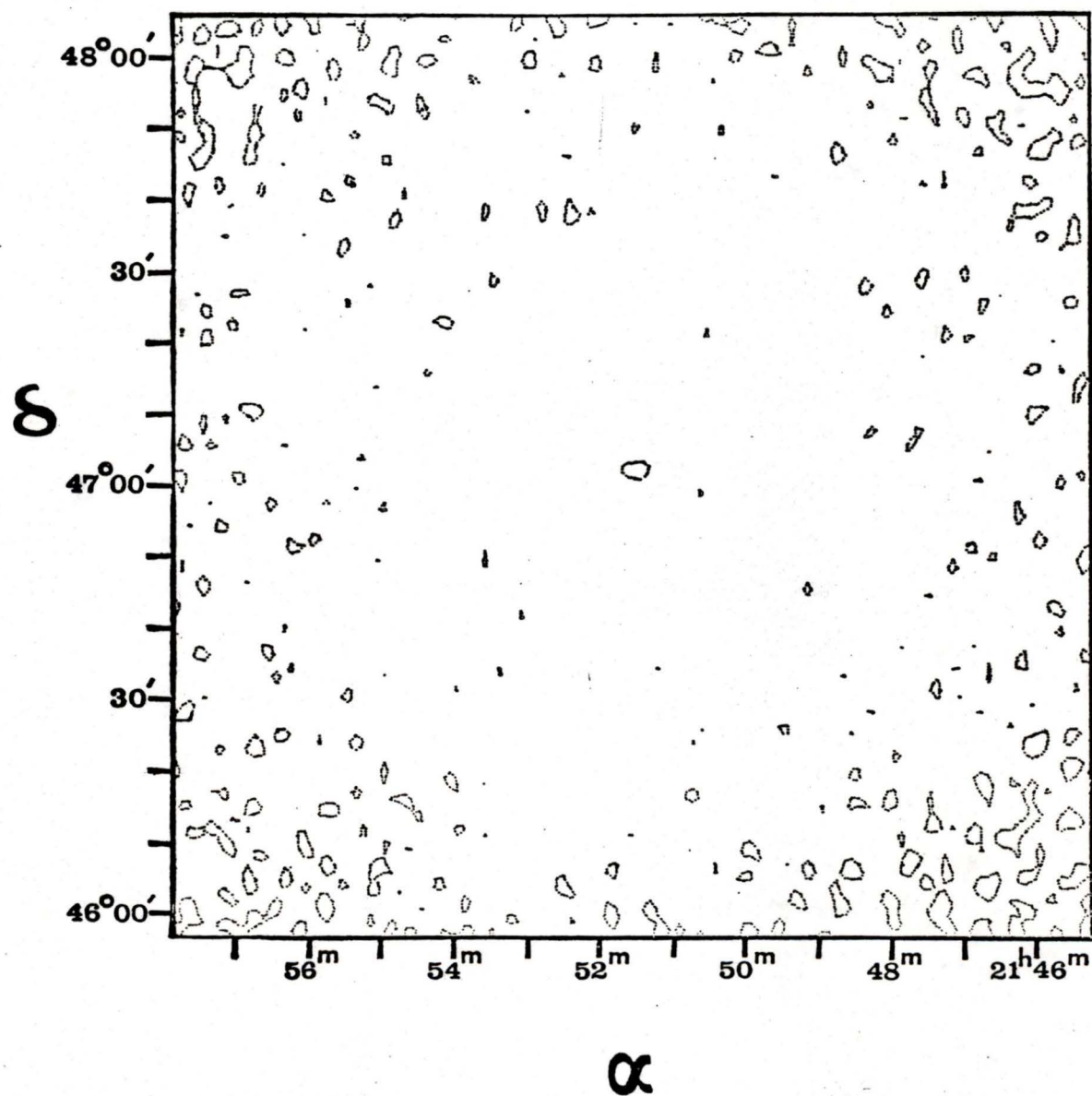
$11.24 \text{ km} \cdot \text{s}^{-1}$ 

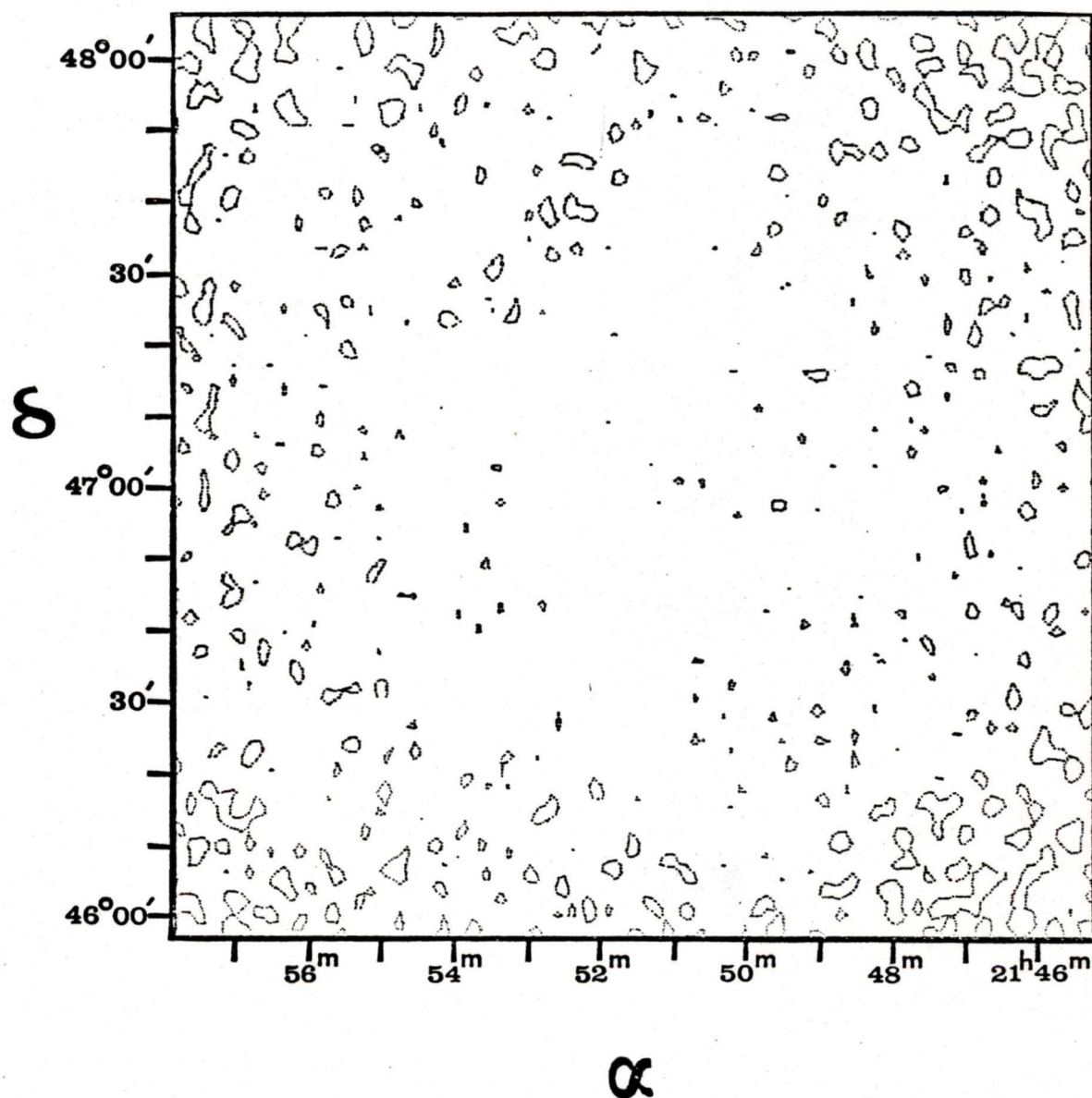
$11.65 \text{ km} \cdot \text{s}^{-1}$ 

$12.06 \text{ km} \cdot \text{s}^{-1}$ 

$12.47 \text{ km} \cdot \text{s}^{-1}$ 

$12.89 \text{ km} \cdot \text{s}^{-1}$ 

$13.30 \text{ km} \cdot \text{s}^{-1}$ 

$13.71 \text{ km} \cdot \text{s}^{-1}$ 

VITA

Surname: IRWIN Given Names: JUDITH ANN

Place of Birth: Saskatoon, Sask. Date of Birth: Feb 14, 1954

Educational Institutions Attended, with Dates of Entering and Leaving:

University of Winnipeg 1972 to 1975

University of Victoria 1975 to 1978

_____ to _____

_____ to _____

Degrees, Diplomas, Etc., Awarded, with Dates and Names of Institutions:

B. Sc. 1975 University of Winnipeg

Honors and Awards:

R. M. Petrie Memorial Fellowship

Publications:

PARTIAL COPYRIGHT LICENSE

I hereby grant the right to lend my thesis or dissertation (the title of which is shown below) to users of the University of Victoria Library, and to make *single copies only* for such users or in response to a request from the library or any other university, or similar institution, on its behalf or for one of its users. I further agree that permission for extensive copying of this thesis for scholarly purposes may be granted by me or a member of the University designated by me. It is understood that copying or publication of this thesis for financial gain shall not be allowed without my written permission.

Title of Thesis/Dissertation

CONTINUUM AND ATOMIC HYDROGEN LINE EMISSION FROM THE IC5146

GALACTIC COMPLEX

Author



Signature

JUDITH ANN IRWIN

Name

JULY 6, 1978

Date